Imperial College London

RF Sensors for Monitoring the Electrical Properties of Electrolyte Solutions

By

Siavash Saremi-Yarahmadi

A dissertation presented to the Imperial College London University in partial fulfilment of the requirements for the degree of Doctor of Philosophy

Department of Electrical Engineering

Imperial College London

South Kensington

London, UK

2012

Acknowledgements

I would like to thank my supervisors Dr. Kristel Fobelets and Professor Chris Toumazou for their support over the past 4 years. Dr Fobelets has been a beacon of knowledge and hope for me. She encouraged me to be better at every stage of my PhD work and learn more. I am greatly indebted to her for this.

I would like to thank Dr. Jürg Fröhlich at ETH Zurich for supervising me for part of my PhD. My gratitude is also extended to Christian Beyer, Dimitra Psychogou and all members of the IFH centre at ETH Zurich who made my stay an unforgettable one.

I would like to extend my gratitude to many people who believed in me and encouraged me to continue with my work. In no particular order I would like to thank Angela Koffman, David Yates, Alex Casson, Esther Rodriguez-Villegas, Eduardo Aguilar Pelaez, Lojini Logesparan, Kaushal Choonee, Evdokia Kardoulaki, Daniel Balint, Clare Balint, David Charles, Yan Liu, Simos Evangelou, Sohasini Sutharasingham, James Field, Yujie Zhao, Christina Morris, Virginia Woods, Dylan Banks, Oghenevworhe Joan Omeru, Alexander Ivanov, Mariam Ayub, Andrew Chamberlain, Timmy Floume, Munir Ahmad, Tom Tate, Steve Wright, and Vanessa Garcia-Larsen.

I would like to thank my parents for their unlimited support and in particular my beloved sister for her love and faith in me. I cannot express my gratitude to them in words.

Declaration

This research and the work described in this thesis were conducted in the Department of Electrical and Electronic Engineering at Imperial College London UK and the Department of Information Technology and Electrical Engineering at ETH Zurich Switzerland. The research spanned from November 2007 to April 2012. The work in this thesis is original, except as acknowledged, and includes nothing, which is the outcome of work in collaboration, and no part of it has been submitted for a degree at any other university.

Publications

Saremi-Yarahmadi, S.; Murphy, O.H.; Toumazou, C.; "RF inductive sensors for detection of change in the ionic strength and pH of liquid samples," Circuits and Systems (ISCAS), Proceedings of 2010 IEEE International Symposium on, vol., no., pp.2279-2282, May 30 2010-June 2 2010

Saremi-Yarahmadi, S.; Fobelets, K.; Toumazou, C.; "Coupled RF inductive sensors for monitoring the conductivity of electrolyte solutions," Medical Information & Communication Technology (ISMICT), 2011 5th International Symposium on, vol., no., pp.20-23, 27-30 March 2011

Saremi-Yarahmadi, S.; Fobelets, K.; Toumazou, C.; "Coupled inductive sensors for monitoring the pH of electrolyte solutions," Dielectric Liquids (ICDL), 2011 IEEE International Conference on, vol., no., pp.1-4, 26-30 June 2011

Abstract

A radio frequency electrical sensor for the qualitative analysis and monitoring of the electrical properties of electrolyte solutions is designed, simulated and experimentally tested in this research. This work is based on the use of planar inductors for the detection of a change in the concentration of ionic species in a liquid sample. At first a literature review on the physical chemistry of electrolyte solutions is provided. This will include topics on the conductivity and relaxation properties of electrolytes. This will be followed by a look at dielectric spectroscopy sensors, electrochemical sensors and inductive sensing devices. The principles of electrodynamics and constitutive equations are discussed. Based on these, the principles of operation of the RF electrical sensors are analysed. Two methods of theoretical analysis of such structures are investigated. These methods are; analytical solution and finite element computation method. The former offers greater insight into the system's parameters whilst the latter offers more information regarding the whole system. Given the qualitative nature of the sensors under investigation and finite element approach was selected and used in latter chapters to obtain grater insight into the behaviour of the system.

Planar inductor coils are designed on an FR4 substrate and packaged using PDMS to be used as sensors in the monitoring of electrical properties of electrolytes. Experimental results on these sensors are provided and discussed. The effects of solvent, acidity of the solutions, and environmental factors on the behaviour of the sensors shall be discussed. This is followed by finite element simulations of the sensor and the effect of various parameters on the overall behaviour of the sensing device. A transformer apparatus is also constructed and experimental data are provided for it. An electrolyte is placed on one of the coils of the transformer and scattering parameters are looked upon for data analysis. The results obtained using the FE method, is then used to obtain further information about the principle of operation of the device.

Table of Contents

List of Figures

List of Tables

List of Acronyms

CMOS	complementary metal oxide semiconductor
CPW	coplanar waveguide
CVD	chemical vapour deposition
DC	direct current
DNA	deoxyribonucleic acid
DSR	double split resonator
FE	finite element
FET	field effect transistor
ICs	integrated circuits
ISFET	ion sensitive field effect transistor
LC	inductor-capacitor
LFDD	low frequency dielectric dispersion
MEMS	microelectromechanical systems
MVP	magnetic vector potential
PCB	printed circuit board
PCR	polymerase chain reaction
PDMS	polydimethylsiloxane
PECVD	plasma enhanced chemical vapour deposition
PMMA	poly(methyl methacrylate)
RF	radio frequency
RLC	resistor-inductor-capacitor
RMS	root mean squared
SRR	split ring resonator
TEM	transverse electromagnetic modes

List of Latin Symbols

A	magnetic vector potential	Wb m^{-1}
A	Debye-Hückel-Onsager coefficient	mS m^2 mol^{-1} $(mol\ L^{-1})^{-0.5}$
B	magnetic flux density	Wb m^{-2}
B	Debye-Hückel-Onsager coefficient	$(mol\ L^{-1})^{-0.5}$
D	electric flux density	C m^2
E	electric field intensity	V m^{-1}
F	force	N
H	magnetic field intensity	A m^{-1}
H	enthalpy	J
J	electric current density	A m^{-2}
M	molar mass	kg mol^{-1}
P	real power	V A
P	polarization	C m^{-2}
P_d	dissipated power	J s^{-2}
Q	reactive power	V A reactive
S	Poynting's vector	J s^{-1} m^{-2}
S	entropy	J K^{-1}
T	temperature	K
c	concentration	mol L^{-1}
n	refractive index	
p	dipole moment	C m
q	electric charge	C
q_v	electric charge density	C m^{-3}
v	velocity	m s^{-1}
$\overline{w_e}$	electric energy density	J m^{-3}
$\overline{w_m}$	magnetic energy density	J m^{-3}

List of Greek Symbols

Λ_m	molar conductivity	S m^{-1} mol^{-1} L
ε	permittivity	F m^{-1}
η	viscosity	Pa s
λ_+ λ_-	limiting molar conductivity	mS m^2 mol^{-1}
μ	permeability	H m^{-1}
ρ	density	kg m^{-3}
σ	conductivity	S m^{-1}
τ	relaxation time	s
ω	angular velocity	rad s^{-1}
φ	electric scalar potential	V

Chapter 1

1 Introduction

Electrical properties of electrolyte solutions are important indicators to the progress of chemical reactions. The dissolution process, oxidation and reduction are examples of chemical reactions that can take place inside a liquid sample. These reactions can lead to changes at deep molecular level, for instance protein folding and refolding [1], or on macroscopic level, like the variation in the permittivity of the bulk solution [2]. Monitoring such changes can lead to important information regarding the status of a chemical reaction and the species responsible for it. Measurement methods like dielectric spectroscopy in radio frequency (RF) and deep infrared (THz) region of operation [3, 4] , optical spectroscopy [5], and various electrochemical techniques [6, 7] are examples of sensory systems developed for the monitoring of chemical reactions.

In this research variations in the properties of planar inductors, like variations in the impedance of these devices, are used to provide qualitative data analysis on an electrolyte solution. Planar inductors are used to produce a magnetic field in the vicinity of a liquid sample under test. The applied magnetic field will induce eddy currents (EC) within this sample. The density of the induced eddy currents is a direct function of the electrolyte conductivity. These induced eddy currents produce their own magnetic field which interacts with the driving magnetic field produced by the inductor. The interactions between the coil's magnetic field and the induced eddy current's magnetic field are translated into a change in the impedance of the coil [8]. This impedance is correlated to the conductivity of the electrolyte solution under test. The variations in the permittivity of the sample will also affect the coupling between the sample and the planar inductor, contributing to the parasitic capacitance. Variation in the permeability of the sample under test is another contributing factor to the change in the properties of the sensor [9]. The use of inductors, due to their inherent electromagnetic properties, also allows for the development of a wireless communication interface. This interface can be used in the transmission of data between the

sensor and a data processing unit with no need for the presence of a physical medium e.g. wire-bonds will not be needed. This could simplify the packaging of the sensor and lead to a reduction in post-processing steps in preparation of the sensing device. The work done in this research offers the potential of adapting this sensor with minimum modifications for use as an implantable device e.g. monitoring gastric juice in the oesophagus. It also offers the potential for the development of remote interrogating systems for implanted sensors inside the human body.

A tag free sample analysis that requires no sensor surface activation will be adapted in this research; hence no external material will be added to the solution in order to amplify the effects of a particular reaction or species. Different packaging materials would be used and their effect on the properties of the inductor will be investigated. Biocompatibility of these packaging materials is also of great importance and shall be investigated. Near field coupling of the sensor with an antenna for wireless readout of the sensory data will be analysed. Finite Element (FE) analysis will be used in order to model the behaviour of the sensor in the presence of various electrolyte solutions. FE will also be used to look at near field characteristics of the sensor for wireless data transmission. The solutions obtained using FE, alongside experimental data, will be used to optimize the design. The coupling between multiple sensors and their response with regards to a readout antenna is also of interest and will be investigated. This is to find the optimum distance and optimum sensitivity between sensors and also between sensors and the readout coil.

In this chapter an overview of the physical chemistry of water in section one. This is followed by an overview of electrical properties of electrolyte solutions. Conductivity and permittivity of the liquids and factors affecting them shall be discussed in this part. Section three will provide a literature review on three main sensing mechanisms and platforms. These sensors are dielectric sensors, electrochemical sensors and inductive sensors. This will be followed by a discussion on the advantages and disadvantages of these sensing platforms in section four. A comparative discussion on the choice of sensors in this research and its applications to the wider research field will be given as well.

1.1 Water

Water is physically the smallest molecule with more than two atoms. It has an effective radius of 1.4 Å. Hydrogen molecule has an effective radius of 3.4 Å [10]. Water is also the only naturally occurring inorganic liquid on planet earth [11] which its existence is intertwined with life on this planet. Due to its electron configuration, water molecules are

capable of forming hydrogen bonds between themselves. This is due to the high electronegativity of the oxygen atom compared with hydrogen atom. Oxygen has an electronegativity of 3.44 and hydrogen has an electronegativity of 2.2. Oxygen atom also contains two free electron pairs. Hence the overall results leads to the formation of hydrogen bonds in water which results in relatively high melting and boiling points. Water assumes a solid form at 273.15 K and reaches its boiling point at 373.15 K. The measured maximum density of water is at its highest value at a temperature of 277.15 K, for more information on experimental and calculated properties of water refer to [12].

Figure 1-1 shows a cluster of water molecules in their frozen state. The size of this cluster is 12 Å, 11 Å, and 6 Å in the x, y, and z directions respectively. Red sticks represent oxygen atoms and white sticks represent hydrogen atoms. The white dashed line is used to show the hydrogen bonds between neighbouring hydrogen and oxygen atoms. Note the orderly fashion in which water molecules are aligned in frozen state. Figure 1-1b shows the state of the same cluster of water molecules as the temperature is increased to 293 K. It can be seen that the rigid structure of ice is now broken to form a more closely packed energetic liquid system. This simulation is performed in CambridgeSoft ChemDraw software. As hydrogen bonds start breaking up whilst frozen water heats up, water molecules start filling in the empty space that was previously unoccupied, compare figures 1.1a and 1.1b. This process reaches its peak value at 277.15 K. Beyond this temperature the kinetic energy of water molecules is high enough to force water molecules to move away from this closely packed fluidic medium and hence the density of water decreases until it reaches the water's nominal density.

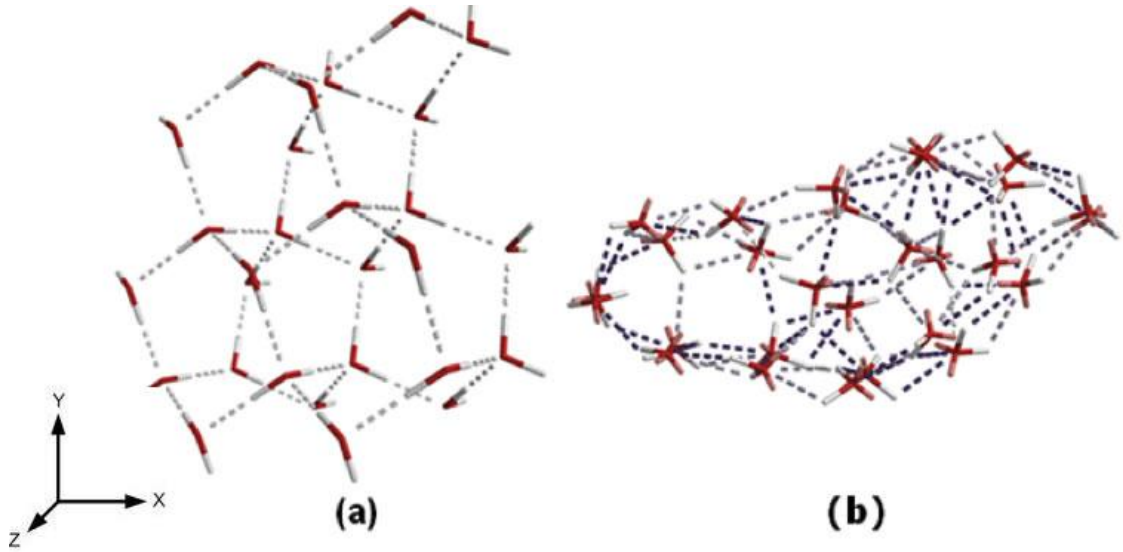

Figure 1-2: showing the molecular structure of water when solid (a) and the departure from this ordered form as the temperature increases to 293 K (b). The size of the frozen cluster is (11,12,6) Å

Water is a polar liquid; water molecule has a permanent electric dipole moment associated with it, and dissolves the majority of ionic compounds. Other examples of polar solvents are diethylether, ethanol and acetone. The oxygen atom has six free electrons from which two are used in the covalent bonds with the two hydrogen atoms. The remaining four electrons form two electron pairs that allow the formation of hydrogen bonds with hydrogen atoms covalently bonded with other oxygen atoms. The formation of hydrogen bond is a dynamic process and these bonds are continuously formed and broken. The time it takes for a hydrogen bond to form and break is in the order of 2 ps to 2.5 ps [13]. The dielectric constant of water is also related to the H-bond formation energy [14]. The dielectric constant of water is related to the H-bond free energy of formation by the following equations.

$$\frac{(\varepsilon_s - \varepsilon_\infty)(2\varepsilon_s + \varepsilon_\infty)}{\varepsilon_s(\varepsilon_\infty + 2)^2} = \frac{4\pi N_{AV} g \mu^{v\,2}}{9kTV\epsilon} \qquad 1.1$$

$$g = 1 + \frac{4e^{\frac{-(H-TS)}{kT}}}{3\left(1 + e^{\frac{-(H-TS)}{kT}}\right)} \qquad 1.2$$

In equations 1.1 and 1.2, H is the enthalpy, S is the entropy, T is the absolute temperature, g is called the structure factor, ε_s is the dielectric constant, V is the volume, k is the Boltzmann constant, N_{AV} is the Avogadro's number and μ^v is the dipole moment of water molecule in vapour phase. ε_∞ is the dielectric constant of water at a high frequency in which dipolar relaxation processes are inoperative however is low enough not to induce atomic and electronic polarization [14]. $\varepsilon_\infty = n^2$ in which n is the refractive index of the material. In the case of water, a refractive index of 1.33 is commonly used. However due to fluctuations in the value of refractive index in IR spectra, a value of 1.8 is also suggested in place of 1.33 [14]. In this research the value of 1.33 is used for the refractive index. Note that water at a temperature of 647.15 K and a pressure of 2.23×10^7 Pa becomes supercritical. In this state water has a density which is a third of its nominal value. Hydrogen bonds within the liquid water are largely destroyed. Water becomes a poor ionizing solvent and a better organic solvent which is contrary to its nominal properties [15].

1.2 Electrolyte Solutions

Solutions that can conduct electricity are called electrolyte solutions. The classical model of electrolyte solutions, the Debye-Hückel model, assumes free ions in the solution as hard

spheres and the space between them filled with a dielectric medium. This dielectric medium has the permittivity of the pure solvent. This model holds for dilute solutions of concentration less than approximately 0.001 mol L^{-1} [16]. Beyond this concentration, the interactions between ions within the sample and the viscosity of the electrolyte solution are no longer negligible and must be taken into account. These factors affect the behaviour of charge carriers in the solution. This leads to non-linear variations in the electrical properties of the electrolyte with respect to the type of solute and its concentration. Hence an understanding of various factors affecting the behaviour of charge carriers in a liquid is desirable. Only solutions with water as the solvent are considered in this research.

Electrolyte solutions can be placed into two categories of strong and weak solutions, based on the degree of ionization of added substances to the solvent [17]. Strong electrolytes are those that are fully dissolved in water and are completely dissociated, e.g. hydrochloric acid, sodium chloride and sodium bromide. Weak electrolytes are those that are partially dissolved in water, e.g. acetone, phosphoric acid and sodium dihydrogen phosphate. Dependent on the type of the electrolyte under investigation, weak or strong, different formulas may be used to describe the variation in their electrical properties. The two electrical properties of interest are conductivity and permittivity.

1.2.1 Electrolyte Conductivity

The conductivity of electrolyte solutions is dependent on the degree of ionization of the added substances. It also depends on the ion-ion interactions of the free ions within the solvent. Hence conductivity is not just directly related to the number of free ions present in the solvent [18]. The molar conductivity of a solution is given by Λ_m and is equal to the conductivity of the sample divided by its concentration, c, expressed in mol L^{-1}. The conductivity, σ, of deionised water is very low due to a lack of free charged carriers, its value at room temperature is $\sigma_{water} = 1 \times 10^{-6}\Omega^{-1}m^{-1}$ [16]. Assume that a very small amount of a soluble substance is added to the solvent. This leads to the formation of a small number of free ions. These free ions will be able to move freely within the solvent and since the concentration of the added electrolyte is extremely low, there will be no interactions between ions within the solvent thus the Debye-Hückel model holds. The value of conductivity at this limit of zero concentration is called the limiting molar conductivity and is represented by Λ_m° [16, 19]. Limiting molar conductivity is the sum of limiting ionic conductivity of all the ions present in the sample.

$$\Lambda_m^\circ = \nu_+\lambda_+ + \nu_-\lambda_- \quad (1.3)$$

In Eq. 1.3 , λ_+ and λ_- represent the limiting ionic conductivity for cations and anions respectively and ν_+ and ν_- are the ratio of the number of cations and anions present in the solution. The limiting molar conductivity of various ions in water at 298 K can be found in Table 1-1 [17].

Table 1-1: Values for the limiting ionic conductivity of several ions, λ/ (mS m^2 mol^{-1})

Ions	λ	Ions	λ
Ca^{2+}	11.9	Na^+	5.01
H^+	34.96	Cl^-	7.635
K^+	7.35	OH^-	19.91
Mg^{2+}	10.6	NO_3^-	7.146

For strong electrolytes at concentrations below 0.001 mol L^{-1}, the molar conductivity follows the Kohlrausch's law and can be found to be:

$$\Lambda_m = \Lambda_m^\circ + (A + B\Lambda_m^\circ)\sqrt{c} \quad (1.4)$$

In Eq.1.4 the term, $A + B\Lambda_m^\circ$, is introduced by Lars Onsager and constants A and $B$are called the Debye-Hückel-Onsager coefficients [17]. They are substance specific and their values are $B = 0.229$ (mol L^{-1})$^{-0.5}$ and $A = 6.02$ mS m^2 mol^{-1} (mol L^{-1})$^{-0.5}$ for single valence electrolytes in water. The single valence electrolytes are also referred to as 1:1 electrolytes in the literature, e.g. NaCl. Note that both A and B depend on the temperature, charge of the ions and dielectric constant. The constant A also depends on the viscosity of the medium [20]. Equation 1.4 was later modified by Flakenhagen to obtain conductivity values for concentrations extending to 0.1 mol L^{-1}. This was achieved by introducing an adjustable parameter, a, which is the distance of closest approach between two ions in the solution [19, 21]. This distance is also referred to as the Debye- Hückel length or Debye length [22]. Equation 1.5 shows the Falkenhagen equation which is valid for electrolytes with concentrations below 0.1 mol L^{-1}. Variables B, B_1, B_2 and F(c) are functions of the solvents' viscosity, dielectric constant and absolute temperature. More information can be found in [19, 22].

$$\Lambda_m = \left[\Lambda^\circ - \frac{B_2\sqrt{c}}{1 + Ba\sqrt{c}}\right]\left[1 - \frac{B_1\sqrt{c}}{1 + Ba\sqrt{c}}F(c)\right] \quad (1.5)$$

An increase in the concentration of the solute in the solvent leads to an increase in the ion-ion interactions within the electrolyte. Hence various empirical equations have been developed to estimate the conductivity of an electrolyte solution reliably. Strong electrolytes of interest for this research are sodium chloride (NaCl), hydrogen chloride (HCl) and potassium chloride (KCl). The formula employed for calculating the conductivity of the samples is derived by Gellings. This formula was chosen based on the comparative analysis between eight widely used empirical formulas offered in [19]. Equation 1.6 shows the Gellings formula.

$$\Lambda_m = \Lambda_m^{\circ}(1 - Gc)e^{\frac{A_G\sqrt{c}}{1+Ba\sqrt{c}}} \quad 1.6$$

$$A_G = \frac{8.2 \times 10^{-7}}{\sqrt{\varepsilon_0 T}} + \frac{82.5}{\Lambda_m^{\circ}\eta_0\sqrt{\varepsilon_0 T}} \quad 1.7$$

$$B = \frac{50.29}{\sqrt{\varepsilon_0 T}} \quad 1.8$$

In the above equations, *a* is the Debye- Hückel length, *G* is an adjustable parameter which its physical meaning is unclear [19], ε_0 and η_0 are solvent's permittivity and viscosity respectively. Values for adjustable parameters *a* and *G* for each of the electrolytes of interest are given in Table 1-2 [19]. The unit of conductivity for the Gellings in Eq. 1.6 is in S mol^{-1} cm^{-2} however all results are converted into mS mol^{-1} m^{-2} for the analysis in this research.

Table 1-2: showing values for adjustable parameters used in Gellings equations [19].

Electrolyte	Conc./ mol L^{-1}	*a*	*G*
HCl	0.0-4.1	7.12	0.1235
NaCl	0.0-5.0	4.09	0.0836
KCl	0.0-4.0	4.28	0.0305

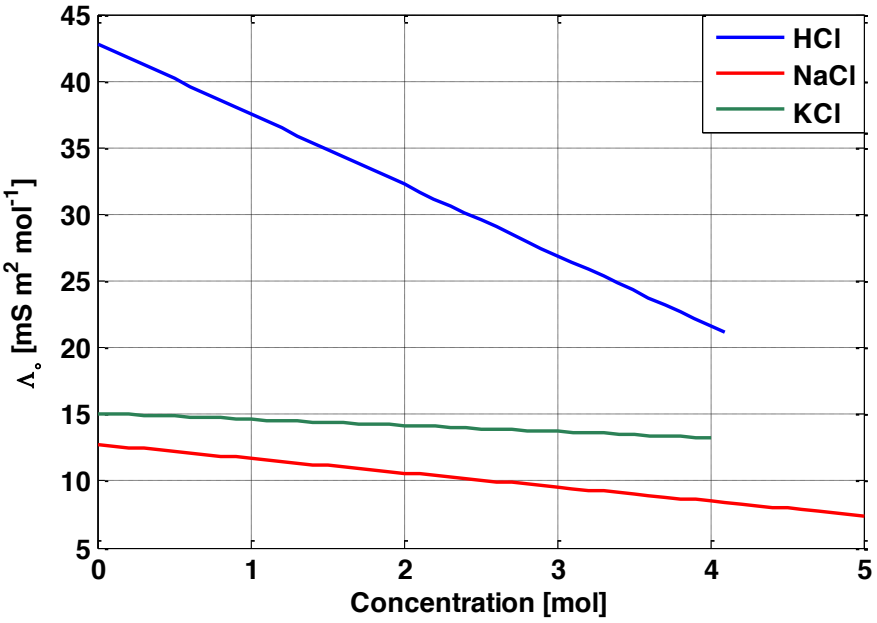

Figure 1-3: showing the variations of molar conductivity of HCl, KCl and NaCl as the concentration varies using the Gellings formula.

The variations in the conductivity of three strong electrolytes using the Gellings formula are shown in Figure 1-3. The formula was verified against reported experimental data for concentrations of 0-4.1 mol for HCl, 0-4 mol for KCl and 0-5 mol for NaCl [19].

The conductivity of weak electrolytes is proportional to the degree of ionization of the solutes in the solvent. Taking c to be the concentration of a solute in water, K_a to be the acidity constant and α the ionization constant, the equation for the molar conductivity of weak electrolytes is found to be [17]:

$$\Lambda_m = \frac{K_a}{2c}\left\{\left(1+\frac{4c}{K_a}\right)^{\frac{1}{2}}-1\right\}\Lambda_m^{\circ} = \alpha\Lambda_m^{\circ} \tag{2.3}$$

The exact explanation for the variation in conductivity of weak electrolytes mixed with other salts or acids in the highly concentrated regime is beyond the scope of this research, refer to [23, 24] for further information. For the analysis of experiments discussed in this research the formulas and data presented in literature, e.g. [23], will be used. Note that equations discussed in this section are aimed at 1:1 electrolytes (symmetric electrolytes). For more information on asymmetric electrolytes refer to [25].

1.2.2 Electrolyte Relative Permittivity

The permittivity of a material is a measure of its polarizability in the presence of an electric field. Polarization is a measure of the contribution of a material to electric displacement. Assume a material placed inside an electric field. Let D be the electric displacement in vacuum, D_m the electric displacement inside a material, χ the material susceptibility and ε_r the relative permittivity of the material. The polarization P can then be found to be [26]:

$$P = D_m - D = \varepsilon_r \varepsilon_0 E - \varepsilon_0 E \tag{1.9}$$

$$P = (\varepsilon_r - 1)\varepsilon_0 E = \chi \varepsilon_0 E \tag{1.10}$$

If the number of material molecules in unit volume is known, we can then calculate the value of polarization using the sum of all dipole moments in the material under test [26]. Let V be the volume of the sample under test, p_i be the dipole moment of a single molecule, N_A the Avogadro's number, ρ the density, M the molar mass of the substance and N the number density. The polarization of the material, using microscopic quantities, can be found to be:

$$\boldsymbol{P} = \frac{1}{V}\sum_{i=1}^{N} p_i \tag{1.11}$$

$$N = N_A\left(\frac{\rho}{M}\right) \tag{1.12}$$

The formula in 1.11 provides the total instantaneous polarization within a sample. The value of P can be broken into three separate contributions. These contributions are electronic polarization, atomic polarization and orientation polarization [27]. Hence the total susceptibility of a material can be defined as:

$$\chi_t = \chi_e + \chi_a + \chi_o = (\varepsilon_r - 1) \tag{1.13}$$

The electric polarization contributions, χ_e, are due to the moment generated by the displacement of electrons with respect to the atoms of the molecule in the presence of an external E-field. The atomic polarization contributions, χ_a, are due to the moment generated by the displacement of atoms with respect to one another. The latter has a larger contribution to the total susceptibility of the material. Electronic and atomic polarizations are collectively referred to as distortion polarization [27]. Due to the nature of these two effects, they are temperature independent or the contribution of temperature is found to be negligible [26].

However the orientation polarization contribution to susceptibility, χ_o, is temperature dependent. Orientation polarization is present in substances that consist of polar molecules. It is based on the alignment of permanent dipoles in the presence of an applied E-field. The polar molecules tend to align themselves with the applied field however if the kinetic energy of the molecules is greater than the orientation energy, random misalignment will be introduced into the sample. This kinetic energy is temperature dependent. This behaviour can easily be seen in the Debye equation which depicts the relationship between molar polarization and absolute temperature [26]. In 1.14, P_{mol} is the molar polarization of the sample, α is the polarizability, N_A is the Avogadro's number, k is the Boltzmann constant, T is the absolute temperature and p_p is the permanent dipole of the molecules under test.

$$P_{mol} \equiv \frac{1}{3\varepsilon_0} N_A \left(\alpha + \frac{p_p^2}{3kT} \right) \qquad 1.14$$

The other factor affecting polarization of a material and hence its permittivity is the frequency of the applied field. Based on the frequency of the applied field, one or more contributors to polarization in a material become dominant. At lower frequencies the orientation polarization is the dominant factor. However as higher frequencies are approached the distortion polarization's contribution increases and as we approach frequencies of about $10^{12} Hz$ the distortion polarization becomes the dominant factor. As the frequency of the applied field increases, the polar molecules can no longer follow the applied E-field due to their large mass. Hence the orientation contribution to the permittivity of the sample decreases and distortion polarization becomes more dominant. Note that at these very high frequencies the Debye equation no longer holds and one must use the Clausius-Mosotti equation. In this region of operation movements of the electron cloud along with rotational and vibrational motions of the atoms and bonds can be detected [18, 26]. The frequency dependence of polarization gives rise to a complex permittivity in which the complex component of the permittivity corresponds to the phase lag between the applied field and various polarization effects in that frequency. This implies power dissipation within the sample which is coined as anomalous absorption.

The derivation of a frequency dependence permittivity function can be found in [27-30]. Only referring to the final derivation in [28], the complex permittivity can be found to be

$$\varepsilon = \varepsilon' - j\varepsilon'' \qquad 1.15$$

$$\varepsilon'(\omega) = n^2 + \frac{\varepsilon_s - n^2}{1 + \omega^2\tau^2} \quad 1.16$$

$$\varepsilon''(\omega) = \frac{(\varepsilon_s - n^2)\omega\tau}{1 + \omega^2\tau^2} + \frac{\sigma}{\omega}\left(\frac{1}{4\pi \times 9 \times 10^{11}}\right) \quad 1.17$$

In equations 1.15 to 1.17, n is the refractive index, ε_s is the static permittivity, ω is the angular frequency, σ is the conductivity in $\Omega^{-1}cm^{-1}$and τ is the macroscopic relaxation time. For water, τ is found to be $0.93 \times 10^{-11}\ s$ at 20°C [28].

So far we have discussed simple electrolyte solutions, e.g. solutions of water and HCl or KCl. There exist another class of solutions that contain macromolecules which biological samples like DNA fell under their category. These solutions are called polyelectrolyte solutions and are defined as "macromolecules which in solution carry a relatively large number of charged groups." [31]. Figure 1-4 shows the structure of a DNA macromolecule and its corresponding 3D visualization. It can be seen that there exist many oxygen and nitrogen atoms in the molecular chain of this macromolecule. These atoms contain many free electron pairs which can lead to a net charge on the molecule. This can also lead to strong static force being generated in the immediate vicinity of the macromolecule. This can affect the dispersion properties of the solvent containing the macromolecule. In this case the orientation polarization of the hydration shell is modified.

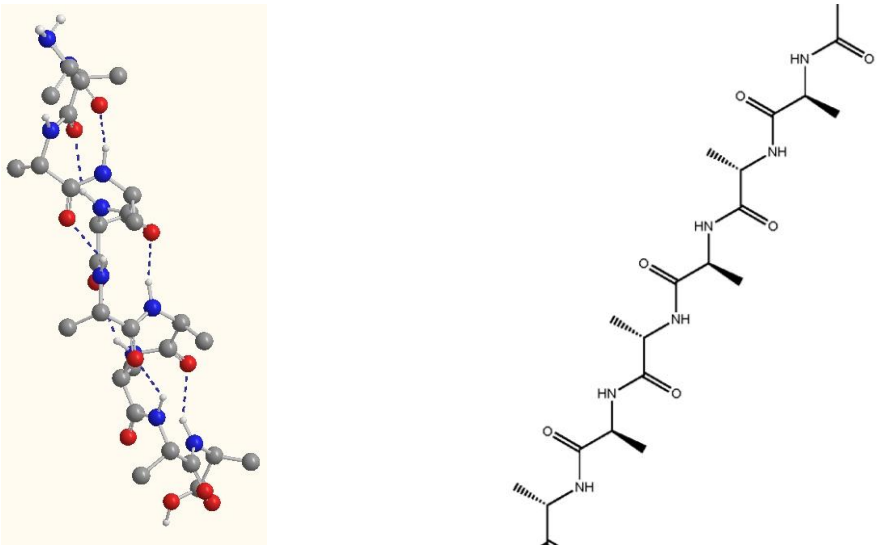

Figure 1-4: showing the 3D structure of a DNA strand and its corresponding formula

Ions and polyions in water are surrounded by two layers of water molecules [32, 33]. These layers are called the primary and secondary hydration shells. The number of water molecules

surrounding an ion is called the hydration number, e.g. Na^+, Mg^{2+} and Cl^- all have six water molecules in their primary hydration shell. Note that water molecules within the primary and secondary shell dynamically change their position between layers however there is at all times a constant number of molecules present in each layer [34]. The water molecules in the secondary layer are H-bonded to the primary shell molecules and face electrostatic force from the ion. This electrostatic force exerted on the water molecules in the hydration shell causes their dispersion to be different from the bulk water. A depiction of the primary and secondary hydration shells can be found in Figure 1-5. A typical macromolecule such as DNA has a diameter of 20 nm and its primary hydration shell has a thickness of 0.3 nm [32]. The secondary hydration shell has a thickness of 0.1 nm to 0.5 nm [33]. Hence, the force exerted by the macromolecule on its surrounding water molecules extends 0.4 nm to 0.8 nm away from the molecule. The bulk solvent maintains its intrinsic permittivity however the two hydration shells will show different values of permittivity. The hydration shells play an important role in the interaction of the macromolecule with its surrounding and also its behaviour, such as the replication of DNA. For more information on the effect of hydration shell refer to [33].

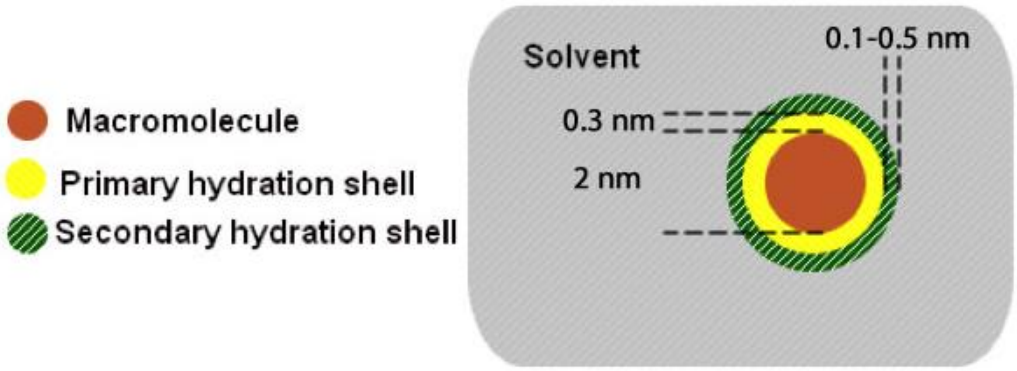

Figure 1-5: showing the presence of primary and secondary hydration shells around a macromolecule.

Polyelectrolyte solutions generally show a large ionic electrical conductivity in the low frequency region of the spectrum which can subsequently mask the relaxation effect of larger molecules in the sample [35]. Some of the fundamental factors contributing to the relaxation process in polyelectrolyte solutions are polyion dipolar orientation relaxation, polarization of condensed counterions, polarization of the ionic atmosphere and long range solvent ordering effects [35].

It must be noted that the dispersion properties of the solvent will also be modified by the solute. As a result these variations in the dispersion of the solvent can be used as an indicator

to monitor chemical reactions. For instance, orientation polarization of some of the solvent molecules is modified by the presence of a solute at high frequencies. Note that when an ion moves in liquid water under an electric field, it carries as many as 40 molecules with it [36] and the ion reaches its terminal velocity in approximately 10^{-13}seconds [16]. Taking this solute-solvent relationship into account, alongside environmental factors, we can provide a list of particular dispersion properties which exist in biological samples, shown in Table 1-3 [37].

Table 1-3: Different mechanism of dispersion within biological samples, from [37].

Type of Dispersion	Description
α-dispersion	Permittivity enhancement by rearrangement of small ions, including screening effect at the fluid-sensor interface.
β-dispersion	Arises from the distortion of cellular membranes and macromolecules. It occurs at frequencies below 100 MHz.
γ-dispersion	Rotation and deformation of small polar molecules, for instance the solvent. It is a wide peak with maximum value at 19.6 GHz for pure water.
δ-dispersion	Bound water dispersion. This arises from the electrostatic force exerted by the solute on the primary and to a smaller extent on the secondary hydration shell. It occurs in a frequency range of 500 MHz to 20 GHz.

α-dispersion or low frequency dielectric dispersion (LFDD) arises from the rearrangement process of ions in the solution [38]. β-dispersion is due to the rotational orientation of macromolecules. Examples of such macromolecules could be a variety of proteins and DNA strands. γ-dispersion deals with the relaxation process in the electrolyte solution. δ-dispersion corresponds to the permittivity of the hydration shell. The latter is of particular interest as its properties can be exploited to detect a change in the geometry of the molecule under investigation [37]. As the shape of a molecule varies the molecular arrangement of the hydration shell also changes. This leads to changes in the permittivity of this layer. For more information on the dispersion in electrolyte solutions refer to [30, 38]. The measured experimental complex permittivity of water is also provided in Figure 1-6 for comparison [39]. Refer to section 5.3.1 for more information on the complex permittivity of electrolyte solutions.

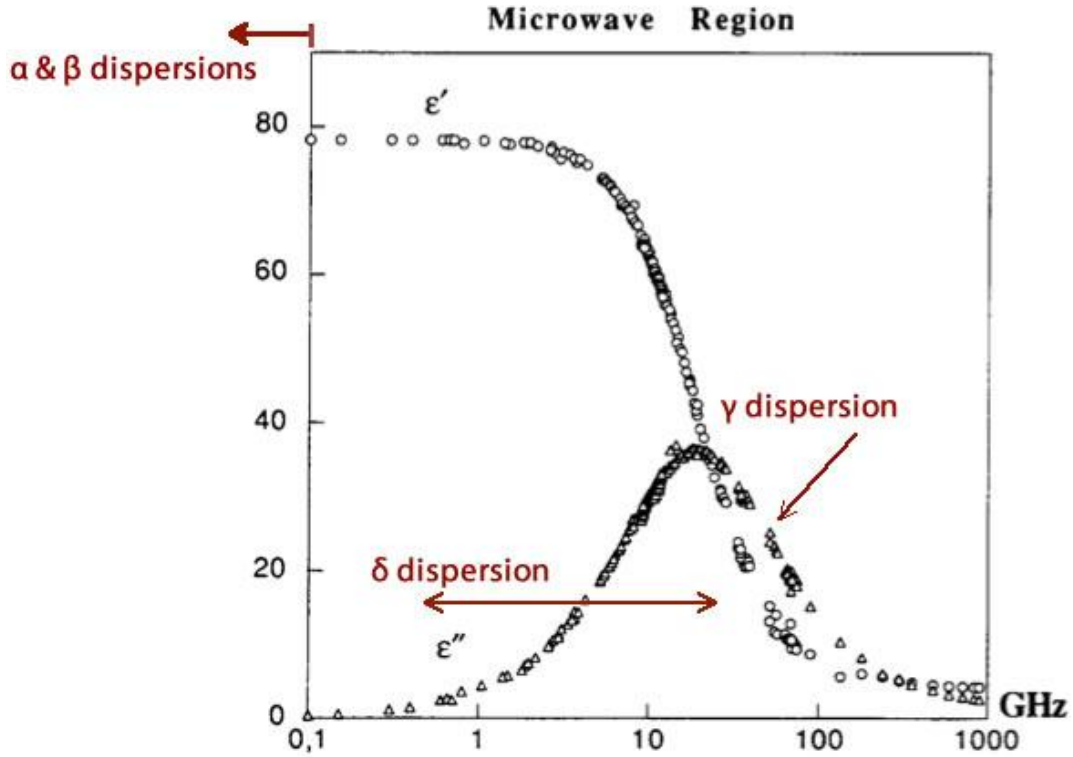

Figure 1-6: showing the plot of complex permittivity of water for a frequency range of 100 MHz to 1 THz. [39]

1.3 Literature Review

We have discussed the physical changes that occur inside a liquid sample when reactions take place. Macro-properties like the bulk conductivity of the sample and its bulk permittivity along with micro-properties like the δ-dispersion. In this section an overview of sensing platforms and architectures that use the afore-mentioned variations as the basis for performing measurement will be provided. The scope of this literature review is limited to three main types of sensors. They are dielectric sensors, electrochemical sensors and inductive sensors.

1.3.1 Dielectric Sensors

Dielectric measurements provide details on the polarization relaxation properties of a sample under test. Relaxation is a lossy process. Hence the amount of energy dissipated into a sample and the frequency at which this energy dissipation happens can be used as indicators to the progress of a change in a liquid sample. Dielectric spectroscopy can be classified as a non-destructive method of measurement in which the sample under test is not destroyed. The perturbation to the system under test can also be minimal. This method can be used in

monitoring various changes including protein folding and refolding, monitoring DNA amplification processes and monitoring the concentration of various electrolyte solutions like HCl. In this section, a range of sensing architectures along with their advantages and disadvantages shall be discussed. The frequency of operation of the reviewed sensors is in the range of a few MHz to the THz region of operation. Higher frequency systems, like X-ray, are not discussed in this research.

In [40] a microwave stripline probe is designed to operate at a frequency of 169 MHz. The stripline has a width of 140 μm and is covered by a PDMS micro channel. As beads or biological cells are passed above the stripline its impedance varies. This is translated as a change in the reflected power at the ports of the probe and is used as an indicator to the presence of biological cells or beads in the chamber above the stripline. This design is used in successfully counting the number of beads passing above the probe in the microfluidic channel. Figure 1-7 shows the structure of the probe along with the positioning of the inlet and outlets for the microfluidic channel [40]. This device has a counting limit of 25 beads/ms, which is comparable with commercial fluorescent cell sorters [40].

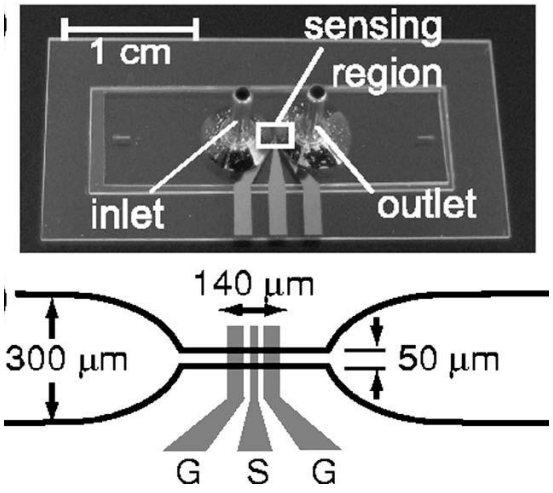

Figure 1-7: showing the structure of the RF probe and the positioning of the microfuluidic channel [40]

In [37] a slotted antenna is used to look at protein folding and refolding by monitoring the protein's hydration shell dispersion. The underlying theory of hydration shells is discussed in section 1.2.2 and is also shown in Figure 1-5. In this design, a cuvette is placed in the middle of the slot of the antenna and the return loss of the antenna-cuvette system is then analysed. A good correlation between the experimental values of the solution's permittivity and sensory data, for values of $\varepsilon < 60$, were found using this system. Strong temperature dependence of data was observed which should be factored in upon performing the analysis. Equation 1.14 can be used to explain this strong temperature dependence given the operational frequency of

3-20 GHz. One of the main challenges with this apparatus was the sensitivity of the system to the position of the cuvette. Every time that the cuvette was removed to replace the protein sample, the characteristics of the system would change. Hence the system showed low repeatability. However the ease of fabrication and the ability of the system to allow for simultaneous optical measurements are two main advantages of this design. The other advantage of this device is its sensitivity. Measurements in concentrations as low as 19 pmole were recorded. The only other method of measurement that can be used in such low concentrations is fluorescence spectroscopy, which requires labelling, and sample pre-processing [37]. Figure 1-9 shows a depiction of this system.

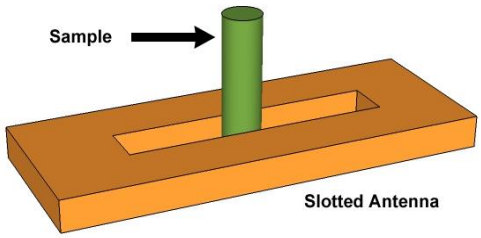

Figure 1-8: showing the conceptual design of slotted antenna being used in dielectric spectroscopy

In [41, 42] a Wilkinson power divider is used to perform dielectric measurements on mixtures of ethanol and methanol with water. Figure 1-10 shows a conceptual depiction of the differential design employed in this paper. Distilled water is placed on one branch of the power divider and the other branch is covered with the sample of interest. A frequency range of 5.4-6.4 GHz was employed in this design. S-parameter data, for a range of ethanol and methanol water mixtures, were used for detection purposes. This design offers a sensitivity of 30 times greater than the one offered by fluorescence spectroscopy [42]. A variation of this design with two Wilkinson power dividers was employed [43] which offers greater sensitivity. A similar approach of placing the test sample over a transmission line is adopted in [44]. In this design a CPW is fabricated by depositing gold on a glass substrate and is used in the analysis of human blood for haemoglobin. The blood sample was then placed on top of the transmission line using a PDMS mold. The authors provide no direct analysis on the sensitivity of this system, as the designed device is used for qualitative measurements only. Figure 1-11 shows a sketch of this apparatus [44]. Due to the simplicity of design, coplanar waveguides are also used in a variety of designs. In [45] the CPW is used in monitoring the formation of lipid layers, frequencies of up to 14 GHz were employed in this design. In [46, 47] CPW were used in a frequency range of 45 MHz to 40 GHz to monitor the complex permittivity of methanol in nano-litre volumes. Similar design were also used in simultaneous

detection of a mixtures of salt and glucose [48] and suspended CPW lines for biosensing purposes [49].

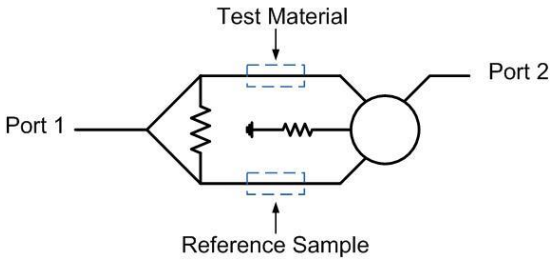

Figure 1-10: showing the conceptual design of a Wilkinson power divider being used in dielectric spectroscopy [42]

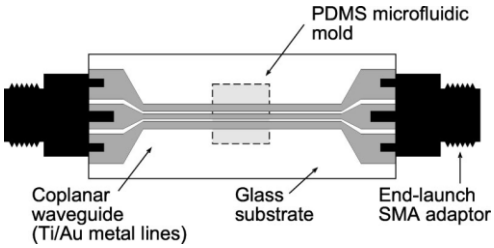

Figure 1-11: showing the conceptual design of a CPW used in the analysis of haemoglobin [44]

All the CPW designs discussed above perform label free measurements on the sample under test. For particular tests, it may be needed to chemically activate the surface of the sensor. In [50, 51] surface activation of a CPW is used in order to undertake monitoring of chemical reactions. In these two designs the transmit time of the RF signal in the transmission line is used as a measure of binding of target molecules to receptors placed on the sensing area. As these receptors react with the target molecules and attach to one another, they change the chemistry of materials in the immediate vicinity of the transmission line. For instance as more target molecules react with receptors, the number of water molecules in the vicinity tend to decrease. Hence the dielectric constants of the areas near the interface of the transmission line and the liquid changes. This change in permittivity leads to variations in the group velocity of the electromagnetic modes travelling in that part of the transmission line [51]. This variation in the permittivity of the areas near the RF signal path is the basis for surface activated measurement devices. Figure 1-12 shows the conceptual depiction of a surface activated CPW used in detecting various proteins [51]. Dimensions of the device are 4 mm wide and 20 mm long. The sensor is employed in monitoring the reaction between protein-A and rabbit immunoglobulins. The surface sensitivity of this device was estimated to be 100 pg mm^{-2} however experimental data showed a sensitivity of 0.5 ng mm^{-2}.

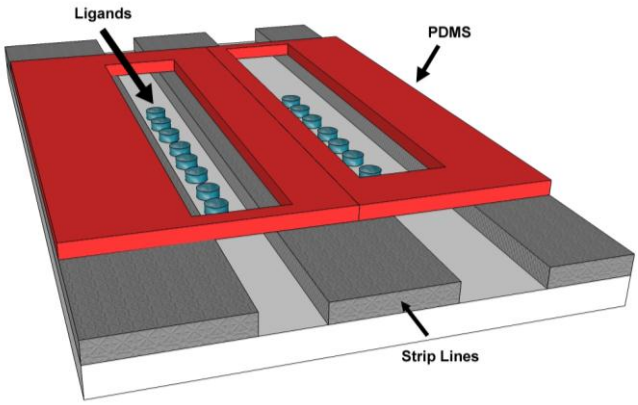

Figure 1-12: showing surface activated coplanar transmission line used in bioanalysis. The structure is 4 mm wide and 20 mm long.

Another method of performing dielectric spectroscopy is the use of resonating devices. A resistor-inductor-capacitor (RLC) resonator is realized in [52, 53]. The RLC is realized by placing a meandered inductor at the centre of an interdigited capacitor. Figure 1-13 shows a depiction of the resonator design used in [52]. The resistance component is the series resistance of the inductor itself. The contact to this resonator is done by a CPW and measurements are performed in the range of 15 to 35 GHz. This device is then used in the analysis of cancerous cells cultures. No data on the sensitivity and detection limits of the device is provided, however, it is noted that beyond 35 GHz the detection limit of the biosensor is reached. This is due to the γ-dispersion of the biological cells, which does not extent beyond this frequency limit, as shown in Table 1-3. In [53] similar structure is used but in the form of a filter for the analysis of single cells. RF filter architectures are adapted for this design. Other methods of detecting various chemicals like the spintronic method are also developed in recent years which makes simultaneous use of optical and RF spectrum [54].

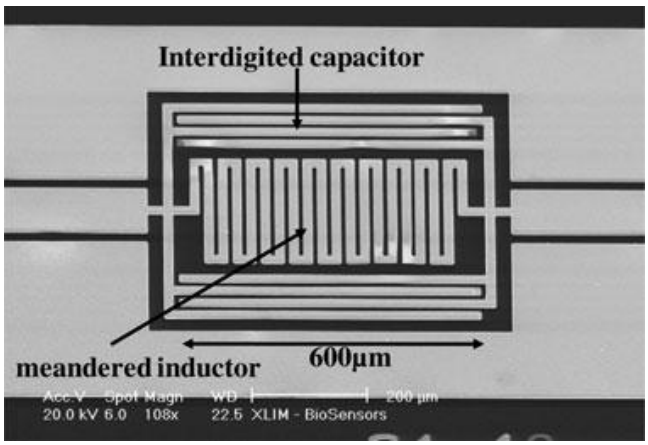

Figure 1-13: showing the layout of the RF RLC resonator [52]

So far we have looked at dielectric methods in the wavelength range of 1.8 m to 0.01 m, equivalent to 167 MHz to 30 GHz. If the analysis is performed in the frequency region of 0.1 THz and 10 THz [55, 56], the analysis is then called THz or far infrared spectroscopy. In this region of operation, the main aim of the measurements is largely the detection of molecular vibrations. In such high frequencies rotational motion of molecules can no longer follow the direction of the E-field fully. This is due to the fact that the frequency of the applied field varies at a much faster rate in which the molecule can change its rotation. However the frequency of the applied field is now comparable to internal vibrational motions within the molecule. Hence more information regarding the internal structure of a molecule can be found [26]. More information on the origin of vibrational modes of molecules can be found in [4, 57, 58]. Given the detailed information that can be realized using this method, THz spectroscopy has found many applications in the analysis of biological systems [59] to conservation of paintings by looking at the constituents of the paint used in a particular painting [60, 61].

One of the main drawbacks of deep infrared spectroscopy is the high relaxation loss of water molecules in the THz frequency which can be a major hurdle for biological sample analysis; the molecular relaxation time of water is $\sim 1\ ps$ [4]. As a result THz measurements should be applied to dry samples or the effect of water must be compensated. One method of overcoming this problem is to freeze the samples of interest to reduce the rotational motion of water molecules. This reduces the effect of water relaxation on the signal [62]. Another method to reduce the effects of water molecules relaxation in the THz region is to use pellets however this is a time consuming process [4]. Alternatively dry thin films can be used however THz sensing is sensitive to film thickness. Hence care must be taken to ensure the minimization of variations in the film thickness [4, 62]. Another technique employed in [63] aims to reduce the path of the THz signal inside the sample under test and hence reduce its sensitivity to the water present in the sample. Various implementations of THz antennas for bio-analysis [64], resonators, transmission line and laser based sensing devices [63, 65] have been investigated and developed in recent years.

Figure 1-14: showing the sketch of two types of resonators used in bioanalysis

A resonant based architecture that can be used in the THz region, for molecular inspection, is the double split resonator (DSR). Figure 1-14 shows two symmetric DSR structures, circular and squared. An asymmetric form of this structure is used in [66] for monitoring the thickness of poly(methyl methacrylate) (PMMA). PMMA thickness of as low as 30 nm has been detected using this system. In [67] a split ring resonator (SRR) is used in the detection of 1-octadecanthiol [$CH_3(CH_2)_{18}SH$] in the range of 67 GHz to 105 GHz. The vibrational mode of the CH_2 bonds in this frequency range is detected by this resonating sensor. The sensor is capable of detecting target concentrations of as low as 40 zepto mole. 1-octadecanthiol has the ability of arranging itself into structured monolayers and can be used in the development of different types of sensors like mercury detectors [68]. THz transmission line bases sensors are an alternative architecture of interest for analysis of samples at molecular level. Micro-strip-line based [69] and Goubau line based sensors [70, 71] are examples of such devices which are used in bio-analysis. Goubau lines are single wire waveguides that allow the propagation of electromagnetic fields and minimise radiation losses [72, 73]. In [74] a set of Goubau line structures and their corresponding microfluidic channels were fabricated on an integrated microsystem to measure the concentration of proteins in a liquid sample. Figure 1-15 shows an image of the final produce and the positioning of the Goubau lines with respect to the liquid under test [74]. Protein concentrations of as low as 7 μmol have been detected using this apparatus. Similar Goubau line structures are also used in the sub terahertz region of 50 GHz to 110 GHz for monitoring the hydration shell of ethanol [75] and enzyme activity in liquid samples [76].

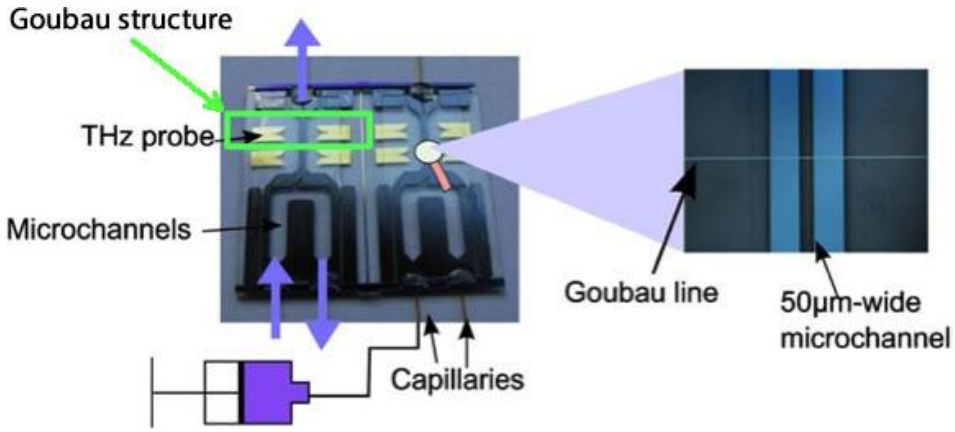

Figure 1-15: showing the fabricated structure including the Goubau lines and the microchannels for the measurement of protein concentration [74]

1.3.2 Electrochemical sensors

An electrochemical transducer that converts chemical information like charge accumulation in a sample into an electric signal is called an electrochemical sensor. More information on the definitions and various sub-divisions within this type of sensors can be found in [77, 78]. In particular, planar electrochemical sensors offer very good integration with electronics and microfluidic systems hence they have enjoyed widespread adoption. Planar electrochemical sensors can be placed in three categories based on their method of fabrication. These categories are thick-film sensors, thin-film sensors and field effect transistor (FET) based sensors [79]. A few important examples of each of these methods shall be provided with emphasis placed on FET based sensors.

Printing of paste (ink) onto conductive and insulating substrates has been used for creating cheap and simple yet effective sensors for a variety of applications. Thick-film printing provides a cheap and controllable method for generating a multi layered structures. In this process a paste is placed above a mask which is placed on top of a substrate. The paste is then pressed onto the mask and in places which the mask is patterned, the paste reaches the substrate. The mask is then removed and the structure is annealed. Using the same procedure, multiple layers can be printed on the substrate leading to the final product. Figure 1-16 shows a conceptual sketch of the basic steps taken in the fabrication of thick-film devices [79]. Note that the paste can be heat treated in oven or using UV light or cold-cured ink can be used instead [79]. In [80] thick film printing is successfully used to develop glucose sensing devices for diabetic patients. A vapour deposited electrode material is coated by a dielectric layer using thick film printing. Laser is then used to drill an array pattern on the dielectric

materials to create sensing holes of diameter 15 μm. Each hole is then filled with a metallised enzyme layer and is able to hold 200 μL of liquid sample. The glucose and lactate test is then carried out, by placing the blood sample over this array pattern [80]. This is an example of using thick film printing for a biomedical application.

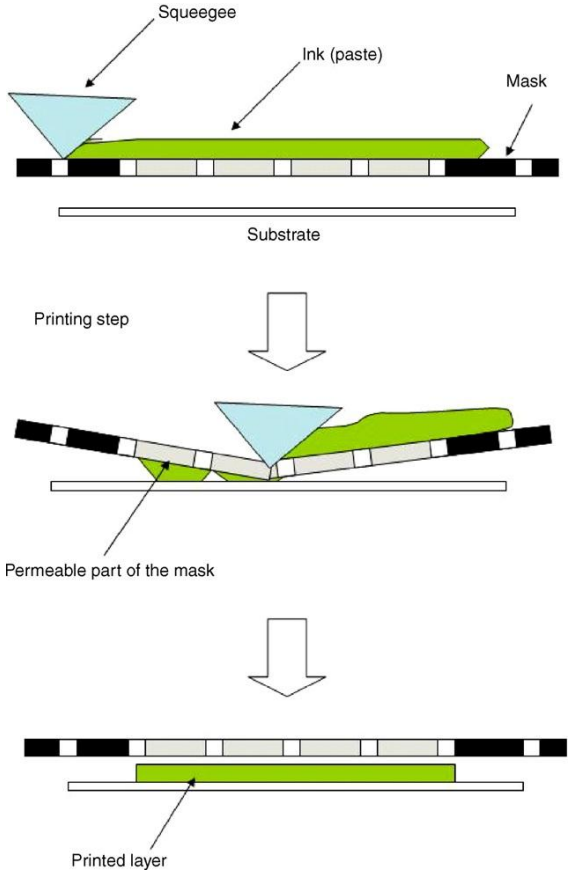

Figure 1-16: showing the printing process for thick-film sensors. The paste is placed on the mask and using a squeegee, the ink is shaped into a desired form by being pressed over the mask. The final product is then treated and similar steps are then taken until the final product is obtained [79]

In [81] a graphite based DNA sensor was developed using thick-film printing techniques. The graphite layer was then modified by DNA samples. This design was used to monitor the damage caused to DNA strands by UV radiation. Similar design was also used in [82] to monitor the concentration of different types of DNA samples. In this work the hybridization process was successfully monitored. Another application of thick-film printing is in the detection of nickel using DNA surface modified sensors [83]. The sensitivity of this sensor was down to a concentration of 7 nM for traces of nickel in the solution. Screen printing is also successfully used in pesticide detection in [84, 85].

Thick-film technology offers a very cheap method of developing sensing devices. It allows for the fabrication and connection of hybrid systems on the same substrate at low cost. It also allows for post-trimming of various objects which are fabricated using this technology. Once

the devices are printed on the substrate they can be trimmed to the right dimension using laser or other methods. Thick-film technology supports dimensions as small as tens of micro-meter [86]. However if the concentration of a species is in the femto-mole region or the volumes of interest are in the nano-litre pico-litre range, much smaller and more sensitive sensors are needed. This leads to the adaptation of thin-film technologies for such sensors as they allow further miniaturization.

Thin-film technologies use photolithography as the basis for creating patterns on a substrate. Hence dimension of less than 1 μm can be achieved using this method. It also allows for the deposition of thin layers of materials hence integrated capacitive elements can be realized easily. This is due to the fact that sputtering and chemical vapour deposition (CVD) techniques along with photolithography are used in thin-film technologies. The cost of thin-films is much higher than thick-film devices however greater integration with integrated circuits (ICs) can be achieved. It also allows for smaller and more sensitive sensing devices and the potential for mass fabrication. For more information refer to [86] and [79].

In [87] interdigited electrodes were used to develop a bio-compatible pH sensor. Chemically modified platinum electrodes were employed for pH detection. The electrodes were connected to the readout circuitry using an ordinary soldering process. Figure 1-17 shows the deposited pattern of working and reference electrodes on an insulating substrate [87]. The interdigited shape is used to increase the surface contact between the sensor and the solution under test thus increasing the sensitivity of the device. The device was used in monitoring a pH range of 3-10. In [88] surface activated gold electrodes were formed on both silicon and Mylar substrates using photolithography. The size of the gold electrodes was 50 μm and 500 μm is size. This sensor was used for glucose and lactate detection purposes. A concentration range of 0-20 mmol for glucose and 0-10 mmol for lactate were detected by this sensor. Figure 1-18 shows the conceptual design and a microscopic image of the fabricated sensor [88]. Thin-film devices are also used in [89] for studying neurotransmitters, [90] for monitoring glucose and [91] for monitoring electrolyte solutions.

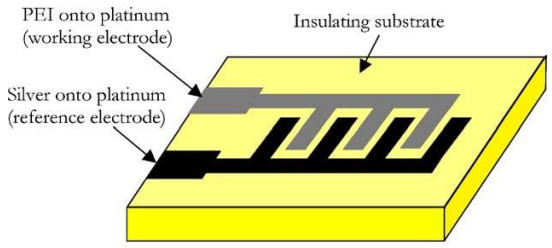

Figure 1-17: showing the structure of the interdigited electrode developed for monitoring the pH of a solution [87]

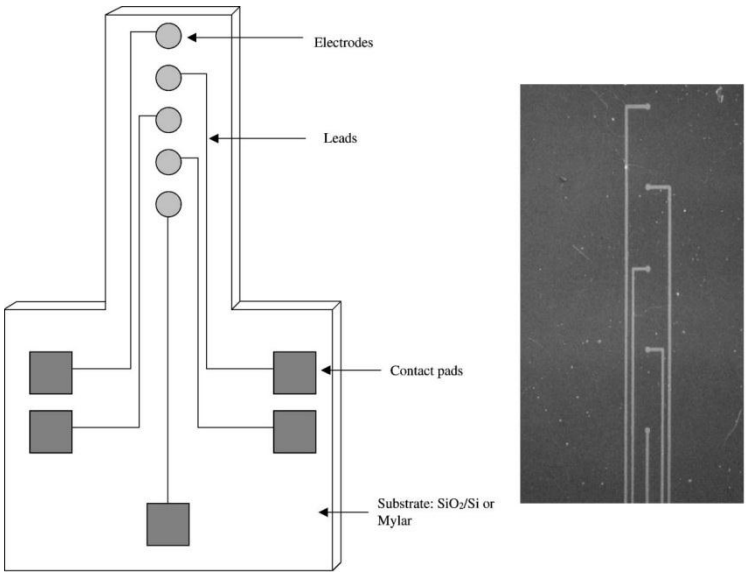

Figure 1-18: showing the schematic design of the functionalized gold sensors arrays and a microscopic image of the fabricated device [88]

Thin-film technology offers better scaling with respect to its thick-film counterpart. Hence ever smaller structures with greater sensitivity can be fabricated using this technology. The cost of a thin-film device is greater than its equivalent thick-film. However, due to miniaturization, mass fabrication can be achieved which reduces the cost of this type sensors. Both thin-film and thick-film devices lack deep integration with electronic systems. In both technologies contact to other units is done using contact pads and soldering of a wire. Although this option is rather cheap and easy to implement, it can pose problems with the packaging of the device and insulating the electronics component from the liquid. The other shortcoming lies in the inherent inductance of these contacts. Hence the high frequency devices should be designed with this extra factor taken into account. There is another family of electrochemical sensors which offers a deeper integration with electronic circuitry, Ion Sensitive Field Effect Transistors (ISFETs) [92].

ISFET is a Field Effect Transistor (FET) in which the polysilicon gate is connected to metal layers by means of vias and is brought up to the oxynitrite layer. The oxynitirite layer is covered with silicon nitride. The silicon nitride layer right above the gate metals is then exposed to a liquid sample for sensing purposes. Figure 1-19 shows a cross section of a p-type ISFET and the positioning of the gate contacts [93]. An electric sensitivity of 46 mV ph^{-1} is observed in this design. As the concentration of H^+ ion in the test solution varies, the electric potential between the silicon nitride and the electrolyte is modulated. As a result the potential due to this layer can be used for measurement purposes of the pH of a

solution [94]. The voltage formed at the silicon nitride layer varies the threshold voltage of the ISFET. For more information regarding the interactions of silicon nitride with water and electromechanical reactions taking place when SiN is exposed to liquids refer to [95-98]. The exposed silicon nitride to water undergoes oxidization. This leads to the formation of silicon dioxide ponds within the silicon nitride layer hence reducing the sensitivity of the silicon nitride layer [94]. The silicon nitride layer is either treated with HF to have these ponds removed or other materials like thallium oxide is used in place of silicon nitride [94]. HF, however, does introduce damage to the SiN layer by reducing the thickness of the SiN layer. As a result the sensor's sensitivity and lifetime are affected by HF treatment. Note that thallium oxide, silicon nitride and aluminium oxide are pH sensitive layers used in the design of ISFETs [99].

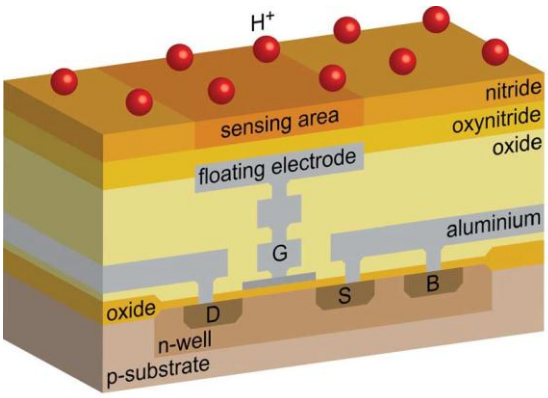

Figure 1-19: showing the structure of an ISFET with the gate of the device being exposed to the test solution [93]

ISFETs have been used in a variety of applications. In [100] they are employed to measure the creatinine and urea for dialysis applications. Other applications of ISFETs are in Glucose sensors [101, 102], water quality monitoring [103], pH measurement [7, 104], DNA hybridisation detection [105, 106] and DNA hybridization detection using surface activated ISFETs [107]. As discussed, silicon nitride undergoes oxidization when exposed to water. Hence other insulating materials were investigated to replace silicon nitride. Thallium oxide is a candidate for this matter. Figure 1-20 shows a depiction of a surface activated ISFET [99]. In this design the thallium oxide is used in place of silicon nitride for the formation of the sensing layer. A molecular detection limit in the micromole range is reported for this design. Another application of thallium oxide based ISFTs is in the measurement of the direction and velocity of the flowing electrolyte [108]. In this design a gold electrode is used for hydroxide anion generation. Two ISFETs are then placed at fixed distances a and $-a$ from the gold electrode. The time it takes for the generation of hydroxide anions to their detection

by one of the ISFETs would provide enough data for determining the velocity of the liquid flow. The detection at position *a* or *–a* would provide information on the direction of the flow. Figure 1-21 shows a conceptual depiction of gold electrodes and ISFETs being used for flow detection in a channel [108]. An electrical sensitivity of 56 mV pH^{-1} is reported for the ISFETs used in this design. Note that similar apparatus can be used with platinum in place of gold. In this case the released ions will be hydrogen ions [109].

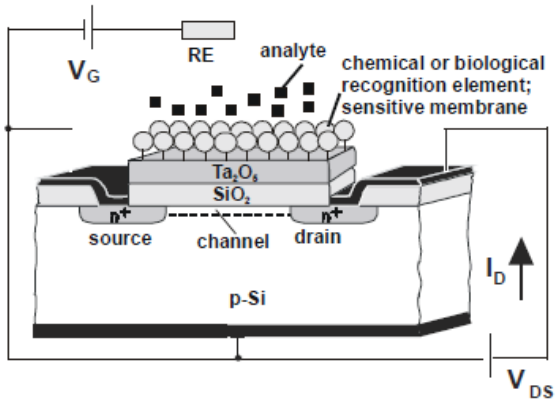

Figure 1-20: showing the conceptual layout of a surface activated ISFET with RE: reference electrode, Id: drain current, Vg: gate voltage and Vds being drain source voltage [99]

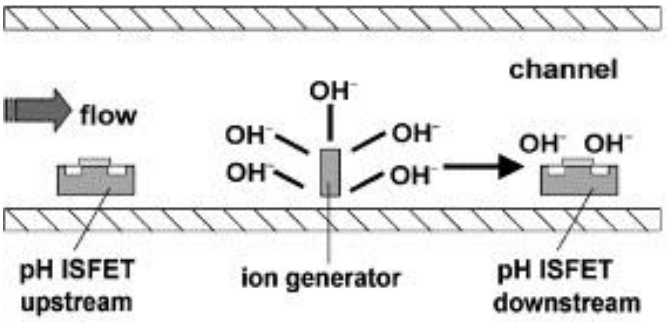

Figure 1-21: showing the process of hydroxide anion release by the gold electrolde and its detection by ISFETs. This apparatus is used in the detection of the direction of the flow in a channel [108]

ISFETs have also been used in direct DNA hybridization detection with no surface activation. In [105] the release of H^+ ions in the sample as a result of DNA hybridization is used for measuring the extent of a polymerase chain reaction (PCR). The release of proton changes the pH of the solution which in turn is sensed by the ISFET as a change in its threshold voltage. ISFETs are also used in liquid level detection [110]. Another application of ISFETs is in the detection of oxygen in an electrolyte [111]. In this application the electrolysis of the dilute oxygen in the liquid leads to a change in the pH of the sample which in turn is detected by the ISFET.

ISFETs offer greater integration with electronic circuitry. Hence they can be batch fabricated using conventional CMOS processes. As a result of this mass fabrication the price of this device can be made low. However ISFETs suffer from drift and also variations in the threshold voltage which differs from one sensor to another. Another shortcoming of ISFETs lies in the fact that it requires direct contact with a sample under test. Hence great care should be taken to isolate the electronic units from the liquid under test. This leads to further post processing steps that can increase the cost and complexity of design. The other shortcoming of ISFETs lies in the 1D structure of the sensing device. There exist only one degree of freedom for sensing purposes; the contact between the sensor and the sample lies in one single plane. This can lead to a reduction of the sensitivity of the device to very low concentrations in the femto mole region.

1.3.3 Inductive Sensors

In this section we shall look at a class of sensors that uses the perturbations in the electric and magnetic flux lines of a coil for sensing purposes. Inductive sensors operate on the principle of eddy current induction in a sample of interest. Eddy current is the motion of charged carriers induced in a conducting material as a result of varying electromagnetic fields. Figure 1-22 shows a conceptual sketch of eddy current induction in a sample of interest. A current i_1 is flowing inside the driving coil or the sensor. This current yields a magnetic field B_1 which interacts with the material under test. The driving field induces a current i_2 inside the sample which flows in the opposite direction to the driving current in the sensor. The current i_2 is the eddy current. The associated magnetic field B_2 of the induced eddy current will be in the opposite direction to B_1. This leads to changes in the total magnetic flux of the sensor. This effect translates itself into a change in the resistive and reactive properties of the sensing coil. A more detailed description of this principle is provided in Chpater-2.

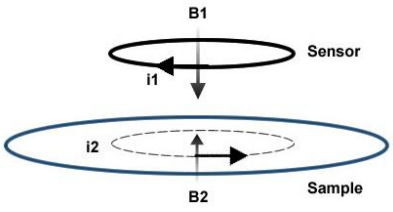

Figure 1-22: showing the principle of eddy current sensor as the driving current i1 induces a current in the opposite direction inside the material i2 (eddy current)

The first fully developed analytical solution to eddy current sensing is provided by Dodd and Deeds [112]. In this paper magnetic vector potential equations are solved in order to obtain the complete behaviour of the system. The underlying assumption is that the displacement

current can be neglected. Hence materials with very large conductivities were considered. Since then eddy current sensors have gained widespread adoption in a variety of non-destructive sensing applications. More information on these different applications and the theory of eddy current sensors can also be found in [8, 113].

One of the applications of inductive sensing is for the high temperature field. In [114, 115] inductive coils are adopted in the measurement of plasma conductivity. A different architecture, using driving and pick up coils, is used in [116] for monitoring shock heated plasma. A similar dual coil system is also used in [117] for measurements of gas conductivity and boundary layer thickness in a shock tube. Another application of inductive sensors for systems at high temperatures is in the Bridgman growth of semiconductors [118]. Figure 1-23 shows a conceptual design of using inductive sensing for monitoring the position of liquid-solid interface in the growth of semiconductors. A driver coil is used to generate a magnetic field in the sample under test. Pick up coils are then used in monitoring the effects of induced eddy currents in the sample. It is then shown that the position of the interface can be measured at higher frequencies whilst the curvature of the interface can be determined by undertaking the measurement at lower frequencies.

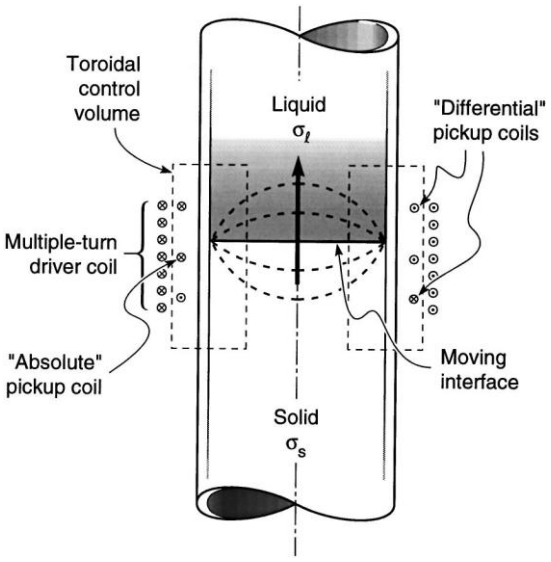

Figure 1-23: showing an application of two coil inductive sensing system to the monitoring of Bridgman growth of semiconductors [118]

Eddy current sensors have also been used in operations at very low temperatures. In [119] planar inductive coils are used for displacement measurements at a temperature range of 20 K to 273 K. Because of the cryogenic temperatures in which the sensor was to be employed in, manganese copper in place of ordinary copper was used for the conductive path. This is due to thermal stability of this alloy for electrical conductivity at low temperatures. The material

for the substrate was polyimide due to its stability at low temperatures [119]. Another example of such sensor is offered in [120] in which eddy current sensing principle is used for proximity sensing and also crack detection. Cracks at depths of down to 200 μm were detected using this sensor. Proximity of an aluminium slab for a distance of up to 8 mm was then successfully measured and simulated using this sensor. Another industrial application of eddy current sensors is in the monitoring of electrical conductivity of metal polymer composites. In this case ensembles of copper coated spheres are processed so they form a dense polymer body. Inductive coupling is then used to monitor the conductivity of this newly formed polymer layer [121].

Inductive coils have also been used in monitoring the properties of electrolyte solutions. In [122] coils are used for the measurement of electrolytic conductivity and magnetic susceptibility. Two transformers are connected in series. The core of one of the transformers is then replaced with the sample of interest. Values for the conductance and magnetic susceptibility of the sample are obtained by monitoring the resistance and output voltage of the transformer setup. In [123] inductive coils are used to monitor the ionic conductivity of rubidium silver iodide ($RbAg_4I_5$). Solenoid structures are used in [124, 125] to monitor the concentration of an electrolyte solution. Figure 1-24 shows the apparatus used in this paper and its principle of operation [124]. This design was used in measurements of the concentration of various electrolytes like NaCl and K_2SO_4. The solutions are placed inside a container which is surrounded by a coil. Variations in the inductance of the coil are then used as an indicator to a change in the concentration of the solution under investigation. A linear 14% change in the inductance of the sensor in response to a 6% change in the concentration of NaCl is observed. No information on the concentration range of NaCl used in this experiment is provided by the authors. In [126-128] a two coil system is used to undertake both inductive and capacitive measurements. These coils are connected in opposition to one another. In the form of inductive sensing the overall inductance and resistance of these coils is measured. In the form of capacitive sensing, these two coils are connected to voltage supplies independent of one another. This allows for undertaking two types of measurements on the sample solution. Hence further improvement in the accuracy of the sensing system can be achieve. Inductive sensors have also been used in the monitoring of biological tissues and phantoms. In [129, 130] inductive coils are used for the monitoring of biological tissues. In [131] resonant coils are used for monitoring the electrical properties of saline solutions.

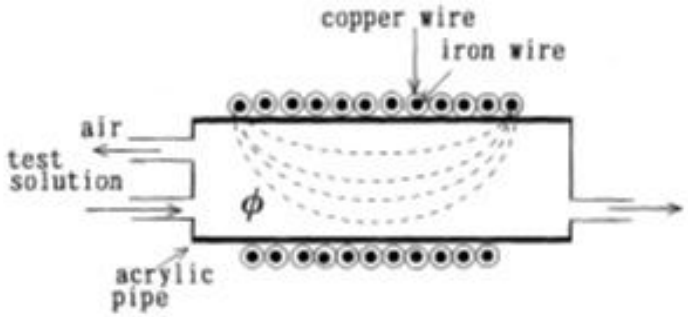

Figure 1-24: showing the sensing system architecture. The electrolytes changes the electrical properties of the medium encircled by the coil and hence modulates the magnetic flux [124]

Planar inductors fabricated using thin film technologies have also been employed in implementing inductive sensors for the monitoring of biological samples. In [132, 133] inductors were used in monitoring DNA hybridization. Fabricated inductors had self-resonances in the region of 3.9 GHz to 40 GHz. Frequency shifts as large as 8 GHz in the self-resonance of inductors were observed. Silver enhancement techniques were employed in order to amplify the effect of DNA hybridization on the sensors. Also tests with two different coating materials, aluminium and titanium oxides, were performed. It was observed that the material with larger dielectric constant, titanium oxide, leads to a greater shift in the self-resonant of inductors.

Inductive sensors offer a non-contact method of monitoring a medium of interest. This can simplify the packaging process and reduce costs. The other advantage is that the complexity that usually arises from the compatibility of the contact layer to the medium of interest no longer exists. Another advantage of inductive sensing is the flexibility in terms of size and shape of the sensing device. Inductive sensors can take both planar and helicoid shapes. Hence they can be applied to a variety of applications with different design constraints. As a result they can be fabricated using conventional CMOS processes, conventional PCB fabrication and thin film techniques. This allows the integration of inductive sensors with a variety of readout circuitry and systems. However the dependence of these sensors on the bulk properties of a material under test may impose certain limitations on the deployment of these sensors. These bulk properties usually reflect a total net effect in a sample by a variety of reactions. As the overall reaction is being measured by this sensor, detailed data on the contribution of one particular reaction may not be readily available. Inductive sensors can however be used in the qualitative data analysis. In this case the only topic of interest is whether a change has taken place inside a sample. The reasons behind this change and the extent of the change are not important.

1.4 Conclusions from the Literature

Three different sensing mechanisms were looked at in the last section. Dielectric spectroscopy, electrochemical sensing and inductive sensing were reviewed and examples of each of the mechanism and methods were provided. It was shown that dielectric spectroscopy in the wavelength range of 180 cm to 1 cm can be used to obtain detailed information regarding molecular orientation mechanics and molecular vibration dynamics. In higher frequencies in the deep infrared range, further information regarding molecular bonds and their resonant points can be found. Dielectric spectroscopy requires a wide frequency span to obtain information regarding a sample. Conventional CMOS processes cannot be employed to cover this range completely as they can only support frequencies of up to 4-5 GHz. Hence other processes and substrates, e.g. GaAs or sapphire, should be used. This introduces an added cost to the design process. The other shortcoming of this method is the lack of detailed quantitative data. This method can provide data on the existence of a particular molecule or bond within a sample however it cannot provide detailed information regarding the number of molecules present. Deep infrared measurements are sensitive to the presence of bulk water, as the intermolecular oxygen-oxygen interaction in bulk water has a vibrational mode at frequencies near 1 THz which can affect the measurement [32]. Thus measurements in this range may have to be done at low temperatures or in a dry environment, limiting the scope of this method.

Electrochemical sensors, like ISFETs, offer a cheaper alternative to dielectric sensors. An advantage of electrochemical sensors is the ease of integration with conventional electronics. This allows for deep embedding of the sensory system in the read out circuitry. Hence lower costs and smaller form factor sensing platforms. This however poses several challenges. For instance the contact to the sensor and its readout unit is usually in the form of a wire bond. The insulation of these wire bonds from the liquid sample under test can lead to several post processing steps. This adds to the complexity of the design and the overall cost. Electrochemical sensors can be used to provide information on the existence of particular molecules in the sample with the help of surface activation. However unlike dielectric systems, they cannot be used to provide detailed microscopic information about molecules in the sample under test. It must also be noted that electrochemical sensors based on planar geometry offer lower sensitivity compared with sensor with the shape of wires and spheres. For sensing purposes, planar structures have one degree of freedom, wires have two degrees of freedom and spheres have three degrees of freedom. Hence for very small molecular

concentrations, femto-moles, planar structures which are the most prevalent structure are the least desired. Hence these sensors suffer from shortcoming for very low concentrations of solute [134]. The other disadvantage of electrochemical sensors is the presence of silicon nitride layer. This limits the deployment of this device in liquid samples and implantable systems. This is due to physical properties of plasma enhanced chemical vapour deposited (PECVD) silicon nitride layer which is used to cover the silicon chips [96, 98].

Inductive sensors are another class of sensors which can provide qualitative data on a sample of interest. Qualitative analysis provides information on whether a change in a system has occurred, e.g. a Boolean answer. This is in contrast to the quantitative analysis in which the extent of the change is also found and exact values are associated with it. Quantitative analysis can be time consuming and expensive. Qualitative analysis, on the other hand, can provide a simple Boolean observation. High Throughput Screening (HTS) systems are an example of a process which takes advantage of both types of measurement [135]. Qualitative measurements are initially performed on the samples to see which targets have led to a reaction. These successful targets are then subjected to the more expensive and time consuming quantitative measurements [136, 137]. The inherent nature of inductive sensors which allows for the sensor to be fabricated using different fabrication techniques and in different shapes makes them an interesting choice for monitoring test samples.

The main aim of this research is to employ planar inductors to perform analysis on electrolyte solutions, or biological samples and systems, with the capability of a wireless data transmission between the sensor and a readout unit. This approach can simplify the packaging process of chemical sensors e.g. replacing bond-wires. The work done in this research offers the potential of adapting this sensor with minimum modifications for use as an implantable device e.g. monitoring gastric juice in the oesophagus. It also offers the potential for the use in a remote interrogation setup for communications between the sensor and the readout unit. A tag free sample analysis that requires no sensor surface activation will be adapted in this research; hence no external material will be added to the solution in order to amplify the effects of a particular reaction or species. Near field coupling of the sensor with other adjacent coils for wireless readout of the sensory data will be analysed. Finite Element (FE) analysis will be used in order to model the behaviour of the sensor in the presence of various electrolyte solutions. FE will also be used to look at near field characteristics of the sensor and its electromagnetic response. The solutions obtained using FE, alongside experimental data, will be used to optimize the design.

In chapter two a brief overview of fundamental electromagnetics and the theory of operation of inductive sensors will be provided. This will be accompanied by solving magnetic vector potential equations for a multi-layered structure to obtain analytical solutions to the eddy current sensing problem. In chapter three initial designs for the sensing system and the corresponding discussions on the best packaging material for the device shall be given. The discussed designs are then improved and a new set of sensors are fabricated. Experimental data related to these new designs and the design process for them is offered in chapter four. This is then followed by further sensor optimization using finite element modelling of the sensor in HFSS. Chapter five includes discussion on the formulation of the simulation problem and the data obtained. Results obtained through the simulation are then used to fabricate optimised sensors which are discussed in chapter six of this thesis. Concluding remarks on the project along with future challenges to this work shall be offered in chapter six.

Chapter 2

2 RF Electrical Sensors

In this chapter the theory of operation of electrically resonating structures operating in the RF range will be discussed. In this family of sensors, variations in the storage of both the electric and magnetic fields are used as indicators for monitoring a system under test. The variations in the stored energy lead to fluctuations in the electrical properties of the sensor. These electrical properties are resistance, inductance and capacitance. Dependent on the medium in which the sensor is operating, all or some of the aforementioned properties may change. This partial change in one or all of these properties can be used to perform a measurement. The circuit equivalent of this condition, variations in the stored and dissipated energy, yields an oscillatory tank. As a result the name of electrically resonating sensors is attributed to such sensing structures. Hence monitoring shifts in the natural oscillatory frequency of the sensor can be used as an indicator for measurement. Alternatively variations in the degree of oscillation for a fixed frequency point can be considered. In this chapter a more detailed review of this type of sensor and their principle of operation shall be provided. Discussions on the best approach to the analysis of these sensors, analytically or computational approach, will also be discussed.

At first Maxwell's equation in both the integral and differential forms will be introduced. This will be followed by a discussion on the interaction of matter and electromagnetic waves leading to the formulation of the Constitutive equations and Poynting's theorem. These will be used to derive the full wave magnetic vector potential (MVP) equation and corresponding boundary equations. The MVP equation will then be used to provide an overview to the principle of operation of electrically resonating sensors. Various effects of the medium, e.g. conductivity, on these sensors will be discussed. Two different approaches to the analysis of electrically resonating structures, analytical and FE computational, will be introduced. A comparison between the two methods shall be performed and tools that can be used in each of

the methods will be introduced. The detailed analysis of the comparison between these two methods will be limited to a 2D eddy current problem.

2.1 Electrodynamics

Following the analysis provided in [138], the propagation of electromagnetic waves and their interactions with matter can be summarized in the four basic laws of electromagnetism. These basic laws are Gauss' law for electric and magnetic fields, Ampere's law and Faraday's law of induction. These equations along with the Lorentz force equation provide a complete picture for the interaction of electromagnetic waves and matter. Gauss' law for the electric field implies that the divergence of the electric flux density is equal to the electric charge density. The geometrical interpretation of this fact is that the total electric flux leaving a closed surface is equal to the charge enclosed. Hence the divergence of the electric field shall be zero in the absence of electric charge. The divergence of the magnetic field is zero. The geometrical interpretation of this equivalent magnetic form of the Gauss' law implies that monopoles do not exist. Ampere's law relates the magnetic field, at each point in space, to the current density at that point. The current density is the total sum of the conduction and displacement currents at that point in space. Faraday's law defines the relationship between a changing magnetic field and the induced electromotive force at a point in space. These four equations are put together to form the Maxwell's equations.

The other fundamental equation is the Lorentz force equation, which looks at the exerted force on a moving charged particle by a field. Equation 2.1 shows the Lorentz force equation in which $\boldsymbol{F}$ is the force exerted on a charged particle, q is the total charge, $\boldsymbol{v}$ is the velocity of the particle and $\boldsymbol{B}$ is the magnetic field. This implies that the force exerted on a moving particle is perpendicular to the applied magnetic field and the direction of motion of the particle. Note that vectors quantities are shown in **bold** and scalar quantities are shown as normal text throughout this document.

$$\boldsymbol{F} = q\boldsymbol{v} \times \boldsymbol{B} \tag{2.1}$$

2.1.1 Maxwell's Equations

Maxwell's equations exist in different forms depending on the problem space to which they are applied. The properties of this problem space are defined by various electrical quantities, which are shown in Table 2-1. In this table, a list of eight fundamental electrical quantities is provided. If the top six quantities and their derivatives are both continuous functions, then the differential form of Maxwell's equation is adopted in the analysis. Otherwise the integral

forms of the Maxwell's equations are used. Table 2-2 shows Maxwell's equation in both of their differential and integral form [138].

Table 2-1: showing various electromagnetic quantities along with their symbols and units

Quantity	Symbol	Unit
Electric field intensity	E	V/m
Magnetic field intensity	H	A/m
Electric flux density	D	C/m^2
Magnetic flux density	B	Wb m^{-2} = T
Electric current density	J	A/m^2
Electric charge density	q_v	C/m^3
Electric scalar potential	ϕ	V
Magnetic Vector Potential	**A**	Wb m^{-1} = V s m^{-1}

In the case where all the aforementioned electrical quantities and their derivatives are continuous and the electromagnetic sources are of harmonic nature, the complex form of the Maxwell's equation can be adopted. This is a variation of the differential form of the Maxwell's equations. Undertaking the analysis in the complex domain simplifies the problem and hence the differential equations can be readily solved in many cases. This proves useful in the analysis of electrically resonating sensing structures using the MVP approach.

Table 2-2: showing the differential form of Maxwell's equation along with its equivalent integral form.

Differential form	Integral form
$\nabla . \boldsymbol{B} = 0$	$\oiint \boldsymbol{B}.d\boldsymbol{s} = 0$
$\nabla . \boldsymbol{D} = \boldsymbol{q_v}$	$\oiint \boldsymbol{D}.d\boldsymbol{s} = \iiint q_v \, d\boldsymbol{\tau}$
$\nabla \times \boldsymbol{E} = -\frac{\partial \boldsymbol{B}}{\partial \boldsymbol{t}}$	$\oint \boldsymbol{E}.d\boldsymbol{l} = -\frac{d}{dt}\iint \boldsymbol{B}.d\boldsymbol{s}$
$\nabla \times \boldsymbol{H} = \frac{\partial \boldsymbol{D}}{\partial \boldsymbol{t}} + \boldsymbol{J}$	$\oint \boldsymbol{H}.d\boldsymbol{l} = \frac{d}{dt}\iint \boldsymbol{D}.d\boldsymbol{s} + \iint \boldsymbol{J}.d\boldsymbol{s}$

Note that the electrical quantities shown in Table 2-2 are of the instantaneous nature. However we are mostly interested in the average power delivered to a load as opposed to an instantaneous value. Hence measurement devices are usually designed to show and measure the root mean squared (RMS) value for voltages and currents. This also has the added effect of removing the factor of two from the power calculations hence simplifying the process of obtaining the delivered power [139]. It can be shown that instantaneous values for the

electrical quantities in the Maxwell's equation can be readily replaced by their corresponding RMS values [138]. Using the Euler's identity we can relate the instantaneous value of the electric and magnetic fields, $\boldsymbol{E}$ and $\boldsymbol{H}$, to a complex value:

$$\frac{\boldsymbol{E}}{\sqrt{2}} = Re\left(\widehat{\boldsymbol{E}}e^{j\omega t}\right) = Re(|E|[cos(\omega t + \alpha) + jsin(\omega t + \alpha)]) \quad 2.2$$

$$\frac{\boldsymbol{H}}{\sqrt{2}} = Re\left(\widehat{\boldsymbol{H}}e^{j\omega t}\right) = Re(|H|[cos(\omega t + \alpha) + jsin(\omega t + \alpha)]) \quad 2.3$$

Note that the spatial component of the electric and magnetic fields are omitted in here and only the general case is provided. RMS values will be used for the rest of this document when reference is made to electrical and magnetic field values. However for simplicity the notation for both the electric and magnetic fields will remain unchanged. The Maxwell's equations mentioned in Table 2-2 lead to the continuity equation. Equation 2.4 shows the differential form of the continuity equation in which the divergence of electric current density is equal the rate of change of charge density. This is a statement of conservation of charge. The equivalent integral form of this equation is also shown in 2.5.

$$\nabla.\boldsymbol{J} = \frac{\partial}{\partial t}q_v \quad 2.4$$

$$\oiint \boldsymbol{J}.d\boldsymbol{s} = -\frac{d}{dt}\iiint q_v d\tau \quad 2.5$$

Applying the aforementioned discussions to the differential form of the Maxwell's equations and assuming a time harmonic source in which $\boldsymbol{E}_t(\boldsymbol{x},t) = \boldsymbol{E}(\boldsymbol{x})e^{j\omega t}$ and $\boldsymbol{H}_t(\boldsymbol{x},t) = \boldsymbol{H}(\boldsymbol{x})e^{j\omega t}$, we can write the Maxwell's equation as:

$$\nabla.\boldsymbol{B} = 0 \quad 2.6$$

$$\nabla.\boldsymbol{D} = Q \quad 2.7$$

$$\nabla \times \boldsymbol{E} = -j\omega\boldsymbol{B} \quad 2.8$$

$$\nabla \times \boldsymbol{H} = j\omega\boldsymbol{D} + \boldsymbol{J} \quad 2.9$$

2.1.2 Constitutive Equations

The interactions of matter with the propagating electromagnetic waves is described by constitutive equations [138, 140]. These equations relate the magnetic flux, electric flux and current densities with characteristic properties of matter. Constitutive equations are:

$$\boldsymbol{D} = \boldsymbol{D}(\boldsymbol{E}, \boldsymbol{H}) \tag{2.10}$$

$$\boldsymbol{B} = \boldsymbol{B}(\boldsymbol{E}, \boldsymbol{H}) \tag{2.11}$$

$$\boldsymbol{J} = \boldsymbol{J}(\boldsymbol{E}, \boldsymbol{H}) \tag{2.12}$$

Each of these properties is a function of the applied electric and magnetic field. However in the case of simple matter, these equations become proportionality relationships. Simple matter is defined as a linear homogeneous isotropic medium [138, 141].

Linear	*The properties of the material do not change when the applied fields are changed*
Homogeneous	*The properties of the material do not change from point to point in space*
Isotropic	*The properties of the material are independent of direction*

Assume a varying electric field, which is applied to a linear material. Atomic particles, e.g. electrons, inside this electric field will have a force exerted on them. This force induces acceleration in the direction of the field. As the field changes its direction, the atomic particles will have to adjust themselves with the new field. This introduces a time lag between the applied field and the new direction of the net acceleration and the velocity of the particles. The time lag and the rate of change of momentum of the atomic particles are incorporated into the complex properties of matter by high order time derivatives of the applied electric field. Similar treatment is applicable to the case in which the magnetic field changes and the magnetic moment of atomic particles and variations in the electric field and the behaviour of charge carriers. The constitutive equations can now be written as:

$$\boldsymbol{D} = \left(\varepsilon + \varepsilon_1 \frac{\partial}{\partial t} + \varepsilon_2 \frac{\partial^2}{\partial t^2} + \cdots\right)\boldsymbol{E} \tag{2.13}$$

$$\boldsymbol{B} = \left(\mu + \mu_1 \frac{\partial}{\partial t} + \mu_2 \frac{\partial^2}{\partial t^2} + \cdots\right)\boldsymbol{H} \tag{2.14}$$

$$\boldsymbol{J} = \left(\sigma + \sigma_1 \frac{\partial}{\partial t} + \sigma_2 \frac{\partial^2}{\partial t^2} + \cdots\right)\boldsymbol{E} \qquad 2.15$$

In these equations ε is the permittivity or capacitivity, μ is the permeability or inductivity and σ is the conductivity of the medium. In the case of a time harmonic source, these equations become:

$$\boldsymbol{D} = (\varepsilon + j\omega\varepsilon_1 - \omega^2\varepsilon_2 + \cdots)\boldsymbol{E} = \hat{\varepsilon}(\omega)\boldsymbol{E} \qquad 2.16$$

$$\boldsymbol{B} = (\mu + j\omega\mu_1 - \omega^2\mu_2 + \cdots)\boldsymbol{H} = \hat{\mu}(\omega)\boldsymbol{H} \qquad 2.17$$

$$\boldsymbol{J} = (\sigma + j\omega\sigma_1 - \omega^2\sigma_2 + \cdots)\boldsymbol{E} = \hat{\sigma}(\omega)\boldsymbol{E} \qquad 2.18$$

In these equations the frequency dependent proportionality terms are; $\hat{\varepsilon}(\omega)$ the complex permittivity, $\hat{\mu}(\omega)$ the complex permeability and $\hat{\sigma}(\omega)$ the complex conductivity of the material. Henceforth any mention of these three quantities implies a frequency dependent complex form unless otherwise stated. For simplicity and clarity the explicit dependent of these terms on the angular frequency will not be shown. The complex permittivity of matter can now be represented in the rectangular form as:

$$\hat{\varepsilon} = \varepsilon_0(\varepsilon' - j\varepsilon'') = |\hat{\varepsilon}|e^{-j\delta} \qquad 2.19$$

In equation 2.19 ε' is the dielectric value of the material, ε'' is the dielectric loss factor and δ is the loss angle. The latter property is the angle between the real and imaginary parts of complex permittivity and is usually reported as loss tangent, $tan(\delta)$. Note that the real and imaginary parts in 2.19 are the overall sum of real and imaginary contributions of various terms in 2.16. As a result both the real and imaginary parts of equation 2.19 are also frequency dependent. The conductivity and permittivity values discussed here refer to the polarisablity of the bound charges and unbounded charges respectively [138]. However in practice the reported values for permittivity and conductivity are the sum of both bound and unbound charge contributions. As a result we define the effective conductivity and effective permittivity to be related through $\sigma^* = j\omega\varepsilon^*$. Using equation 2.19 we can write the effective complex conductivity as:

$$\sigma^* = \mathrm{j}\omega\varepsilon^* = \sigma' + j\sigma'' + j\omega\varepsilon' + \omega\varepsilon'' \quad 2.20$$

$$\sigma^* = \mathrm{j}\omega\varepsilon^* = \sigma' + \omega\varepsilon'' + j(\sigma'' + \omega\varepsilon') \quad 2.21$$

The effective complex permittivity can now be written as:

$$\varepsilon^* = \frac{\sigma^*}{j\omega} = -j\frac{\sigma^*}{\omega} = -j\frac{(\sigma^{*\prime} + j\sigma^{*\prime\prime})}{\omega} \quad 2.22$$

$$\varepsilon^* = \frac{(\sigma'' + \omega\varepsilon')}{\omega} - j\frac{(\sigma' + \omega\varepsilon'')}{\omega} \quad 2.23$$

$$\varepsilon^* = \varepsilon' + \frac{\sigma''}{\omega} - j\varepsilon'' - j\frac{\sigma'}{\omega} \quad 2.24$$

Equation 2.24 and $\sigma^* = \mathrm{j}\omega\varepsilon^*$ will be the basis of our analysis for the rest of this thesis. The distinction between the permittivity of the sample due to bound charge and its effective permittivity, which includes contributions from bound charge and free charge, will be noted as appropriate.

2.1.3 Energy & Power

In the previous section we looked at electrical properties of matter and how they relate to the electromagnetic fields. In this section a brief introduction to the concept of power and energy shall be provided. Assume a point in space with no source of electromagnetic power. Multiply equation 2.8 by the conjugate of the magnetic flux density, B^*, and the conjugate of equation 2.9 by E.

$$\boldsymbol{B}^*.\nabla \times \boldsymbol{E} = -j\omega(\boldsymbol{B}.\boldsymbol{B}^*)$$

$$\boldsymbol{E}.\nabla \times \boldsymbol{B}^* = \mu\boldsymbol{E}.(\boldsymbol{J}^* - j\omega\boldsymbol{D}^*)$$

Subtracting these equations from one another:

$$\boldsymbol{E}.\nabla \times \boldsymbol{B}^* - \boldsymbol{B}^*.\nabla \times \boldsymbol{E} = \mu\boldsymbol{E}.(\boldsymbol{J}^* - j\omega\boldsymbol{D}^*) + j\omega(\boldsymbol{B}.\boldsymbol{B}^*) \quad 2.25$$

Using the vector identity:

$$A.\nabla \times B - B.\nabla \times A = \nabla.(B \times A) \quad 2.26$$

We can write 2.25:

$$\nabla.(\boldsymbol{E} \times \boldsymbol{B}^*) + \mu\boldsymbol{E}.(\boldsymbol{J}^* - j\omega\boldsymbol{D}^*) + j\omega(\boldsymbol{B}.\boldsymbol{B}^*) = 0$$

$$\nabla.(\boldsymbol{E}\times\boldsymbol{B}^*)+\mu\boldsymbol{E}.(\sigma\boldsymbol{E}^*-j\omega\varepsilon\boldsymbol{E}^*)+j\omega(\boldsymbol{B}.\boldsymbol{B}^*)=0$$

$$\nabla.(\boldsymbol{E}\times\boldsymbol{B}^*)+\mu\sigma\boldsymbol{E}.\boldsymbol{E}^*-j\omega\varepsilon\mu\boldsymbol{E}.\boldsymbol{E}^*+j\omega(\boldsymbol{B}.\boldsymbol{B}^*)=0$$

This leads to:

$$\nabla.(\boldsymbol{E}\times\boldsymbol{B}^*)+\mu\sigma|\boldsymbol{E}|^2+j\omega(|\boldsymbol{B}|^2-\varepsilon\mu|\boldsymbol{E}|^2)=0 \qquad 2.27$$

Changing a variable by using $\boldsymbol{B}=\mu\boldsymbol{H}$, equation 2.27 can be written as:

$$\mu\nabla.(\boldsymbol{E}\times\boldsymbol{H}^*)+\mu\sigma|\boldsymbol{E}|^2+j\omega\mu(\mu|\boldsymbol{H}|^2-\varepsilon|\boldsymbol{E}|^2)=0 \qquad 2.28$$

$$\nabla.(\boldsymbol{E}\times\boldsymbol{H}^*)+\sigma|\boldsymbol{E}|^2+j\omega(\mu|\boldsymbol{H}|^2-\varepsilon|\boldsymbol{E}|^2)=0 \qquad 2.29$$

Multiplying and dividing the third term by a factor of two:

$$\nabla.(\boldsymbol{E}\times\boldsymbol{H}^*)+\sigma|\boldsymbol{E}|^2+j2\omega\left(\frac{1}{2}\mu|\boldsymbol{H}|^2-\frac{1}{2}\varepsilon|\boldsymbol{E}|^2\right)=0 \qquad 2.30$$

Now by setting:

Poynting's vector	$\boldsymbol{S}=\boldsymbol{E}\times\boldsymbol{H}^*$
Dissipated power	$P_d=\sigma\|\boldsymbol{E}\|^2$
Magnetic energy density	$\overline{w_m}=\frac{1}{2}\mu\|\boldsymbol{H}\|^2$
Electric energy density	$\overline{w_e}=\frac{1}{2}\varepsilon\|\boldsymbol{E}\|^2$

Defining the complex volume density of power leaving a point in space as:

$$P_f=\nabla.\boldsymbol{S}$$

We can write the following equation for a source free simple media:

$$P_f+P_d+j2\omega(\overline{w_m}-\overline{w_e})=0 \qquad 2.31$$

Assuming a time harmonic source in the space denoted by P_s and using 2.30, the total complex power passing through a point in the space is:

$$P_f+P_d+j2\omega(\overline{w_m}-\overline{w_e})+P_s=0 \qquad 2.32$$

$$\nabla.(\boldsymbol{E}\times\boldsymbol{H}^*)+\sigma|\boldsymbol{E}|^2+j2\omega\left(\frac{1}{2}\mu|\boldsymbol{H}|^2-\frac{1}{2}\varepsilon|\boldsymbol{E}|^2\right)-\boldsymbol{E}.\boldsymbol{J}^{i*}=0 \qquad 2.33$$

The added term accounts for energy supplied by the source into the space. The variable $\boldsymbol{J}^i$ represents the impressed currents, due to the power source. The first term in 2.33 represents the transported energy per unit time per unit area by the electromagnetic fields. In the case of a point in space, this quantity represents the average energy density leaving the point. The

second term of 2.33 is the dissipated power at the point inside the matter. The constituents of the third term are electric and magnetic energy densities. This represents the stored energy at that point in the system. Given that non-magnetic substances will be discussed in this research, dissipating magnetic terms will not be discussed further. As a result the magnetic current contributing term to the source power density is not mentioned here. It can readily be seen that equation 2.33 is in fact the statement of conservation of energy.

In equation 2.33 it was shown that in the process of energy transmission, part of the energy is dissipated into the matter and part is stored. In the case of the complex power, the real component represents the dissipation of power into the medium and the imaginary component is the energy storage property. The latter is also referred to as reactive power. It was shown that both these properties are related to material characteristics via the constitutive equations. As a result by monitoring the energy transmission properties of a system, certain properties of a material can be realized. Hence by calculating energy storage properties of a sensing system, like inductance and capacitance, and energy losses, like ohmic losses, one can realize permittivity, permeability and conductivity of a sample under test. This is the basis of measurement for electrical resonating structures.

2.1.4 Vector Potentials

The discussion offered in the previous section paves the way for the formalization of the magnetic vector potential equation. In this part we shall look at the derivation of magnetic vector potentials for Maxwell's equations. Using the general current theory, we can write the total current, J^t, as the sum of:

Conduction currents	$\boldsymbol{J}^c = \sigma \boldsymbol{E}$
Free space displacement currents	$\boldsymbol{J}^{d'} = j\omega\varepsilon_0 \boldsymbol{E}$
Polarization currents	$\boldsymbol{J}^p = j\omega(\varepsilon - \varepsilon_0)\boldsymbol{E}$
Impressed currents	$\boldsymbol{J}^i$

Invoking the differential form of the Ampere's law:

$$\nabla \times \boldsymbol{B} = \mu \boldsymbol{J}^t \qquad 2.34$$

$$\nabla \times \boldsymbol{B} = \mu\left(\boldsymbol{J}^c + \boldsymbol{J}^{d'} + \boldsymbol{J}^p + \boldsymbol{J}^i\right) \qquad 2.35$$

The conduction current is dependent on the conductivity of the material in which the EM wave is propagating. The free space displacement current can be interpreted as the current

due to the polarisability of the free space. The polarization current deals with the total movement of bound charge within matter as an electromagnetic field is applied. In this case the realignment of various bounded charged entities within the sample leads to an overall current represented by this term. Note that the permittivity term used in the definition of the polarization current is a complex entity. The term, $j\omega\varepsilon\boldsymbol{E}$, is called the displacement current. At last the current flowing in the source of the electric or the magnetic fields is called the impressed current and its contribution is represented by the added term, $\boldsymbol{J}^i$. We can now rewrite equation 2.35 as:

$$\nabla \times \boldsymbol{B} = \mu\left[\sigma\boldsymbol{E} + j\omega\varepsilon_0\boldsymbol{E} + j\omega(\varepsilon - \varepsilon_0)\boldsymbol{E} + \boldsymbol{J}^i\right] \quad 2.36$$

$$\nabla \times \boldsymbol{B} = \mu\left[\sigma\boldsymbol{E} + j\omega\varepsilon\boldsymbol{E} + \boldsymbol{J}^i\right] \quad 2.37$$

Equation 2.37 is a differential equation relating variations in the magnetic field to changes in electric field in time and space. It also relates the variations in the magnetic field and its curl to material properties. Using this equation, we can write the total current density, excluding the source contributions, to be:

$$\boldsymbol{J} = (\sigma + j\omega\varepsilon)\boldsymbol{E} \quad 2.38$$

In which the terms inside the bracket are referred to as the admittivity or the effective complex conductivity of the medium [142, 143]. Keeping the contributions of the bound charge and free charge separate, we can simplify equation 2.38 further, as all the variables are all of the same type. This allows us to apply readily available mathematical methods to the differential equation and solve equation 2.37.

We know from 2.6 that the magnetic field is divergence free and using the vector identity $\nabla.(\nabla \times \boldsymbol{A}) = 0$ for any vector $\boldsymbol{A}$, we can set $\boldsymbol{B} = \nabla \times \boldsymbol{A}$. Magnetic vector potential is parallel to the path in which the current flows and is in the direction of the flow of the current. Figure 2-1 shows a conceptual depiction of the magnetic vector potential and its contour with respect to the flowing current. Similar treatment can be given to the electric field, which gives rise to the concept of electric scalar potential. Electric scalar potential can be interpreted as the work done on a charged particle when moved inside an electric field [144].

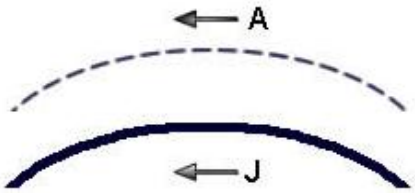

Figure 2-1: showing the path that the current J is passing through and its corresponding magnetic vector potential, shown by dashed lines.

Using equation 2.8 we can write:

$$\nabla \times \boldsymbol{E} + j\omega \boldsymbol{B} = 0 \tag{2.39}$$

$$\nabla \times \boldsymbol{E} + j\omega \nabla \times \boldsymbol{A} = 0 \tag{2.40}$$

$$\nabla \times (\boldsymbol{E} + j\omega \boldsymbol{A}) = 0 \tag{2.41}$$

The quantity inside the brackets can be written as the gradient of a scalar function as this term is irrotational [29]:

$$\boldsymbol{E} + j\omega \boldsymbol{A} = -\nabla \varphi \tag{2.42}$$

$$\boldsymbol{E} = -j\omega \boldsymbol{A} - \nabla \varphi \tag{2.43}$$

This scalar function is called the electric scalar potential. This equation implies that the total sum of the work done on a moving charged particle and the local temporal variations in the magnetic vector potential yield the electric field. In a conducting medium, the electric field $\boldsymbol{E}$ generates a current. Equation 2.37 can now be written as:

$$\nabla \times \nabla \times \boldsymbol{A} = \mu\left[\sigma(-j\omega \boldsymbol{A} - \nabla \varphi) + j\omega\varepsilon(-j\omega \boldsymbol{A} - \nabla \varphi) + \boldsymbol{J}^i\right] \tag{2.44}$$

Using the identity

$$\nabla \times \nabla \times \boldsymbol{A} = \nabla(\nabla . \boldsymbol{A}) - \nabla^2 \boldsymbol{A}$$

Invoking Coulomb's gauge by setting $\nabla . \boldsymbol{A} = 0$

$$-\nabla^2 \boldsymbol{A} = \mu\left[\sigma(-j\omega \boldsymbol{A} - \nabla \varphi) + j\omega\varepsilon(-j\omega \boldsymbol{A} - \nabla \varphi) + \boldsymbol{J}^i\right] \tag{2.45}$$

$$\nabla^2 \boldsymbol{A} = \mu\left[j\omega\sigma \boldsymbol{A} - \omega^2 \varepsilon \boldsymbol{A} + (\sigma + j\omega\varepsilon)\nabla \varphi - \boldsymbol{J}^i\right] \tag{2.46}$$

Letting

$$\varepsilon = \varepsilon' - j\varepsilon''$$
$$\sigma = \sigma' + j\sigma''$$

$$j\omega\varepsilon\nabla\varphi = j\omega\varepsilon_0(\varepsilon' - j\varepsilon'')\nabla\varphi$$

$$j\omega\varepsilon\nabla\varphi = j\omega\varepsilon_0\varepsilon'\nabla\varphi + \omega\varepsilon_0\varepsilon''\nabla\varphi$$

We can rewrite equation2.46 as:

$$\nabla^2\boldsymbol{A} = \mu\big[j\omega(\sigma' + j\sigma'')\boldsymbol{A} - \omega^2(\varepsilon' - j\varepsilon'')\boldsymbol{A} + [\sigma' + j\sigma'' + j\omega(\varepsilon' - j\varepsilon'')]\nabla\varphi - \boldsymbol{J}^i\big] \quad 2.47$$

$$\nabla^2\boldsymbol{A} = \mu\big[j(\sigma' + \omega\varepsilon'')\omega\boldsymbol{A} - (\sigma'' + \omega\varepsilon')\omega\boldsymbol{A} + (\sigma' + \omega\varepsilon'')\nabla\varphi + j(\sigma'' + \omega\varepsilon')\nabla\varphi - \boldsymbol{J}^i\big] \quad 2.48$$

The first term in equation 2.47 is the eddy current contributing term. In another words this is the energy dissipated into the system by the unbound charge. The second term is called the dynamic radiation current [145-147] and deals with the effect of the energy dissipated into the system by the unbound charge. In this case the bound charge is accelerated by the magnetic vector potential originated from the source current. The third term deals with the effect of the electric potential on bound and unbound charges. The last term is the current contribution due to the source. This equation can be further expanded into equation 2.48 in which the contributions of bound and unbound charges are separated. In here, the first term deals with the energy dissipation into the medium due to the movement of bound and unbound charges. The second term represents the polarisation effect on the bound and unbound charges. This polarisation also leads to radiation. If the dimension of device or sample under test is smaller than the wavelength of operation, radiation losses can be completely neglected. The third term deals with the energy dissipation into the system by the movement of current due to the scalar potential. The fourth term is the polarisation effect induced by the scalar potential. In both third and fourth terms, bound and unbound charges are present. The last term represents the impressed currents.

Note that radiation occurs due to acceleration of a charged particle, which leads to a change in its momentum. Imagine a charged particle in vacuum that is stationary or travelling with a constant velocity; in this case the line of fields associated with the particle will travel at the same speed of the particle. However if a force is exerted on the particle, the particle will accelerate. As a result, there will be a time lag between the movement of the particle and adjustment of its associated fields. This leads to the field changing its organised shape. For a repetitive applied force, this process introduces a newly formed waveform into the lines of

the field that will travel through its contours. This waveform carries with it energy and this process is the basis of radiation [148]. Table 2-2 shows a conceptual depiction of radiation.

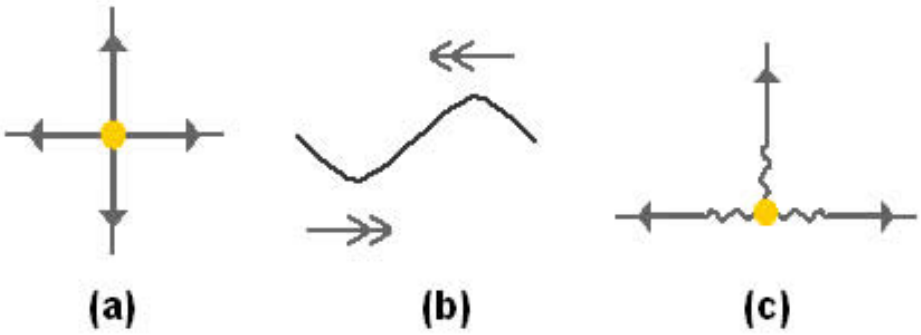

Figure 2-2: (a) showing the fields associated with a charged particle in a stationary position or at constant velocity, (b) a periodic force is now applied to the charge with acceleration in opposite directions, (c) due to the acceleration of the charge, there is a lag between the position of the charged particle and contour of the fields associated with it. This leads to a change in the shape of the fields associated with the particle.

The other factor that must be visited here are the boundary conditions. The boundary conditions govern the behaviour of a propagating electromagnetic wave as it crosses the interface between two materials. Defining an interface between two materials in line with the horizon, the boundary condition for the behaviour of fields perpendicular to the interface can be written as [149]:

$$(\boldsymbol{B}_{k+1} - \boldsymbol{B}_k) \cdot \hat{\boldsymbol{j}} = 0 \qquad 2.49$$

In which, $\hat{\boldsymbol{j}}$ is the unit vector in the y-direction. This implies that the magnetic field is continuous as it passes through the interface between two materials. However, parallel to the interface of two materials, due to the difference in the magnetisation between the two materials, the magnetic intensity shall behave differently. In the presence of a current source in one of the two layers under consideration, the tangential boundary condition becomes [149]:

$$\left(\frac{1}{\mu_{k+1}}\boldsymbol{B}_{k+1} - \frac{1}{\mu_k}\boldsymbol{B}_k\right) \times \hat{\boldsymbol{\imath}} = K \qquad 2.50$$

In which $\hat{\boldsymbol{\imath}}$ is the unit vector in the x-direction and K is the surface current density. In the absence of a source in any of the two layers of interest, the surface current density tends to zero.

2.2 Principles of Operation

In this section we shall look at the principle of operation of electrically resonating structures for sensing purposes. These structures are designed to resonate at a predetermined frequency. Similar to any other electrically resonating system, these structures store energy in their corresponding electric and magnetic fields. Variations in the medium in which these structures are placed, leads to changes in the amount of stored energy in the electric and magnetic fields. Fluctuations in these fields are translated into variations in the electrical properties, e.g. shift in resonant frequency, of the sensing system. We can model a simple electrically resonating structure as a resonating tank. In this case the energy storage in the magnetic and electric fields and ohmic losses of the resonating structure can be modelled as an inductor and a capacitor in parallel along with a resistor in series with the coil. This model is shown in Figure 2-3. We can use this equivalent circuit model to discuss and analyse the principles of operation of such structures in more detail.

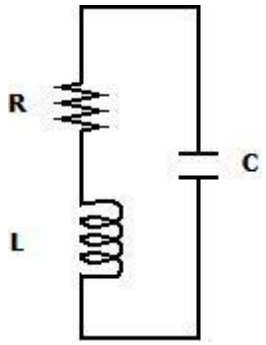

Figure 2-3: showing the LCR equivalent circuit of an electrically resonating structure

2.2.1 Magnetic Losses

Assume a coil of finite resistivity, driven by a time varying current placed inside a medium of finite permittivity and permeability. The current flowing in the coil will yield a time varying magnetic field in the surroundings of the coil. This time varying magnetic field will yield an electromotive force (Faraday's law). This force induces acceleration in bound and unbound charges along its path. This principle is shown in Table 2-2 in which the rotational component of the time varying magnetic field equals the current due to bound and unbound charge carriers. This results in the flow of a type of current, called eddy current, in the sample space. The induced eddy currents will yield their own magnetic flux. As these eddy currents would flow in the opposite direction to the driving source of the coil, their resulting magnetic field will also be in the opposite direction to the driving magnetic field. This situation is depicted in Figure 2-4. It is shown that the current, i_1, yields a magnetic field, B_1, which in

turn induces the corresponding eddy current, i_2. The induced eddy current generates a magnetic field, B_2, which is in the opposite direction to B_1.

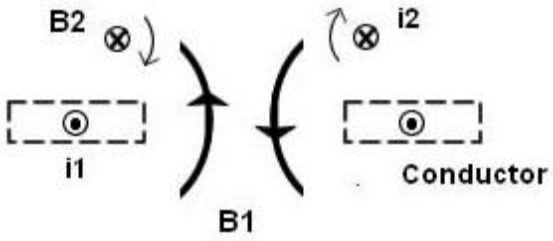

Figure 2-4: showing the direction of magnetic fields, B2, associated with the induced eddy currents, i2, due to current i1 flowing in coil conductors

The generated eddy currents will affect the inductance and the resistance of the structure. The generation of the magnetic field, B_2, affects the total magnetic flux surrounding the coil. The strength of B_2 is dependent on the conductivity of the medium in which the coil is placed. The more conductive mediums will result in the generation of larger amount of eddy currents. Hence a stronger magnetic field, B_2, will be generated. This effect reduces the total energy stored by the coil in the magnetic form. This can be translated as a change in the inductance of the resonating tank in Figure 2-3.

The other effect of these eddy currents and their associated magnetic fields is the increase in the resistance of the coil. In a time-varying current carrying conductor, the internally generated eddy currents reinforce the flow of the current in the surface of the conductive layer and oppose the flow near the core of the conductor [150]. This is a frequency dependent phenomenon. It was mentioned that if the coil were placed near a conductive layer, eddy currents would be generated in the layer. These eddy currents will yield their own magnetic flux that in turn will interact with the conductive layer of the sensing coil. This leads to the generation of current loops inside the conductive layer, which oppose the flow of current near the surface of the conductor. Figure 2-5 shows a depiction of this situation.

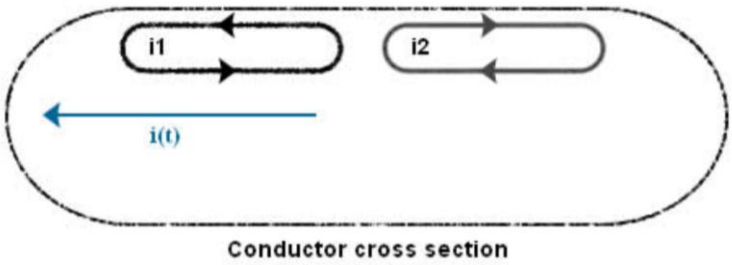

Figure 2-5: showing the flow of a time varying current, i(t), in a conductive layer along with the internally generated eddy currents, i1, and secondary generated currents due to external eddy currents, i2.

These current loops reduce the cross section of the conductive layer hence increasing the

resistance. Variations in both the inductance and resistance of the structure can be monitored and used as indicators for measurement. The changes in the inductance of the system will result in frequency shifts in the resonant frequency of the sensing structure. The variations in the resistance can also be monitored and correlated to the electrical properties of the sample space.

2.2.2 Electric Losses

Assume a coil of finite resistivity, driven by a time varying current placed inside a medium of finite permittivity and permeability. As the current travels through the length of the conductor, it faces the resistance of the coil. This leads to a slight voltage drop between different segments or turns of the coil. Thus an electric field is formed between the tracks. This electric field exerts a force on the charged particles in its vicinity that leads to polarisation effects in the sample space inside this electric field. Dependent on the frequency of the electric field different polarising effects is observed. For instance low frequency oscillations can be used to monitor the rotational movement of large molecules and high frequency oscillations can be used in the monitoring of electronic configurations of the material under investigation. In this process some energy is also lost to the medium under test. This electric field and its effect on the surrounding space are shown in Figure 2-6. The overall response of the electric field is a function of the polarisation properties of the medium. This polarisation property is depicted by the permittivity of the system. Hence data attributed to the electric losses of the system can be used to measure the permittivity of the sample space under investigation.

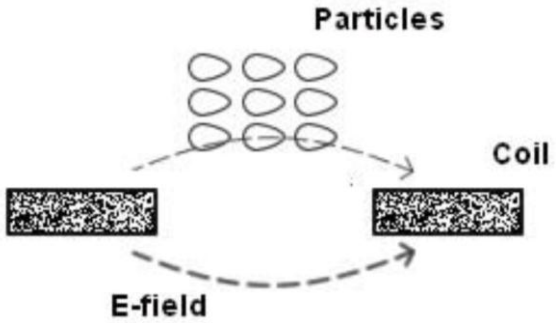

Figure 2-6: showing the electric field formed between different turns of a coil and its effect on the medium in its immediate vicinity.

In the case of an electrically resonating structure this variation in the electric field is modelled by a change in the value of the capacitor in Figure 2-3. As this capacitance changes, the overall resonant frequency of the system changes as well. This effect can be monitored by

appropriate use of read out units that monitor the variations in the overall resonance of the structure.

2.2.3 Inductors & Monitoring Electrolytes

The superposition of all the aforementioned changes in the electric and magnetic fields of an electrical sensing structure would yield a sensing device. The level of contribution of each of these factors is dependent on the material, which is being analysed. For a metal, which has very high conductivity, the magnetic losses are the dominant factors. Hence the electric losses are usually discarded and the response of the system is assumed to be base on the flow of eddy currents in the sample. In this case we can refer to an electrically resonating structure as an eddy current sensor. However if the material under test has very low conductivity, then the electric losses could become the dominant factors. In this situation the sensor can be used to monitor the permittivity of a sample of interest. In an electrical sensor the overall effect of all the discussed power losses should be used to make and interpret a set of measurements. However with prior knowledge of the sample under test, the complexity of the analysis can be reduced so only the dominant factor is taken into account.

In this research we are interested in the use of inductor coils for the monitoring of the electrical properties of electrolyte solutions. In these devices, a sample of an electrolyte solution is placed in the vicinity of the inductor coil. The electrolyte solution will affect the magnetic and electric flux density of the sensor. This effect is a function of the permittivity and the conductivity of the electrolyte. Variations in the magnetic and electric flux densities lead to changes in the stored energy within the coil. As a result the self-resonance of the coil will change. The other factor that changes is the resistance of the coil. Monitoring the self-resonance of the coil and its resistance would yield information regarding the conductivity and permittivity of the electrolyte solution under test.

Figure 2-7 shows a depiction of these properties for a coated single turn coil in the presence of a sample under test. The current flowing in the conductor coils, i1, yields eddy currents in the sample. The interaction of the magnetic flux of the eddy currents, B2, with the driving magnetic field would provide information with regards to the conductivity of the sample. The electric field between the turns will interact with polarisable species in the sample and provide information on the permittivity of the sample and the species within it.

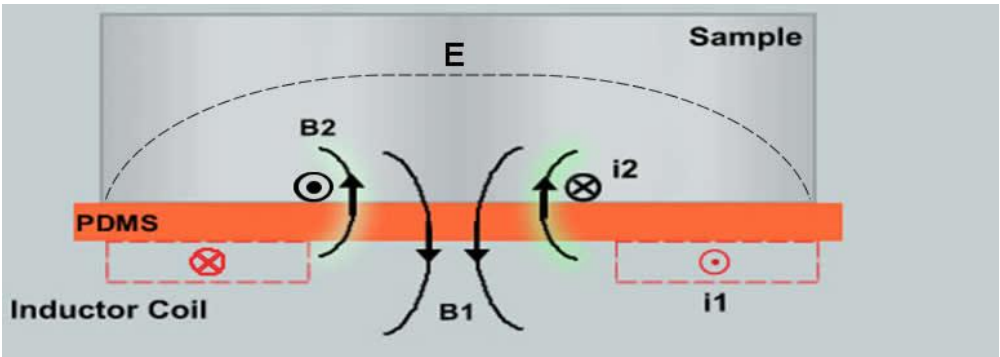

Figure 2-7: showing the interactions of the electric and magnetic fields of a single turn sensing coil with a sample under test. The driving currents and magnetic fields are i1 & B1 and the generated eddy currents components are i2 & B2 respectively.

Use of inductors paves the way for passive and active implementation of the sensing system. In the former the inductor is directly connected to a measurement unit, e.g. network analyser. As a result a physical contact between the sensor and the analysing device must be maintained. In the latter the inductor is connected in parallel with a capacitor to form an active resonating system. This system has its own natural resonance frequency, which is changed by the electrical properties of a sample placed in its vicinity. A closely coupled coil can now be used to monitor the variations in the resonance frequency of this device. As a result remote interrogation can be adopted for such implementation, replacing bondwires and other physical contacts required to make a direct connection from the sensor to the analysing unit. The other advantage of this approach is that multiple resonating devices can be interrogated simultaneously for measurement purposes. A depiction of these two strategies is shown in Figure 2-8.

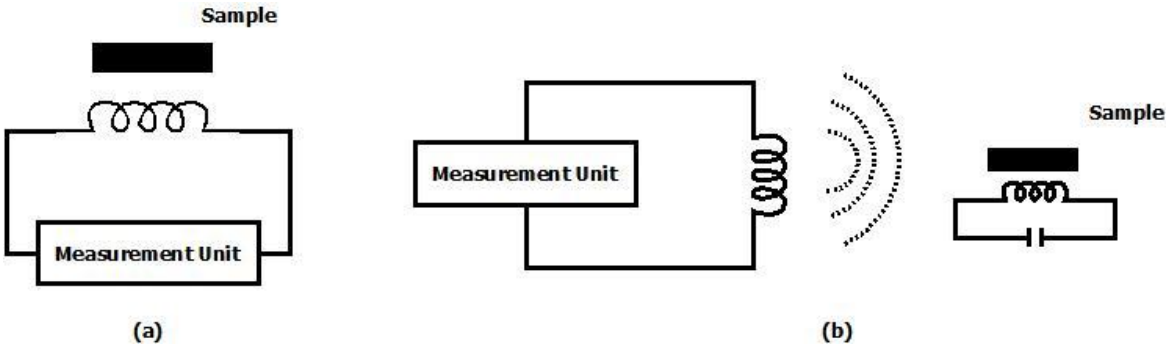

Figure 2-8: showing two different implementations of the resonating sensor: (a) showing the active approach and (b) showing the passive remote interrogation

2.3 Theoretical Analysis

In the previous section we looked at a general description of the RF electrical sensors. We shall now look at methods of analysis of such structures. Two different approaches to analysing electromagnetic problems are discussed here, analytical approach and finite element computational approach. The former requires the derivation of MVP equation for a problem space and solving it using algebraic methods. The latter takes a 3D or 2D model of the problem space and divides it into smaller subsections. The electromagnetic equations are approximated and derived for each subsection and are then put together and solved for the whole space. In this section we shall at first look at the analytical approach to solving electromagnetic problem and its corresponding solution flow. A 2D eddy current problem will be used to demonstrate the solution flow. This will be followed by a look at the finite element computational approach to solving electromagnetic problems. This method will also be applied to eddy current problems. The aim of this section is to provide an overview on the steps taken in solving electromagnetic problems using these two methods.

2.3.1 Analytical Approach

In this approach to solving electromagnetic problems, Maxwell's equations for the problem space are derived and solved. Dependent on the type of the problem space under investigation different approaches may be taken. In the presence of discontinuities in the system, integral forms of the Maxwell's equation are adopted. However, if no discontinuity is present the differential forms of the equations are adopted. The advantage of the latter is that a simpler mathematical approach can be used in solving the equations. Maxwell's equations can be treated in the form of simultaneous equation and techniques used in matrix algebra can also be invoked in solving these differential equations. In this section we shall only look at the differential form of Maxwell's equations.

The general process flow for solving the Maxwell's equations in differential form is:

1. Define a problem space and associate each different material into a separate layer.
2. Derive the differential form of Maxwell's equations for each layer separately.
3. Guess the solutions to each of the differential equations and apply appropriate boundary conditions to them. This yields a set of simultaneous equations.
4. Calculate the Poynting's vector for each layer so power losses as energy flows from one layer to another can be realised.
5. Apply the previous step to each of the turns in the inductor coil.

6. The superposition of all the power losses for each element yields the total power losses in the system.

The steps mentioned here are for a 2D problem space. In the case of a 3D problem, we have to define objects in the problem space and then calculate the power flow on each surface (side) of the object. The method mentioned here can be applied to simple structures readily. However the presence of complicated shapes, e.g. curved surfaces, can complicate the solution finding process. This process flow is now applied to a 2D eddy current problem. The analysis on eddy current formulation in the following sections are based on the word done in [145]. This will be used as an example to demonstrate the analytical approach to solving electromagnetic problems. We shall also use this example to compare analytical approach to computational methods. For the full derivation of the following analysis, refer to Appendix-I.

Eddy Current Problem

Assume that a coil driven by a time varying source is placed in a multi-layered structure with one being the sample of interest, which is a highly conductive. A depiction of this scenario is shown in Figure 2-9. In this problem a multi-turn inductor is placed in between two layered structure. Suffix k is used to depict the layers in the positive y-axis and k' is used to depict layers for the negative y-axis. Distance d is from the centre of the coil to the centre of the current carrying filaments of the inductor. The analysis will only be done for the layers located on the positive side of the y-axis, $k = [1, N]$. Similar treatment can be applied for the negative y-axis, $k' = [1, N']$. The superposition of these two sets of solutions provides a complete picture for the power losses in the system. We have also assumed that apart from the sample, k=3, all other layers have low conductivity and negligible displacement current losses.

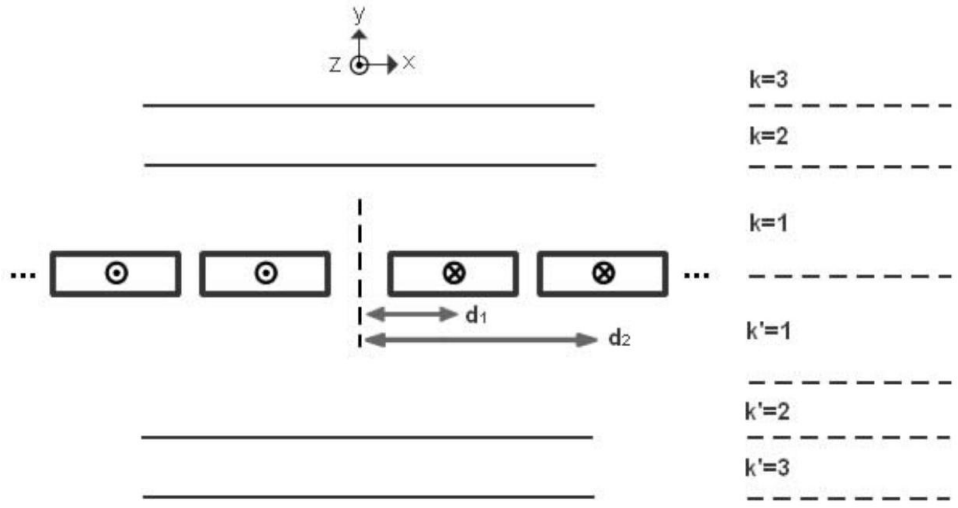

Figure 2-9: showing a coil tracks inside a multi-layered structure with k, k' being the number of layers in both direction of the y-axis and d being the distance of the centre of a conductive element to the centre of the coil.

Given the high conductivity of the sample under test the first term of equation 2.46 becomes dominant. The other terms that include permittivity contributions are neglected as $\sigma \gg \omega\varepsilon$ for conductive materials. We can now write the MVP equation for an eddy current problem as:

$$\nabla^2 \boldsymbol{A} = j\mu\omega\sigma \boldsymbol{A}$$

This differential equation can be solved for each layer separately, hence, allowing independent calculations for the power flowing through each layer. However since the sensing coil is placed at $y = 0$, the solution should be obtained at this coordinate. As a result the differential equation is solved for the layers immediately beneath and above the coil. These two solutions are then added together to obtain the effect of materials in both positive and negative y-direction. Thus the MVP can be rewritten as equation 2.51, with k being the number of the layer.

$$\nabla^2 A_k = j\omega\mu_k\sigma_k A_k \qquad 2.51$$

Using the method of separation of variables [151] and the analysis in [145], we can write the solution to this differential equation for this 2D problem in Figure 2-9 as:

$$A_k(x,y) = Y_k(y)X_k(x)\hat{\boldsymbol{z}} \qquad 2.52$$

Set Y_k and X_k to be:

$$X_k = cos(mx) \qquad 2.53$$

$$Y_k = M_k e^{\gamma_k y} + N_k e^{-\gamma_k y} \tag{2.54}$$

The coefficients, *m* and γ, are constrained by equation 2.55. As non-magnetic materials are employed in this analysis the relative permeability of each layer is set to the permeability of free space. Note that *k* is the number of the layer.

$$\gamma_k^2 - m^2 = j\omega\mu_0\sigma_k \tag{2.55}$$

Given that the applied current flows in the z-direction, the $\boldsymbol{B}$ field is calculated from equation 2.52 to be:

$$\boldsymbol{B} = \nabla \times \boldsymbol{A}_z \tag{2.56}$$

$$\boldsymbol{B} = \mathbf{i}\frac{\partial}{\partial \mathrm{y}}\boldsymbol{A}_z - \boldsymbol{j}\frac{\partial}{\partial x}\boldsymbol{A}_z \tag{2.57}$$

Applying boundary conditions and solving for X_k and Y_k, we can construct a solution matrix for all values of $k > 1$ and $k' > 1$.

$$\begin{bmatrix} M_{k+1} \\ N_{k+1} \end{bmatrix} = \frac{1}{2}\begin{bmatrix} (1+\lambda_k)e^{(\gamma_k - \gamma_{k+1})y} & (1-\lambda_k)e^{-(\gamma_k+\gamma_{k+1})y} \\ (1-\lambda_k)e^{(\gamma_k+\gamma_{k+1})y} & (1+\lambda_k)e^{(-\gamma_k+\gamma_{k+1})y} \end{bmatrix}\begin{bmatrix} M_k \\ N_k \end{bmatrix} \tag{2.58}$$

At the layer in which the source lies, $y = 0$, the boundary condition in equations 2.49 and 2.50 we can derive the MVP for all the layers of interest [145, 152].

$$\frac{\partial}{\partial x}A_1 = \frac{\partial}{\partial x}A_{1'} \tag{2.59}$$

$$\frac{1}{\mu_1}\frac{\partial}{\partial y}A_1 - \frac{1}{\mu_{1'}}\frac{\partial}{\partial y}A_{1'} = \frac{I}{\pi}\int_0^\infty cos(mx)\, dm \tag{2.60}$$

These equations provide a complete set of values for the coefficients of the solution to the differential equation narrated for an eddy current problem. Note that the material properties, which affect the sensing mechanism, are incorporated into the coefficient values M_k, $M_{k'}$, N_k and $N_{k'}$. The total sum of the vector potential equations in both negative and positive directions of *y* will then provide us with the complete expression for *A*.

We can now use the expression for the MVP to calculate the total resistive and reactive power losses in the system of interest. As discussed previously, the Poynting's vector can be calculated as:

$$\boldsymbol{S} = \frac{1}{2}(\boldsymbol{E} \times \boldsymbol{H}^*)$$

Applying this equation to Figure 2-9, at $y = 0$ and integrating over the x-axis we can find the power crossing into various layers including the material under test [145]. Thus:

$$P + jQ = \int_{-\infty}^{+\infty} \frac{1}{2}(\boldsymbol{E} \times \boldsymbol{H}^*) \cdot \hat{\boldsymbol{y}} dx \tag{2.61}$$

As we are interested in the magnetic effects in the system we can let $\boldsymbol{E} = -j\omega\boldsymbol{A}$, hence:

$$P + jQ = \int_{-\infty}^{+\infty} \frac{1}{2}\left(-j\omega\boldsymbol{A} \times \frac{1}{\mu}\nabla \times \boldsymbol{A}^*\right) \cdot \hat{\boldsymbol{y}} dx \tag{2.62}$$

$$P + jQ = -\frac{j\omega}{2\mu}\int_{-\infty}^{+\infty} (\boldsymbol{A} \times \nabla \times \boldsymbol{A}^*) \cdot \hat{\boldsymbol{y}}\, dx \tag{2.63}$$

Noting that the magnetic vector potential flows in the z-direction for our 2D problem:

$$\nabla \times \boldsymbol{A}_z^* = \begin{vmatrix} \boldsymbol{i} & \boldsymbol{j} & \boldsymbol{k} \\ \partial_x & \partial_y & \partial_z \\ 0 & 0 & \boldsymbol{A}_z^* \end{vmatrix}$$

$$\nabla \times \boldsymbol{A}_z^* = \mathbf{i}\frac{\partial}{\partial \mathrm{y}}\boldsymbol{A}_z^* - \boldsymbol{j}\frac{\partial}{\partial x}\boldsymbol{A}_z^*$$

$$\mathbf{A}_z \times \nabla \times \boldsymbol{A}_z^* = \begin{vmatrix} \boldsymbol{i} & \boldsymbol{j} & \boldsymbol{k} \\ 0 & 0 & \boldsymbol{A}_z \\ \frac{\partial}{\partial \mathrm{y}}\boldsymbol{A}_z^* & -\frac{\partial}{\partial x}\boldsymbol{A}_z^* & 0 \end{vmatrix} \Rightarrow \begin{bmatrix} \boldsymbol{i}\boldsymbol{A}_z\frac{\partial}{\partial x}\boldsymbol{A}_z^* \\ \boldsymbol{j}\boldsymbol{A}_z\frac{\partial}{\partial \mathrm{y}}\boldsymbol{A}_z^* \\ 0 \end{bmatrix}^T \tag{2.64}$$

We can write the magnetic vector potential for a single layer as:

$$A = (M_k e^{\gamma_k y} + N_k e^{-\gamma_k y}) \cos mx \tag{2.65}$$

With the more general solution being

$$A = \int_0^{+\infty} (M_k e^{\gamma_k y} + N_k e^{-\gamma_k y}) \cos mx \; dm \tag{2.66}$$

As γ_k is a function of *m*, we can replace the terms inside the brackets of equation 2.66 by $f(y, m)$. Thus:

$$A = f(y, m) \cos mx$$

Hence

$$P + jQ = -\frac{j\omega}{2\mu}\int_{-\infty}^{+\infty} \boldsymbol{A}_z \frac{\partial}{\partial \mathrm{y}}\boldsymbol{A}_z^* dx$$

$$P + jQ = -\frac{j\omega}{2\mu}\int_{-\infty}^{+\infty}(f(y,m)\cos mx)\left(\frac{\partial}{\partial \mathrm{y}}f^*(y,n)\cos nx\right)dx \qquad 2.67$$

Equation 2.67 is the core part of the power flow calculation from a sensing coil to a material under test. Note the introduction of the dummy variable *n*, which is for mathematical rigidity of the expression, however the nature of this variable is similar to *m*.

$$P + jQ = -\frac{j\omega}{2\mu}\int_{-\infty}^{+\infty} dx\left[\int_{0}^{+\infty} f(y,m)\cos mx\, dm\right]\left[\int_{0}^{+\infty}\frac{\partial}{\partial \mathrm{y}}f^*(y,n)\cos nx\, dn\right]$$

$$P + jQ = -\frac{j\omega\pi}{2\mu}\int_{0}^{+\infty} f(y,m)\frac{\partial}{\partial \mathrm{y}}f^*(y,m)dm \qquad 2.68$$

We can use similar approach to calculate this expression for an N-turn coil depicted in Figure 2-9. Following the analysis in [145], equation 2.68 can be rewritten for an N-turn coil as:

$$P + jQ = -\frac{j\omega\pi}{2\mu}\int_{0}^{+\infty}\left(f(y,m)\frac{\partial}{\partial \mathrm{y}}f^*(y,m)\right)\left(\sum_{i=1}^{N} sin(md_1 \cdots md_N)\right)dm \qquad 2.69$$

Equation 2.69 the general solution for the power crossing the surface enclosing an multi-turn coil for the case of $y > 0$. Similar principle is used to calculate the power crossing the surface in the direction of $y \to -\infty$. The total sum of these two contributions will yield the total energy crossing the enclosing materials of the inductor coils [152]. In another word this equation provides the power losses to the system from the coils. The real part of this power loss is a resistive loss and the imaginary part is the reactive one. The latter causes a shift in the resonant frequency of the coil and the former is modelled as an equivalent resistor in series with the coil carrying the current *I*. The value of this resistor can be found as:

$$R_{eq} = \frac{Re\{2(P + jQ)\}}{I^2} \qquad 2.70$$

The value of this resistor is a direct result of the eddy currents flowing in the sample under test. Monitoring its value provides us with data on the conductivity of the sample of interest.

2.3.2 Finite Element Approach

In this approach to solving electromagnetic problems, the problem space is divided into a finite number of elements. A finite number of parameters are then used to define the behaviour of each of the elements and the electromagnetic solution is calculated for each of them. The solutions are then assembled together to find the complete solution to the system

[153]. The process of dividing the system into smaller elements is called meshing. The shape of the newly formed elements (mesh) and their size are important factors in deciding the accuracy of the final solution. These factors also affect the time it takes to solve a particular problem. The shape of the mesh can take many forms as shown in Figure 2-10. Dependent on the type of problems at hand and the computation power available a particular size or type of mesh can be chosen [154, 155]. Note that the boundary conditions should also be satisfied for at the face of each of the mesh elements.

There are various software packages that can perform FE electromagnetic analysis on an object like ANSOFT HFSS, Agilent MOMENTUM, and Computer Software Technology (CST). The package used in this research is ANSOFT HFSS. HFSS can perform full-wave electromagnetic analysis on an object drawn in a 3D CAD software. As a result no prior assumptions on the properties of materials need to be made. There are also no assumptions on the maximum frequency of simulation for the object of interest (within the capabilities of the package). Other quasi-static software packages, e.g. Maxwell 3D, assume the dimensions of the object of interest are much smaller than the frequency at which the simulation is taking place. As a result generated modes inside the system are neglected. HFSS uses a tetrahedron meshing system for the all the structures imported for analysis.

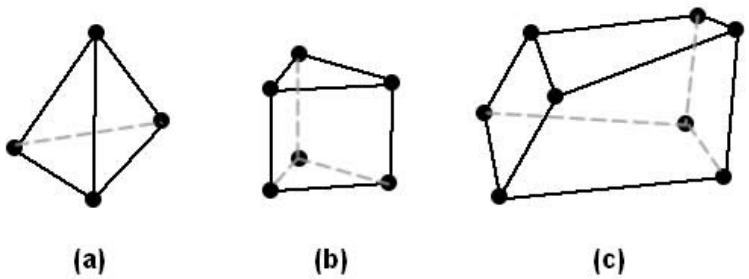

Figure 2-10: showing different geometrical representations used in the meshing process, (a) tetrahedron, (b) pentahedron, and (c) hexahedron

HFSS provides scattering matrix data on the structure of interest. The scattering data can then be converted into Y or Z matrices to calculate the inductance, capacitance, and resistance of the structure. The general solution flow for HFSS FE electromagnetic analysis of a two-port structure is:

1. Divide the structure into a finite element tetrahedral mesh
2. Compute the modes on each port
3. Electric and magnetic fields are calculated at the nodes (vertex) of the tetrahedron. Their values are then stored at the vertex and midpoint of the tetrahedrons.

4. The electromagnetic field inside the structure is then computed, one mode at a time.

5. The field quantities are then expanded using the interpolation software. These interpolation functions are called basis functions or shape functions.

6. Compute scattering matrix for the structure.

The steps mentioned here are also common to any other FE package. The order of final steps may vary or S-matrix may not be computed but the process of discretising the system into sub-elements and solving for each element separately followed by interpolation of data is common to all FE systems. Figure 2-11 shows a depiction of the mesh elements in HFSS and its application to a 3D object. Note that in HFSS the electromagnetic fields are calculated at the vertex and edge midpoints of each element. These points are shown in red. Grey arrows show direction of the extrapolation of each field, inward towards the centre of the tetrahedron.

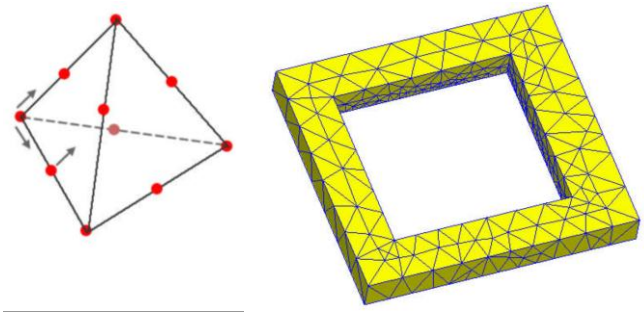

Figure 2-11: showing the structure of a tetrahedron element in HFSS and its application to a 3D object. The red points represent vertex and midpoints of an element for which the values of E and M fields are saved.

Eddy Current Problem

The FE solution flow in HFSS is applied to a simple eddy current problem. A block of copper is placed at a distance of 2.5 cm of a current carrying coil. The thickness of the slab of copper is then changed from 4 μm to 12 μm. S-matrix is calculated for the current carrying coil for each of the slab thicknesses. Using this data, the resistance of the current carrying coil is found and used as an indicator to changes in the thickness of the slab under test. Figure 2-12 shows the construction of this sensing system. A rectangular coil is placed in the vicinity of a slab of copper. Copper is depicted as a purple cube. The two terminals of the coil are connected to two square sheets, which are the ports of the system. A magnified version of the system is also shown to depict the meshing process of the environment. It can be seen that tetrahedron meshing is used for various elements of this system. HFSS would excite each of the ports one at a time and look at the propagation of electromagnetic waves inside the structure. This would yield the scattering matrix of the system under investigation. The

simulation was done for a frequency range of 150 MHz to 380 MHz and an air enclosure was chosen as the simulation space for this problem. All the conductive tracks are made of copper.

The scattering data are then converted into Z-matrix to obtain the complex impedance of the coil. The magnitude of this impedance is used as an indicator to the variations in the copper slab thickness. Figure 2-13 shows the changes in the impedance of the coil as the thickness of the coil varies from 4 μm to 12 μm. An increase of approximately $15000\ \Omega$ in the impedance of the coil is observed. This is due to an increase in the amount of induced eddy currents as the thickness of the slab is increased. This can be explained by looking at the skin depth, δ, of copper at a frequency of 240 MHz. Assuming a conductivity of $5.7 \times 10^7 Sm$ for copper, we use the following formula to calculate the skin depth [141] :

$$\delta = \sqrt{\frac{2}{\omega\mu\sigma}}$$

Note that once the thickness of a slab becomes substantially larger than the skin depth, the thickness is no longer an effective variable in changing the impedance properties of the coil. This is due to the fact that the majority of the induced current will flow at skin depth levels. A skin depth of 4.2 μm is calculated for copper at the frequency of interest. In this simulation no prior assumption with regards to the electrical properties of the system under investigation was made. Both conductivity and permittivity contributions of all the materials were taken into account.

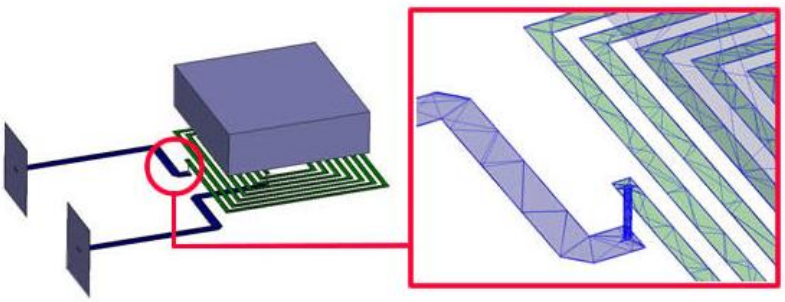

Figure 2-12: showing the structure of the sensing environment, with a slab of copper placed above a current carrying coil. The magnified version shows the meshing of the system.

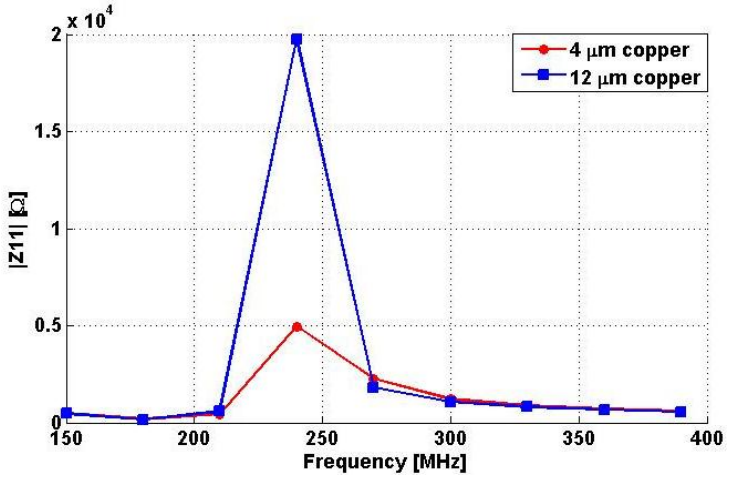

Figure 2-13: showing variations in the magnitude of Z_{11} of the coil as the thickness of a slab of copper is increased from 4 μm to 12 μm.

2.4 Comparative Analysis

In the previous section two method of analysing a sensing structure were discussed, FE computational and an analytical approach based on solving the Maxwell's equation using the method of separation of variables. In this section we shall use two examples to undertake an analysis on both methods. Hydrochloric acid and titanium silicide are the two materials used in this analysis. There is experimental data on the complex conductivity and permittivity of both materials in the literature. TiSi is a conductor with fixed value of conductivity, whilst the conductivity of HCl is concentration dependent. As a result, they can provide a good comparison for the difference in analysis of a conductor and a material with varying electrical properties. The former is a 1:1 electrolyte and the latter is a metal. Comparison of the data for these two materials will provide us with the basis of our choice of theoretical approach, analytical or computational FE.

2.4.1 Material Properties

The data provided for the HCl is obtained experimentally at room temperature. 600 mL of deionised water is placed inside a beaker with maximum capacity of 1000 mL. 2 mol solution of HCl are then added to the beaker in steps of 10 mL. This titration yields a concentration range of 0.0328 $molL^{-1}$ to 0.2353 mol. The effective permittivity of the solutions is then measured using an Agilent 85070E high temperature dielectric probe for a frequency range of 200 MHz to 1.6 GHz. Further information on the experiment and the process of obtaining the results can be found in Chapter-VI. Using the discussion in [156], we can approximate the

complex conductivity of the hydrochloric acid to its DC value. Hence the molar conductivity of the sample can be written as:

$$\Lambda_{\circ} = \alpha \frac{\sigma_0}{c} \tag{2.71}$$

In which $\Lambda_{\circ}$ is the molar conductivity, α is the constant of proportionality and assumes a value of one with appropriate units , c is the concentration of the sample in moles and σ_0 is the specific conductivity of the sample. The specific conductivity of the HCl sample is equal to its DC conductivity. Using the Gelling's formula discussed in section 1.2.1 we can calculate the molar conductivity of the HCl solution at $c = 0.0328\, mol^{-1}$ to be 42.62 mS m^2 mol^{-1} and at $c = 0.2353\, mol^{-1}$ to be 41.53 mS m^2 mol^{-1}. Table 2-3 shows the electrical properties of HCl solutions at two different concentrations with a driving frequency of 433.8 MHz. The reported data for the complex permittivity are effective values, which take both bound charge and free charge into account. Given that the factor $\frac{\sigma_0}{\omega}$ will be in the order of 10^{-12}, it is neglected and measured values of effective permittivity are directly used in the table.

The complex permittivity of titanium silicide ($TiSi_2$) was found from [157]. These equations used in this calculations are given below [157].

$$\varepsilon'(\omega) = \varepsilon_{\infty}\left[1 - \frac{\omega_p^2}{\omega_\tau^2\left(1 + \frac{\omega^2}{\omega_\tau^2}\right)}\right] \tag{2.72}$$

$$\varepsilon''(\omega) = \frac{\varepsilon_{\infty}\omega_p^2}{\omega_\tau\omega\left(1 + \frac{\omega^2}{\omega_\tau^2}\right)} \tag{2.73}$$

$$\rho = \frac{\omega_\tau}{\left[\varepsilon_{\infty}\varepsilon_0\omega_p^2\right]} \tag{2.74}$$

In these equations, ε_{∞} is the permittivity of the sample at very high frequencies. This frequency is usually taken to be the frequency at which the first electronic resonance takes place and can be found in the infrared region of the spectrum [29]. ω_τ is the relaxation frequency that refers to the time it takes for the charged particles in the system to rearrange themselves to a state of zero momentum in the materials once an external electric field is

removed. ω_p is called the plasma frequency which occurs beyond the last resonant frequency of the system and refers to the oscillations of the electron gas [29]. This can be explained as the angular velocity of precession of the sea of electrons in the metal. ρ is the resistivity of the material. For $TiSi_2$, $\omega_p = 3.2\ eV$ and $\omega_\tau = 0.03\ eV$. These values can be converted into Hz by using the reduced plank constant and the Planck relation for energy and frequency:

$$2\pi f_p = \frac{E}{\hbar} \Rightarrow f_p = \frac{E}{h} \tag{2.75}$$

The resulting permittivity calculated using equations 2.72 and 2.73 is an effective complex permittivity that takes into account the contributions from the free charges as well. The values found using these two equations are calculated and plotted for an energy range of 0.009926 eV to 0.992 eV which is equivalent to 2.4×10^{12} and 2.3986×10^{14} in Figure 2-14. This was to compare the formula used with the reference data [157]. The complex conductivity of the material, which only takes free charge carrier contributions into account, is calculated using the Drude theory [158]. The formulas used in the calculation of the Drude model are shown in equations 2.76, 2.77, and 2.78. Experimental data for energy levels of up to 10 eV and theoretical data plots of up to 0.08 eV are shown in Figure 2-15 [157]. The aim of this comparison is to show the accurate and correct implementation of the formulas discussed in producing the data in Figure 2-14.

$$\sigma(\omega) = \sigma_{dc} \frac{1}{1 - j\omega\tau} \tag{2.76}$$

$$\sigma(\omega) = \sigma_{dc} \frac{1}{1 - j\omega\tau} \frac{1 + j\omega\tau}{1 + j\omega\tau} \tag{2.77}$$

$$\sigma(\omega) = \frac{\sigma_{dc}}{1 + (\omega\tau)^2} + j \frac{\sigma_{dc}}{1 + (\omega\tau)^2} \tag{2.78}$$

In here, τ is the relaxation time and is found using the value given for ω_τ previously, and σ_{dc} is the conductivity at DC, which is found from the resistivity value in equation 2.74. The theoretical values for the complex conductivity and permittivity of the titanium silicide are shown in Table 2-4 [157]. It can be seen that the theoretical calculations provide good agreements with experimental data for energy levels of up to 10^{-1}. However given that the terms $\frac{\sigma''}{\omega}$ and $\frac{\sigma'}{\omega}$ are in the order of 10^{-6} and 10^{-2}, the calculated numbers for the effective permittivity were directly reported and the conductivity contributions to the complex part of

the permittivity were neglected. The values reported for the HCl and titanium silicide were then used to calculate various terms in equation 2.48 which is the full wave MVP equation. The calculated values are shown in Table 2-5.

Table 2-5 shows calculated values for various terms in the MVP equation, equation 2.48. It can be seen that the first term represents lossy contribution from both bound and unbound charged due to the effect of the magnetic vector potential. The second term represents the total polarisation losses of the sample due to the magnetic vector potential. Conduction losses for bound and unbound charges due to the variations in the electric potential are represented by the third term. The last term deals with polarisability losses of a sample due to changes in the scalar electric potential.

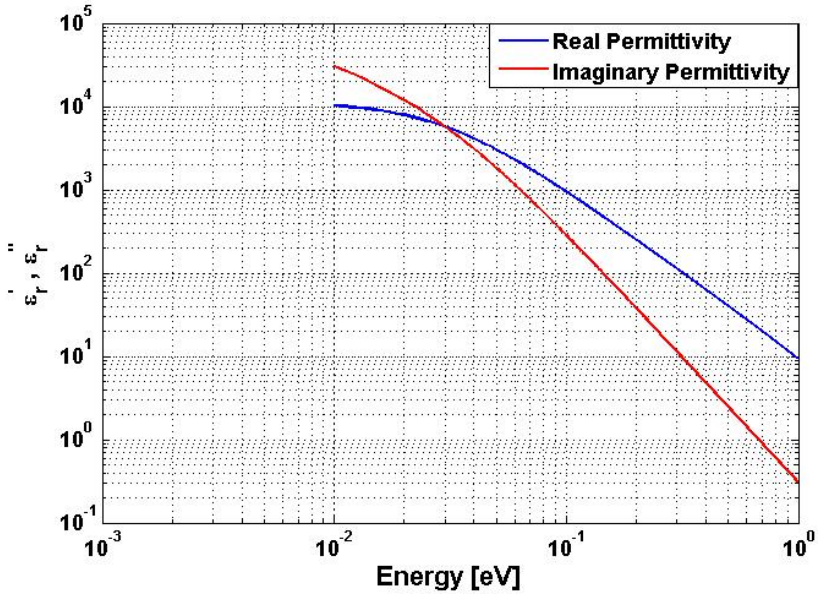

Figure 2-14: showing the plot of real and imaginary values of TiSi permittivity against energy in a log scale

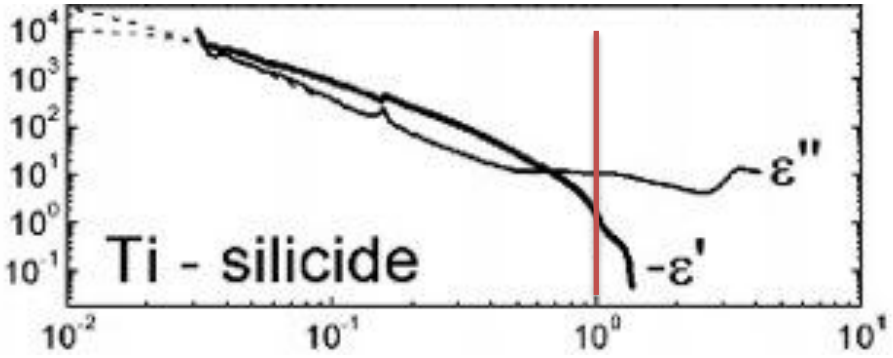

Figure 2-15: showing the experimental data for the complex permittivity of Ti-silicide for a range of frequencies. The dashed lines are theoretical data points [21]

Table 2-3: showing the electrical properties of HCl at a an absorption peak occurring at a frequency of 433.8 MHz

HCl: $c = 0.0328$		
$\sigma_0 = 0.0014$	$\varepsilon' = 8.436$	$\varepsilon'' = 12.767936$
HCl: $c = 0.2353$		
$\sigma_0 = 0.0098$	$\varepsilon' = 3.618867$	$\varepsilon'' = 861.6887$

Table 2-4: showing the electrical properties of titanium silicide at a frequency of 433.8 MHz

$TiSi_2$			
$\sigma' = 4.592 \times 10^6$	$\sigma'' = 1725$	$\varepsilon' = 1.138 \times 10^4$	$\varepsilon'' = 1.903 \times 10^8$

However given that the terms $\frac{\sigma''}{\omega}$ and $\frac{\sigma'}{\omega}$ are in the order of 10^{-6} and 10^{-2}, the calculated numbers for the effective permittivity were directly reported as permittivity with no conductivity contribution with no modifications. The values reported for the HCl and titanium silicide were then used to calculate various terms in equation 2.48 which is the full wave MVP equation. The calculated values are shown in Table 2-5.

Table 2-5: showing the calculated MVP terms for HCl at two different concentrations and $TiSi_2$, all at the frequency of 433.8 MHz

HCl: $c = 0.0328\ mol\ L^{-1}$			
$j(\mu\omega\sigma' + \mu\omega^2\varepsilon'')$	$\mu\omega\sigma'' + \mu\omega^2\varepsilon'$	$\mu\sigma' + \mu\omega\varepsilon''$	$j(\mu\sigma'' + \mu\omega\varepsilon')$
$j(0.76 + 3.019 \times 10^{12})$	$0 + 1.995 \times 10^{12}$	$1.76 \times 10^{-9} + 6.96 \times 10^{3}$	$j(0 + 4.599 \times 10^{3})$
HCl: $c = 0.2353\ mol\ L^{-1}$			
$j(\mu\omega\sigma' + \mu\omega^2\varepsilon'')$	$\mu\omega\sigma'' + \mu\omega^2\varepsilon'$	$\mu\sigma' + \mu\omega\varepsilon''$	$j(\mu\sigma'' + \mu\omega\varepsilon')$
$j(5.34 + 2.0377 \times 10^{14})$	$0 + 8.5578 \times 10^{11}$	$1.23 \times 10^{-8} + 4.697 \times 10^{5}$	$j(0 + 1.9727 \times 10^{3})$
$TiSi_2$			
$j(\mu\omega\sigma' + \mu\omega^2\varepsilon'')$	$\mu\omega\sigma'' + \mu\omega^2\varepsilon'$	$\mu\sigma' + \mu\omega\varepsilon''$	$j(\mu\sigma'' + \mu\omega\varepsilon')$
$j(2.5 \times 10^{9} + 4.5 \times 10^{19})$	$9.4 \times 10^{5} + 2.6911 \times 10^{15}$	$5.77 + 1.0374 \times 10^{11}$	$j(0.0022 + 6.2 \times 10^{6})$
(i)	(ii)	(iii)	(iv)

2.4.2 MVP Analysis

Table 2-5 shows calculated values for various terms in the MVP equation, equation 2.48. It can be seen that the first term represents lossy contribution from both bound and unbound charged due to the effect of the magnetic vector potential. The second term represents the total polarisation losses of the sample due to the magnetic vector potential. Conduction losses for bound and unbound charges due to the variations in the electric potential are represented by the third term. The last term deals with polarisability losses of a sample due to changes in the scalar electric potential.

The imaginary vector potential contribution for HCl increases 67 times as the concentration of the HCl solutions is increased. At the same time the polarisablity contributing terms' magnitude of the solution are reduced in half. This can be readily observed from Table 2-3 in which the real permittivity of the sample is decreased but the imaginary part of the permittivity is increased substantially. Note that the effect of unbound charge carriers is negligible in this analysis. Similar analysis can be applied to the electric scalar potential term to explain the increase in the real component and decrease in the imaginary part of the electric scalar potential contributing terms. In the case of HCl, at lower concentration, we can see that the magnitude of the real and imaginary contributions of both vector potential and

scalar potential terms are of comparable size. In the case of the titanium silicide, it can be seen that the contribution from the sea of electrons to the imaginary term of the vector potential effect is 10^{10} times smaller than the dispersion term at the given frequency. However the total value is still 10^4 times larger than the largest term in the full wave MVP equation. In the case of the electric scalar potential, the size of the real electric scalar potential is 10^5 times larger than the imaginary one.

As a result in the case of the HCl solutions the full wave MVP equation must be solved. In the case of $TiSi_2$ once can make an assumption of neglecting the second term of the MVP equation as the magnitude of the first term is 10000 times larger than the second term [145]. This is the basis of the eddy current sensor for conductive materials in which the contributing effect of the imaginary component of the magnetic vector potential is the dominant factor and hence all other terms can be safely neglected. It must be noted that the contributing terms from the scalar potential components should be taken into account if the effect of the displacement current is of importance. Displacement current affects the energy storage property of a system and also the amount of energy dissipated into the system by bound charges. This was shown in equation 2.33 as the displacement current will contribute to the values of the second and forth terms in the equation. As a result their contribution to the MVP equation in section 2.1.4 and in here should be taken into account.

2.4.3 Discussion

In the previous section we looked at the derivational steps for both analytical and FE computational approaches to solving electromagnetic problems. An eddy current problem was also used to demonstrate the solution flow for each of the methods. Analytical solutions can offer a more in depth description of the problem space. They can also lead to more accurate solutions, as the user is free to make any or no assumptions with respect to the problem space. Hence the analytical solution can be made as complicated or as simple as the user would like it to be. However, this can lead to differential equations that cannot be readily solved. As a result assumptions are usually made with regards to the problem space in terms of its electrical properties. This was demonstrated in the eddy current example in the previous section. It was observed that by assuming a medium with large conductivity and negligible polarization, we could reduce the full wave Maxwell's equation to a simple differential equation that can be solved readily.

$$\nabla^2 \boldsymbol{A} = j\mu\omega\sigma\boldsymbol{A}$$

In this process we neglected the radiation losses, electrically induced conductive currents and electrically induced displacement currents. These assumptions are usually valid in the case of metals and other highly conductive materials. For instance this analysis can be readily applied to metal detectors and crack detection systems. The same analysis can be applied for the case in which the subject of the measurement or design is a dielectric. The MVP equation now has the following form.

$$\nabla^2 \boldsymbol{A} = -\mu\omega^2\varepsilon\boldsymbol{A}$$

Note that in both aforementioned cases, the effects of electrically induced conductive and displacement currents were neglected from the equation. For the case in which the analysis of these contributions is necessary, one can use the Poisson's equation of the electric scalar potential equation to account for those contributions:

$$\nabla^2\varphi = \frac{\rho}{\varepsilon(\omega)} \qquad 2.79$$

In this equation the quoted permittivity is the effective complex permittivity that includes contributions from the unbound charges. As a result one can calculate the effects of the scalar potential from here instead of solving the full wave MVP equation. Hence depending on the type of materials in the system and the frequency of interest, the right assumptions and the right approaches should be adopted.

Similar precautions should also be adopted when dealing with FE computational packages. Some packages are designed for low frequency applications, e.g. ANSOFT Maxwell 3D, and the others are devised for high frequency analysis, e.g. COMSOL Multiphysics. Thus the right package should be selected prior to any simulations. The other difficulty may be on the accuracy of the result; this can be addressed by the use of ever-finer mesh. However this requires more computational power and a longer time for simulation. The real power of FE is however is in its ability to model complex structures and complex shapes. This leads to the full exploration of the design space and hence more parameters can be looked at and further fine-tuning can be achieved. This is one of the advantages of the FE approach to an analytical one as calculating the behaviour of EM fields in the boundary between complex surfaces analytically can be a challenging task. The other advantage of FE packages is their ability to provide an environment in which design, analysis and optimisation can be done without producing a prototype. This can lead to a shorter design cycle and hence a lower cost. This, along with the ability to allow for computer visualisation of the problem space allows for an enormous amount of physical insight into the problem.

Given the analysis on values provided in Table 2-5, full wave MVP equation must be solved for solutions of hydrochloric acid. Finding the solutions to the full wave MVP equation is time consuming and complex. In complex structures the process of defining boundary conditions could be a difficult task, which can in turn complicate the solution flow process. Given the advantages of FE packages in terms of being able to deal with complex geometries and providing greater insight over the system as a whole, the latter will be used in further theoretical analysis of this work. The chosen software for this purpose is Ansoft HFSS for which the license is provided by ETH Zurich in Switzerland. For the rest of this research we shall only use data obtained in HFSS and will only refer to the MVP equation for explaining the physics behind the results obtained and their theoretical significance.

Chapter 3

3 Primary Investigation

In this chapter we shall look at the primary prototypes of an electrically resonating structure and their experimental data. The primary structures were tested with electrolyte solutions and their high frequency electrical properties were monitored. The aim of the initial work was to obtain a better understanding of the sensing system and obtain further confirmation on the suitability of the sensor for the research target. At first a background to the project and its inception shall be provided. This will be followed by a discussion on the two primary prototypes that were fabricated in order to test the initial hypothesis, and obtain greater insight into the system. Further discussion on the suitability of the structures for the purpose of monitoring electrolyte solutions will also be provided.

3.1 Initial Stage

As discussed in the first chapter, monitoring electrical properties of electrolyte solutions can yield important information regarding the species present in the sample and types of reactions taking place inside the sample. Several methods of monitoring electrolyte solutions were discussed in Chapter–I. A type of sensor with deep integration with the CMOS fabrication process was ISFETs. Their advantageous and disadvantageous were discussed in Chapter–I. Among the disadvantageous were drift and variations in the threshold voltage of ISFETs fabricated on different chips. This difference could be as large as ±25 V between ISFETs on different chips. In order to address this issue various fabrication processes offered by different foundries were investigated to find the most suitable process. In due course power CMOS chips by the Austria Microsystems (AMS) foundry were also looked upon. It was found that in this particular process, the CMOS chip undergoes an extra polyimide-packaging step. This layer needs to be removed in order for the ISFETs to function. However the removal of this layer could damage the silicon nitride layers beneath it, so the outcome may be an uneven surface. The uneven surface could pose problems to the deposition of other

materials like platinum for the reference electrode. The removal process also adds an extra post-processing step, which increases the fabrication cost of the sensor. Figure 3-1 shows the cross section of a 35 µm 50 V AMS chip in which the top layer grey area represents the polyimide layer. It can be seen that this process offers four metal layers with the top metal layer being the thickest. The top metal layer is covered by silicon nitride followed by polyimide.

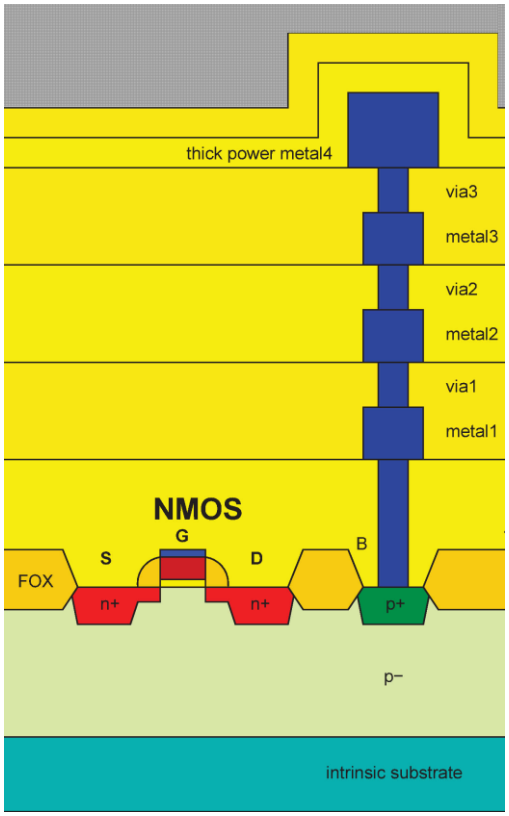

Figure 3-1: showing the structural layout of a high voltage 35µm AMS process showing various metal layers along with section of an NMOS transistor. FOX stands for the field oxide.

Polyimide is an insulating material with good resistance to chemical attacks which makes this fabrication technology unsuitable for ISFET design [159]. However given the built in insulating layer into the technology and the thick top metal layer, it was readily observed that an electrically resonating sensor could be realised by placing an inductor beneath the polyimide layer. This places the coil in the immediate vicinity of the sample that can be easily placed on the polyimide layer. The thicker top metal layer provides smaller resistance to the flow of current and hence reducing the risk of the coil heating up the sample. Hence the use of inductors for monitoring and analysis of electrolyte solutions was further investigated.

3.2 Primary Prototype

The sensitivity of inductors to changes in the electrical properties of liquid samples was investigated to ensure adequate sensitivity. The first structure to be tested was a helicoid. The helicoid inductors have already been used in monitoring liquid samples, e.g. liquid flow (refer to Chapter–I). One of the advantages of a helicoid is its ability to store the magnetic field in its interior space and hence its high sensitivity to changes in the conductivity of a sample placed inside it. A helicoid inductor can be fabricated using MEMs processes. However for this particular test, a helicoid was constructed by wrapping a silicone covered single core tinned copper wire around a small cylinder, i.e. a pen. The diameter of the conductive element is 0.6 mm and the diameter of the wire is 1 mm. The created helicoid has a diameter of 6 mm with 20 turns and a length of 10 cm. An image of a similar device is shown in Figure 3-2.

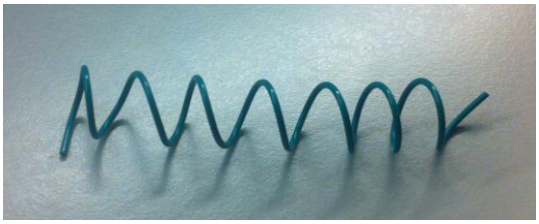

Figure 3-2: showing an image of a helicoid inductor made by wrapping a single core plastic coated wire around a cylindrical object

If n the number of turns, r the radius of the helicoid, and l the length of the helicoid, we can use the Wheeler formula to calculate the inductance, L in μH, of the created coil [162].

$$L = \frac{\mu_0 n^2 \pi r^2}{l + 0.9r}$$

This leads to an inductance of 138.4 nH for this coil. The helicoid inductor is then placed inside a container, which will be filled with a solution of deionised water. The inductor will not be fully immersed in the solution. 0.5 ml of 1 M HCl were then added to the solution. It was assumed that the height of the sample remains unchanged. An AGILENT PNA network analyser was used to monitor the S–parameters of the inductor coil. The measurement was performed in the range of 10 MHz to 1 GHz and the test was done at room temperature. A conceptual sketch of this test is shown in Figure 3-3. The experimental data for this test are shown in Figure 3-4. The red trace represents the S_{11} response of the coil immersed in deionised water. The data point m1 at a frequency of 688.6 MHz is chosen as an indicator for monitoring the shift in frequency of the coil. Upon the addition of hydrochloric acid, there is a shift to lower frequencies at this point, which implies a greater transfer of energy at lower

frequencies compared with the case of deionised water. This is the result of a shift in the complex permittivity of the electrolyte solution to higher values. As a result the stored energy in the form of electric field in the system increases. This leads to a shift of the coil's resonance frequency to lower values, which in turn reduces the frequency at point m1. The theory behind the electrolyte permittivity is discussed in Chapter-I. Experimental data on the complex permittivity of HCl is also provided in Chapter-V. The data point m2 is found to be at a frequency of 661.8 MHz. This is a frequency shift of 26.8 MHz, which is equivalent to 3.89% shift from the nominal frequency.

The 3.89% shift can be measured by any suitable network analyser and also by circuits made using conventional CMOS process. However the helicoid cannot be realised using conventional CMOS processes due to its non–planar structure. It requires the use of MEMs' based fabrication technologies, which can add to the fabrication cost. The other shortcoming is the creation of a microfluidic channel inside the helicoid, as the coil needs to be insulated from the sample. Although the electrical properties of the helicoid are well known and have been used extensively in the industry for the liquid flow measurement, the helicoid is not the most suitable structure for our purposes. Hence the use of planar inductors, which are CMOS and microfluid friendly, was then investigated.

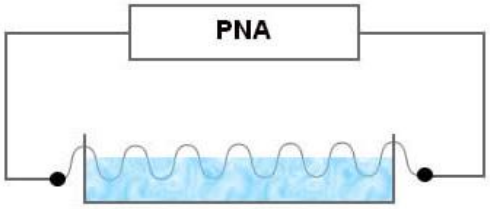

Figure 3-3: showing the conceptual sketch of a partially immersed inductor coil and its connection to a PNA network analyser

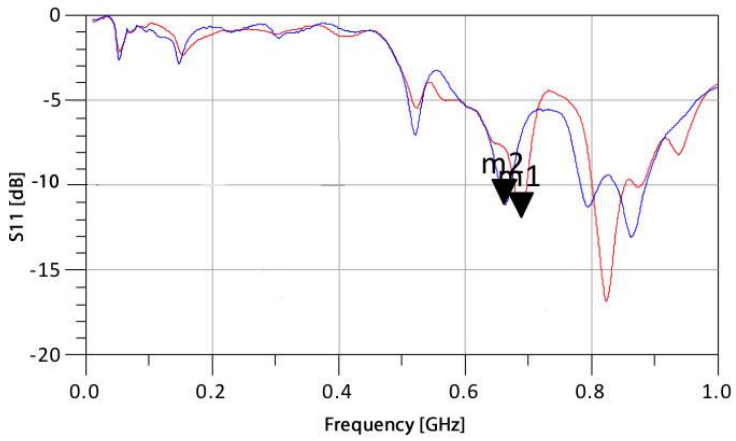

Figure 3-4: showing the variations in the S11 of a helicoid immersed in a solution as the value of the pH is changed. Red trace (m1) depicts the behaviour of the coil with deionised water and blue trace (m2) with HCl

3.3 Equivalent Circuit Model

The data analysis on the inductors can be done using the S–parameters. However given that these parameters are the ratios of incident and reflected powers, they do not correspond to physical quantities readily. In order to achieve this, equivalent circuit models of inductors are developed. Data obtained from S–parameter measurements are converted into admittance (Y) parameters, the conversion process is explained in [160]. The admittance data can then be fitted into an inductor model to undertake parameters extraction. The most basic inductor model that takes into account capacitive losses into the substrate is the 1-π model, as shown in Figure 3-5.

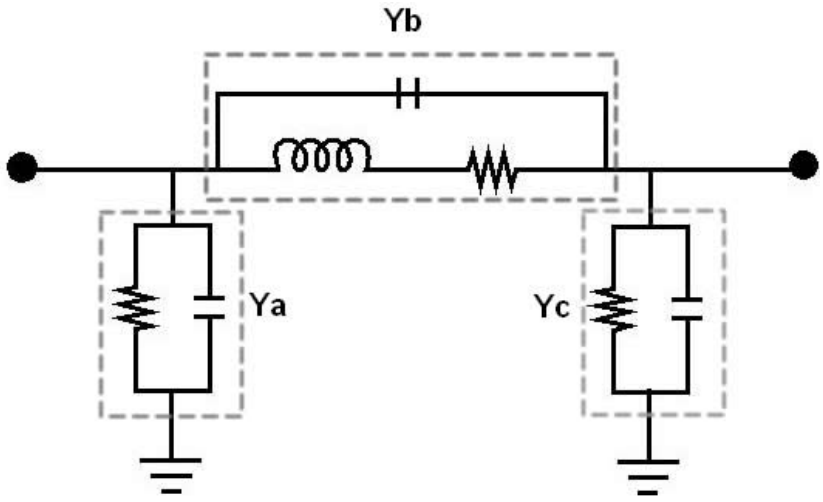

Figure 3-5: showing the equivalent 1–π model of an inductor with parasitic losses to the substrate, at each port, represented by admittance parameters to the ground

In here the inductor is modelled by Y_b, as an inductor in series with a resistance and a parasitic capacitance in parallel with the coil. The ohmic and capacitive losses to the substrate at each port are represented by Y_a and Y_c. In a symmetric system the values for Y_a and Y_c are equal. The admittance blocks, $Y_{a,c}$ can be calculated in terms of Y–parameters. Figure 3-6 shows equivalent admittance blocks of the π–model with applied voltages and currents at each port. Invoking Kirchhoff's current law (KCL) at both the input and output respectively, we obtain:

$$i_1 - v_1 y_a - (v_1 - v_2) y_b = 0$$
$$i_2 - v_2 y_c - (v_2 - v_1) y_b = 0$$

Rearranging these equations will yield

$$i_1 = (y_1 + y_b) v_1 - v_2 y_b$$
$$i_2 = (y_c + y_b) v_2 - v_1 y_b$$

Assuming a reciprocal and symmetric system, the admittance values for blocks *a*, *b* and *c* are derived to be:

$$y_a = Y_{11} + Y_{12} = Y_{11} + Y_{21}$$
$$y_b = -y_{12} = -y_{21}$$
$$y_c = Y_{22} + Y_{12} = Y_{22} + Y_{21}$$

Further information on the equivalent π–model of an inductor can be found in [160-162]. Hence the Y–parameter matrix of this system can be written as:

$$Y = \begin{bmatrix} y_a + y_b & -y_b \\ -y_b & y_c + y_b \end{bmatrix}$$

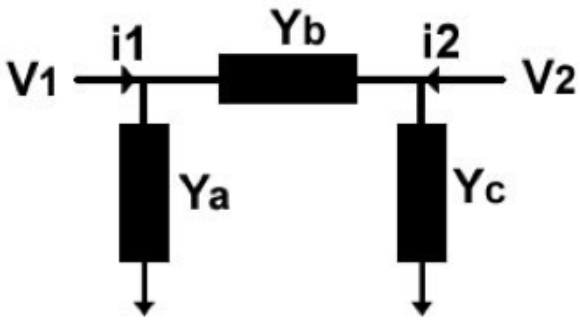

Figure 3-6: showing the equivalent π-model of an inductor in a 2-port set up

The inductance and the resistance in block *b* can now be found from measurement data using the following formulas:

$$R = re\left(-\frac{1}{Y_{12}}\right)$$

$$L = \frac{im\left(-\frac{1}{Y_{12}}\right)}{2\pi f}$$

The analysis of data obtained by inductors will be based on the π–model in which the inductance and resistance are calculated from the $-Y_{12}$ parameters. The self-resonance of the inductor will be monitored and its variations with respect to the liquid sample shall be discussed. This approach is only valid for frequencies of up to the first resonance point of the inductor coil. Beyond this point, the resistance shall drop and reach negative values. At this point the π–model is no longer valid. This is due to the fact that the resistance used in this model is a real component and hence not valid for negative values. We have however shown the values of the resistance and inductance for all frequencies in certain graphs to provide a more detailed picture.

3.4 Secondary Prototype

Planar inductors can be realised easily in a conventional CMOS process or on any suitable substrate. Hence a planar coil was fabricated on a FR4 substrate given its availability and low cost for rapid prototyping. The inductor coils were designed in AGILENT Technology's Advanced Design Technology (ADS) software package. The width of the tracks was set to $w = 1.5mm$ and the spacing between the tracks was set to be $s = 2mm$. The dimension of the substrate was chosen to be $3cm \times 4cm$ to provide easy handling of the sample and ease of packaging. Figure 3-7 shows the conceptual design and the size of contacts to the inductor. The DC inductance of this design can also be estimated using the equation mentioned in [162]. In here, c_1-c_4 are shape specific coefficients (such as hexagon), and ρ is the fill factor defined by the ratio of inner and outer diameters of the inductor. This formula is used for symmetric shapes, however, it is mentioned here for discussion purposes. For non-regular shapes Grover method can be used [162].

$$L = \frac{\mu n^2 d_{avg} c_1}{2}\left[ln\left(\frac{c_2}{\rho}\right) + c_3\rho + c_4\rho^2\right]$$

$$\rho = \frac{d_{out} - d_{in}}{d_{out} + d_{in}}$$

These formulas yield DC values of inductance. The network analysers used in this research can only measure S-parameters down to a frequency of 9 kHz. As a result no direct comparison can be made between our experimental data and analytical formula. The nature of the sensing mechanism, the self-resonance of the coils, also means that the sensor shall operate at frequencies much higher than the ones that the analytical formula is used for. Hence, we only measured the inductance of this prototype using a Fluke RLC measurement instrument at a frequency of 1 kHz. This measurement provided an inductance value of 1.5 μH. From our experimental data, we have got an inductance of 4.2 μH at a frequency of 9 kHz.

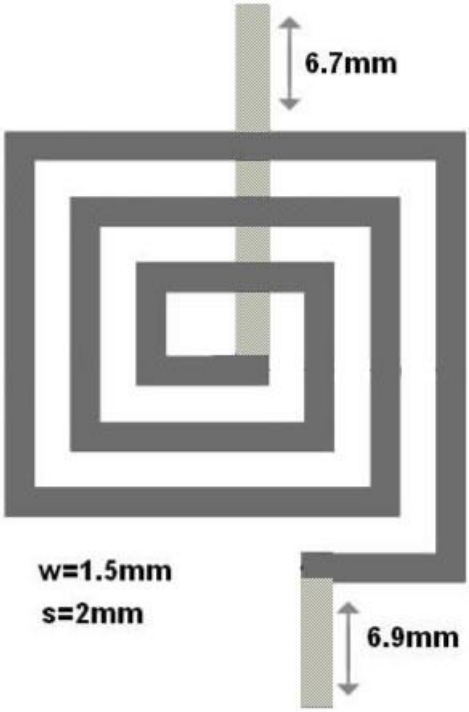

Figure 3-7: showing the sketch of the fabricated prototype and dimensions of the copper contacts

The contacts to the inductor were made at the back of the FR4 substrate. Two holes were made at each end of the coil and a piece of metal, obtained from a multi–threaded wire, was then inserted into the holes. The ends of the wires were soldered at the top and bottom of the substrate to make contact between the copper tracks and the coil. The soldering was done by hand due to the lack of access to through–hole copper plating. As a result copper spheres were formed at the point of soldering. Figure 3-8 shows the image of a soldered inductor and the position and shape of the copper spheres. These spheres pose a difficulty at the packaging stage. Hence, multiple prototypes were made and soldered and samples with the smallest soldering footprint were selected for packaging.

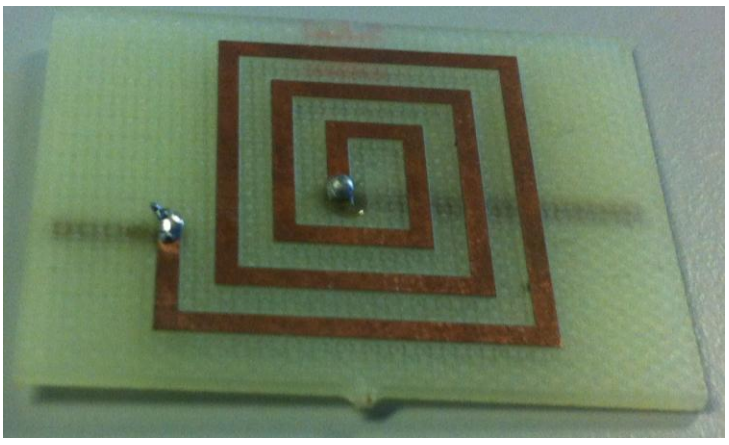

Figure 3-8: showing the fabricated inductor and the solder spheres created at each end of the coil

The fabricated coils were then hand sprayed by a thin layer of acrylic from a distance of approximately 10 cm. Given the presence of copper spheres at the soldering point, several attempts were made in order to find the sufficient time required to spray the device and cover all contacts with acrylic so no area of the sensor is exposed to the solution placed on the top of the inductor. To test for the exposure, an ohmmeter was used to measure the resistance between the insulated top layer copper and the copper tracks at the back of the inductor. In this case a low resistance implied an exposed area and hence a failed packaging. The bottom copper tracks were then soldered to gold plated SMA contacts. The SMA contacts were certified to operate up to 3 GHz. The measurements were performed in the range of 9 kHz to 6 GHz in steps of 30 MHz for testing purposes and are shown here in full for demonstration purposes only. The analysis will look into data points of up to 1 GHz only.

To contain the liquid sample placed on the device, a reservoir was created on the top of the inductor coil using insulating epoxy glue. This was made by hand and a depiction of it can be seen in Figure 3-9. As a result the height of the reservoir was short and its width was large. As a result a large outer area of the inductor was covered by the epoxy. However given that most this was a qualitative test to check for the feasibility of these devices as sensors, this shortcoming in the design was dismissed.

The experiments were performed by placing 24 ml of 1 M hydrochloric acid inside the reservoir shown in Figure 3-9 and titration with a solution of sodium hydroxide. Given that the aim of this test was to obtain proof of concept for the planar inductor no further characterisation of the liquid solutions were performed.

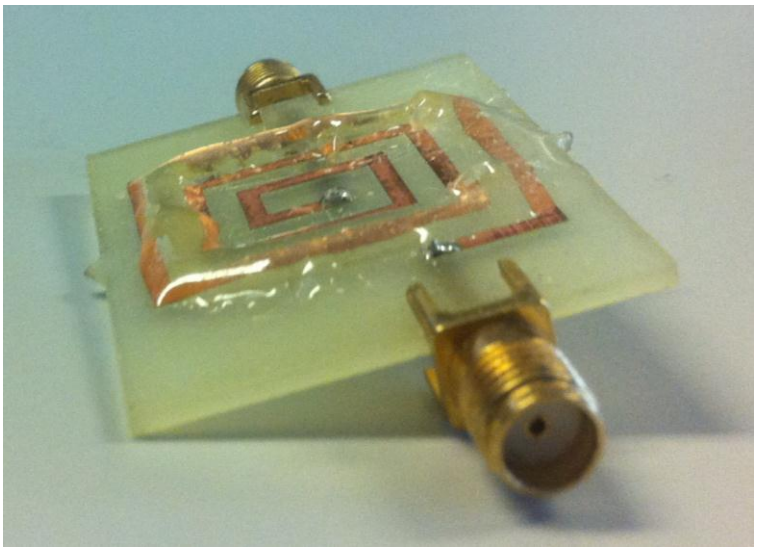

Figure 3-9: showing the packaged inductor with SMA contacts at each end

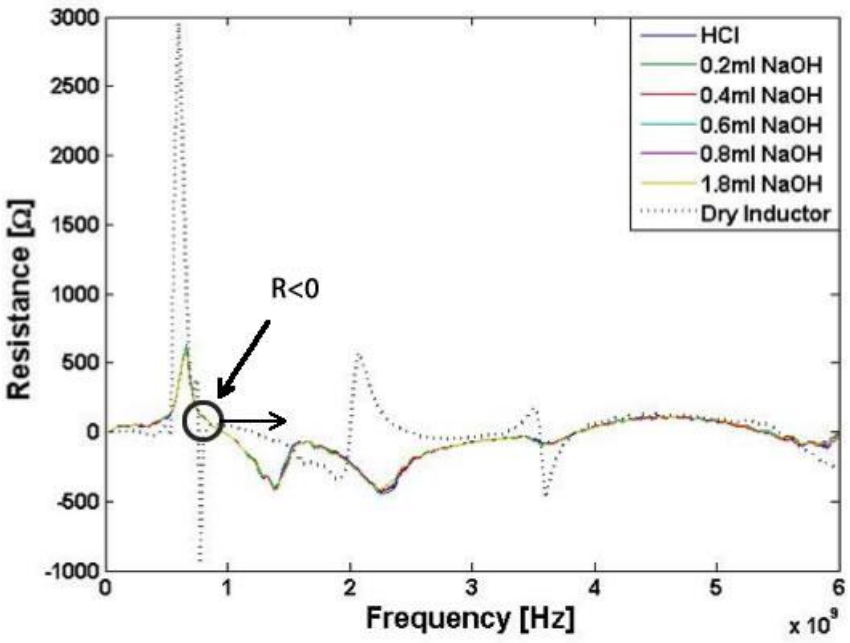

Figure 3-10: showing the plots of resistance against frequency for the case of dry and wet inductor in the full frequency span

Figure 3-10 shows the plot of the variations in the resistance of the coil in the full frequency sweep. The data beyond the 608 MHz are not valid based on the π-model as the resistance reaches negative values. Hence, all data beyond R<0 circle highlighted in the above figure, are not valid and not of interest. The dotted line represents the resistance of the packaged inductor when dry. It can be seen that the presence of liquid in the vicinity of the inductor reduces the maximum resistance from 3000 Ω to 600 Ω.

Variations in the maximum value of the resistance in the range of 30 MHz to 1 GHz were monitored. The inductor could be considered as a coil in parallel with its parasitic capacitance. As a result the resonance for this LC system (self-resonance) occurs at a point of maximum resistance [139]. Figure 3-11 shows the behaviour of the resistance of the coil as HCl is being titrated with NaOH. Using the resistance of the coil in the presence of HCl as the reference, the maximum resistance values for the titrations were calculated and then subtracted from the reference resistance. The following equation was used for this analysis.

$$\Delta R = R_{HCl} - R_{NaOH}$$

This titration leads to the formation of NaCl in the solution and the neutralisation of the H_3O^+ cations. As the limiting molar conductivity of Na^+ is much smaller than the ones of H^+, refer to Table 1-1, the titration will lead to a reduction in the value of conductivity. In [163] it is shown that this titration leads to a near linear decreasing conductivity function. The calculation of the conductivity of titration reactions is beyond the scope of this thesis. For

more information on conductivity calculations for titration reactions refer to [17], [156], and [164].

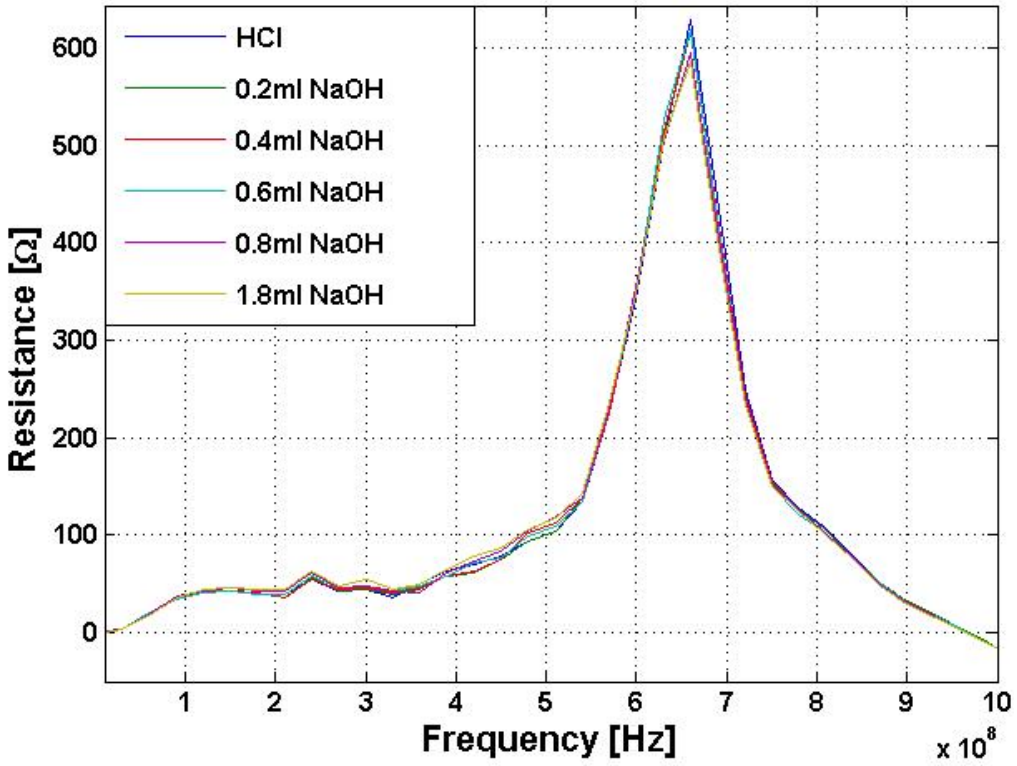

Figure 3-11: showing the variations in the resistance of the coil as NaOH is titrated with HCl

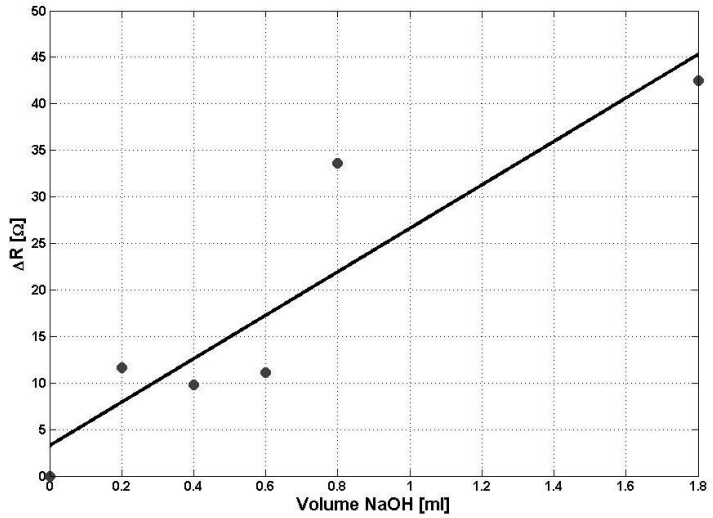

Figure 3-12: showing experimental data for the variations in the resistance of the coil with respect to the reference resistance of HCl. The black line is the linear line of best fit

Figure 3-12 shows a plot of the differential resistances against the volume of the added NaOH to the HCl reference solution. The black line is the line of best fit for the measurement data points. A total change of 44 Ω can be observed. The resistance value of zero represents

the resistance with only the reference solution being present. The resistance values were found to peak at a frequency of 660 MHz. This is the resonance frequency of the inductor. The increase in the ΔR values corresponds to a reduction in the resistance of the coil. This could be attributed to a decrease in the conductivity of the sample with respect to the conductivity of the HCl solution. It can be seen that the resistance varies nonlinearly for small volumetric titrations. However if the volumetric titration steps are increased a qualitative sensor can easily be realised. A variation of 44 Ω can also be measured using conventional CMOS circuitry or discrete operational amplifiers.

Figure 3-13 shows the variations in the inductance of the device under dry and wet conditions as HCl is titrated with NaOH. In this case, the resonance takes place at the point in which the inductance has a value of zero. We can perform the analysis based on two different approaches. The first approach looks at the shift in the self-resonance frequency. In this case the inductor can be placed in an oscillatory circuit like an Schmitt trigger and changes in the oscillation frequency are then monitored. The second approach involves monitoring the value of the inductor at a fixed frequency. Note that the data beyond the first resonant point are not valid. This is due to the failure of the π–model as the resistance reaches negative values in the immediate aftermath of self–resonance.

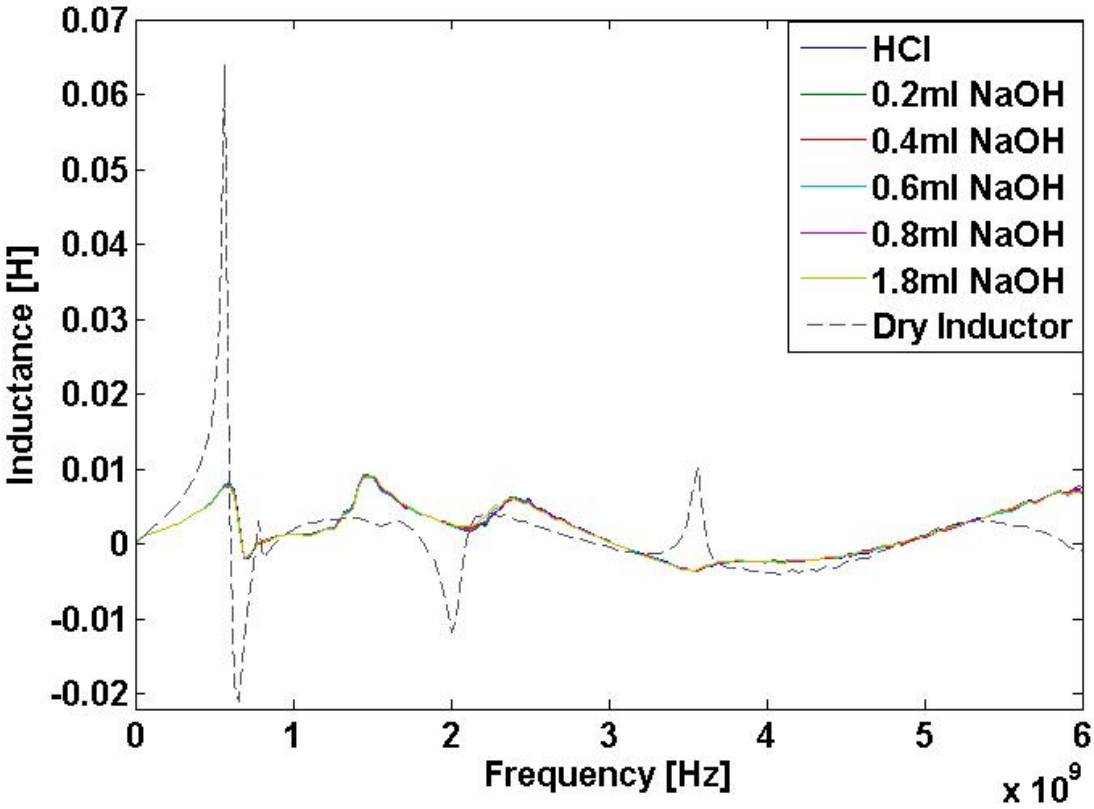

Figure 3-13: showing the inductance of the coil for the cases of dry and wet inductors in the full frequency span

Using the parameters of the inductor in the presence of HCl as the reference, we can calculate the changes in the resonance frequency by using the following formula:

$$\Delta f = f_{HCl} - f_{NaOH}$$

The resonance of the system was found to be 678.6 MHz for the case of the HCl. The discrepancy with regards to the maximum value of the resistance can be explained by noting that the measurements were performed in 30 MHz steps. Hence for the frequencies of interest we have the following measurement steps.

$$[\ldots \quad 630\ MHz \quad 660\ MHz \quad 690\ MHz \quad \ldots]$$

Given that there are no data points in the interval of 660 MHz to 690 MHz, interpolated data in MATLAB software are used in order to calculate the point at which inductance reaches a value of zero, L=0. Figure 3-14 shows the variations in the resonance frequency of the device against the added volume of NaOH to HCl solution. A quadratic line of best fit is obtained using MATLAB and is shown in black.

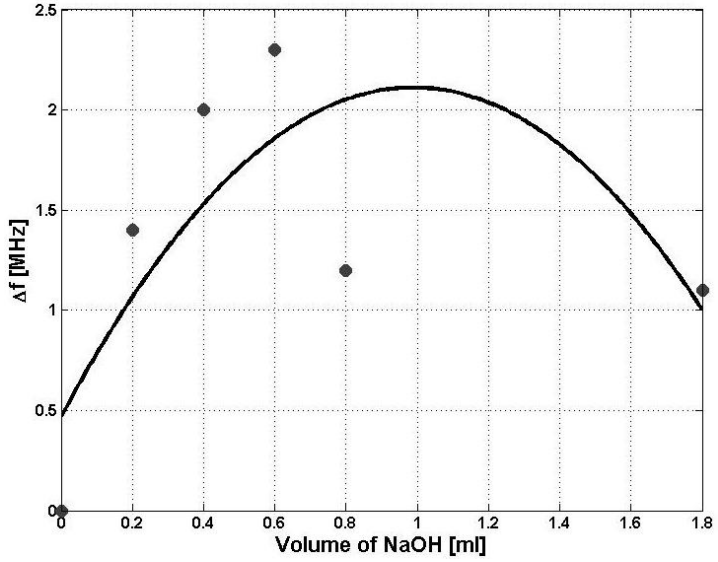

Figure 3-14: showing the variations in the self–resonance frequency of the device with respect to the reference HCl solution. A quadratic fitting function is used to depict the behaviour of the data points.

It can be deduced that the decrease in the value is attributed to an increase in either the inductance or parasitic capacitance (or both) of the device. This is due to changes in the physical properties of the material in the vicinity of the sensor. A reduction in the resistance of the solution could reduce the amount of eddy currents flowing in the sample under test. Hence leading to an increased value of the inductance. It could also be argued that an increase in the permittivity of the sample can increase the parasitic capacitance of the inductor and hence help lower the resonant frequency. However as at this stage, the analysis was only performed for qualitative proof of principle for the planar inductor, so no further

theoretical data analysis or measurements on the exact electrical properties of the HCl and NaOH samples were undertaken.

The analysis was also performed at the fixed frequency of 400 MHz. Figure 3-15 shows the variations in the inductance of the system as the volume of the NaOH is increased from zero to 1.8 ml in the reservoir. As the amount of the NaOH increases, the magnitude of the inductance decreases. A linear line of best fit is provided for this set of data. Similar analysis can be done for a frequency of 500 MHz as shown in Figure 3-16. The data presented in these two figures shows that by using the current sensor design at a fixed frequency, a qualitative sensor can be realised.

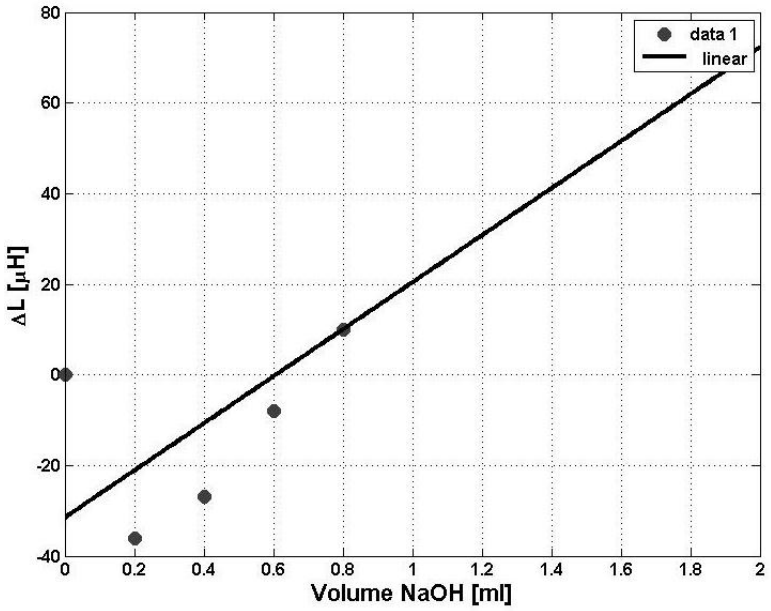

Figure 3-15: showing the changes in the inductance of the system at fixed frequency of 400 MHz as NaOH is added to the HCl solution. The line of best fit is shown in black

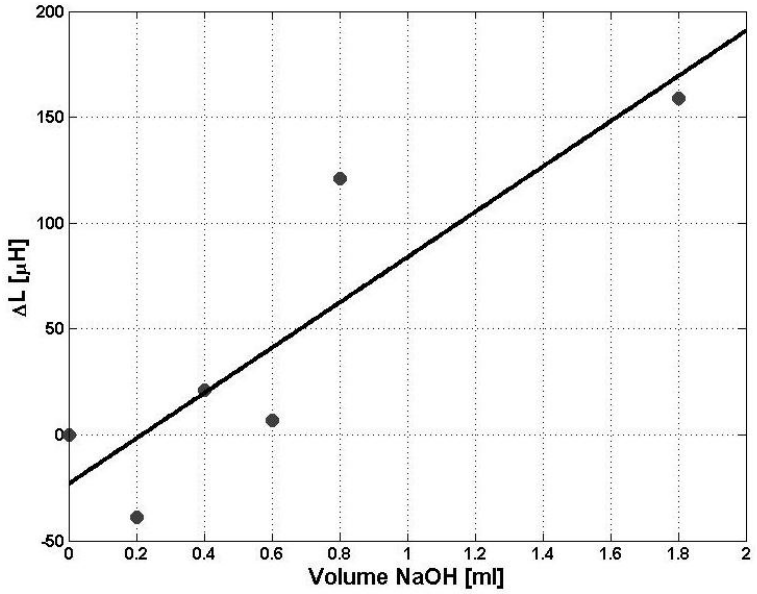

Figure 3-16: showing the variations in the inductance at the fixed frequency of 500 MHz. The line of best fit is shown in black

3.5 Discussion

A discrete planar inductor with resonance frequency of 660 MHz was designed and tested. In this test hydrochloric acid was titrated with sodium hydroxide and changes in the resistance and inductance of the system were monitored. It was seen that a reduction of 44 Ω in the nominal resistance of the coil can be observed, for this titration. This change is detectable using conventional CMOS based or discrete impedance monitoring circuitries. The resonance frequency of the device was also monitored. It was seen that a shift of approximately 2.5 MHz occurs as the titration takes place. However this variation is non–linear. As a result the inductor can be safely used as a qualitative sensor but care must be taken if quantitative data is to be extracted. The quantitative data extraction can only be achieved in the full range of operation if prior knowledge with regards to the sample under test is already available. Data analysis can also be done for a fixed frequency as the inductance of the device is monitored. Data for two frequencies of 400 MHz and 500 MHz were provided and compared. It was seen that in both cases of a linear response was observed in the titration

The parameter extraction process is an essential part of inductor design. Obtaining more accurate values for various parasitic parameters allows for further fine-tuning of the circuits that interface with the inductor, hence, various equivalent models for the inductors to account for different loss mechanisms have been developed. This procedure is not applicable to the application in which our designed inductors will be employed for. In the case of planar inductors, a liquid is placed immediately on top of an inductor coil. As a result this liquid

layer can be treated as another substrate with variable electrical properties. So any parameter extraction process will only be valid for a given state of the liquid sample. More detailed equivalent circuit models of an inductor, e.g. 2–π model, can be used to obtain a complete picture of various parameters affecting the inductor. However, this has to be done for every state of a liquid under test. This can be a limiting factor for data analysis as prior knowledge of what is to be tested is required. Detailed parameter extraction could be done for a specific application with known variables and known variations. This can lead to the design of more sensitive sensing systems

The resistance calculated using the π–model is a real physical quantity. However as the frequency is increased beyond the first resonant point of the device, its value drops until it reaches a negative value [164-166]. As a result the π model is further expanded to address this issue. Hence a 2π–model is developed and the Y–parameter data are fitted with it. In this case the resistance in series with the coil is no longer a real physical resistance but a mathematical convenient. Thus it can take a negative value [166]. To void this problem, the Y_{11} and Y_{22} components can be employed instead, to represent the resistance and inductance seen from an outside circuitry at ports one and two. The nominal values of inductance are not calculated using this technique, but what is observed from a particular port. Given that no detailed data regarding specific loss mechanism in the inductor are required in this technique, it will be solution of choice for the rest of this research.

3.6 Conclusions

In this chapter we looked at the feasibility of helicoid inductors and planar inductors for monitoring the electrical properties of electrolyte solutions. As part of this research I designed and fabricated helicoid and planar inductors and investigated their sensitivity to electrolyte solutions. Although a helicoid structure could offer superior sensitivity to variations in the conductivity of a sample placed inside it, it is unsuitable for our purpose. A helicoid is microfluidic unfriendly due to its non–planar structure. In a discrete implementation of the helicoid the size of the overall system can also be large which increases the sample consumption for testing purposes. Although small discrete helicoids could be purchased, however they have an extra cost, which makes them unsuitable for disposable systems. In the case of integrated and miniaturised system, MEMs friendly fabrication technologies should be adopted that could have an added cost too. Planar inductors are, however, microfluidic friendly so such channels can be easily placed above them at a very low cost. They can also be fabricated on a variety of substrates in different size

and electrical configurations. Hence they provide a roadmap for further device design, fabrication and CMOS integration if necessary. Hence helicoids were disregarded and the direction of research was focused on planar inductors.

The suitability of inductor equivalent models based on Y–parameters was also looked upon. It was shown that using the π–model and admittance parameters we can find the nominal values of inductance, resistance and parasitic capacitance of an inductor coil. However to obtain more accurate results, more detailed models (e.g. 2π–model) should be employed. This process strips resistance values from their real physical meaning and converts them into a mathematical convenience. To avoid this, inductors were treated a 2–port device along with Y_{11} and Y_{22} being representative of resistance and inductance seen at ports-1,2 by an external circuitry. This allows us to treat the sensing device as a black box with no requirement on finding exact loss mechanisms. This approach is employed for data analysis in the rest of this research.

These initial primary tests and data analysis showed that planar inductors could be used in the monitoring of electrolyte solutions. Planar inductors, due to their geometry, are microfluidic friendly. This allows for easier packaging of the inductors and placement of liquid samples over the sensing coils. Further packaging and implementation of the inductors for monitoring the electrical properties of electrolyte solutions will be provided in the next chapter.

Chapter 4

4 Sensor Design & Prototyping

This chapter sets out to investigate the use of planar inductors in the detection of a change in the electrical properties of electrolyte solutions. Newly designed inductors were fabricated on FR4 substrates and packaged with polydimethylsiloxane (PDMS). These inductors were then used to test for variations in the electrical properties of a buffer solution, sodium dihydrogen phosphate, as it is titrated with hydrochloric acid (HCl) and sodium chloride (NaCl) [167]. This buffer was chosen because it is commonly used in DNA amplification and DNA hybridization processes. Finite element modelling of these structures will also be looked at, in order to obtain a better understanding of the system under test. Using the FE 3D model, the inductors will then be simulated and experimentally tested in a transformer set up to find out the effect of the sample on the mutual coupling of the system [168, 169].

First, we will focus on the design process and the fabrication of the inductor. This will be followed by a discussion of the packaging steps and the measurement apparatus. Advantages and disadvantages of different packaging materials will be discussed. Next, an in depth analysis of the experimental data will be provided. Two methods used in the analysis of experimental data are discussed. The first method of analysis looks at the variations in the inductance of the sensor at a fixed frequency whilst the titration takes place. The second method of analysis is based on the variations in the self-resonance frequency of the inductor sensors. This analysis will be followed by finite element simulation of the sensing structure. This modelling process will be used to obtain greater insight into the designed system and investigating the deployment of the sensors into a transformer setup. Discussion of the acquired experimental data and the insights gained from simulations of the sensing devices is provided. This discussion will be followed by concluding remarks on this aspect of the research and its potential applications.

4.1 Primary Sensors

4.1.1 Inductor Design

The inductors were designed using Agilent Advanced Design System (ADS) software. The planar inductors were fabricated on 1.6 mm FR4 sheets with 0.035 mm thick copper tracks. Each inductor had 7 turns and an inner diameter of 4.3 mm. The width of the tracks and the spacing between them was set to 0.5 mm. The inductors were placed on a 33x38 mm printed circuit board (PCB). These dimensions were chosen so that the design criteria were within the operating tolerance of the drilling machine, while also ensuring that good inductor performance was achieved. The milling machine was only capable of moving in x or y directions at the time of fabricating these inductors. Therefore, only 90 degrees angles could be realised for the turns on the path of the track. The milling machine was used to remove the copper from the top layer, excluding the inductor tracks.

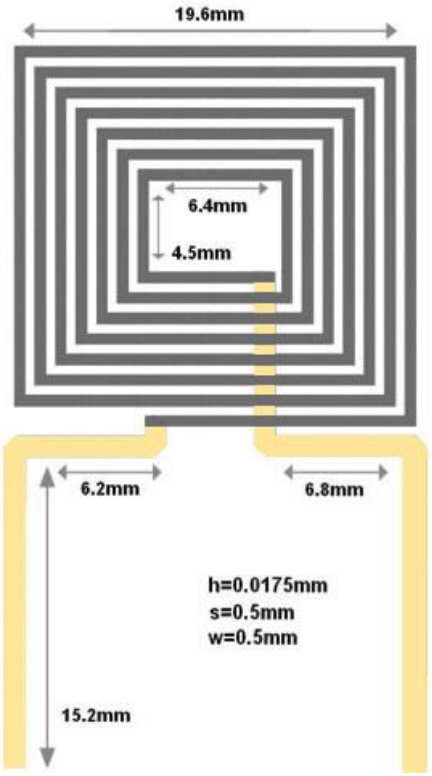

Figure 4-1: showing the layout and dimensions of the inductor sensor made on FR4 substrate. Thickness, width and spacing between the tracks are shows as *h*,*s* and *w* respectively.

This process resulted in inductor tracks with a height of 0.1 mm. SMA contacts, with an impedance of 50 Ω and operating range of 0-3 GHz, were used to connect the measurement equipment to the inductors. The distance between the SMA contacts was 18.6 mm. Figure 4-1 shows a diagram of the layout of this structure along with the dimensions of the inner turns.

The inductors were then packaged with Sylgard 184 PDMS. This material has a volume resistivity of $2.9 \times 10^{12}\ \Omega m$ equivalent to a conductivity of $3.45 \times 10^{-13}\ \Omega^{-1}\ m^{-1}$. It has a dielectric constant of 2.68 and a loss tangent of 0.00133 at a frequency of 100 kHz. PDMS was spin coated on the inductor with a thickness of 200 μm. The coated inductor was cured for 2 hours at 90°C in an oven. Rectangular walls were then carved out of the already cured PDMS and were attached to the inductor surface using Araldite insulating epoxy in order to create a sample container for liquids. The liquid sample under test was poured into this container, which was placed immediately above the inductor being measured. PDMS is susceptible to solutions with a low pH value, e.g. HCl, as these solutions etch away the PDMS. In taking our measurements, care was taken not to expose the sample to low pH values for more than two minutes. The S-parameters of the inductors were also measured before and after the measurements under dry conditions, i.e. when no sample was present on the inductor. No difference was seen between the inductance values of the sensor in the relevant frequency range of the measurements. Figure 4-2, shows an image of a packaged inductor.

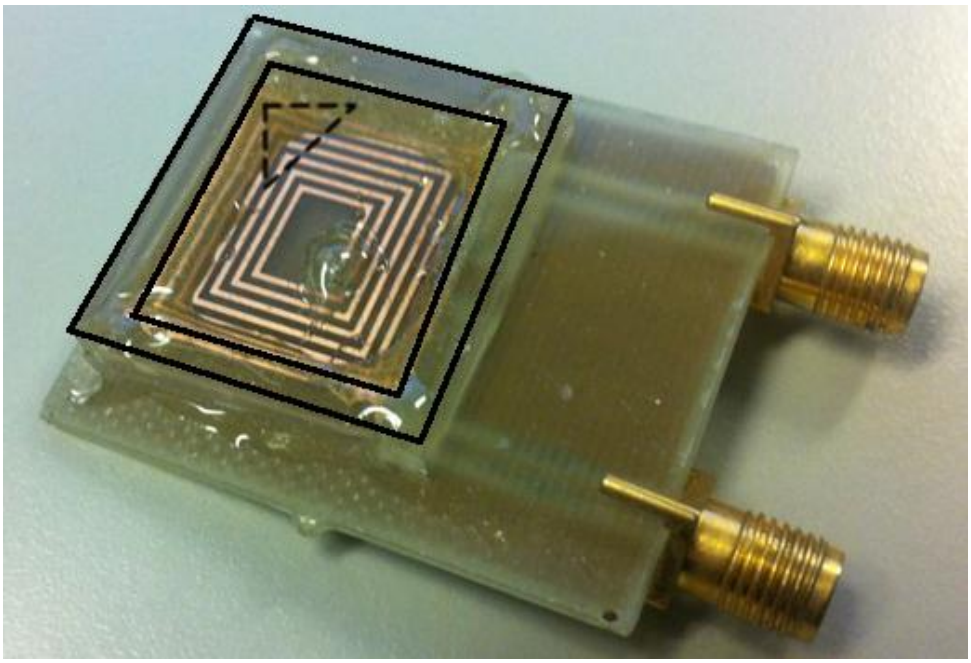

Figure 4-2: showing the contour lines of the reservoir above the inductor. The dashed triangle shows the advance of epoxy into the reservoir hence affecting the volume of the reservoir

To connect the inductor tracks with the tracks on the bottom layer, a drill hole was made at each end of the inductor track. A wire was then placed inside these drill holes and soldered at each end of the PCB. This produced an uneven area, which could not be covered by the PDMS and remained exposed to the environment. The outer drill hole was covered by epoxy

glue in the packaging process when the reservoir walls were placed on the PCB. The inner drill hole was thus covered by a droplet of epoxy glue to ensure its insulation from the material inside the reservoir. In the process of applying epoxy to the walls, an area inside the reservoir was also covered by the epoxy. This reduced the maximum volume of the liquid that could be placed inside the reservoir. This also prevented the liquid sample from reaching the corners of the inductor where the magnetic field has a larger value. The droplet of epoxy is assumed to be semi-spherical with a radius of 2mm leading to a volume of 16.75 mm^3. We can approximate the space taken inside the reservoir to be 2 mm and 3 mm from the dimensions of the inductor. Taking these into account along with a 3 mm height of the reservoir, there is 353 mm^3 of epoxy inside the reservoir. This corresponds to a reservoir capable of holding approximately 800 mm^3 of liquid. These conditions are depicted and highlighted by a dashed triangle in Figure 4-2.

4.1.2 Measurements

The measurements were performed at room temperature. An Agilent Microwave PNA Network Analyser was used to connect to the terminals of the inductor and to perform 2-port S-parameter measurements. For more information on S-parameters, different ways of performing an S-parameter measurement and their accuracy, refer to [160, 162, 170]. S-parameter data were then imported into ADS software and converted into Y-parameters using the formulation in [160]. This is due to the fact that data obtained using Y-parameters refer to more meaningful physical quantities and are, therefor, easier to interpret. The inductance, as seen at port-1, is found by dividing the inverse of the imaginary part of Y_{11} by the angular frequency. The conductance of the coil was also found by looking at the real part of Y_{11}. At the point of self-resonance, the inductor is modelled as a coil in parallel with a capacitor (seen Chapter-II). Hence, the inductor's conductance reaches a minimum value at this point. This is equivalent to the resistance of the device reaching a maximum value. As a result, for better depiction of the properties of the device, we shall look at the real part of $\frac{1}{Y_{11}}$, measured in Ohms. Figure 4-3 shows the plot of inductance against frequency under dry conditions. It can be seen that the inductor has multiple resonance points. The largest value of inductance near the first resonance point is 100 times larger than the maximum value near the second resonance point. For this reason, other resonance points are magnified in Figure 4-3 for clarity. Figure 4-4 shows the variations in the input resistance of the same device. It can be seen that the resistance of the device reaches maximum values at the points of self-resonance. The maximum value of resistance was 25.08 kΩ at the first self-resonance

point, and 1.75 kΩ at the second self-resonance point. The first (three) self-resonance points were found to be at frequencies of 94 MHz, 319 MHz, and 550.8 MHz. The other self-resonance points are not considered in this analysis. For characterisation purposes we shall consider the effects of an electrolyte on the first and second self-resonance frequencies, f1 and f2.

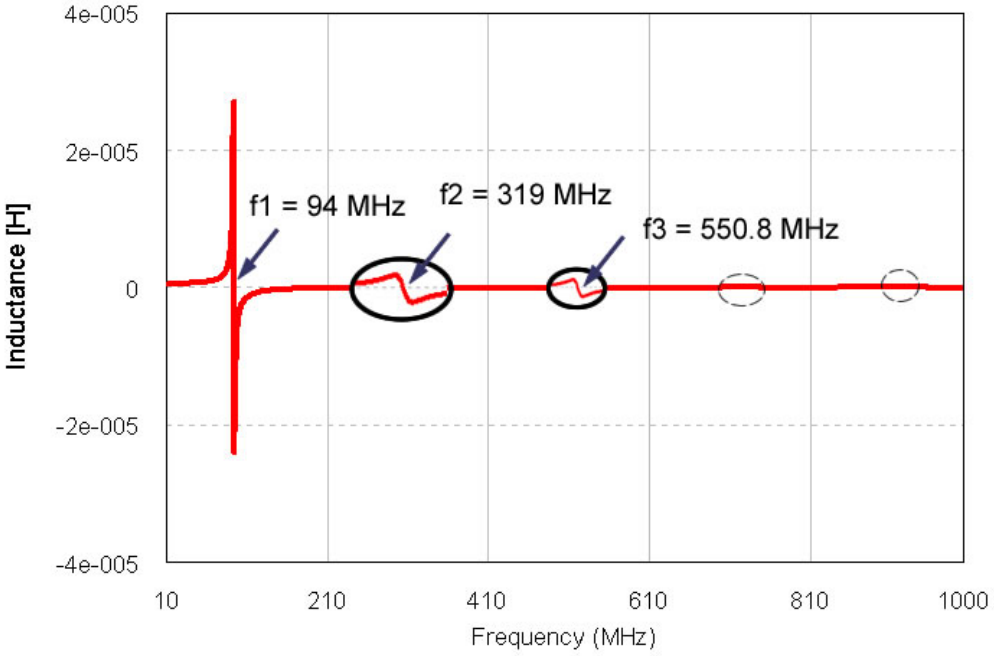

Figure 4-3: showing the plot of the inductance against frequency with multiple resonance points of the inductor having been magnified for lucidity

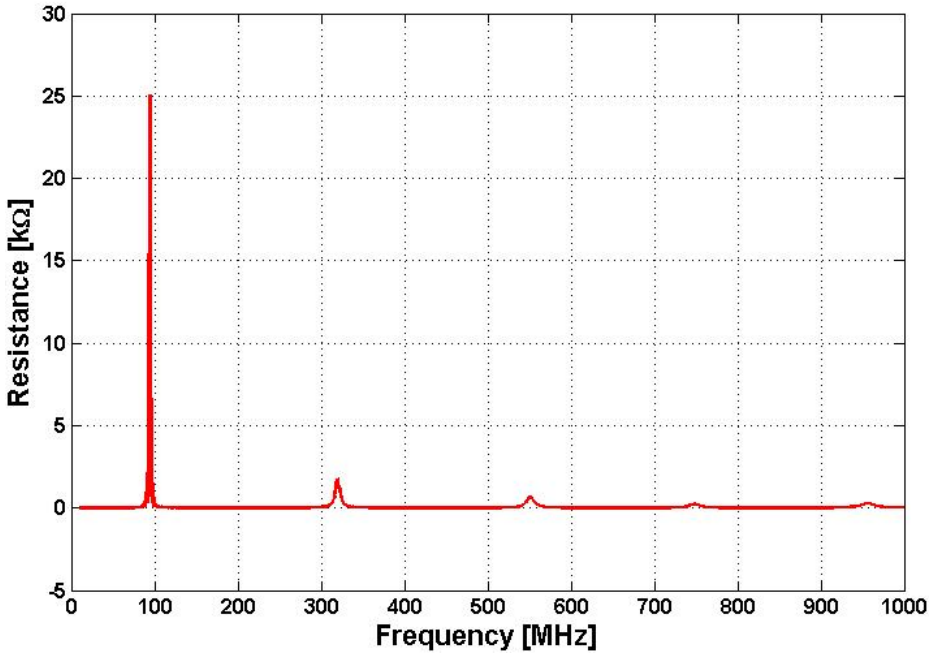

Figure 4-4: showing the plot for real($1/Y_{11}$) of the inductor under dry conditions

To investigate the properties of the sensor in the presence of an electrolyte solution, the sensor was tested with 600 μL of 200 mM sodium dihydrogen phosphate (NaH_2PO_4). This buffer was chosen because it is an electrolyte solution commonly used in keeping and preserving biological samples such as DNA. Two sets of titrations were performed on the sensing structure using this buffer solution, in order to obtain data for the following scenarios:

1. To determine the effect of the concentration of different cations and anions on an electrolyte sample of constant pH and varying ionic strength
2. To characterise the effect of the variations in pH of the electrolyte, where the ionic strength of the electrolyte sample remains unchanged

The buffer was titrated with 1 to 190 μL of 1M NaCl to obtain data on case-1. The second titration of the buffer was with HCl under similar conditions to obtain data for case-2. The pH of the solutions was measured experimentally using a pH meter. This measurement was performed to investigate the resistance of the buffer to variations in the pH as it was titrated with HCl and NaCl. HCl can damage PDMS and as a result care was taken when performing the HCl titration. The HCl was not allowed inside the reservoir for more than 30 seconds in each part of the test. The S-parameters were also measured before and after each HCl experiments to ensure that the properties of the sensor are unchanged. No variations in the S-parameters of the sensing device were observed implying that the PDMS layer is kept intact.

4.1.3 Experimental Data

Figure 4-5, shows the variations in the pH of the buffer solution for up to 142.5 μL of added NaCl to 600 μL of the buffer solution. It can be seen that the value of the pH decreased from 4.44 to 4.25. This is a reduction of 0.19 in the pH of the solution. It can also be seen that the initial five data points fluctuate within a pH range of 4.4 to 4.45. This corresponds to an added NaCl volume of 15 μL to the buffer solution equivalent to a NaCl concentration of 24.4 mM. Attention will be paid to these titration points in the analysis of experimental data for the NaCl experiment. Figure 4-6, shows the variations in the pH of the buffer solution for up to 190 μL of added HCl to 600 μL of buffer solution. It can be seen that the pH decreased from 4.13 to 1.18. This is a pH drop of 2.95. The steepest drop in the pH is seen for the region of up to 20 μL of added HCl. The experimental data is based on monitoring the variations in the first and second self-resonance points of the inductor as liquid solutions are placed in the reservoir. Note that f1 occurs at 76.02 MHz and f2 occurs at 348.1 MHz when 600 μL of buffer solution is used. This is a reduction of 17.98 MHz for the f1 of the inductor.

Conversely, f2 is increased by 29.9 MHz. This resonance frequency is then reduced as the titration continues and more HCl or NaCl is added to the buffer solution.

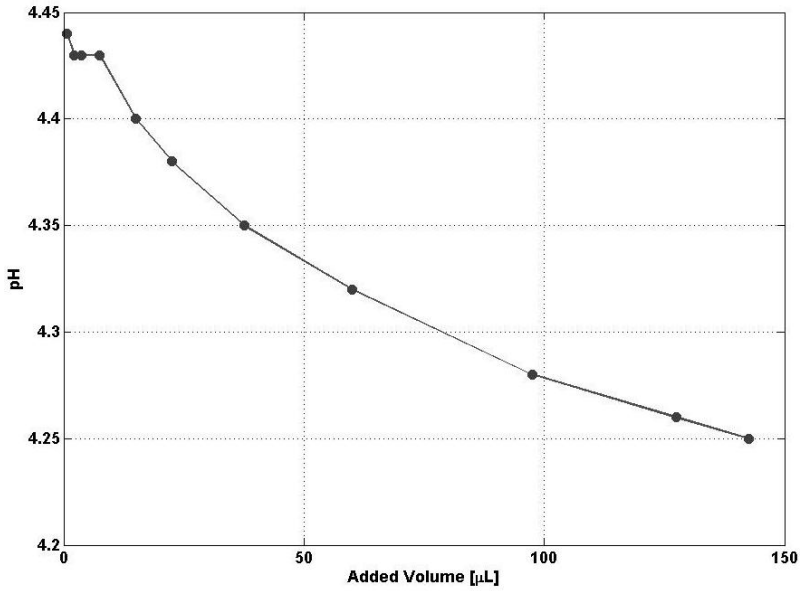

Figure 4-5: showing the variations in the pH of the buffer solution as NaCl is incrementally added to the mixture

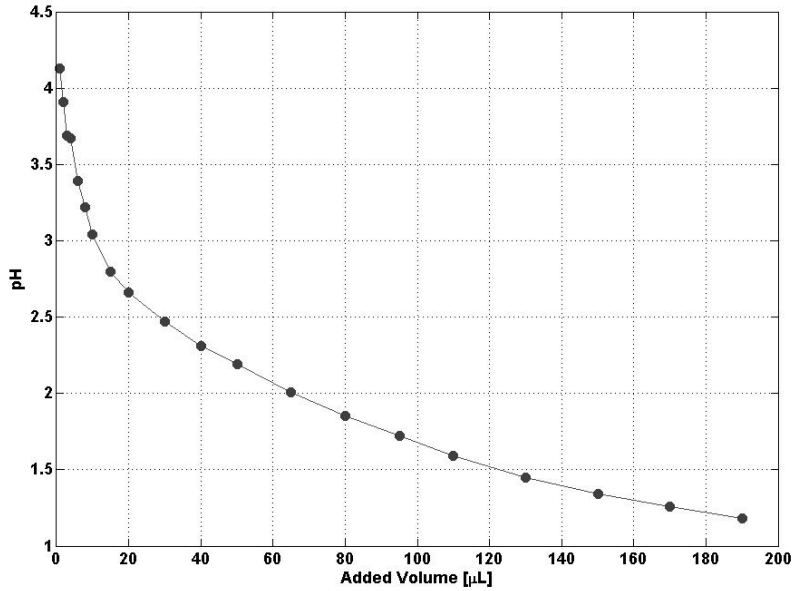

Figure 4-6: showing the variations in the pH of the buffer solution as HCl is incrementally added to the mixture

The first set of tests was performed with the buffer solution, NaH_2PO_4, as the only sample under test, while the volume of the test sample was varied between 600-790 μL. This test aimed at finding the sensor's volumetric sample dependence in the presence of the buffer only. Figure 4-7, shows the deviation of the resonance points as the volume of the buffer solution was increased. The resonance frequency point for 600 μL was set to be f_i and any subsequent resonance frequency for each test was subtracted from this reference point,

leading to $\Delta f = f - f_i$. It can be seen that for a range of 600 to 790 µL of volume of the buffer solution, the variation in frequency was 940 kHz for the second resonance point and 500 kHz for the first resonance point. The first resonance point also demonstrated a saturating behaviour as the volume of the solution reached approximately 700 µL.

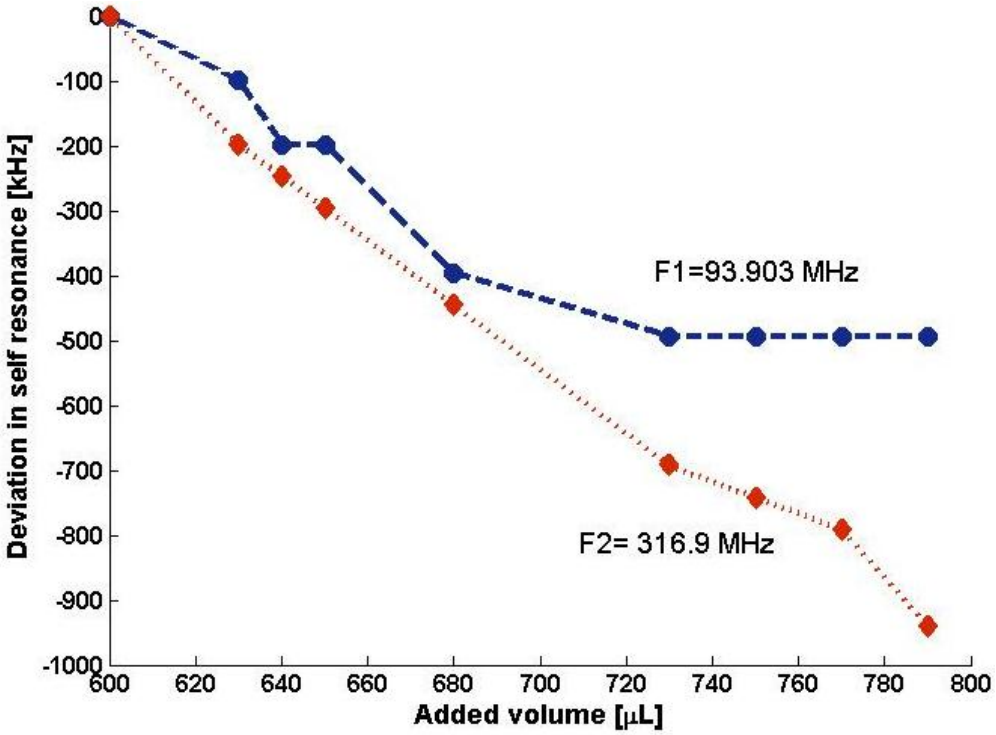

Figure 4-7: showing the variations in the first and second self-resonance points of the inductor as the volume of the buffer solution is increased from 600 µL to 790 µL

This test was followed by an investigation into the effect of the HCl titration on the behaviour of the sensor. Figure 4-8, shows the variations in the self-resonance frequencies of the inductor. The first self-resonance frequency of the inductor was reduced by a value of 2.228 MHz. To account for the effect of the buffer, we shall compare the experimental data, generated at a volume of 680 µL, in Figure 4-7 and Figure 4-8. The addition of 80 µL of HCl corresponds to a pH value of 1.85. It can be seen that, at this point, the buffer solution reduced the resonance frequency by 400 kHz. However in the case of the mixed solution this reduction was in the order of 1.609 MHz. This shows that the results between the two titrations can be distinguished and that the buffer was not masking the effect of the added HCl. The second self-resonance frequency of the inductor was reduced to lower frequencies by a total value of 15.35 MHz. This change is substantially greater than the 940.5 kHz drop caused by the addition 190 µL of buffer only. Hence, the buffer does not screen the effect of HCl. The sensitivity of the measurements at both first and second self-resonant frequencies is

also calculated and plotted in Figure 4-9. It can be seen that the sensitivity of the device for pH values of greater than 2.5 is less than 1%. However, at much lower values of pH the sensitivity is increased.In the case of the second self-resonance the sensitivity of the device for a pH range of 1.2 to 5 is approximately 5%.

The inductance of the system was also measured under fixed frequency conditions. Figure 4-10, shows the variations in inductance at a frequency of 71 MHz. This frequency is chosen because it is near the first self-resonance of the inductor. It can be seen that a decrease in the pH value of the solution leads to an decrease in the magnitude of the inductance. This increase in inductance is of the order of 736 nH.

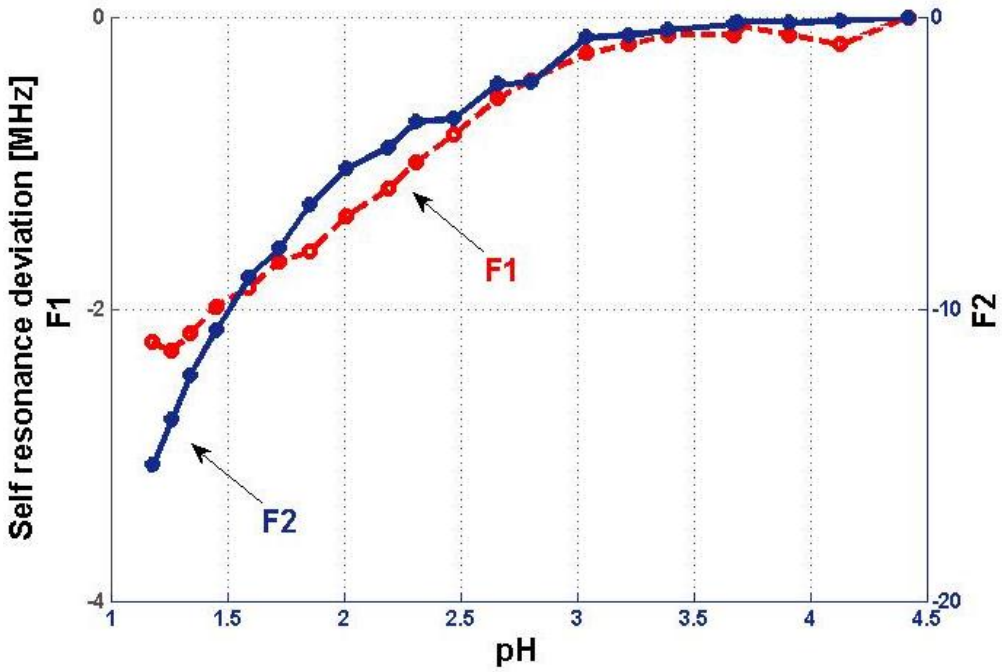

Figure 4-8: showing the variations in the self-resonance frequencies of the inductor as the pH of the buffer solution is modified by the presence of HCl

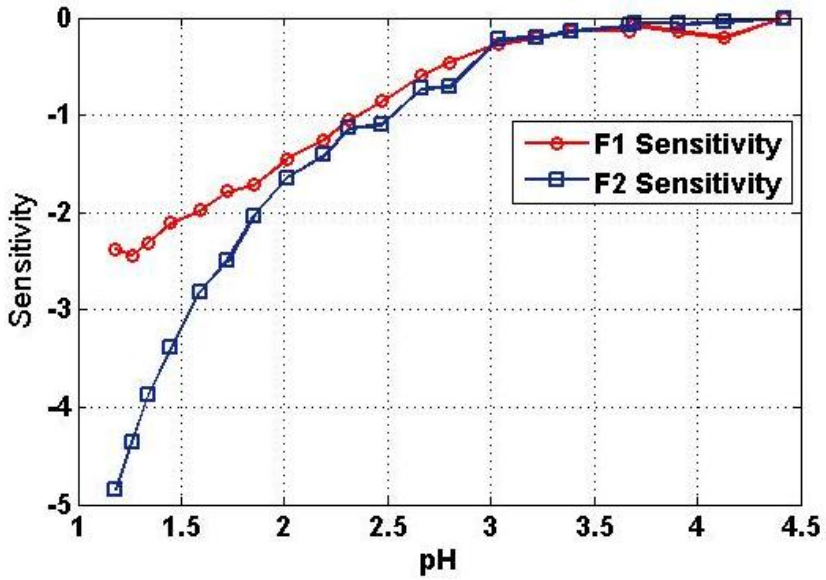

Figure 4-9: showing the sensitivity of the sensor to changes in pH for the 1st and 2nd self-resonance frequencies

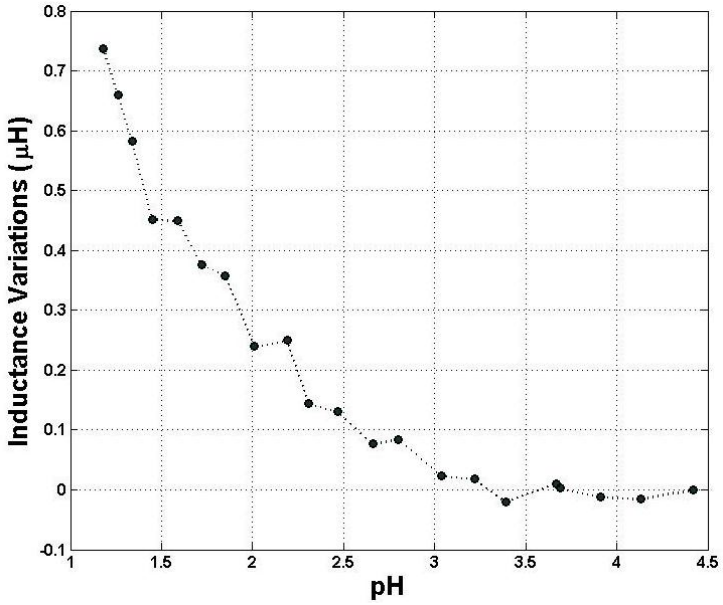

Figure 4-10: showing the variations in the inductance of the sensor at a fixed frequency of 71 MHz as the pH of the solution is affected by the presence of HCl

Next, the effect of NaCl titration on the inductor was examined. It can be seen that, as the amount of salt increases in the buffer solution, the self-resonance of the system moves to lower frequencies. This shift was of the order of 2.326 MHz for F1 and 20.54 MHz for F2. These values were larger than the variations shown in Figure 4-7. Note that the variations in

both F1 and F2 became asymptotic as the concentration of NaCl was increased inside the sample. Figure 4-12 shows the sensitivity plot for the variations in the concentration of NaCl in the sample solution. It can be seen that the sensitivity of the sensor at the first self-resonant point reaches a value of 2.5% for a change of 0-0.25 mol L^{-1} in the concentration of NaCl. In the case of the second self-resonant point, the sensitivity reaches a value of 6.5% for the same variation in concentration. This implies that the sensor can be used as a good qualitative sensor for monitoring substantial variations in the concentration of a solute.

The variations in the inductance of the system were also measured at a frequency of 71 MHz. It can be seen that this process led to an increase of approximately 2.5 μH in the inductance of the system. The outcomes observed here, and in Figure 4-10, are consistent with the observation of a reduction in the self-resonance of the system. This can be attributed to an increase in the value of *L*, which reduces the resonance frequency. Note that $\omega = \frac{1}{\sqrt{LC}}$. In Figure 4-14 we have plotted the sensitivity of the inductance of the sensor at a fixed frequency of 71 MHz to changes in the concentration of NaCl from 0-0.25 mol L^{-1}. It can be seen that a sensitivity of 90% for the full range of titration can be achieved. We have also looked at the region of titration in which the pH remains constant, as shown in Figure 4-5. This is the case for NaCl concentrations of below 24.4 mM. Figure 4-15, shows the variations in the self-resonance frequencies of the inductor for this particular range. A reduction of 1.139 MHz for F1 and 9.108 MHz for F2 can be observed. Thus, the sensor can also be considered for the monitoring of the electrical properties of samples under constant pH regimes.

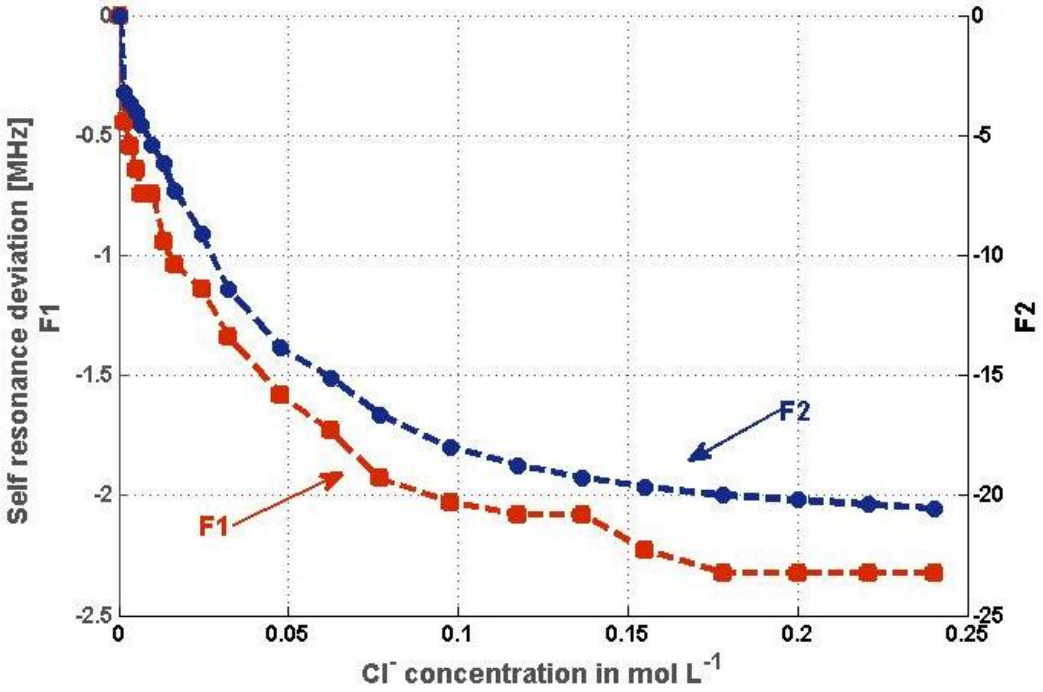

Figure 4-11: showing the variations in the first and second self-resonance of the inductor as NaCl is added to the buffer solution

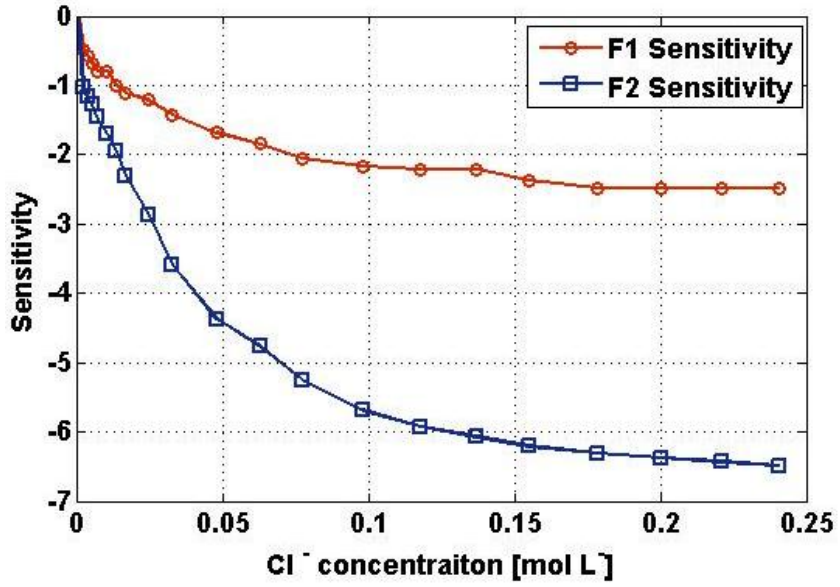

Figure 4-12: showing the sensitivity of the device to various concentrations of NaCl

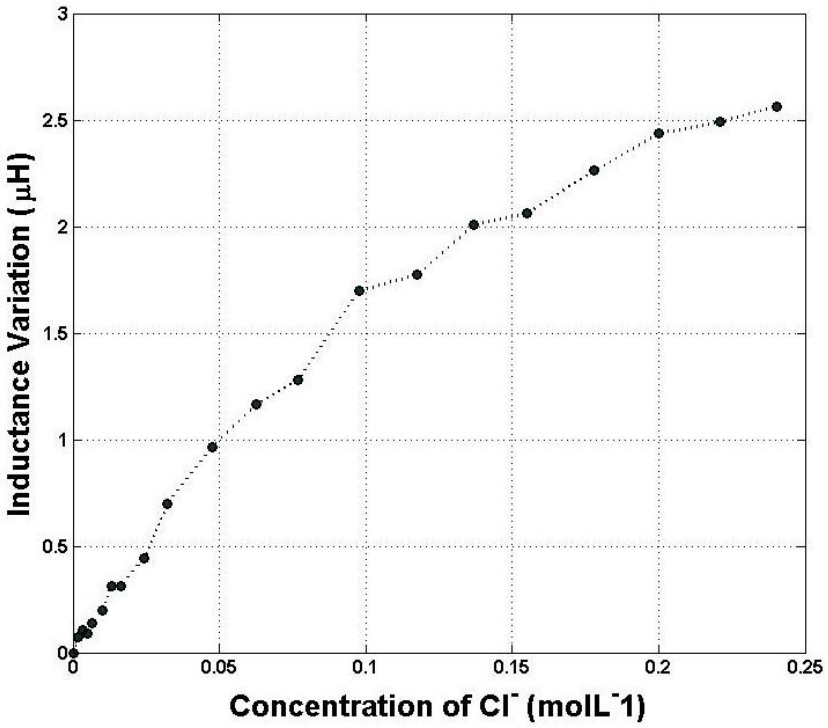

Figure 4-13: showing the variations in the inductance of the sensor at the frequency of 71 MHz as NaCl is added to the buffer solution

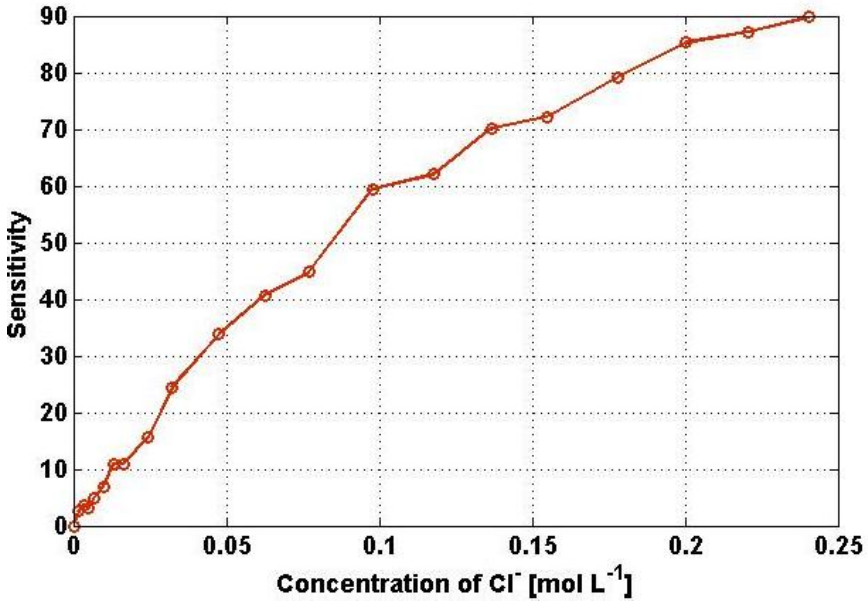

Figure 4-14: showing the percentage sensitivity of the sensor to the variations in the concentration of NaCl at a fixed frequency of 71 MHz

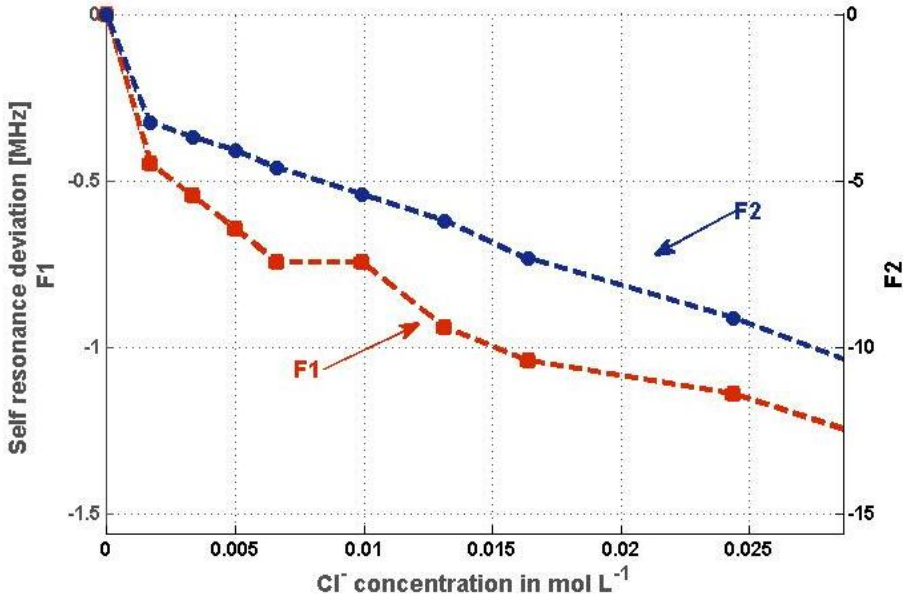

Figure 4-15: showing the variations in F1 and F2 for NaCl concentrations of less than 24.4 mM

We have looked at experimental data on the variations in the admittance properties of a planar inductor fabricated on a FR4 substrate. The reported results show a variation of 3.06% at f1 and 6% for f2 under the constant pH regime (NaCl titration). A variation of 2.86% at f1 and 4.417% at f2 are reported for the varying pH experiment (HCl titration). These results correspond to the full titration range of the experiment. In the case of constant pH for a NaCl concentration of less than 24.4 mM, we observed a change of 1.5% for F1 and of 2.62% for F2. The frequency of the operation of the sensor, along with the variations in the self-resonance frequency points, is within the operational frequency of a conventional CMOS process. The values of interest are below 1 GHz, which is within the boundary of conventional CMOS. It must be noted that variations in the value of inductance are much larger in our device compared with other equivalent sensors, such as [124, 133]. In [124] no exact value for the concentration of the NaCl is given, however, they obtain a 14% change in inductance for a 6% change in the concentration of NaCl. If we normalise the values of the concentration in our experiments, we shall achieve a 90% variation in inductance for a 25% change in normalised concentration of the added NaCl. In [133] a much higher frequency of 30 GHz is used and variations in the range of 52% are achieved. However, the variations experienced by our sensor can still be monitored using PLL devices and oscillatory units operating at much lower frequencies. The other factor to be taken into account is that the main aim of this work is to produce a sensor suitable for qualitative data analysis. Hence, we are not looking to obtain precise measurement data for a test sample but, instead, a Boolean

answer as to whether a change has occurred within the sample. Another aspect of central interest is the wireless communication capability of the device. Most commonly used sensors require a physical medium to transmit data from the transducer to a processing unit. The inherent properties of inductive sensors can be used to communicate the data in a wireless manner, leading to more versatile sensory platforms. Applications like gastric juice monitoring in the oesophagus can benefit from the development of such sensors, as only the presence or lack of presence of gastric juice is of interest. The wireless capabilities of this sensor are also valuable for the purposes of this application.

4.2 Simulations

To obtain further insight into this system, a 3D model of the sensor was created and simulated in ANSOFT HFSS Finite element software. The aim of this task was to create a theoretical model that can follow and reproduce the behaviour of the sensor. This is beneficial as any further optimization of the design or deployment of the sensor can then be modelled using a computer. Finite element modelling also provides us with great insights into the behaviour and functions of the sensor in different environments. The basic steps for performing FE modelling in HFSS were discussed in Chapter-II. Here, both the process of creating a 3D model in HFSS, and the environmental setting used for setting up the simulation, will be looked into in detail. The steps in applying boundary conditions, such as suitable excitations and mesh operations, shall be discussed. The simulation of this model in HFSS will then be used to model the inductor with its packaging and to analyse how the simulation data compares with experimental measurements.

4.2.1 3D Model

The inductor was initially designed in ADS software, discussed in section–I. This structure was then exported to a GDS file format and imported into HFSS software. Figure 4-16, shows the layout of the sensing system in ADS software. The copper in the top and bottom layers along with drilling points can be seen here.

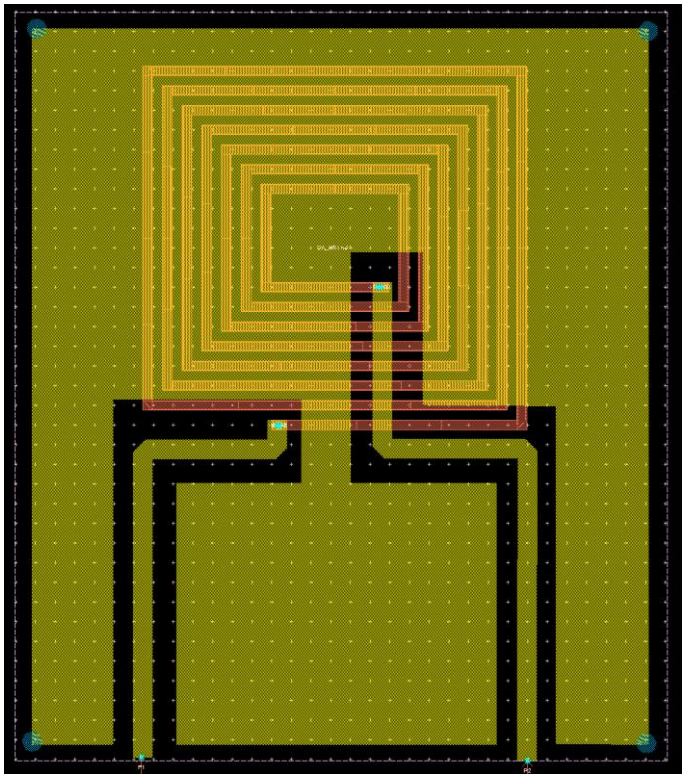

Figure 4-16: showing the layout of the sensing system in ADS software. The yellow area is the bottom layer copper and the red is the top layer inductor.

Figure 4-17, shows the structure of the 3D model used to represent the sensor in HFSS. In this model, a reservoir sample size of 16x17x3 mm was assumed inside a PDMS reservoir of the same height and of 24x26 mm width and length respectively. The thickness of the PDMS wall used in the construction of the reservoir was assumed to be 4 mm. The thickness of the copper was set to be 0.035 mm. As a milling machine was used to remove the excess copper on the top layer, the thickness of the PCB with and without the copper tracks was measured using a vernier scale. It was found that the thickness of the areas of the PCB, which includes the top layer tracks, was 0.1 mm larger than the areas with no top layer of copper present. Hence, a 0.065 mm layer of FR4 was assumed to reside beneath the inductor tracks. A conceptual sketch of such a system is shown in Figure 4-18.

Apart from the PDMS material, all other materials were modelled using the built-in material libraries of HFSS. For the PDMS, data provided by the manufacturer at the frequency of 100 kHz was used. The manufacturer provided no data on the frequency response of the Sylgard84 for high RF frequencies and, given the nature of the product, it cannot be characterised by available dielectric probes. In the course of this work, simulation results, which agreed with the experimental data, were obtained. For this reason, no further attempts were made to obtain the RF response of the PDMS.

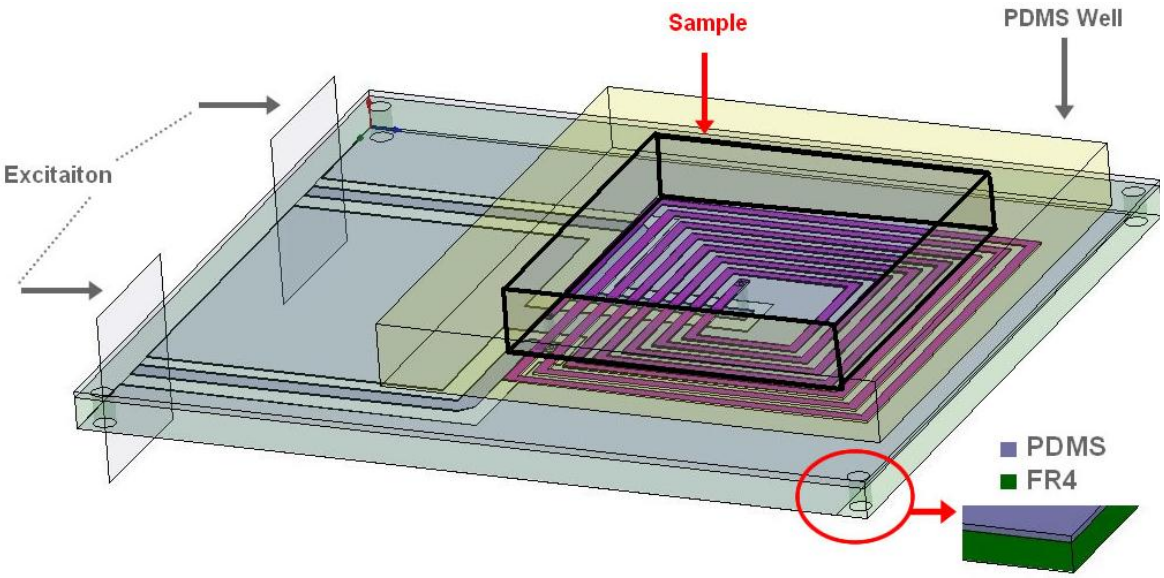

Figure 4-17: showing the constructed 3D structure, which was used in FE modelling of the sensing device. A thin layer of PDMS, which is shown in the magnified colour coded image, covers the inductor coil.

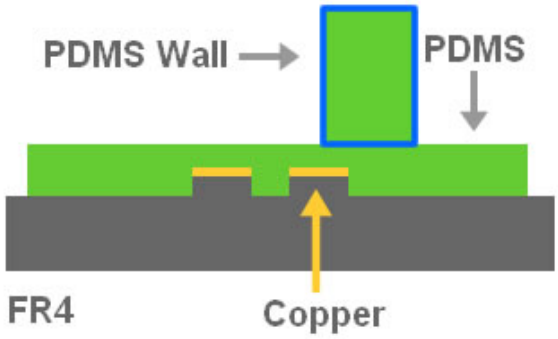

Figure 4-18: showing a 2D layout of the sensing system including the FR4, copper and PDMS used for making the reservoir and the surface of the inductor.

The two vias connecting the top and bottom layer tracks were modelled as two cylinders level with the height of the substrate. The radius of the drilled hole was set to 0.25 mm, and a radius of 0.1 mm was assumed for the copper wire placed inside this cylinder. This estimation was to allow for the radius of the thread of metal inserted into the drilled hole, along with any solder that may have made its way into the drilled hole during the soldering process. Figure 4-19, shows the structure used in the modelling of the via. In order to allow for the spillage of the epoxy into the reservoir, the location of the sample and the PDMS walls were slightly modified so that the sample was not perfectly on top of the inductor.

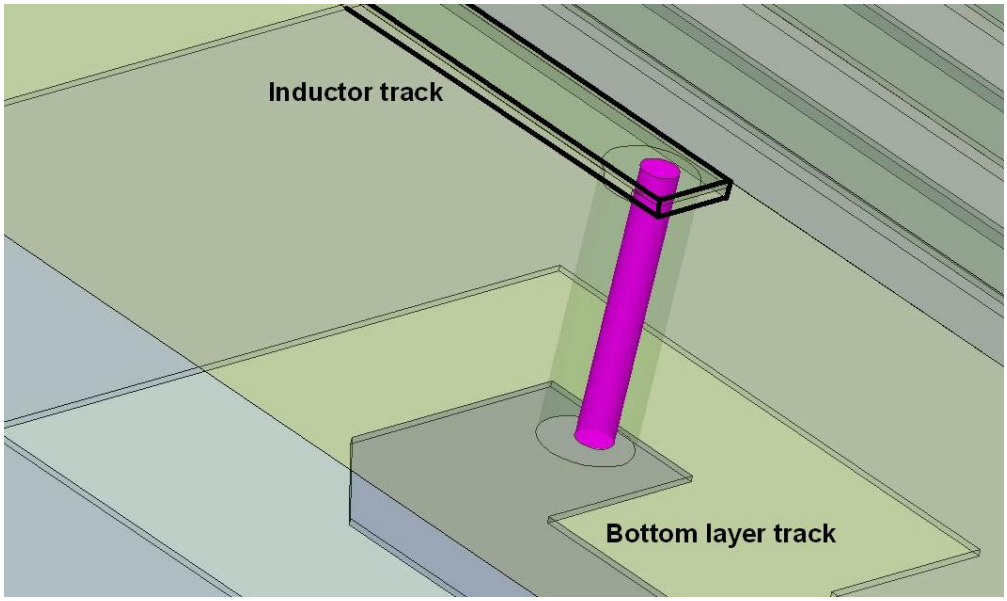

Figure 4-19: showing the realisation of a via in the 3D HFSS model. A copper cylinder inside an air filled cavity is used for this purpose

4.2.2 Simulation Sources & Boundaries

The 3D model of the simulation was placed inside a cube of air and an HFSS first order absorbing boundary condition (ABC or Radiation thereof) was imposed on the faces of this simulation space. This boundary condition absorbs normal and near normal incident waves. As a result, it should be placed at a distance of at least a quarter of wavelength from the structure. In this configuration, any normal or near-normal incident waves on the faces of the simulation space are absorbed and, hence, terminated at infinity. For the system of interest at a frequency of 90 MHz, the wavelength is 3.331 m, so the quarter value is 832.8 mm. As a result, the length of the simulation space in the direction of propagation of the wave should be 832.8 mm. However, in the course of simulations it was observed that this size does not have a noticeable effect on the accuracy of the simulation results. This was attributed to the lack of radiation from the inductor system and means that the boundary condition could be placed closer to the structure. The 832.8 mm dimension also led to a prolonged simulation time and required extensive computational power.

The inductor sensor was placed inside an air enclosure of the size 292x292x292 mm in the (x,y,z) domain. This value corresponds to a wavelength of 1168 mm, or a frequency of 256.67 MHz. This simulation frequency was chosen as a trade-off between the size of the simulation space and the accuracy of the data. The simulations performed in this setup were done in a range of approximately 256.67±200 MHz.

Figure 4-17, also shows the location of the two waveports used for the excitation of the device. These sources have a dimension of 7x8 mm. The dimensions of this system were chosen so that the right transverse electromagnetic modes (TEM) were generated for the simulation of the device. Given the structure of the contacts in the bottom layer of the substrate, a coplanar waveguide was used as the connecting point between the inductor and the SMA contacts. In order to ensure that the dimensions of the waveports were appropriate, the behaviour of the modes at the excitation ports was analysed for all the measurements. Thus, the appropriate TEM mode was generated. Figure 4-20, shows the modes of a CPW device along with a plot of the TEM modes at port-1 of the simulated structure. This test was performed for all of the simulations in order to confirm that no arbitrary modes were generated in the excitation of the system.

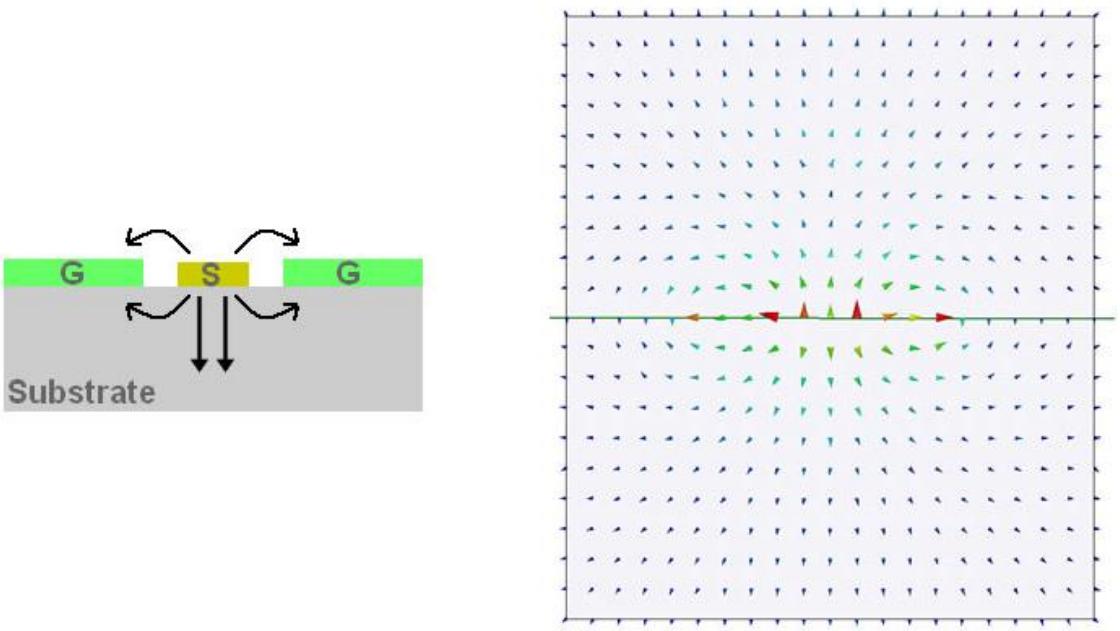

Figure 4-20: showing the CPW realisation of the inductor contacts and their corresponding modes. The modes present at the ports of the simulated model are also shown.

4.2.3 Meshing Process

The default setting of the HFSS software was used for most of the elements in the 3D model. To increase the accuracy of the results, and decrease the computational power required for the simulation, the vias and the inductor track were initially meshed differently. A length based mesh of 0.5 mm was applied to these elements. This value limited the length of the longest edge of the tetrahedron element to 0.5 mm. However, it was found that decreasing the size of the mesh elements in the lossy medium increases the accuracy of the simulation to a greater extent. Hence, a length based mesh of 0.1 mm was applied to the PDMS layers. The

simulation space was meshed at a length of 50 mm. It was found that, by increasing the size of the length based mesh for this component; the computation power required for the simulation decreased. However, no observable change in the accuracy of the data was seen. For this reason, the default mesh settings were used for this element for all other simulations. It was observed that the accuracy of the model greatly increased as the size of the mesh decreased. These factors led to an increase in the simulation time. As a result, the value of 0.1 mm for PDMS layers and default value for all other elements was chosen.

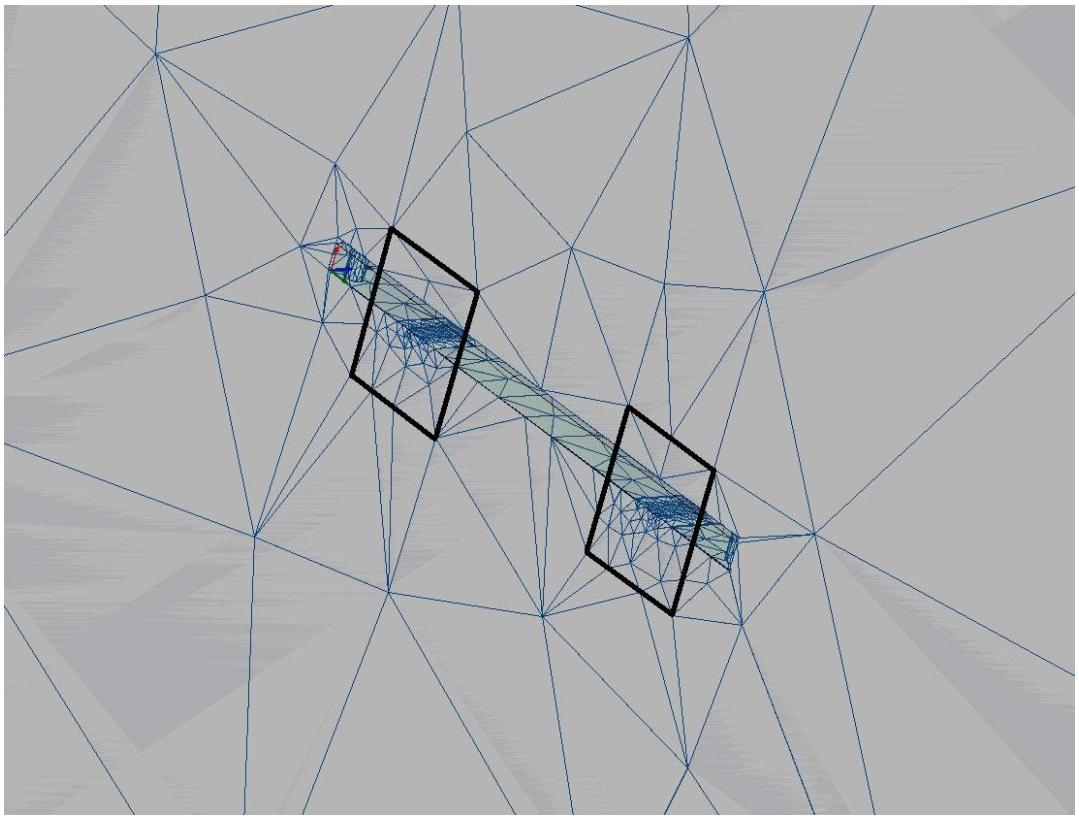

Figure 4-21: showing an image of the meshing for the 3D model. The excitation ports are reemphasised by black lines. sample of the meshed structure along with the increase in the density of the mesh as the body of the sensor is approached

4.3 Analysis of Data

4.3.1 Model Validation

The simulations were performed using the HFSS fast sweep. In this setting, full field solutions are calculated at each simulation frequency point. S-parameter and Y-parameter data were then extracted from the simulation and compared with the experimental data. Figure 4-22, shows the plot of inductance against frequency, for both experimental data and simulation data points, for a frequency range of 70 MHz to 110 MHz. It can be seen that the

experimental data reached the resonance point at a frequency of 93.1 MHz. The self-resonance of the device was calculated to be 94.12 MHz using the 3D model in HFSS software. This is a deviation of 1.02 MHz or 1.08% from the experimental data. The same analysis was done at the second self-resonance point of the system. Figure 4-23, shows a plot of inductance against frequency for experimental and simulation results. In this case, the self-resonance frequency for experimental data was found to be 319.6 MHz and, in the case of simulation results, to be 322.4 MHz. This is a variation of 2.8 MHz or 0.876% from the experimental data. The observed deviations between the simulation results and the experimental data may result from inconsistencies between the 3D model and the actual prototype. These inconsistencies are due to the fact that:

The epoxy used at the centre of the reservoir for the insulation of the solder (see Figure 4-2) is not included in this model.

The exact thickness of the FR4 layer, immediately beneath the copper, cannot be measured accurately. This is due to the limitations of the fabrication process, which lead to the inductor track having to be milled instead of being etched.

A thread of wire had to be inserted into each via and soldered on both sides, due to the lack of through-hole plating. The soldering process introduces losses into the system.

The exact structure of the conductive element inside the via is also not known, which adds to the uncertainty of the model.

The mismatch between the width of the track and the width of the SMA contact can contribute to inconsistencies in the model.

Material models can affect the outcome of the simulation as well. The material properties in HFSS are quoted for a range of frequencies, and beyond those frequencies, they are assumed to remain constant. The dielectric properties of the PDMS used in this simulation are quoted for a frequency of 100 kHz. However the simulation spans a frequency range of up to 500 MHz. This can be a source of mismatch between the model and the experimental data.

The size of the mesh used in the 3D model is of great importance. The size of the mesh elements affects the accuracy of the results. The smaller the size of the elements the more accurate is the outcome of the simulation. This accuracy is achieved at a cost of computing time and RAM requirements.

Measurement uncertainty can also cause a discrepancy between the simulated and measured values. This is due to environmental factors that interact with the inductor. Some of these factors are:

The placement of the inductor and the effect of nearby objects on the induced noise and energy losses in the vicinity of the inductor coil, e.g. the table on which the inductor is placed.

Variations in temperature and humidity affect the outcome of a measurement. The electrical properties of the materials, used in the fabrication of the sensor, vary with these factors.

The quality and length of the SMA cables, which were used to perform these measurements, can introduce noise into the measurement results.

A self-resonance frequency deviation of less than 1.1% between the simulated and experimental results was observed. Some of the possible sources of error in the measurement results and simulation data were tabled and discussed. Given all the uncertainties present in the inductor measurements and within the corresponding 3D model, and taking into account the time needed to perform the simulations, the observed deviations in the order of 1% were deemed acceptable. No further modifications to the setting of the simulation or the 3D physical model were made. The HFSS simulations were then used to look at the behaviour and distribution of electromagnetic fields and the associated current contours. These simulations were used to gain further knowledge of the operation of the system and of further optimisation of the designs.

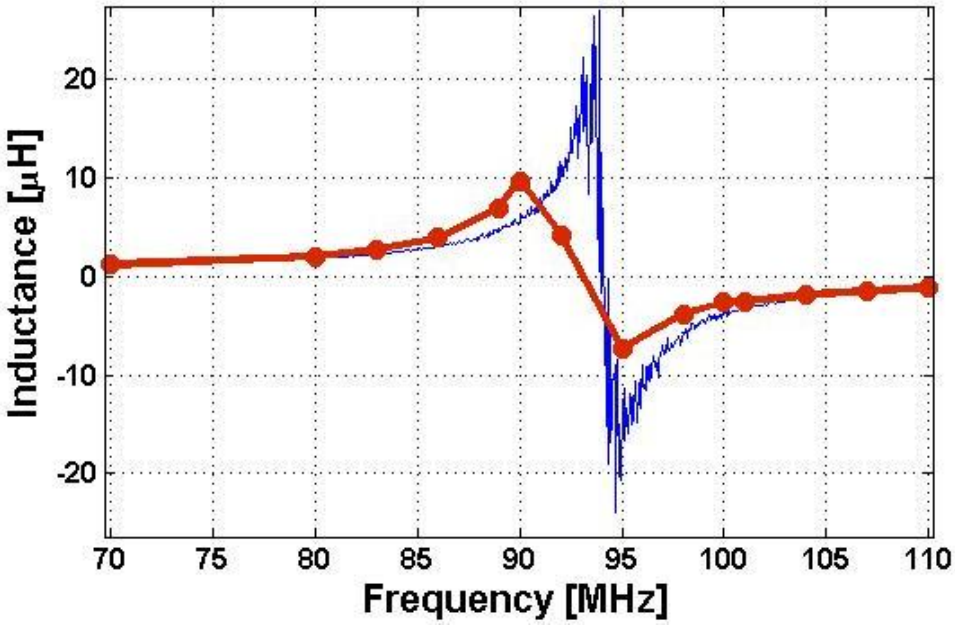

Figure 4-22: showing the plot of inductance against frequency for experimental data (blue) and the HFSS simulation (red) at the first self–resonance of the inductor

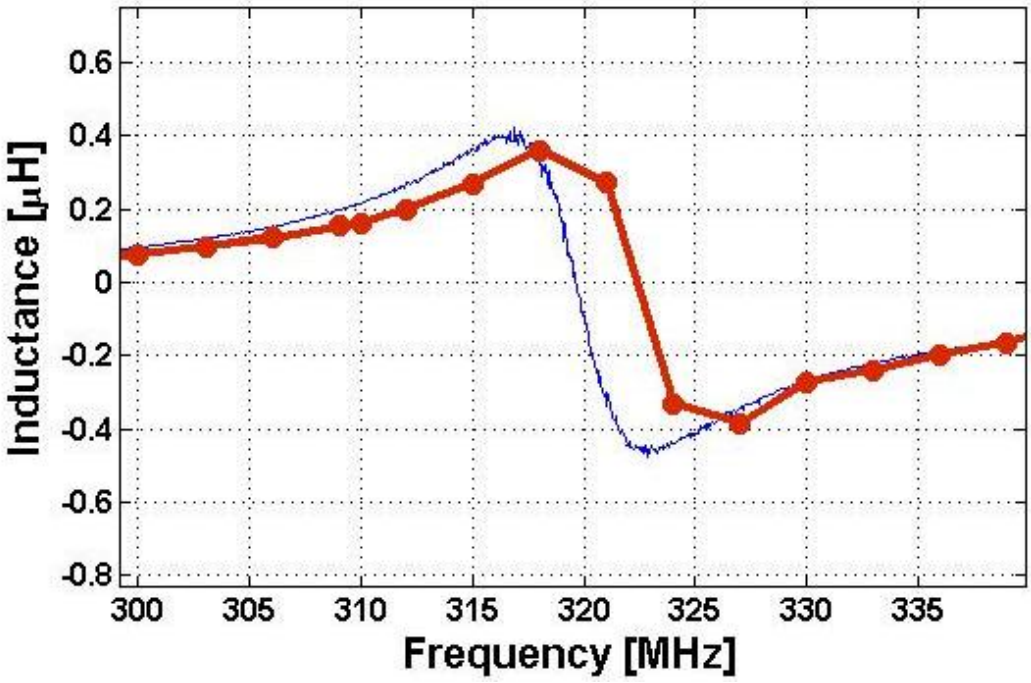

Figure 4-23: showing the plot of inductance against frequency for simulation (red) and experimental (blue) data at the second self-resonance point of the system

4.3.2 Electromagnetic Field Distribution

Figure 4-24, shows a plot of the magnitude of the magnetic field on a plane that is 35 μm inside the sample space. The plot is provided for two frequencies, 92 MHz and 321 MHz. These frequencies were chosen because they were close to the first and second self-resonance

frequencies of the device. It can be seen that the magnitude of the H-field was larger towards the top left hand side of the coils. A black circle is used to highlight this part in Figure 4-24. This can be attributed to the misalignment of the reservoir walls in the 3D model. This misalignment was introduced to account for the space taken by the insulating epoxy in the reservoir, Figure 4-17.

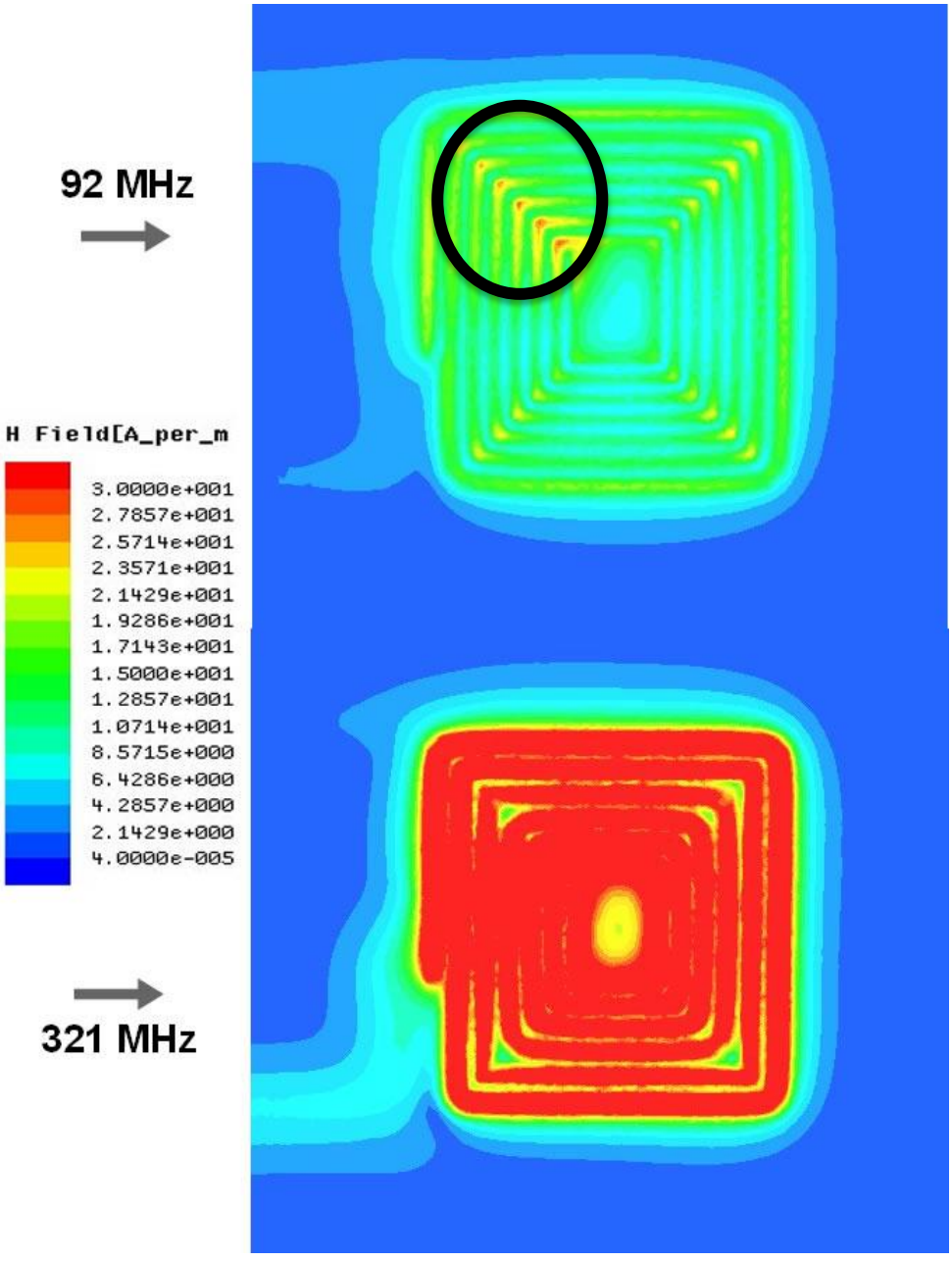

Figure 4-24: showing the magnitude of the H-field at 35 µm of elevation inside the sample space. The black circle highlights the skewed magnitude of the field caused by the packaging.

A further observation, which can be made from Figure 4-24, is that the magnitude of the H-field was much larger at the second self-resonance frequency of the sensing device. The increased value of the magnitude can be used to explain the greater sensitivity of the device at

the second resonance point. It can be seen that, in Figure 4-11 and Figure 4-15 that the deviation in the second self-resonance frequency is approximately 10 times larger than the first self-resonance frequency. Figure 4-25 shows the magnitude of magnetic field at elevations of 50% and 100% inside the sample space for the two frequencies of 92 MHz and 321 MHz. It can be seen that in both cases, the magnitude of the H-field at a frequency of 321 MHz is much larger compared with the same elevation at a frequency of 92 MHz. It can readily be observed that the magnitude of the magnetic field decreases as we move to higher elevations. This implies that the device is most sensitive to the solution in its immediate vicinity. Therefore, the sensitivity of the device can be increased, by reducing the thickness of the protective PDMS layer. This allows for a more compact packaging of the sensor. It can also be deduced that the height of the reservoir can be reduced without major impact on the sensitivity of the sensor. This has the added advantage of reducing the electrolyte volume needed to undertake a measurement.

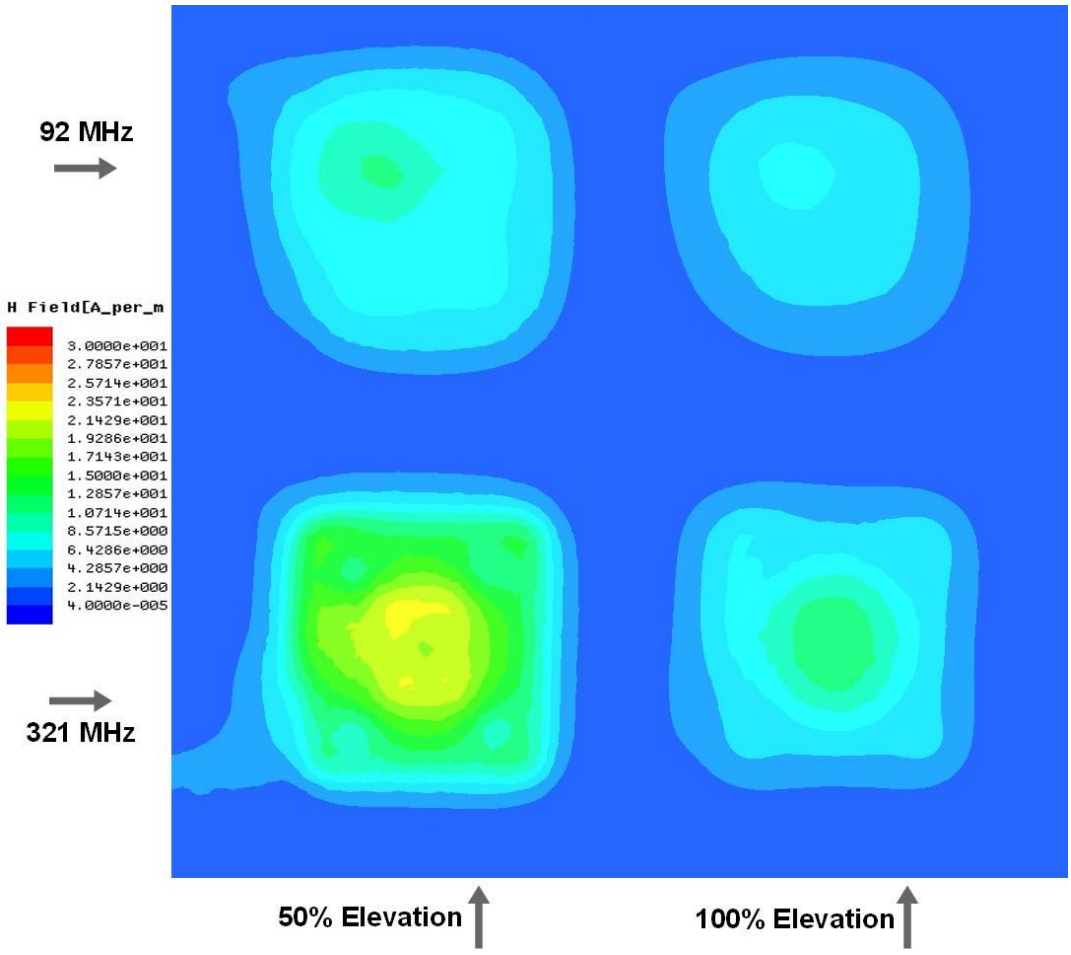

Figure 4-25: showing the plot for the magnitude of the H-filed at 50% & 100% elevations inside the sample space at two frequencies of 92 MHz and 321 MHz.

The magnitude of the electric field at three elevation points inside the sample space for frequencies of 92 MHz and 321 MHz is also shown in Figure 4-26. As in the case of the magnetic field, it can be observed that the strength of the electric field declined rapidly as we moved to higher elevation points. It can also be observed that the magnetic field at the lower self-resonance frequency provided a more uniform but weaker magnetic field distribution throughout the reservoir. In the case of the 321 MHz field plots, there was a clear contrast between the regions of high intensity and low intensity. In both resonance cases, the regions further from the centre of the device had the largest magnitude. This fact can be used to explain the minimal impact of the epoxy droplet at the centre of the inductor track, which was neglected in the 3D model, on the simulation results.

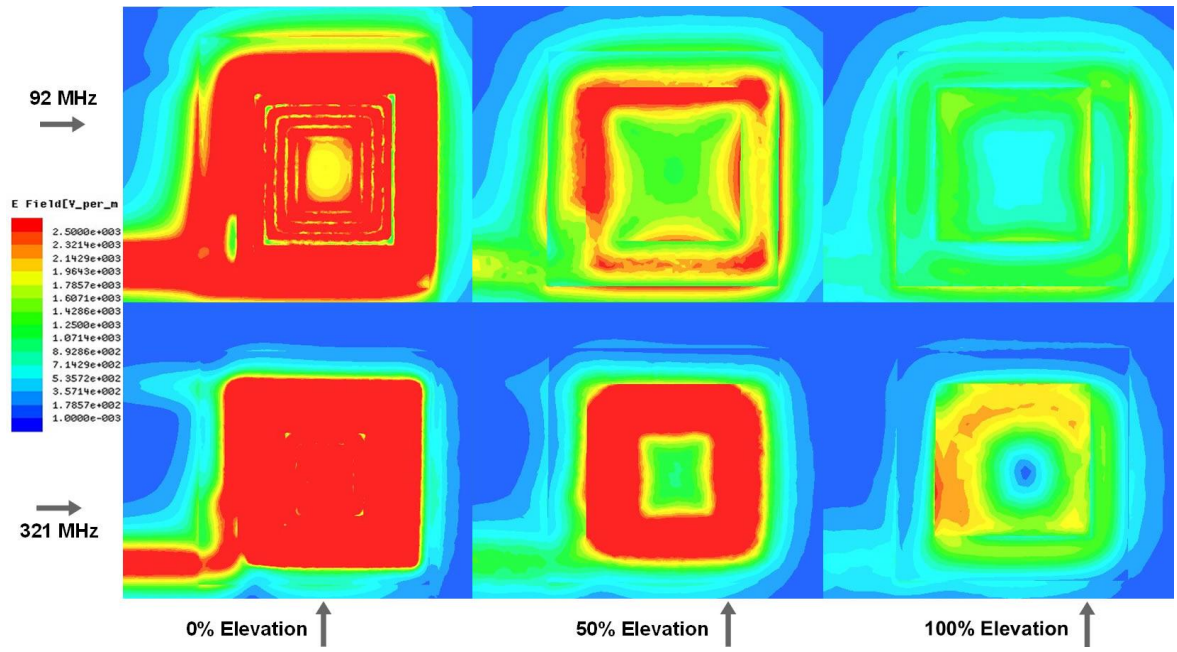

Figure 4-26: showing the magnitude of the electric field at three elevations of 0%, 50%, and 100% inside the sample reservoir.

The preceding observations can be analysed further by looking at the real part of the H_z component of the magnetic field at the same elevation points, as shown in Figure 4-27. Here, the magnetic field was plotted for a range of -30 Am^{-1} to 30 Am^{-1}. This is to allow a direct comparison with the magnitude plots in Figure 4-26. In this plot, the green areas represent the areas with the weakest magnetic field. Red and blue colours are used to show areas with the strongest magnetic field. The skewed strength of the field on the top left hand side of the plots can be seen. It may also be observed that the strength of the magnetic field decreases as we move away from the surface of the coil. At 92 MHz, a more uniform field distribution can be seen than that found at 321 MHz. However, the strength of the field is of lower value at 92

MHz in comparison to the latter frequency of 321 MHz. At 321 MHz, we can observe that the outer areas of the inductor have a larger magnetic field even at higher elevations.

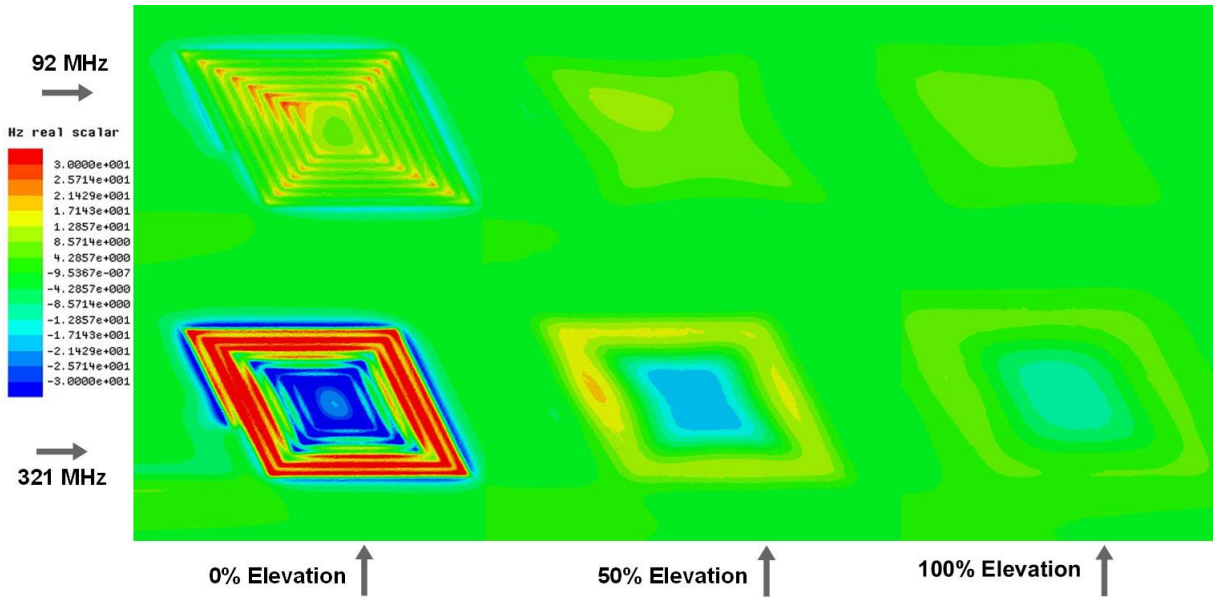

Figure 4-27: showing the plot of the real part of the Hz on three elevations inside the reservoir sample space

Figure 4-28 shows the view for the E-field vector distribution at frequency of 92 MHz inside the sample space. It can be seen that the strength of the electric field is substantially smaller at higher elevations than the closest to the inductor track. It can also be observed that the electric field is stronger on the top left corner of the device due to the introduced misalignment of the reservoir. The magnitude of the electric field at three elevation points inside the sample space for two frequencies of 92 MHz and 321 MHz are also shown in Figure 4-29, Figure 4-30, and Figure 4-31. Similar to the case for the magnetic field, it can be observed that the strength of the electric field declines rapidly as we move to higher elevation points. The other factor to be realised is that the droplet of epoxy placed inside the reservoir to insulate the inner soldering point is not reducing the sensitivity of the device substantially. This is due to the weaker electric and magnetic fields at the centre of the inductor. This could be the reason behind the lack of this droplet in the 3D model having minimal effect on the outcome of the simulations.

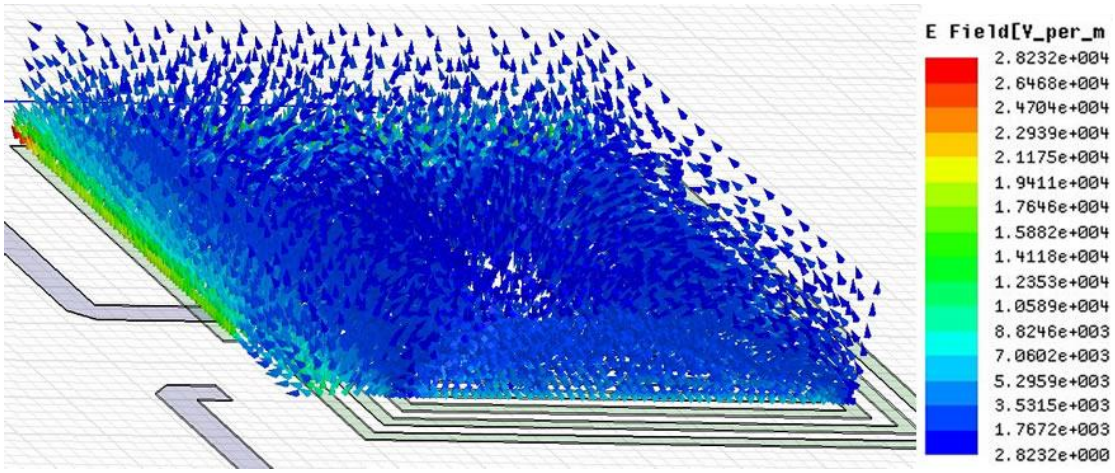

Figure 4-28: showing the E-field distribution in the sample space for a frequency of 92 MHz

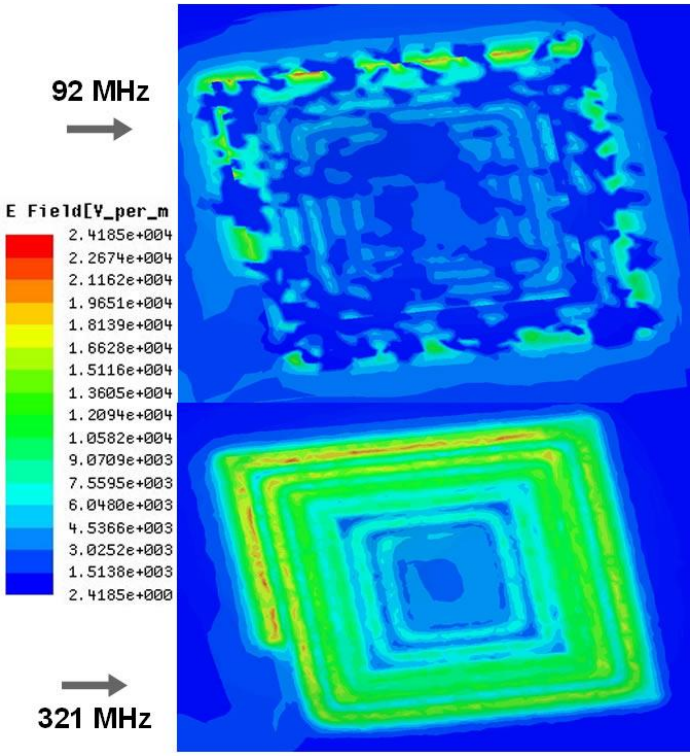

Figure 4-29: showing the magnitude of the electric field at an elevation of 0%

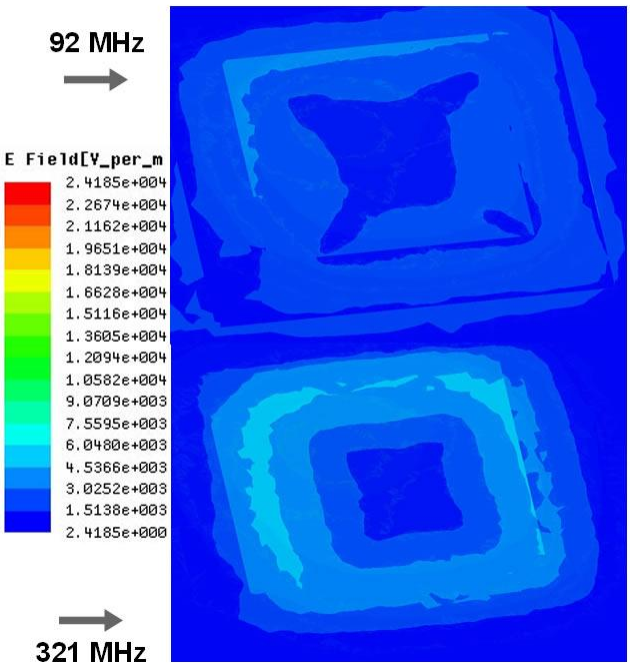

Figure 4-30: showing the magnitude of the electric field at an elevation of 50%

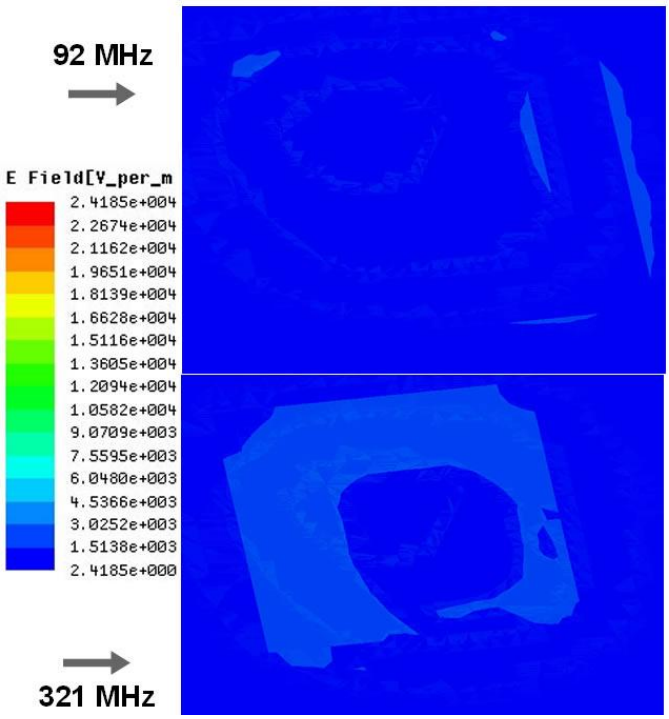

Figure 4-31: showing the magnitude of the electric field at an elevation of 100%

It must be noted that the self-resonant frequencies mentioned here are based on the Y-parameter analysis. We can undertake this analysis using S-parameters. The S_{11} data for this device, simulated in the range of 50 MHz to 500 MHz, is shown in Figure 4-32.

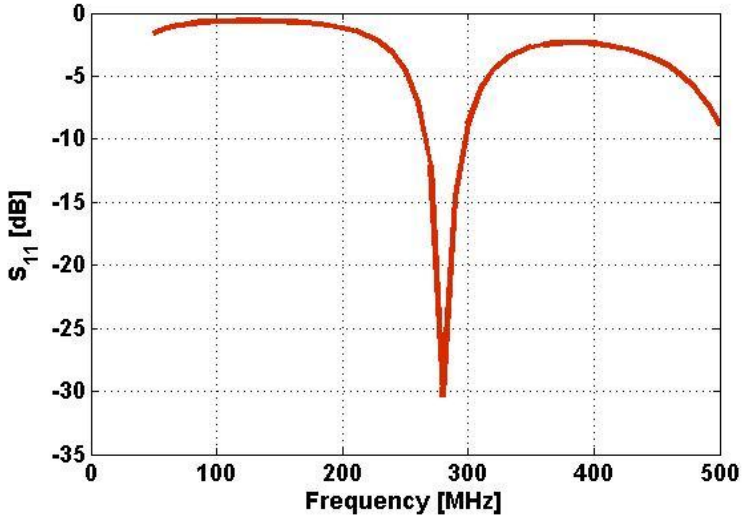

Figure 4-32: showing the S_{11} plot of the simulated 3D model for a frequency range of 50-500 MHz

4.4 Conclusions

As part of this research I designed an RF inductor sensor and fabricated it on a FR4 substrate and packaged it with PDMS. The experimental data, resulting from the effect of the titration of a buffer solution with HCl and NaCl in the reservoir over the sensor, are reported here. The inductor was designed to have multiple resonance points. It was observed that the inductor provided greater sensitivity at the second self-resonance point, albeit at a much higher frequency. However, both frequencies are within the range of operation of ordinary CMOS fabrication processes. Hence, integrated circuits can be designed and developed for the readout part of the sensing system. A sensitivity of 5% change for NaCl, in concentration range of 0-0.25 mol L^{-1}, and 6.5% change for HCl, in the pH change of 1.2-4.5, in the second self-resonant frequency of the sensor was achieved. I also looked at the value of inductance at fixed frequency of 71 MHz and monitored its sensitivity in the case of NaCl titration. The designed sensor provided a sensitivity of 90% change in inductance for the full range of titration of NaCl which is from 0 to 0.25 mol L^{-1}.

Simulation data is also provided for the sensor when there was no liquid in its reservoir. The experimental data were used to validate this model. Upon validation, field distribution plots were generated and discussed for two self-resonance points of the inductor. It was observed

that the intensity of the magnetic field was greater in outer areas of the inductor in all cases. It was also observed that there were two areas of great strength, at the centre and outer limits of the sensor, at the second self-resonance points. This information provided a key insight into the correct physical design of the reservoir and the positioning of the liquid samples over the device. This model was then used to realise a transformer device and investigate the effects of the liquid on its mutual coupling.

Chapter 5

5 Coupled Sensors

Our investigation into the development of an electrical sensor for the monitoring of the electrical properties of electrolyte solutions has been discussed in the previous chapter. The next research step was to utilise the inherent characteristics of this sensor in the development of coupled passive electrolyte monitoring units. Inductor coils were employed in a transformer set-up to investigate the effects of an electrolyte on the mutual inductance of the transformer. An electrolyte solution was placed between the two inductors. The coupling between the two inductors was used as an indicator to the concentration of the electrolyte solution. This experiment was used to obtain further information regarding the near field behavior of the inductors when a sample is placed between them. These Data help in the design of remote interrogating units, which perform measurements on standalone sensing devices. These devices require no physical contact with other readout circuitries, enabling multiple simultaneous readings from a number of sensors. Lack of physical media for data transmission also simplifies the packaging of the sensing devices. The general aspects of the work discussed in this chapter are also published in [168, 169].

At first, the apparatus for a transformer, constructed using the inductors described in the previous chapter, is discussed. This is followed by an account of experiments carried out under dry conditions, which aimed at characterizing the coupling between the inductors. Simulation data for this apparatus were obtained and analyzed to gain insights into the behavior of the electric and magnetic fields. This discussion is followed by experimental data on the titration of deionized water and HCl, and its effect on the mutual inductance of the device. Concluding remarks on this part of the research shall also be provided at the end of this chapter.

5.1 Transformer Apparatus

The 2-port inductors described in the previous chapter were used in the construction of the transformer here. One port of each of the inductors was soldered to the ground plane to form

a 1-port inductor. Figure 5-1 shows the equivalent circuit of the transformer apparatus. The presence of the liquid and its effect on the packaged inductor is represented by a coupled coil in parallel with a resistor. This coil feeds into the packaged inductor and its effect is observed as a change in the complex admittance of the system, observed from port-1 or port-2.

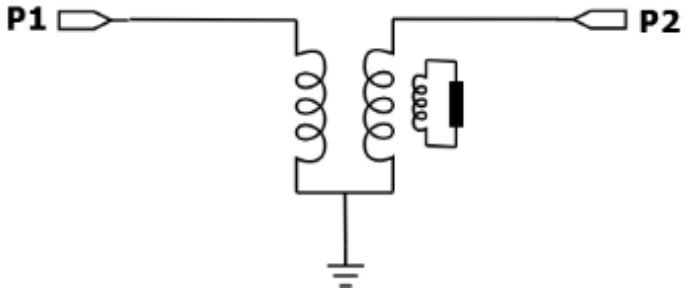

Figure 5-1: showing the equivalent circuit of the transformer set up

A Perspex slotted pad was used in order to find the optimum distance between the two inductors and to construct a transformer. This device was used to place the inductors in known positions relative to one another. The distance between each slot was 3.175 mm. Care was taken to ensure maximum alignment between the two inductors by aligning the edge of each inductor with the edge of the slotted pad. Figure 5-2, shows a depiction of the edge aligned single port inductors on a Perspex slotted pad. One inductor was placed in the bottom slot of the Perspex plate, while the other inductor was positioned from 9.525 mm to 476.25 mm in steps of 3.175 mm. The minimum distance was imposed by practical limitations caused by the SMA contacts and the cables connected to them.

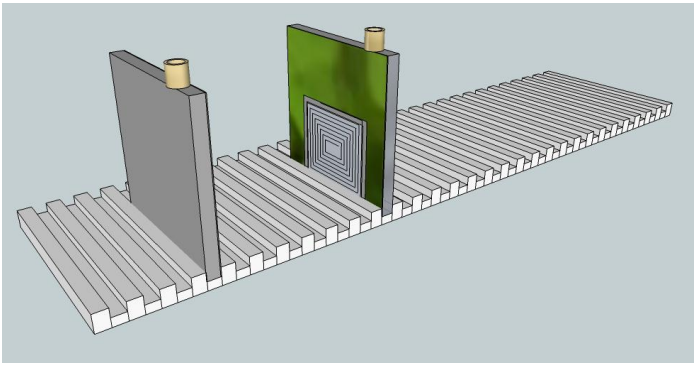

Figure 5-2: showing a depiction of the one-port inductors placed on a Perspex slotted pad

These 1-port inductors, together, formed the transformer set up. Each of the inductors was connected to one port of an Agilent PNA analyser. Figure 5-3 shows the apparatus used in this experiment.

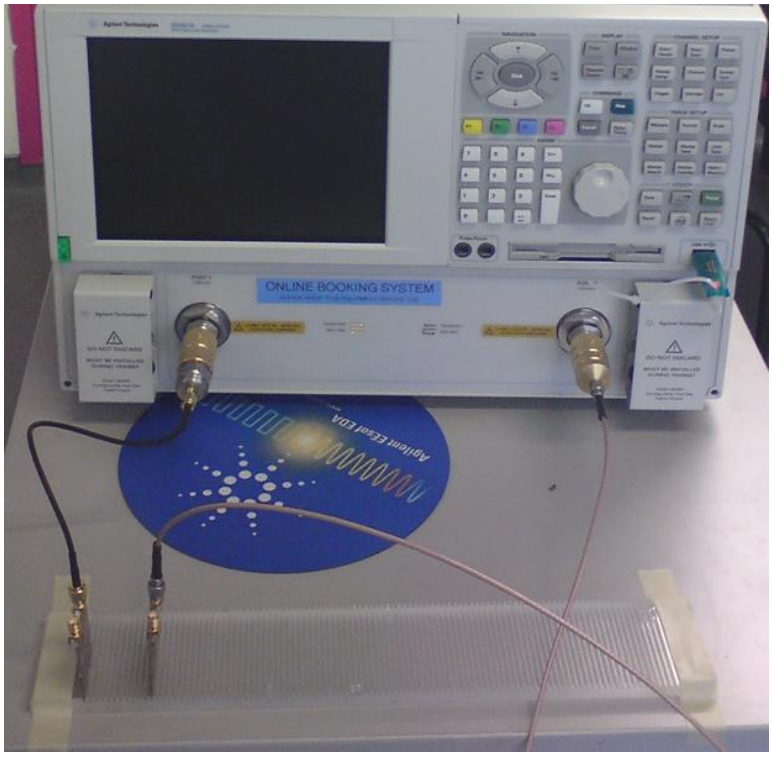

Figure 5-3: showing the apparatus used in the characterisation of the transformer w.r.t distance between the inductors

Using this apparatus, S-parameter measurements were performed on the two inductors. This test was performed in order to discover the relationship between the distance of the two inductors and the magnitude of the S_{12} parameter. This parameter is a measure of the mutual coupling between the two inductors. Note that the Y_{12} parameter can be extracted and used to obtain the mutual inductance of the system. However, care must be taken to distinguish the effects of the parasitic component so that the real value of the mutual inductance can be calculated [171-173]. The inductors and the transformer set up used in this research were developed for qualitative sensing and data extraction. As a result, we did not undertake a parameter extraction process of the transformer set up.

Figure 5-4 shows the experimental data for the variations in the S_{12} parameter for a range of 9.525 mm to 47.625 mm. A complete S_{12} frequency sweep of the apparatus was performed, in the frequency range of 10 MHz to 1 GHz. The peak amplitude of the S_{12} parameter in the region of 150 MHz to 450 MHz is of central interest. In the diagram, the coupling occurring at the closest distance of 9.525 mm is shown in red, and that at the farthest distance of 476.25 mm is shown in purple. It can be seen that a coupling of -12.4 dBs for a distance of 9.525 mm, and a coupling of -45.43 dBs for a distance of 476.25 mm, is obtained in this experiment. Based on this data, and on the physical constraints imposed by the device

structure, a distance of 15.875 mm (blue) was chosen for the positioning of inductors. The physical constraints imposed by the device structure were the presence of SMA contacts on each inductor and ease handling of the inductors by hand during the wet experiment.

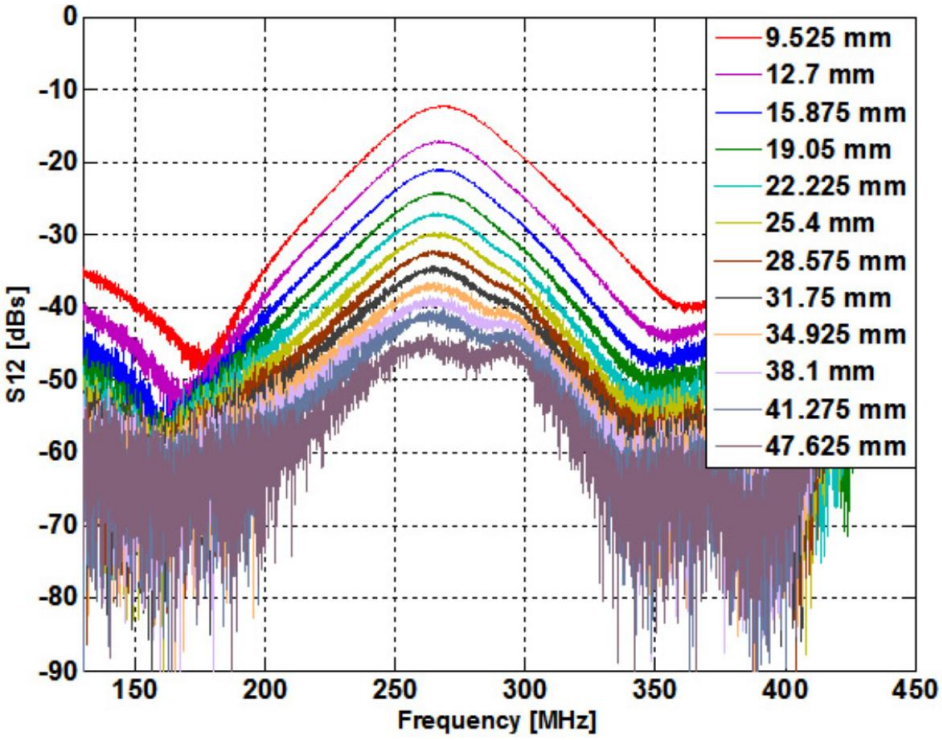

Figure 5-4: showing the variations in the magnitude of the S12 parameter as the distance between the two inductors is changed

5.2 Simulations

5.2.1 Effect of Distance

Simulations were performed in the ANSOFT HFSS FE package. The constructed 3D inductor models were placed at a distance of 15.875 mm from one another. The simulations were carried out for a range of 50 MHz to 500 MHz, at steps of 10 MHz. This range was chosen based on the experimental results shown in Figure 5-4. Figure 5-5 shows the 3D model constructed for this part of the simulation. The 3D models constructed for the simulations in the previous chapter were also used for the current simulation. However, the PDMS elements and the sample space were removed. This is due to the fact that the inductors used in obtaining the optimum distance were not packaged. Figure 5-6 shows the plot of the excitation modes for the simulation setup. In this simulation, the weight factor for the incident power was set to 0.5. This was due to the fact that there were two structures coupled with one another. In this case, half of the "simulation" incident power was applied at each

port. Minor deviation from the CPW modes can be observed. However, as the outcome of the simulations was consistent with the experimental data, no further investigation or simulation modifications were carried out. The grounding of the second port of each inductor was realized by placing a metallic layer between the signal track and the ground layer at the back of the inductor.

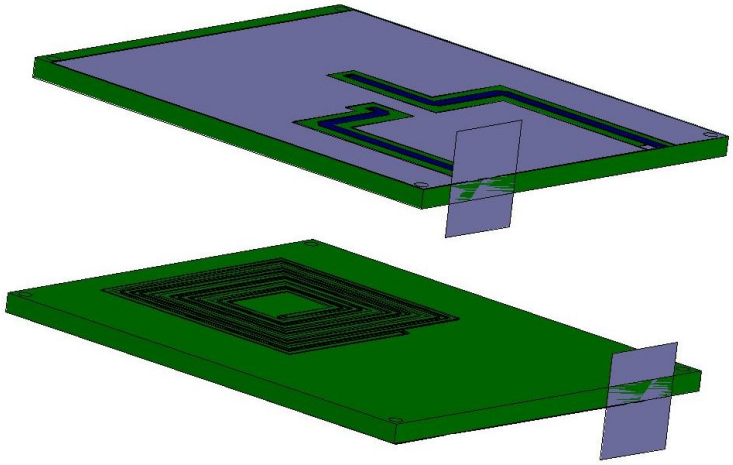

Figure 5-5: showing the constructed 3D model used for simulating the effect of distance on the coupling between the two inductors

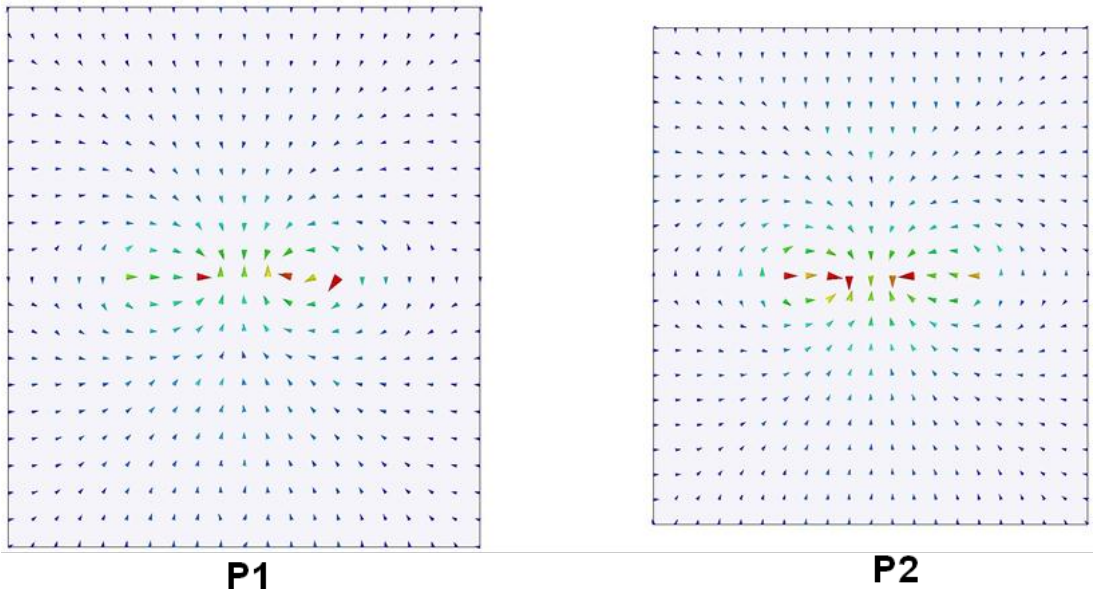

Figure 5-6: showing the excitation modes at ports 1 & 2 of the simulation model

Figure 5-7, shows the plot for the S_{12} parameter for both the simulated and the experimental data. It can be seen that both plots follow a similar trend. However, the simulated data do not decrease at the same rate as the experimental data points after reaching a peak. A peak occurs at a frequency of 267 MHz for the experimental data and at 280 MHz for the simulation data. This is a difference of 13 MHz or 4.87%. The deviation of the simulation results from the

experimental data can be explained by the differences between the simulation model and the experimental apparatus. Comparing Figure 5-2 and Figure 5-5, it can be seen that the Perspex slotted pad is not present in the 3D structure. It can also be seen that the table on which this apparatus is placed is not modeled either. These two factors along with material models could contribute to this shift in frequency and a slower decrease in S12 beyond the maximum coupling value. The other factor that can contribute to this effect is the presence of the small metallic connector that links the signal track to the ground. This can cause a discrepancy between the simulated and experimental data given that in the actual device, this process is realized by soldering the SMA contact to the ground layer. Note that the inductors were not placed at exact locations although great care was taken to ensure such behavior. The inductors were placed at the edges of the slotted pad to ensure perfect positioning. However, this, along with inconsistencies in the size of the inductor substrate means that the coils were not aligned accurately. This matter can also affect the inconsistencies observed between the simulation and measured values.

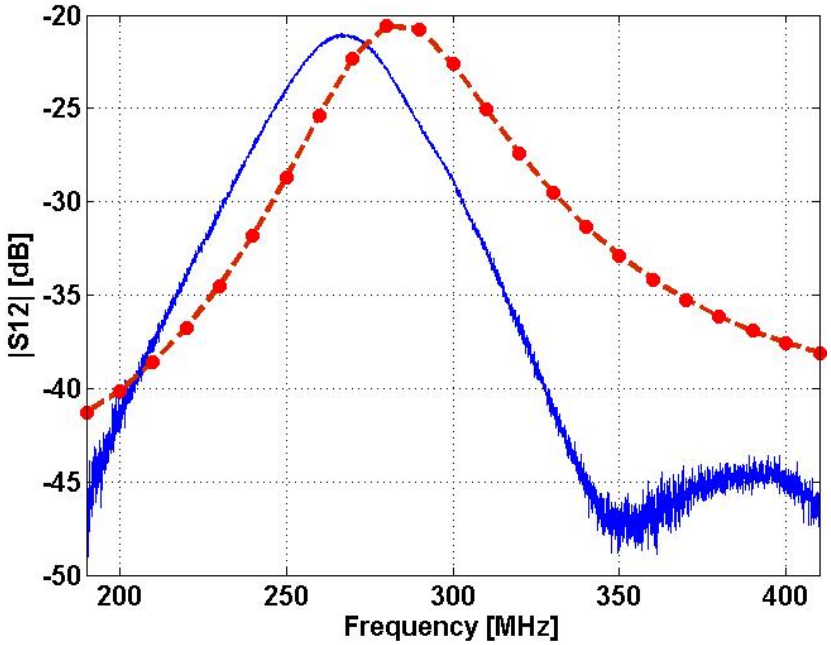

Figure 5-7: showing the comparison between the S_{12} parameters for the simulated model, shown in red, and experimental data, shown in blue

5.2.2 Effect of Distilled Water

The simulation was then modified to simulate the effect of distilled water on the transformer inductor pair. Distilled water is used in this part of the analysis, as it is readily available in laboratories and its electromagnetic model is also available in the HFSS software. The lower inductor in Figure 5-5 is replaced with the packaged 3D model developed in the previous

chapter. All other factors are kept without change. The port modes were also checked and no inconsistencies were observed. Two simulations were performed at this stage. The first simulation was performed for the PDMS coated transformer and no liquid present in the reservoir. The second simulation was done using the built in HFSS model for the distilled water. Figure 5-8 shows the plot for the simulated and measured values of the S_{12} parameter. The experimental maximum coupling occurs at a frequency of 267.75 MHz with a value of -21.11 dB. Simulation of this system yields a maximum coupling at a frequency of 274 MHz with a value of -20.62 dB. There is a 0.49 dB difference between the simulated and measured S_{12} values. There is also a frequency deviation of 6.25 MHz between the simulated and experimental values. This corresponds to a deviation of 2.33% from measured results. It can also be observed that the measurement data fall at a faster rate compared with the simulation results. This is attributed to measurement imperfections, along with the shortcoming of the 3D model used in the simulation, which is discussed in the previous section. An added factor is the addition of the PDMS to the inductor. The added thickness to the inductors causes them to be an angle to the horizon and not be parallel with one another. This can be another factor that causes this different between the experimental and measured values.

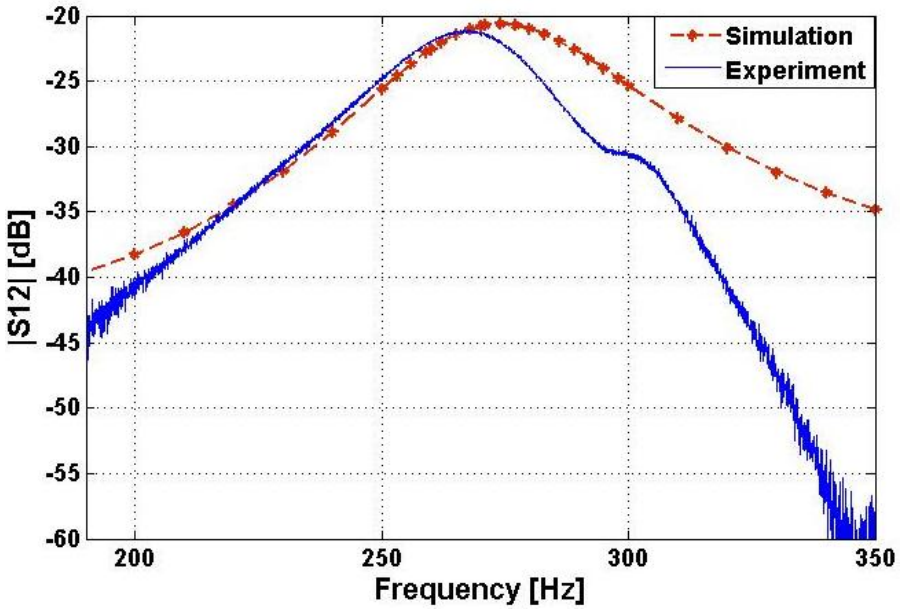

Figure 5-8: showing the comparison between the measured and simulated values of S_{12} for coupled inductors

Using the same 3D model and set up in HFSS, distilled water was placed within the reservoir above the inductor coil. To make a more realistic simulation, the height of the sample space was reduced to 2.206 mm in order to realise a volume of 600 µL in the sample space. Figure 5-9 shows the plot for the S_{12} parameter for this particular simulation. The maximum coupling occurs at a frequency of 229.34 MHz with a S_{12} value of -23.44 dB. The equivalent

simulated values for frequency and S_{12} parameter are 235 MHz and -24.38 dB. The simulated value of the S_{12} parameter is 0.96 dB larger than the measured one. The simulated frequency at which the coupling occurs is 5.66 MHz higher than the measured value. This is a deviation of 2.47% from the experimental value. It can be seen that the simulated trace follows the experimental data up to maximum coupling. However it does not fall at the same rate as the experimental measurements. This could be attributed to dissimilarities between the 3D mode of the sample space and its real shape. This is discussed in the previous chapter. The other factor to be taken into account is the effect of carbon dioxide on water. The carbon dioxide in the air is absorbed by the distilled water [174], which reduces its pH slightly. This addition of a new substance to the water changes the complex dielectric behaviour of the solution. Care was taken throughout this experiment to limit the exposure of the distilled water to air. However, this is an effect that cannot be completely prevented in this apparatus. This is another contribution factor to the deviations of the experimental data and simulated values from one another.

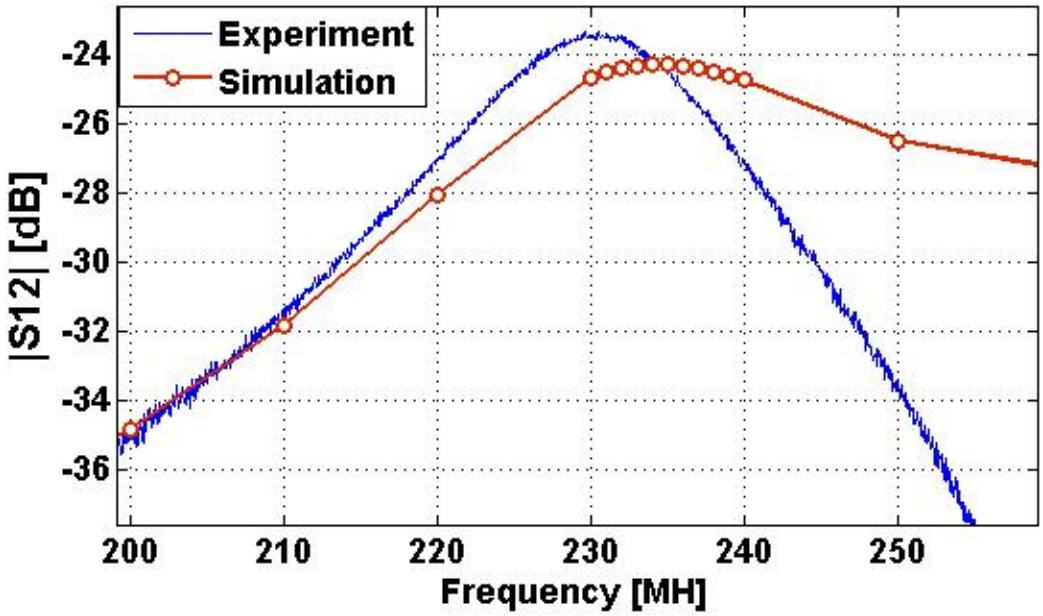

Figure 5-9: showing a plot of the S_{12} parameter against frequency for experimental and simulated values for distilled water

5.2.3 Analysis of Fields

The other factor investigated in this simulation was the effect of distilled water on the magnetic fields. First, we will consider the case in which no liquid was present. Figure 5-10 shows the variations in the real part of the Hz at frequencies of 200 MHz and 270 MHz. The latter frequency was chosen because the maximum coupling between the two inductors

occurs at this point. It can be seen that the magnitude of the magnetic field increased substantially as it reached the resonance point. The magnetic field lines were terminated at the ground planes beneath each inductor. The residue fields beyond the ground planes were due to the presence/absence of part of the ground plane, which had been removed to allow for drill holes and contact tracks to be made.

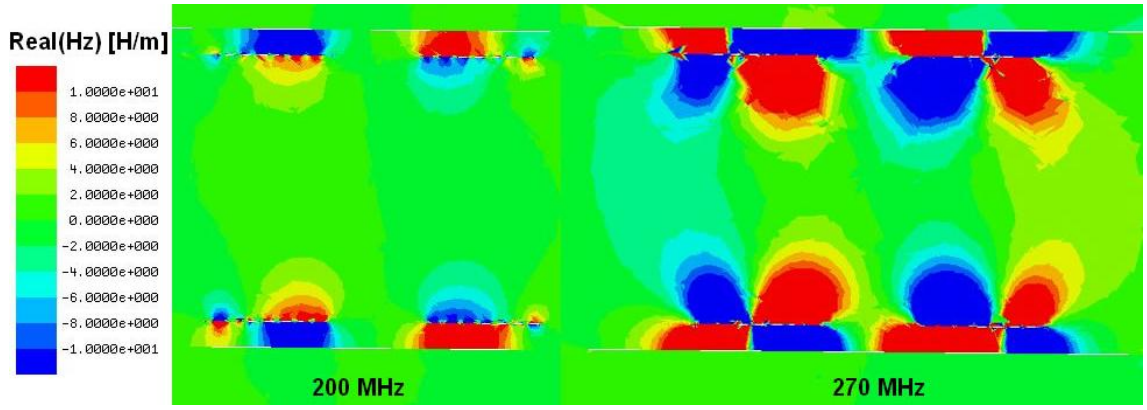

Figure 5-10: showing the variations in the real part of the Hz at frequencies of 200 MHz and 270 MHz

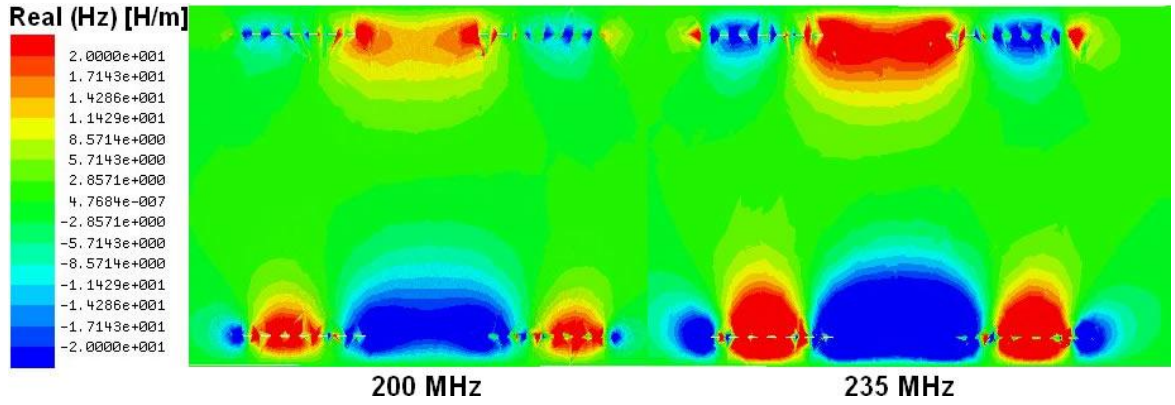

Figure 5-11: showing the plot for Real(Hz) for two frequencies of 200 MHz and 235 MHz in the presence of distilled water

Figure 5-11 shows the plot for the real part of the Hz in the presence of distilled water. The range of values used in this plot was twice as large as the one used in the previous plot. This was done to enable clearer demonstration of the plots. It is readily observed that, in the case of air, the resonance of the system was of the second order. However, when water was placed inside the reservoir, the coupling occurred as a first order mode. It must be noted that the presence of liquid water in the reservoir changed the properties of the system completely. Hence, the new system should be treated as a separate entity from that in which air was the only material in the vicinity of the sensing coils.

5.3 Experimental Data

Three sets of measurements were performed at this stage of the research. The first test measured the complex dielectric coefficients of hydrochloric acid at different concentrations. This test was followed by measurements of the response of an individual 1-port inductor to hydrochloric acid. Finally, a transformer apparatus was constructed, and the effect of HCl on the coupling of the transformer was investigated.

5.3.1 Hydrochloric Acid

Variations in the conductivity of the HCl solution for concentrations of up to 0.5 M calculated using the following formula [175]:

$$\Lambda = \Lambda_{\circ} - S\sqrt{c} + \left(Ec + Gc^{\frac{3}{2}}\right) log(c) + Ac + Bc^{\frac{3}{2}} + Cc^{2} + Dc^{\frac{5}{2}} \qquad 5.1$$

An overview of this formula is provided in Chapter-I. In this instance, $\Lambda_{\circ} = 426.06$ mS m^2 mol^{-1}, $E = 185.76$ mS m^2 mol^{-3} L^2, $S = 158.63$ mS m^2 mol^{-1} (mol L^{-1})$^{-0.5}$, $A = 702.39$, $B = -490.05$, $C = 157.3$, $D = 9.6574$ and $G = 615.0$. A, B, C, and D are completely empirical coefficients used in the data fitting function. G is a thermodynamic coefficient and the author in [175] has not provided further details on its origin. The pH range of interest lies in the range of 0.2 to 4.2. This corresponds to an HCl concentration range of 631 mM to 0.631 mM. Assume that the width and length of the reservoir are the dimensions of the inductor coil. Deduct 2 mm & 3 mm from the dimensions of the inductor to allow for the space taken by the packaging. We may now calculate the conductance of the sample inside the reservoir using the physical dimensions of the sample and the aforementioned equation. The plot for the DC conductance of HCl against pH is shown in Figure 5-12. At a pH value of 4.2, the conductance of the HCl sample was 1.53 S and, at a pH of 0.2, the conductance assumed a value of 1.275 S.

The complex dielectric values of the HCl were measured using an Agilent high temperature probe connected to a PNA. 600 mL of deionised water was placed inside an 800 mL beaker. A 2 M solution of HCl was then added to the deionised water in increments of 10 mL. This led to a variation of between 32.8 mM to 285.7 mM in the concentration of the HCl inside the beaker. The dielectric properties of the deionised water were also measured and analysed. This was to check the validity of the data obtained using the dielectric probe. Figure 5-13 and Figure 5-14 show the variations in the real and imaginary parts of the complex dielectric function for deionised water, in a frequency range of 200 MHz to 1.6 GHz. The real part of

the permittivity varied within a range of 77.9 to 78.7. Given that the dielectric sensor displays an inaccuracy of up to 5% in measurements, no effort was made to obtain and investigate absolute values. The general trend of the data obtained in this experiment conforms to expected theoretical results.

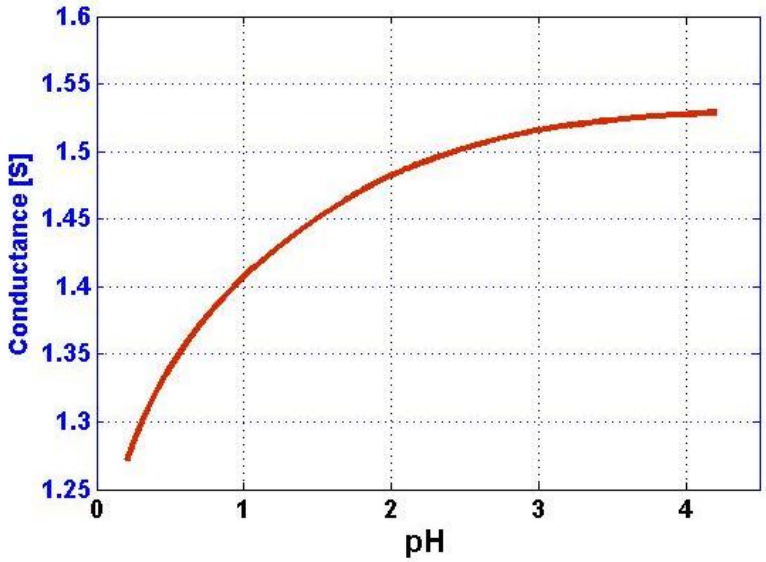

Figure 5-12: showing the variations in conductance of the HCl solution inside the reservoir against pH

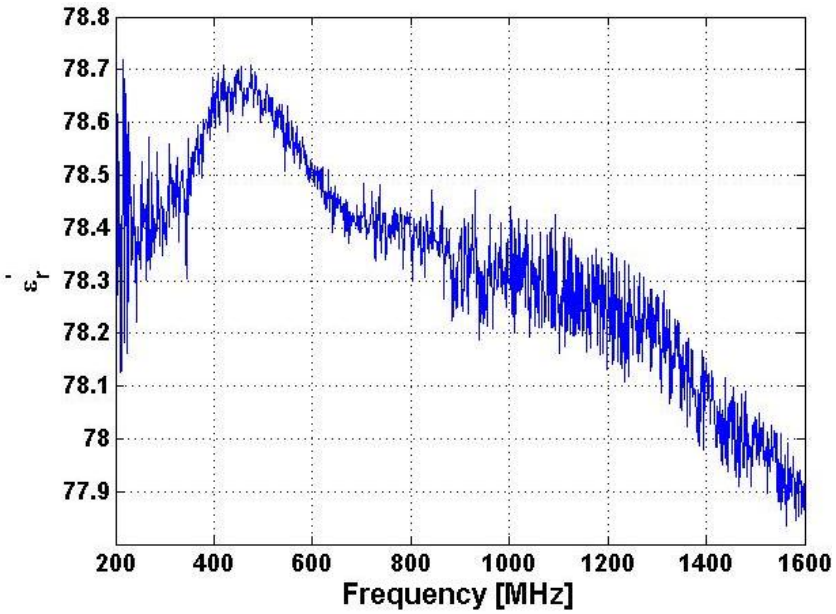

Figure 5-13: showing the variations in the real part of complex permittivity for water

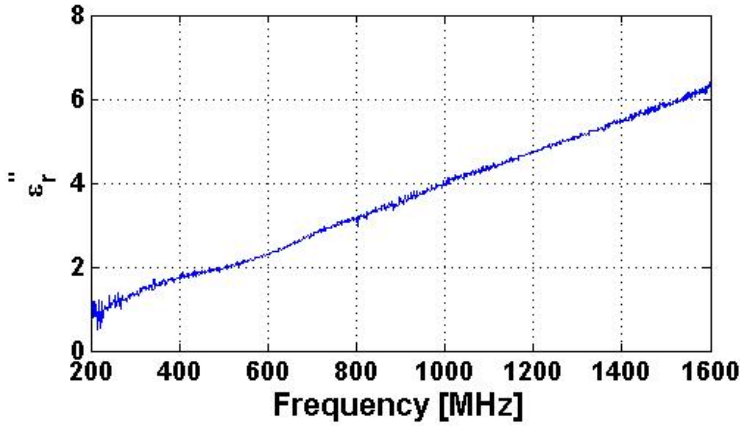

Figure 5-14: showing the variations in the imaginary part of the complex permittivity for deionised water

The other observation drawn from the deionised water measurements was the level of noise in the trace. This was due to the faulty attenuator in the PNA. All of the measurements performed using the PNA exhibited a higher than usual level of noise. Given that we are only interested in the trends and not in the absolute values, the data is provided as measured. Using the same apparatus, the complex permittivity of the HCl was also measured. Figure 5-15 shows the variations in the real part of the permittivity of the HCl. It can be seen that at a frequency of 433.8 MHz, the real part of the dielectric function increased from a value of 80.5 to a value of 87.4. Beyond this concentration, the real part of the dielectric function began to decrease rapidly to a value of 3.14, as shown in Figure 5-16.

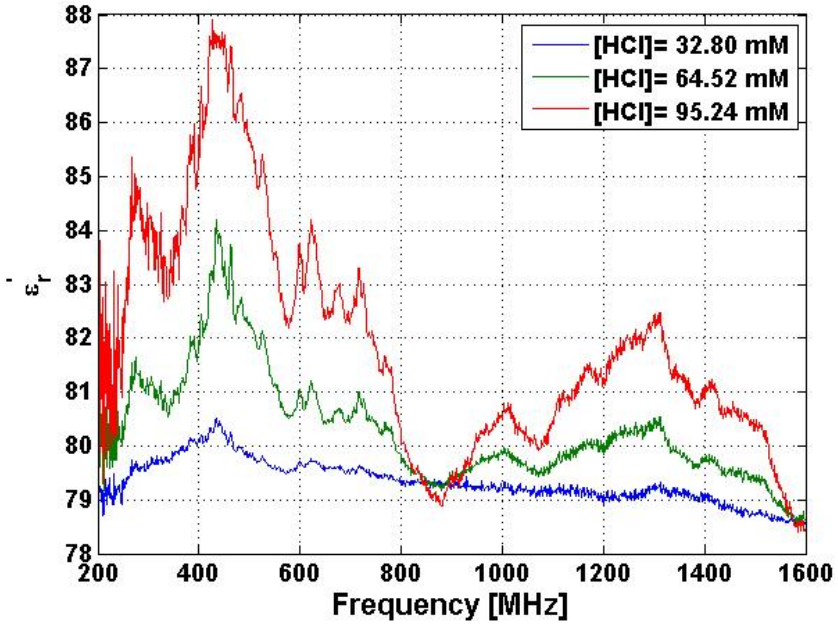

Figure 5-15: showing the variations in the real part of permittivity for three different concentrations of HCl

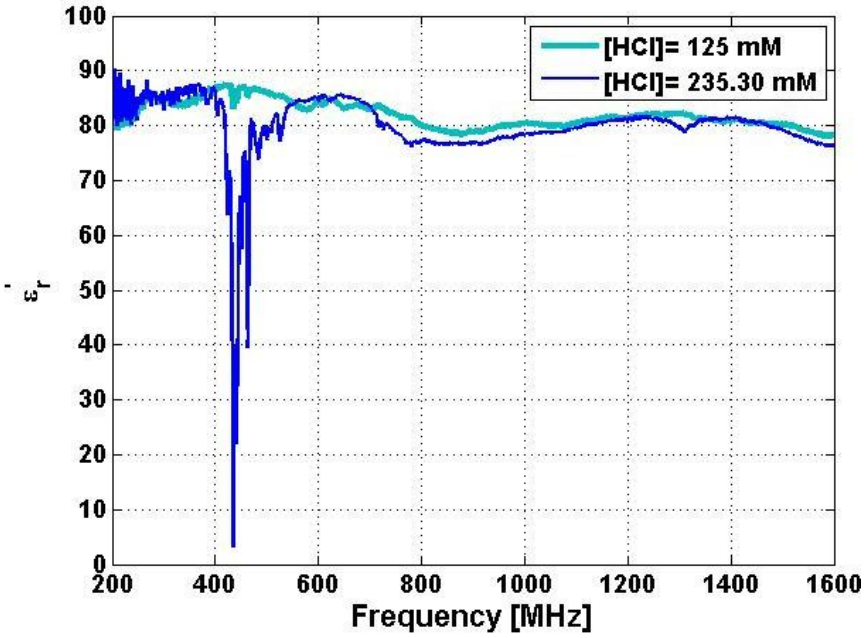

Figure 5-16: showing the variations in the real part of complex permittivity of HCl for two different concentrations

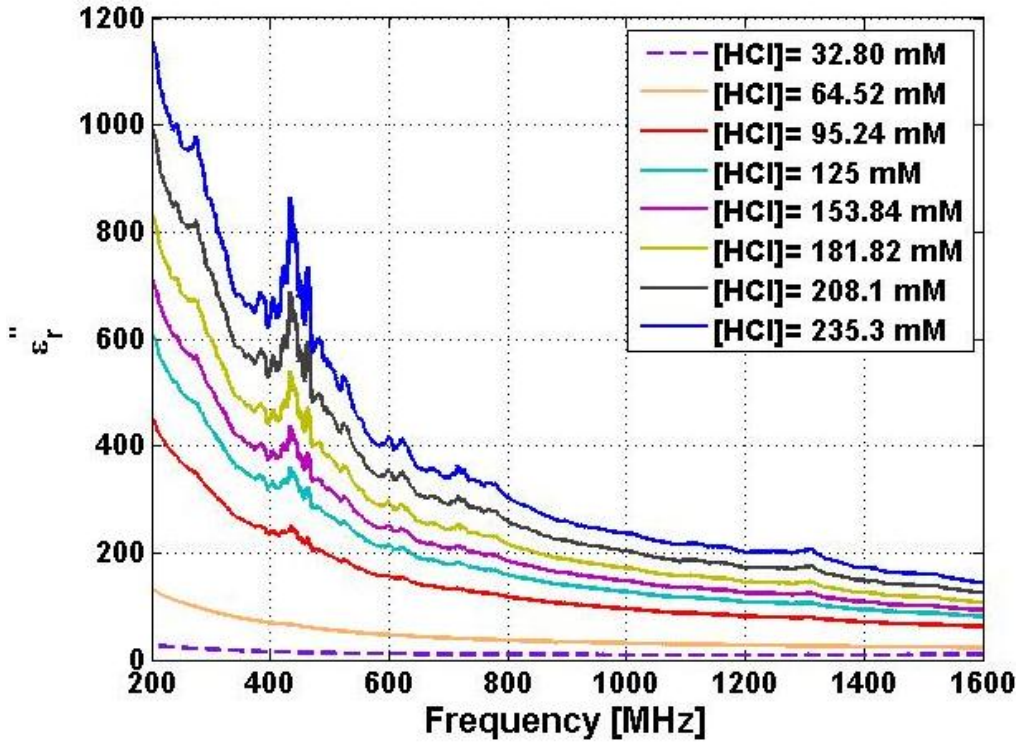

Figure 5-17: showing the variations in the imaginary part of permittivity for HCl at different concentrations

Figure 5-17 shows the variations in the imaginary part of the permittivity of a solution of hydrochloric acid. It can be seen that at a frequency of 433.8 MHz, the imaginary value of the

permittivity started to increase. It increased from a value of 14.14 to a value of 863.9. This decrease in the real part of the permittivity, and the increase in its imaginary parts, corresponds to the presence of molecular resonance in the solution containing the HCl. As a result, designing a sensor operating at that frequency could yield important information regarding samples containing HCl.

5.3.2 1-port Inductor

The measurements were performed at room temperature. Deionised water and HCl were titrated at a constant volume of 800 μL. After each individual measurement, the inductor containing the liquid was disconnected from the apparatus washed with deionized water and dried using compressed air. A 30 second delay was observed between the time stamp of adding the HCl to the solution and taking the measurement. This was to allow for the complete dilution of HCl by the deionized water in the reservoir. The variations in the second self-resonance frequency of the inductor against the change in the pH of the electrolyte from 4.2 to 0.2 are investigated. The s parameters of the inductor were measured and then converted into y parameters, to obtain inductance values, using $L=\text{imag}(1/Y_{11})/2\pi f$

Figure 5-18 shows the plot of the change in the second self-resonance of the inductor against pH. A plot of DC conductance against pH is also provided. The shift in the self-resonance of the system was deduced from the self-resonance frequency of the system in the presence of deionised water at 406.54 MHz. It can be seen that as the value of pH decreased from 4.2 to 0.2, its conductance also reduced from 1.53 to 1.28 S. This drop in conductance was accompanied by a shift in the self-resonance frequency to lower values. This shift was in the order of 19.6 MHz. It can be observed from the discussion in the previous subsection that at around 400 MHz, the real part of the dielectric function was reduced as the concentration increased. This factor, along with the substantial increase in the energy absorption properties of the system (imaginary permittivity), led to an overall reduction in the self-resonance of the sensing device. This part of the measurement was concerned with obtaining a general overview of the performance of a 1-port inductor. Hence, no investigation of the effect of the solvent (deionised water) on the sensor was undertaken.

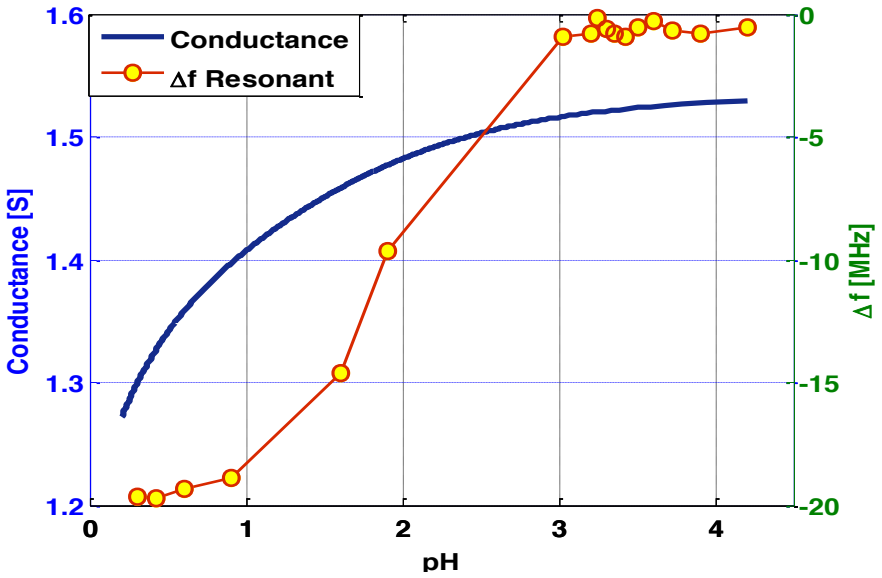

Figure 5-18: showing the variations in the self-resonance frequency of the sample against pH. The conductance of the sample is also plotted here

5.3.3 Transformer Data

Using the data obtained in the previous section, a fixed distance of 15.875 mm was chosen for the positioning of the inductors. The slotted Perspex pad was fixed in a vertical position and one PDMS packaged sensor was used to replace the bottom inductor to prepare the apparatus for the HCl titration test. The conditions for the measurements were the same as those set out in the previous subsection. Figure 5-19 shows the variations in the coupling between the inductors for a volumetric titration of deionised water from 600 µL to 790 µL. The data is differential with respect to the S_{12} parameter at 600 µL.

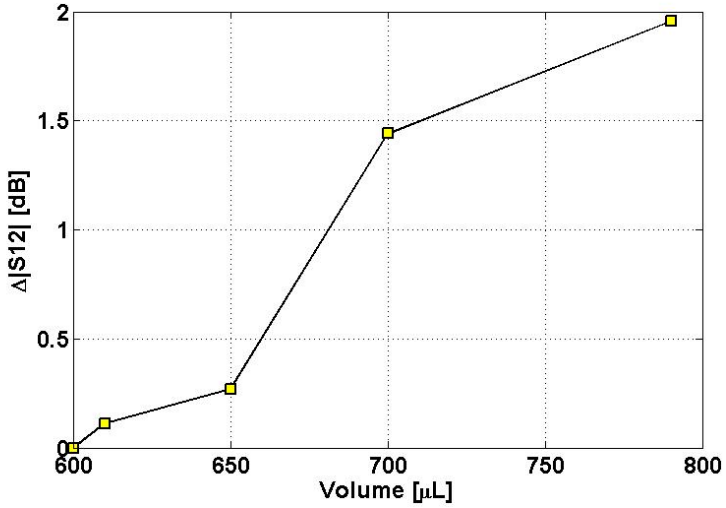

Figure 5-19: showing the effect of the deionised water on the transformer apparatus

Figure 5-20, shows the plot of the variations of the frequency at which the maximum S12 occurs against pH of the sample. The frequency deviation was calculated with respect to the coupling of the system in the presence of deionised water. A negative deviation represents a drop in the self-resonance frequency. In the present case, a reduction of 14 MHz was observed for the full pH range. It must be noted that the response of the system is saturated for pH values greater than 3. For lower pH values, the coupling decreased rapidly. This can be attributed to the increase in the losses occurring within the system as the imaginary part of permittivity increased. Note that the DC conductance of the HCl decreased as the concentration of the HCl was increased. Refer to chapter-II for more information on the complex dielectric function.

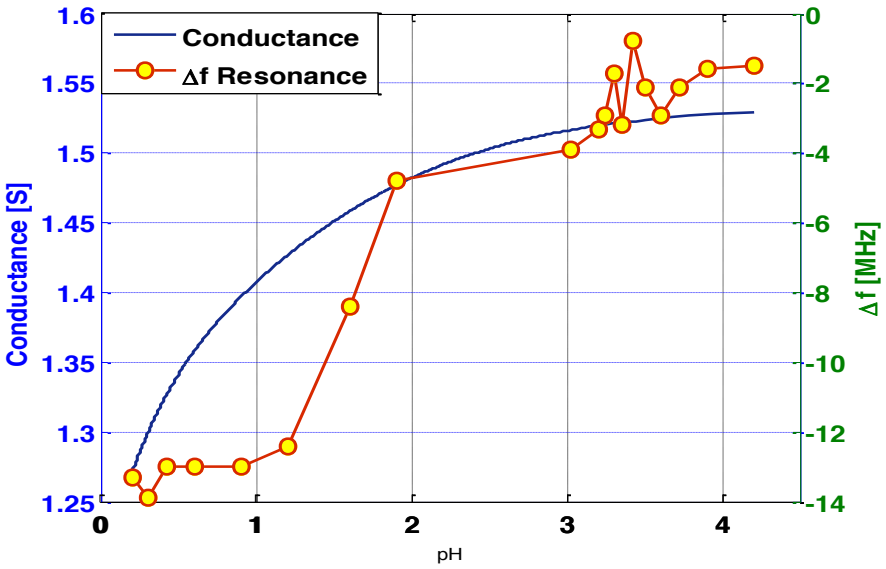

Figure 5-20: showing the variations in the frequency at which the mutual coupling is at its peak value, against pH. The DC conductance of the system is also provided here.

5.4 Conclusions

As part of this research I looked into the use of a transformer set up for monitoring the concentration of ionic species in a liquid sample. This was achieved by monitoring the S_{12} parameter and the coupling between the two single port inductors. The optimum distance at which to carry out measurements was determined by the mechanical connections to the inductors, as well as the electromagnetic coupling between inductors. A distance of 15.875 mm was chosen, which showed a S_{12} value of -19.7 dB in air. Three sets of tests were performed to assess the effect of distance on the coupling between the inductors, the effect of the electrolyte on a single inductor, and the effect of the electrolyte on the mutual inductance of the transformers. The S_{12} parameter was used as a figure of merit for the coupling between

the two inductors. It was shown that the maximum coupling frequency between the inductors was reduced by 14MHz in the HCl titration. The pH of the sample was reduced from 4.2 to 2 in this test. The S_{12} simulation results had a deviation of 2.33% from experimental values under dry conditions. The same deviation in the case of deionised water was 2.47%, compared with measured values. A clear variation in the coupling between the inductors was observed as the concentration of the sample was increased. The transformer set up can be used in monitoring the pH of the solution in the range of 1-2 as it provides a linear response. Outside this region the sensors can be used as qualitative sensing devices detecting a change in the overall pH of the solution.

Chapter 6

6 Conclusions & Future Work

6.1 Conclusions

The main contribution of my research is the development of an electrical sensor, operating in the radio frequency range of 50 MHz to 500 MHz, that can be used in the monitoring of the electrical properties of electrolyte solutions. As part of this research I used RF sensor to monitor the variations in the complex dielectric values of NaH_2PO_4 (sodium dihydrogen phosphate) solutions, when titrated with NaCl (sodium chloride) and HCl (hydrogen chloride). The complex dielectric function of the electrolyte solution affects the amount of energy stored in the electric and magnetic fields of the electrical sensor. These changes affect the resonance properties of the sensing device. The fabricated electrical sensor resonates at multiple frequencies.

NaCl titrations with NaH_2PO_4, in which the pH varies by a value of 0.19, led to a variation of 1.906 MHz at the 1st self-resonance frequency of the sensor and of 15.35 MHz at the 2nd self-resonance frequency. For a NaCl concentration range of 1.71 mmol/L to 24.37 mmol/L, the ionic strength of the solution changed by a value of 2.3 mmol and its pH remained unchanged. In this region, a linear response was obtained from the 2nd self-resonance of the device, which had a gradient of 258.8 MHz/mmol. HCl titrations with NaH_2PO_4, in which the pH of the solution varied, led to a variation of 9.108 MHz at the 1st self-resonance frequency of the sensor and 14.212 MHz at the 2nd self-resonance frequency. Similar analysis of HCl, for a region in which the ionic strength varied by 2 mmol, showed a more complex picture. The response of the sensor was flat at very low concentrations of HCl, in a pH region of 3.91 to 3.61. However, an approximately linear response was observed for a pH range of 3.61 to 3.04, which was equivalent to a change of 2 mmol in the ionic strength of the solution. This was a drop of 761 kHZ/pH, equivalent to 49.5 kHZ/mmol, in the resonance frequency of the sensor. The sensor that I designed as part of this work, showed a 5% and 6.5% change in self-

resonance frequency to variations in concentration of NaCl from 0 to 0.25 mol L^{-1} and variations in the pH of the HCl solution from 1.2 to 4.5. However, at a fixed frequency of 71 MHz for the case of NaCl titration, 90% change in the value of inductance for the whole titration range of 0 to 0.25 mol L^{-1} was observed. This sensitivity is not reported in literature to date to my knowledge. The sensor displayed good sensitivity and response at very low concentrations of NaCl. It also provided good sensitivity and response for the full titration range of NaCl and HCl. Thus, the sensor can be employed to provide qualitative data on the titration of NaCl with the buffer and qualitative data on both HCl and NaCl titrations by monitoring the self-resonance frequency. The sensor also has the potential to provide qualitative data if employed in a fixed-frequency implementation given its high sensitivity.

The sensors were then used to construct a transformer apparatus to monitor variations in the concentration of HCl solutions placed in between the coils. A single inductor was first specified for this purpose. A variation of 19.62 MHz in the 3rd self –resonance of the inductor was observed for a change in pH of 4.2 to 0.2. A linear response of 7.45 MHz/pH was seen for a pH range of 1.9 to 0.6. The response of the sensor to pH values smaller or greater than 0.6 and 1.9 was non-linear and, therefore, requires further investigation. However, This sensor can be used for general qualitative measurements. A transformer was created by placing two inductors opposite each other at a distance of 15.875 mm. The maximum coupling between the two inductors in the presence of deionised water was observed at a frequency of 230 MHz. A variation of 13.3 MHz was observed in the frequency at which the maximum coupling between the inductors occurred. A linear response was obtained for a pH range of 0.6 to 1.9.

This design addresses common issues faced in the packaging of sensing devices, as the sensor itself does not require direct access to the sample under test. Hence, the sensor can be placed at a distance from the contacts and the readout unit. It was noted that Acrylic could be used to provide a thin layer of insulation above the inductor sensor. However, the thickness of the layer cannot be controlled easily if Acrylic is used. Thus, PDMS packaging was found to provide the most appropriate solution. Its thickness can be controlled easily and its properties with regards to biological matter, such as DNA or different types of proteins, are well known and understood. However, one of the shortcomings of PDMS packaging is the attractive force over its surface, which can hinder the flow of liquid samples.

These sensors can be made at a very low cost on ordinary FR4 substrates, or can be integrated into miniaturised CMOS systems on the chip. This makes the sensor a good candidate for disposable sensing devices. The inherent scalablity of the inductor allows for such flexibility. The sensor provides data of a qualitative nature, which can be used to observe whether a particular reaction has taken place inside a chamber or not. This could be beneficial in areas such as high throughput screening in drug discovery, DNA amplification and implanted medical devices. In the case of drug discovery, expensive time consuming quantitative measurements need only be taken of samples in which the relevant reaction has in fact taken place. In the case of DNA amplification processes, DNA is placed inside buffer solutions and conditions similar to those arising in the titration of NaCl and HCl with NaH_2PO_4 are present. Given the high sensitivity of this device, it could be used for monitoring the acidity of stomach content and at the same time used for wireless data transmission of the measured values.

I also developed a complete design flow for both analytical and finite element modelling of the inductor coils. The effects of material properties on the full wave Maxwell equations based on magnetic vector potential (MVP) have been looked into. Analytical expressions were derived for the power flow from filaments into various layers in the vicinity of the sensor. Finite element modelling using the HFSS software was used to model the system and to obtain information regarding the behaviour of electric and magnetic fields. The data obtained using the simulation model provided a deviation of less than 2.5% compared with experimental data. The increased sensitivity at the 2^{nd} self-resonance of the device was explained using the results of the finite element simulation..

6.2 Future Work

6.2.1 Packaging Optimisation

New packaging materials should be investigated and deployed. It was shown through FE simulations that the RF electrical sensor is sensitive to the permeability of the packaging material. Thus, whether the material is diamagnetic or paramagnetic can improve or decrease the efficiency of the sensor. Investigation into new polymers that offer paramagnetic capabilities is beneficial, and could be used to improve the sensitivity of the device without the need for further design modification.

6.2.2 Remote Interrogation

The design, fabrication and testing of a multi-resonance remote interrogating unit should take place. The implementation of passive multi-resonance sensing system allows the simultaneous readings to be obtained from the sensors. This system does not require physical contact between the sample and the sensing device. Hence, multiple samples can be analysed simultaneously. This approach can also simplify the packaging and design of sensing devices, as no physical contact between the sensor and the readout unit is required. The design process could include investigations into possible CMOS readout units, such as the integration of the inductor coil into an oscillating circuitry, and methods of tracking variations in the oscillation.

6.2.3 Quantitative Sensor

The scope of this research was limited to qualitative measurement and data analysis. It would be of great interest to investigate the system for obtaining quantitative data from samples under test. Using paramagnetic packaging materials, eigenmode analysis of the device and further parameter extraction on the inductors can pave the way for the implementation of this device as a quantitative sensor.

Appendix-I

AP-I: Eddy Current Problem

In this part, we shall derive an analytical solution to the eddy current problem using Maxwell's equations and the method of separation of variables. We shall define a 2D multi-layered problem space similar to the one shown in Figure 0-1. In this case, current is flowing in the $\boldsymbol{z}$ direction and hence the magnetic vector potential lies in this plane as well. The current carrying elements reside in the $y = 0$ position. The tracks that carry the current are shown as rectangles in the figure below. Layers above the current carrying elements are in the positive y-axis and are referred to by a *k* index. The layers beneath the current carrying tracks are in the negative y-axis and are referred to by the *k'* index.

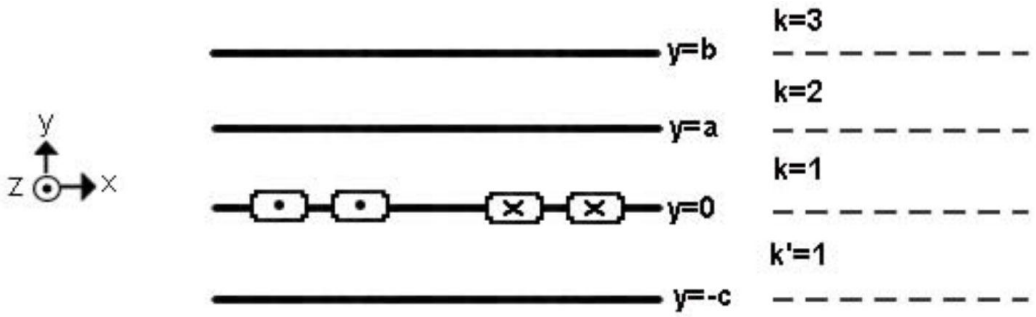

Figure 0-1: showing the layout for a 2D multi-layered eddy current problem

The eddy current formulation of Maxwell's equation can be reduced to [145]:

$$\nabla^2 \boldsymbol{A} = j\mu\omega\sigma\boldsymbol{A}$$

This differential equation can be solved for each layer separately, hence, allowing calculating the power flowing through that layer. However since the sensing coil is placed at $y = 0$, the solution should be obtained at this coordinate. As a result the differential equation is solved for the layers immediately beneath and above the coil. These two solutions are then added together to obtain the effect of materials in both positive and negative y-direction. The eddy current formulation does satisfy the boundary conditions discussed in Chapter–II as well. These boundary conditions are:

$$(\boldsymbol{B}_{k+1} - \boldsymbol{B}_k) \cdot \hat{\boldsymbol{j}} = 0 \quad (2)$$

$$\left(\frac{1}{\mu_{k+1}}\boldsymbol{B}_{k+1} - \frac{1}{\mu_k}\boldsymbol{B}_k\right) \times \hat{\boldsymbol{\imath}} = K \quad (3)$$

Thus the MVP can be rewritten as equation 4 with *k* being the index of the layer.

$$\nabla^2 A_k = j\omega\mu_k\sigma_k A_k \quad (4)$$

Using the method of separation of variables [151] and the analysis in [145], we can write the solution to this differential equation for the 2D case of Figure 0-1 with $\hat{\boldsymbol{z}}$ being a unit vector in the z-direction as:

$$A_k(x, y) = Y_k(y)X_k(x)\hat{\boldsymbol{z}} \quad (5)$$

Set Y_k and X_k to be:

$$X_k = cos(mx) \quad (6)$$

$$Y_k = M_k e^{\gamma_k y} + N_k e^{-\gamma_k y} \quad (7)$$

The coefficients, *m* and γ, are constrained by equation 8. As non-magnetic materials are employed in this analysis the relative permeability of each layer is set to the permeability of free space.

$$\gamma_k^2 - m^2 = j\omega\mu_0\sigma_k \quad (8)$$

Given that the applied current flows in the z-direction, the $\boldsymbol{B}$ field is found to be:

$$\boldsymbol{B} = \nabla \times \boldsymbol{A}_z \quad (9)$$

$$\boldsymbol{B} = \begin{bmatrix} \boldsymbol{i} & \boldsymbol{j} & \boldsymbol{k} \\ \dfrac{\partial}{\partial x} & \dfrac{\partial}{\partial y} & \dfrac{\partial}{\partial z} \\ 0 & 0 & \boldsymbol{A}_z \end{bmatrix} \quad (10)$$

$$\boldsymbol{B} = \mathbf{i}\frac{\partial}{\partial \mathrm{y}}\boldsymbol{A}_z - \boldsymbol{j}\frac{\partial}{\partial x}\boldsymbol{A}_z \quad (11)$$

Equation 11 can now be substituted into equations 2 and 3. Dropping the *z* subscript for convenience and only referring to the layer number, from equation 2 we have:

$$\frac{\partial}{\partial x}\boldsymbol{A}_k = \frac{\partial}{\partial x}\boldsymbol{A}_{k+1} \quad (12)$$

$$\frac{\partial}{\partial x}Y_k(y)X_k(x) = \frac{\partial}{\partial x}Y_{k+1}(y)X_{k+1}(x) \quad 13$$

$$\frac{\partial}{\partial x}Y_k(y)X_k(x) = -m(M_k e^{\gamma_k y} + N_k e^{-\gamma_k y})sin(mx) \quad 14$$

Hence

$$-m(M_k e^{\gamma_k y} + N_k e^{-\gamma_k y})sin(mx) = -m(M_{k+1} e^{\gamma_{k+1} y} + N_{k+1} e^{-\gamma_{k+1} y})sin(mx)$$

$$M_k e^{\gamma_k y} + N_k e^{-\gamma_k y} = M_{k+1} e^{\gamma_{k+1} y} + N_{k+1} e^{-\gamma_{k+1} y} \quad 15$$

Using a similar approach and for any layer with $k > 1$ or $k' > 1$, from equation 3 we shall have:

$$\frac{1}{\mu_k}\frac{\partial}{\partial y}(Y_k X_k) = \frac{1}{\mu_{k+1}}\frac{\partial}{\partial y}(Y_{k+1} X_{k+1}) \quad 16$$

$$\frac{1}{\mu_k}(\gamma_k M_k e^{\gamma_k y} - \gamma_k N_k e^{-\gamma_k y})cos(mx)$$

$$= \frac{1}{\mu_{k+1}}(\gamma_{k+1} M_{k+1} e^{\gamma_{k+1} y} - \gamma_{k+1} N_{k+1} e^{-\gamma_{k+1} y})cos(mx)$$

Leading to

$$\frac{1}{\mu_k}\gamma_k M_k e^{\gamma_k y} - \frac{1}{\mu_k}\gamma_k N_k e^{-\gamma_k y} = \frac{1}{\mu_{k+1}}\gamma_{k+1} M_{k+1} e^{\gamma_{k+1} y} - \frac{1}{\mu_{k+1}}\gamma_{k+1} N_{k+1} e^{-\gamma_{k+1} y}$$

Thus

$$\frac{\mu_{k+1}}{\mu_k}\frac{\gamma_k}{\gamma_{k+1}}(M_k e^{\gamma_k y} - N_k e^{-\gamma_k y}) = M_{k+1} e^{\gamma_{k+1} y} - N_{k+1} e^{-\gamma_{k+1} y}$$

$$\lambda_k = \frac{\mu_{k+1}}{\mu_k}\frac{\gamma_k}{\gamma_{k+1}} \quad 17$$

$$\lambda_k(M_k e^{\gamma_k y} - N_k e^{-\gamma_k y}) = M_{k+1} e^{\gamma_{k+1} y} - N_{k+1} e^{-\gamma_{k+1} y} \quad 18$$

We can now use equations 15 and 18 to derive the formula for coefficients *M* and *N*. These two equations are repeated below:

$$M_k e^{\gamma_k y} + N_k e^{-\gamma_k y} = M_{k+1} e^{\gamma_{k+1} y} + N_{k+1} e^{-\gamma_{k+1} y}$$

$$\lambda_k(M_k e^{\gamma_k y} - N_k e^{-\gamma_k y}) = M_{k+1} e^{\gamma_{k+1} y} - N_{k+1} e^{-\gamma_{k+1} y}$$

This is a set of simultaneous equations. To find the unknown values, M_k and N_k, we shall at first add the two equations:

$$(1 + \lambda_k)M_k e^{\gamma_k y} + (1 - \lambda_k)N_k e^{-\gamma_k y} = 2M_{k+1} e^{\gamma_{k+1} y}$$

$$M_{k+1}e^{\gamma_{k+1}y} = \frac{1}{2}[(1+\lambda_k)M_k e^{\gamma_k y} + (1-\lambda_k)N_k e^{-\gamma_k y}]$$

Dividing the terms inside square bracket by $e^{\gamma_{k+1}y}$, we now have:

$$M_{k+1}e^{\gamma_{k+1}y} = \frac{1}{2}e^{\gamma_{k+1}y}[(1+\lambda_k)M_k e^{\gamma_k y-\gamma_{k+1}y} + (1-\lambda_k)N_k e^{-\gamma_k y-\gamma_{k+1}y}]$$

$$M_{k+1} = \frac{1}{2}[(1+\lambda_k)M_k e^{\gamma_k y-\gamma_{k+1}y} + (1-\lambda_k)N_k e^{-\gamma_k y-\gamma_{k+1}y}] \quad 19$$

Subtracting equations 17 and 18 from one another will lead to:

$$(1-\lambda_k)M_k e^{\gamma_k y} + (1+\lambda_k)N_k e^{-\gamma_k y} = 2N_{k+1}e^{-\gamma_{k+1}y}$$

Rearranging this equation and taking out $e^{-\gamma_{k+1}y}$ as the common factor:

$$N_{k+1}e^{-\gamma_{k+1}y} = \frac{1}{2}e^{-\gamma_{k+1}y}\left[(1-\lambda_k)M_k e^{(\gamma_k+\gamma_{k+1})y} + (1+\lambda_k)N_k e^{(-\gamma_k+\gamma_{k+1})y}\right]$$

Cancelling out common terms leads to:

$$N_{k+1} = \frac{1}{2}\left[(1-\lambda_k)M_k e^{(\gamma_k+\gamma_{k+1})y} + (1+\lambda_k)N_k e^{(-\gamma_k+\gamma_{k+1})y}\right] \quad 20$$

Equations 19 and 20 can be put together in a matrix to form:

$$\begin{bmatrix}M_{k+1}\\N_{k+1}\end{bmatrix} = \frac{1}{2}\begin{bmatrix}(1+\lambda_k)e^{(\gamma_k-\gamma_{k+1})y} & (1-\lambda_k)e^{-(\gamma_k+\gamma_{k+1})y}\\(1-\lambda_k)e^{(\gamma_k+\gamma_{k+1})y} & (1+\lambda_k)e^{(-\gamma_k+\gamma_{k+1})y}\end{bmatrix}\begin{bmatrix}M_k\\N_k\end{bmatrix} \quad 21$$

This matrix holds for all values of $k > 1$. Similar approach can be used to derive the same matrix for *y*-values in the negative direction with the matrix being valid for all $k' > 1$. Taking the boundary conditions into account and the fact that as the distance from the coils tends to infinity, $y \to \pm\infty$, the vector potential becomes weaker and $A \to 0$. Hence for *k* layers above the coil and *k'* layers beneath the coil we can write $M_{k+1} = 0$ and $N_{k'+1} = 0$. At $y = 0$ the boundary condition in equations 2 and 3 provides us with another set of equations. Using these equations along with equation 11, we can write a set of equations for the two layers in which the coil is embedded [145, 152]:

$$\frac{\partial}{\partial x}A_1 = \frac{\partial}{\partial x}A_{1'} \quad 22$$

$$\frac{1}{\mu_1}\frac{\partial}{\partial y}A_1 - \frac{1}{\mu_{1'}}\frac{\partial}{\partial y}A_{1'} = \frac{I}{\pi}\int_0^\infty cos(mx)\,dm \quad 23$$

The quantity on the right hand side of the equation 23 is the surface current density due to the current flowing inside the sensing coil. Equation 21 for all layers $k > 1$ and its equivalent for all layers $k' > 1$ along with the two equations in 22 and 23 for the interface of $k' = 1$ and $k = 1$, provide a complete set of values for the coefficients of the solution to the differential equation narrated for an eddy current problem. Note that the material properties, which affect the sensing mechanism, in another word they are sensed, are incorporated into the coefficient values M_k, $M_{k'}$, N_k and $N_{k'}$. The total sum of the vector potential equations in both negative and positive directions of *y* will then provide us with the complete expression for *A*.

We treated the MVP equation for a multi-layered system for eddy current measurements in the previous section. However the analysis was only done for one filament. We shall now define an N-turn inductor for eddy current measurements and then undertake an energy analysis on the structure. Figure 0-2 shows the 2D structure of an N-turn coil. Only two turns of the coil are shown here. The values $d_1 \cdots d_N$ represent the distance from the centre of the coil, shown by a vertical dashed line, to the centre of the current carrying conductor. Also assume that end effects at the filaments can be neglected and a universal average length shall be taken for all of the conducting filaments. This is to simplify the analysis at hand.

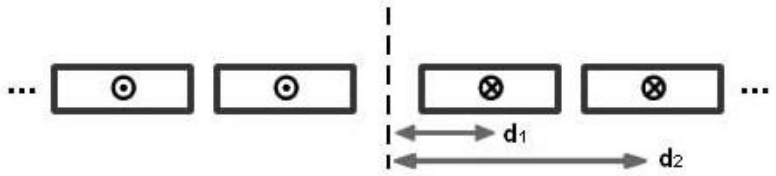

Figure 0-2: showing the 2D structure of a multi turn coil. Distances are shown from the centre of the coil.

Poynting's vector is found to be:

$$\boldsymbol{S} = \frac{1}{2}(\boldsymbol{E} \times \boldsymbol{H}^*)$$

Applying this equation to Figure 0-2 at $y = 0$ and integrating over the x-axis we can find the power crossing into various layers including the material under test [145]. Thus:

$$P + jQ = \int_{-\infty}^{+\infty} \frac{1}{2}(\boldsymbol{E} \times \boldsymbol{H}^*) \cdot \hat{\boldsymbol{y}} dx \qquad 24$$

As we are interested in the magnetic effects in the system we can let $\boldsymbol{E} = -j\omega \boldsymbol{A}$, hence:

$$P + jQ = \int_{-\infty}^{+\infty} \frac{1}{2}\left(-j\omega \boldsymbol{A} \times \frac{1}{\mu}\nabla \times \boldsymbol{A}^*\right) \cdot \hat{\boldsymbol{y}} dx \qquad 25$$

$$P + jQ = -\frac{j\omega}{2\mu}\int_{-\infty}^{+\infty} (\boldsymbol{A} \times \nabla \times \boldsymbol{A}^*) \cdot \hat{\boldsymbol{y}}\, dx \qquad 26$$

Noting that the magnetic vector potential flows in the z-direction for our 2D problem:

$$\nabla \times \boldsymbol{A}_z^* = \begin{vmatrix} \boldsymbol{i} & \boldsymbol{j} & \boldsymbol{k} \\ \partial_x & \partial_y & \partial_z \\ 0 & 0 & \boldsymbol{A}_z^* \end{vmatrix}$$

$$\nabla \times \boldsymbol{A}_z^* = \mathbf{i}\frac{\partial}{\partial \mathrm{y}}\boldsymbol{A}_z^* - \boldsymbol{j}\frac{\partial}{\partial x}\boldsymbol{A}_z^*$$

$$\mathbf{A}_z \times \nabla \times \boldsymbol{A}_z^* = \begin{vmatrix} \boldsymbol{i} & \boldsymbol{j} & \boldsymbol{k} \\ 0 & 0 & \boldsymbol{A}_z \\ \dfrac{\partial}{\partial \mathrm{y}}\boldsymbol{A}_z^* & -\dfrac{\partial}{\partial x}\boldsymbol{A}_z^* & 0 \end{vmatrix} \Rightarrow \begin{bmatrix} \boldsymbol{i}\boldsymbol{A}_z \dfrac{\partial}{\partial x}\boldsymbol{A}_z^* \\ \boldsymbol{j}\boldsymbol{A}_z \dfrac{\partial}{\partial \mathrm{y}}\boldsymbol{A}_z^* \\ 0 \end{bmatrix}^T \qquad 27$$

Using equations 5 to 7 we can write the magnetic vector potential for a single layer as:

$$A = (M_k e^{\gamma_k y} + N_k e^{-\gamma_k y}) \cos mx \qquad 28$$

The more general solution is

$$A = \int_0^{+\infty} (M_k e^{\gamma_k y} + N_k e^{-\gamma_k y}) \cos mx \;\; dm \qquad 29$$

From equation 8 we have:

$$\gamma_k^2 = m^2 + j\omega\mu_k\sigma_k \qquad 30$$

As γ_k is a function of *m*, we can replace the terms inside the brackets of equation 28 by $f(y, m)$. Thus:

$$A = f(y, m) \cos mx$$

Hence

$$P + jQ = -\frac{j\omega}{2\mu}\int_{-\infty}^{+\infty} \boldsymbol{A}_z \frac{\partial}{\partial \mathrm{y}}\boldsymbol{A}_z^* dx$$

$$P + jQ = -\frac{j\omega}{2\mu}\int_{-\infty}^{+\infty} (f(y, m) \cos mx)\left(\frac{\partial}{\partial \mathrm{y}} f^*(y, n) \cos nx\right) dx \qquad 31$$

Equation 31 is the core part of the power flow calculation from a sensing coil to a material under test. Note the introduction of the dummy variable *n*, which is for mathematical rigidity of the expression however the nature of this variable is similar to *m*. Using equation 29 we can write:

$$P + jQ = -\frac{j\omega}{2\mu}\int_{-\infty}^{+\infty} dx \left[\int_{0}^{+\infty} f(y,m)\cos mx\, dm\right]\left[\int_{0}^{+\infty} \frac{\partial}{\partial \mathrm{y}} f^{*}(y,n)\cos nx\, dn\right]$$

Using the Fubini's theorem for a set of converging functions:

$$\int F(x)\, dx \int F(y) dy = \int F(x,y) dx dy$$

We can change the order of the integration and rearrange the variables to obtain:

$$P + jQ = -\frac{j\omega}{2\mu}\int_{-\infty}^{+\infty} \cos mx \cos nx\, dx \int_{0}^{+\infty} f(y,m)\frac{\partial}{\partial \mathrm{y}} f^{*}(y,n) dm\, dn \qquad 32$$

The first part of the integration can be evaluated to be [176]:

$$\int \cos mx \cos nx\, dx = \frac{sin\big(x(m-n)\big)}{2(m-n)} + \frac{sin\big(x(m+n)\big)}{2(m+n)}$$

For a bounded integral, we can set the limits of the integration to a finite number, *L*, and then take the limit of the overall equation. Using the identity $-\sin ax = sin - ax$, we can write:

$$\lim_{L\to\infty}\int_{-L}^{+L} \cos mx \cos nx\, dx$$

$$= \lim_{L\to\infty}\left[\frac{\sin L(m-n)}{2(m-n)} + \frac{\sin L(m+n)}{2(m+n)} + \frac{\sin L(m-n)}{2(m-n)} + \frac{\sin L(m+n)}{2(m+n)}\right]$$

Leading to

$$\lim_{L\to\infty}\left[\frac{\sin L(m-n)}{(m-n)} + \frac{\sin L(m+n)}{(m+n)}\right] = \pi\big(\delta(m-n) + \delta(m+n)\big)$$

This expression is equal to π as long as $m = n$ or $m = -n$. Assuming the former case, we can reduce equation 32 to:

$$P + jQ = -\frac{j\omega\pi}{2\mu}\int_{0}^{+\infty} f(y,m)\frac{\partial}{\partial \mathrm{y}} f^{*}(y,m) dm \qquad 33$$

We can use similar approach to calculate this expression for an N-turn inductor depicted in Figure 0-2. Following the analysis in [145], equation 33 can be rewritten for an N-turn inductor as:

$$P + jQ = -\frac{j\omega\pi}{2\mu}\int_0^{+\infty}\left(f(y,m)\frac{\partial}{\partial \mathrm{y}}f^*(y,m)\right)\left(\sum_{i=1}^{N} sin(md_1 \cdots md_N)\right)dm \qquad 34$$

Equations 33 and 34 provide the foundation for the power crossing the surface enclosing a single filament and an array of them for the case of $y > 0$ in Figure 0-1. Similar principle is used to calculate the power crossing the surface in the direction of $y \to -\infty$. The total sum of these two contributions will yield the total energy crossing the enclosing materials of the inductor coils [152].

References

[1] R. L. Baldwin, "Energetics of Protein Folding," *Journal of Molecular Biology,* vol. 371, pp. 283-301, 2007.

[2] J. B. Hubbard, L. Onsager, W. M. Vanbeek, and M. Mandel, "KINETIC POLARIZATION DEFICIENCY IN ELECTROLYTE-SOLUTIONS," *Proceedings of the National Academy of Sciences of the United States of America,* vol. 74, pp. 401-404, 1977.

[3] L. Lijie and D. Uttamchandani, "Flip-Chip Distributed MEMS Transmission Lines (DMTLs) for Biosensing Applications," *Industrial Electronics, IEEE Transactions on,* vol. 56, pp. 986-990, 2009.

[4] A. G. Markelz, "Terahertz dielectric sensitivity to biomolecular structure and function," *Ieee Journal of Selected Topics in Quantum Electronics,* vol. 14, pp. 180-190, Jan-Feb 2008.

[5] R. Richards-Kortum and E. Sevick-Muraca, "QUANTITATIVE OPTICAL SPECTROSCOPY FOR TISSUE DIAGNOSIS," *Annual Review of Physical Chemistry,* vol. 47, pp. 555-606, 1996.

[6] Z. Hou, B. Cai, and H. Liu, "Sensing of atomized liquids through field effects of polarization and ionization induced by nanostructures," *Applied Physics Letters,* vol. 94, pp. 223503-3, 2009.

[7] L. Shepherd and C. Toumazou, "Weak Inversion ISFETs for ultra-low power biochemical sensing and real-time analysis," *Sensors and Actuators B: Chemical,* vol. 107, pp. 468-473, 2005.

[8] W. E. Gardner, *Improving the effectiveness and reliability of non-destructive testing*: Pergamon Press, 1992.

[9] R. S. Popovic, J. A. Flanagan, and P. A. Besse, "The future of magnetic sensors," *Sensors and Actuators A: Physical,* vol. 56, pp. 39-55, 1996.

[10] M. George, "Liquid water and ices: understanding the structure and physical properties," *Journal of Physics: Condensed Matter,* p. 283101, 2009.

[11] J. N. Murrel and A. D. Jenkins, *Properties of Liquids and Solutions*, 2nd ed.: John Wiley & Sons, 1994.

[12] A. G. Donchev, N. G. Galkin, A. A. Illarionov, O. V. Khoruzhii, M. A. Olevanov, V. D. Ozrin, *et al*., "Water properties from first principles: Simulations by a general-purpose quantum mechanical polarizable force field," *Proceedings of the National Academy of Sciences,* vol. 103, pp. 8613-8617, June 6, 2006 2006.

[13] E. Zoidis, J. Yarwood, and M. Besnard, "Far-Infrared Studies on the Intermolecular Dynamics of Systems Containing Water. The Influence of Ionic Interactions in NaCl, LiCl, and HCl Solutions," *The Journal of Physical Chemistry A,* vol. 103, pp. 220-225, 1999.

[14] S. J. Suresh and V. M. Naik, "Hydrogen bond thermodynamic properties of water from dielectric constant data," *The Journal of Chemical Physics,* vol. 113, pp. 9727-9732, 2000.

[15] B. Dirk, K. Claudia, K. Alexander, K. Petra, R. Thomas, J. Matthias, *et al*., "Chemistry in Supercritical Water," *Angewandte Chemie International Edition,* vol. 38, pp. 2998-3014, 1999.

[16] S. I. Smedley, *The Interpretation of Ionic Conductivity in Liquids*: Plenum Press New York and London, 1980.

[17] P. W. Atkins, *Physical Chemistry Atkins*, Sixth ed.: Oxford University Press, 1999.

[18] P. Atkins, J. d. Paula, and R. Friedman, *Quanta, Matter and Change: A Molecular Approach to Physical Chemistry*: Oxford University Press, 2009.
[19] A. de Diego, A. Usobiaga, and J. M. Madariaga, "Critical comparison among equations derived from the Falkenhagen model to fit conductimetric data of concentrated electrolyte solutions," *Journal of Electroanalytical Chemistry,* vol. 446, pp. 177-187, 1998.
[20] A. Chandra, R. Biswas, and B. Bagchi, "Molecular Origin of the Debye−Huckel−Onsager Limiting Law of Ion Conductance and Its Extension to High Concentrations: Mode Coupling Theory Approach to Electrolyte Friction," *Journal of the American Chemical Society,* vol. 121, pp. 4082-4083, 1999.
[21] H. Falkenhagen, "The Principal Ideas in the Interionic Attraction Theory of Strong Electrolytes," *Reviews of Modern Physics*, vol. 3, p. 412, 1931.
[22] R. F. Douglas E. Goldsack, Arlene (Anttila) Franchetto, "Solvation effects on the conductivity of concentrated electrolyte solutions," *Canadian Journal of Chemistry,* vol. 54, pp. 2953-2966, 1976.
[23] E. N. Tsurko, R. Neueder, J. Barthel, and A. Apelblat, "Conductivity of Phosphoric Acid, Sodium, Potassium, and Ammonium Phosphates in Dilute Aqueous Solutions from 278.15 K to 308.15 K," *Journal of Solution Chemistry,* vol. 28, pp. 973-999, 1999.
[24] J. Quint and A. Viallard, "Electrical conductance of electrolyte mixtures of any type," *Journal of Solution Chemistry,* vol. 7, pp. 533-548, 1978.
[25] H. L. Bianchi, I. Dujovne, and R. Fernández-Prini, "Comparison of Electrolytic Conductivity Theories: Performance of Classical and New Theories," *Journal of Solution Chemistry,* vol. 29, pp. 237-253, 2000.
[26] H. C. W. H. Haken, *Molecular Physics and Elements of Quantum Chemistry*: Springer, 2003.
[27] N. E. Hill, W. E. Vaughan, A. H. Price, and M. Davies, *Dielectric Properties & Molecular Behaviour*, 1st ed.: Van Nostrand Reinhold Company London, 1969.
[28] J. B. Hasted, *Aqeous Dielectrics*: William Clowes & Sons Limited, 1973.
[29] J. D. Jackson, *Classical Electrodynamics* Wiley, 1999.
[30] V. V. Daniel, *Dielectric Relaxation*: Academic Press, London & New York, 1967.
[31] M. Mandel and T. Odijk, "Dielectric Properties of Polyelectrolyte Solutions," *Annual Review of Physical Chemistry,* vol. 35, pp. 75-108, 1984.
[32] N. Nandi, K. Bhattacharyya, and B. Bagchi, "Dielectric Relaxation and Solvation Dynamics of Water in Complex Chemical and Biological Systems," *Chemical Reviews,* vol. 100, pp. 2013-2046, 05/12/ 2000.
[33] B. Bagchi, "Water Dynamics in the Hydration Layer around Proteins and Micelles," *Chemical Reviews,* vol. 105, pp. 3197-3219, 2005.
[34] M. Y. Kiriukhin and K. D. Collins, "Dynamic hydration numbers for biologically important ions," *Biophysical Chemistry,* vol. 99, pp. 155-168, 2002.
[35] F. Bordi, C. Cametti, and R. H. Colby, "Dielectric spectroscopy and conductivity of polyelectrolyte solutions," *Journal of Physics-Condensed Matter,* vol. 16, pp. R1423-R1463, Dec 2004.
[36] J. Barret, *Inorganic Chemistry in Aqueous Solutions*: The Royal Society of Chemistry, 2003.
[37] K. M. Taylor and D. W. van der Weide, "Ultra-sensitive detection of protein thermal unfolding and refolding using near-zone microwaves," *Ieee Transactions on Microwave Theory and Techniques,* vol. 53, pp. 1576-1586, May 2005.
[38] C. Grosse and A. V. Delgado, "Dielectric dispersion in aqueous colloidal systems," *Current Opinion in Colloid & Interface Science,* vol. 15, pp. 145-159, 2010.

[39] W. J. Ellison, K. Lamkaouchi, and J. M. Moreau, "Water: a dielectric reference," *Journal of Molecular Liquids,* vol. 68, pp. 171-279, 4// 1996.
[40] D. K. Wood, S. H. Oh, S. H. Lee, H. T. Soh, and A. N. Cleland, "High-bandwidth radio frequency Coulter counter," *Applied Physics Letters,* vol. 87, pp. 184106-3, 2005.
[41] C. Song and P. Wang, "A radio frequency device for measurement of minute dielectric property changes in microfluidic channels," *Applied Physics Letters,* vol. 94, pp. 023901-3, 2009.
[42] C. Song, J. E. Harriss, and P. Wang, "Compensating on-chip transmission line losses for a high-sensitivity microwave sensor," *Sensors and Actuators A: Physical,* vol. 154, pp. 7-11, 2009.
[43] Y. Yang, H. Zhang, J. Zhu, G. Wang, T.-R. Tzeng, X. Xuan, *et al*., "Distinguishing the viability of a single yeast cell with an ultra-sensitive radio frequency sensor," *Lab on a Chip,* vol. 10, pp. 553-555, 2010.
[44] G. R. Facer, D. A. Notterman, and L. L. Sohn, "Dielectric spectroscopy for bioanalysis: From 40 Hz to 26.5 GHz in a microfabricated wave guide," *Applied Physics Letters,* vol. 78, pp. 996-998, Feb 2001.
[45] M. Olapinski, S. Manus, M. George, A. Bruggemann, N. Fertig, and F. C. Simmel, "Detection of lipid bilayer and peptide pore formation at gigahertz frequencies," *Applied Physics Letters,* vol. 88, pp. 013902-3, 2006.
[46] J. C. Booth, N. D. Orloff, X. L. Lu, Y. Wang, E. Rocas, J. Mateu, *et al*., "Quantitative permittivity measurements of nanoliter fluid volumes from 50 MHz to 40 GHz with microfluidic channels," in *Precision Electromagnetic Measurements (CPEM), 2010 Conference on*, 2010, pp. 353-354.
[47] J. C. Booth, N. D. Orloff, J. Mateu, M. Janezic, M. Rinehart, and J. A. Beall, "Quantitative Permittivity Measurements of Nanoliter Liquid Volumes in Microfluidic Channels to 40 GHz," *Instrumentation and Measurement, IEEE Transactions on,* vol. 59, pp. 3279-3288, 2010.
[48] L. J. Li, "Simultaneous detection of organic and inorganic substances in a mixed aqueous solution using a microwave dielectric sensor," *Progress In Electromagnetics Research C,* vol. 14, p. 8, 2010.
[49] L. Li and Z. Liu, "Study of Temperature Characteristics of Micromachined Suspended Coplanar Waveguides for Biosensing Applications," *Sensors,* vol. 11, pp. 2640-2651, 2011.
[50] Q. Chen, D. Roitman, and A. Knoesen, "Detection of biomolecular surface interactions by transit time measurements with a coplanar transmission line probe," *Sensors and Actuators A: Physical,* vol. 152, pp. 151-159, 2009.
[51] C. Qin, J. McMurdie, D. Roitman, and A. Knoesen, "Microwave transmission line dielectric probe to detect biomolecular surface interactions," in *Engineering in Medicine and Biology Society, 2004. IEMBS '04. 26th Annual International Conference of the IEEE*, 2004, pp. 1990-1993.
[52] C. Dalmay, A. Pothier, M. Cheray, F. Lalloue, M.-O. Jauberteau, and P. Blondy, "Label-free RF biosensors for human cell dielectric spectroscopy," *International Journal of Microwave and Wireless Technologies,* vol. 1, pp. 497-504, 2009.
[53] C. Dalmay, M. Cheray, A. Pothier, F. Lalloué, M. O. Jauberteau, and P. Blondy, "Ultra sensitive biosensor based on impedance spectroscopy at microwave frequencies for cell scale analysis," *Sensors and Actuators A: Physical,* vol. 162, pp. 189-197, 2010.

[54] X. F. Zhu, M. Harder, A. Wirthmann, B. Zhang, W. Lu, Y. S. Gui, *et al*., "Dielectric measurements via a phase-resolved spintronic technique," *Physical Review B,* vol. 83, p. 104407, 2011.
[55] M. C. Beard, G. M. Turner, and C. A. Schmuttenmaer, "Terahertz Spectroscopy," *The Journal of Physical Chemistry B,* vol. 106, pp. 7146-7159, 2002.
[56] J.-H. Son, "Terahertz electromagnetic interactions with biological matter and their applications," *Journal of Applied Physics,* vol. 105, pp. 102033-10, 2009.
[57] A. Moran and S. Mukamel, "The origin of vibrational mode couplings in various secondary structural motifs of polypeptides," *Proceedings of the National Academy of Sciences of the United States of America,* vol. 101, pp. 506-510, January 13, 2004 2004.
[58] M. Bykhovskaia, B. Gelmont, T. Globus, D. L. Woolard, A. C. Samuels, T. H. Duong, *et al*., "Prediction of DNA far-IR absorption spectra based on normal mode analysis," *Theoretical Chemistry Accounts: Theory, Computation, and Modeling (Theoretica Chimica Acta),* vol. 106, pp. 22-27, 2001.
[59] B. M. Fischer, H. Helm, and P. U. Jepsen, "Chemical Recognition With Broadband THz Spectroscopy," *Proceedings of the Ieee,* vol. 95, pp. 1592-1604, 2007.
[60] K. Fukunaga, I. Hosako, Y. Ogawa, and S. Hayashi, "THz Spectroscopy for analysis of paintings," in *Electrical Insulation and Dielectric Phenomena, 2007. CEIDP 2007. Annual Report - Conference on*, 2007, pp. 715-718.
[61] K. Fukunaga, I. Hosako, Y. Ogawa, and S. Hayashi, "THz spectroscopy for art conservation science," in *Infrared and Millimeter Waves, 2007 and the 2007 15th International Conference on Terahertz Electronics. IRMMW-THz. Joint 32nd International Conference on*, 2007, pp. 678-679.
[62] J.-Y. Chen, J. R. Knab, S. Ye, Y. He, and A. G. Markelz, "Terahertz dielectric assay of solution phase protein binding," *Applied Physics Letters,* vol. 90, pp. 243901-3, 2007.
[63] A. J. Baragwanath, G. P. Swift, D. Dai, A. J. Gallant, and J. M. Chamberlain, "Silicon based microfluidic cell for terahertz frequencies," *Journal of Applied Physics,* vol. 108, pp. 013102-8, 2010.
[64] J. Grade, P. Haydon, and D. van der Weide, "Electronic Terahertz Antennas and Probes for Spectroscopic Detection and Diagnostics," *Proceedings of the Ieee,* vol. 95, pp. 1583-1591, 2007.
[65] P. C. Ashworth, E. Pickwell-MacPherson, E. Provenzano, S. E. Pinder, A. D. Purushotham, M. Pepper, *et al*., "Terahertz pulsed spectroscopy of freshly excised human breast cancer," *Opt. Express,* vol. 17, pp. 12444-12454, 2009.
[66] B. Lahiri, A. Z. Khokhar, R. M. De La Rue, S. G. McMeekin, and N. P. Johnson, "Asymmetric split ring resonators for optical sensing of organic materials," *Opt. Express,* vol. 17, pp. 1107-1115, 2009.
[67] E. Cubukcu, S. Zhang, Y.-S. Park, G. Bartal, and X. Zhang, "Split ring resonator sensors for infrared detection of single molecular monolayers," *Applied Physics Letters,* vol. 95, pp. 043113-3, 2009.
[68] T. Zhang, Z. Cheng, Y. Wang, Z. Li, C. Wang, Y. Li, *et al*., "Self-Assembled 1-Octadecanethiol Monolayers on Graphene for Mercury Detection," *Nano Letters,* vol. 10, pp. 4738-4741, 2010.
[69] T. Ohkubo, M. Onuma, J. Kitagawa, and Y. Kadoya, "Micro-strip-line-based sensing chips for characterization of polar liquids in terahertz regime," *Applied Physics Letters,* vol. 88, pp. 212511-3, 2006.

[70] M. H. A. Treizebre, and B. Bocquet, "Terahertz spiral planar goubau line rejectors for biological characterization," *Progress In Electromagnetics Research M,* vol. 14, p. 13, 2010.
[71] A. Treizebre, T. Akalin, and B. Bocquet, "Planar excitation of Goubau Transmission Lines for THz BioMEMS," *Microwave and Wireless Components Letters, IEEE,* vol. 15, pp. 886-888, 2005.
[72] C. Yeh and F. Shimabukuro, *The Essence of Dielectric Waveguides*: Springer, 2008.
[73] I. G. Inc, *Fiber Optics User's Manual & Design Series*: Information Gatekeepers Inc.
[74] S. Laurette and et al., "Co-integrated microfluidic and THz functions for biochip devices," *Journal of Micromechanics and Microengineering,* vol. 21, p. 065029, 2011.
[75] S. Laurette, A. Treizebre, F. Affouard, and B. Bocquet, "Subterahertz characterization of ethanol hydration layers by microfluidic system," *Applied Physics Letters,* vol. 97, pp. 111904-3, 2010.
[76] A. Abbas, A. Treizebre, P. Supiot, N.-E. Bourzgui, D. Guillochon, D. Vercaigne-Marko, *et al*., "Cold plasma functionalized TeraHertz BioMEMS for enzyme reaction analysis," *Biosensors and Bioelectronics,* vol. 25, pp. 154-160, 2009.
[77] D. R. Thévenot, K. Toth, R. A. Durst, and G. S. Wilson, "Electrochemical Biosensors: Recommended Definitions and Calssification," *Analytical Letters,* vol. 34, pp. 635 - 659, 2001.
[78] J. R. Stetter, W. R. Penrose, and S. Yao, "Sensors, Chemical Sensors, Electrochemical Sensors, and ECS," *Journal of The Electrochemical Society,* vol. 150, pp. S11-S16, 2003.
[79] S. Laschi and M. Mascini, "Planar electrochemical sensors for biomedical applications," *Medical Engineering & Physics,* vol. 28, pp. 934-943, 2006.
[80] J. Wang and Q. Chen, "Enzyme Microelectrode Array Strips for Glucose and Lactate," *Analytical Chemistry,* vol. 66, pp. 1007-1011, 1994/04/01 1994.
[81] J. Wang, G. Rivas, M. Ozsoz, D. H. Grant, X. Cai, and C. Parrado, "Microfabricated Electrochemical Sensor for the Detection of Radiation-Induced DNA Damage," *Analytical Chemistry,* vol. 69, pp. 1457-1460, 1997.
[82] J. Wang, X. Cai, B. Tian, and H. Shiraishi, "Microfabricated thick-film electrochemical sensor for nucleic acid determination," *Analyst,* vol. 121, pp. 965-969, 1996.
[83] A. Ferancová, L. Rassaei, F. Marken, J. Labuda, and M. Sillanpää, "dsDNA modified carbon nanofiber—solidified paste electrodes: probing Ni(II)—dsDNA interactions," *Microchimica Acta,* vol. 170, pp. 155-164, 2010.
[84] A. Cagnini, I. Palchetti, I. Lionti, M. Mascini, and A. P. F. Turner, "Disposable ruthenized screen-printed biosensors for pesticides monitoring," *Sensors and Actuators B: Chemical,* vol. 24, pp. 85-89, 1995.
[85] I. Palchetti, A. Cagnini, M. Del Carlo, C. Coppi, M. Mascini, and A. P. F. Turner, "Determination of anticholinesterase pesticides in real samples using a disposable biosensor," *Analytica Chimica Acta,* vol. 337, pp. 315-321, 1997.
[86] S. B. Ben G. Streetman, *Solid State Electronic Devices*, 5th ed.: Prentice Hall, 2000.
[87] B. Lakard, G. Herlem, M. de Labachelerie, W. Daniau, G. Martin, J.-C. Jeannot, *et al*., "Miniaturized pH biosensors based on electrochemically modified electrodes with biocompatible polymers," *Biosensors and Bioelectronics,* vol. 19, pp. 595-606, 2004.
[88] A. F. Revzin, K. Sirkar, A. Simonian, and M. V. Pishko, "Glucose, lactate, and pyruvate biosensor arrays based on redox polymer/oxidoreductase nanocomposite thin-films deposited on photolithographically patterned gold microelectrodes," *Sensors and Actuators B: Chemical,* vol. 81, pp. 359-368, 2002.

[89] K. B. Male and J. H. T. Luong, "Chiral analysis of neurotransmitters using cyclodextrin-modified capillary electrophoresis equipped with microfabricated interdigitated electrodes," *Journal of Chromatography A*, vol. 1003, pp. 167-178, 2003.
[90] W. Laureyn, D. Nelis, P. Van Gerwen, K. Baert, L. Hermans, R. Magnée, *et al*., "Nanoscaled interdigitated titanium electrodes for impedimetric biosensing," *Sensors and Actuators B: Chemical*, vol. 68, pp. 360-370, 2000.
[91] P. Van Gerwen, W. Laureyn, W. Laureys, G. Huyberechts, M. Op De Beeck, K. Baert, *et al*., "Nanoscaled interdigitated electrode arrays for biochemical sensors," *Sensors and Actuators B: Chemical*, vol. 49, pp. 73-80, 1998.
[92] P. Bergveld, "Thirty years of ISFETOLOGY: What happened in the past 30 years and what may happen in the next 30 years," *Sensors and Actuators B: Chemical*, vol. 88, pp. 1-20, 2003.
[93] M. J. Milgrew and D. R. S. Cumming, "Matching the Transconductance Characteristics of CMOS ISFET Arrays by Removing Trapped Charge," *Electron Devices, IEEE Transactions on*, vol. 55, pp. 1074-1079, 2008.
[94] D. L. Harame, L. J. Bousse, J. D. Shott, and J. D. Meindl, "Ion-sensing devices with silicon nitride and borosilicate glass insulators," *Electron Devices, IEEE Transactions on*, vol. 34, pp. 1700-1707, 1987.
[95] J. N. Chiang, S. G. Ghanayem, and D. W. Hess, "Low-temperature hydrolysis (oxidation) of plasma-deposited silicon nitride films," *Chemistry of Materials*, vol. 1, pp. 194-198, 1989.
[96] N. Jehanathan, B. Walmsley, Y. Liu, and J. Dell, "Oxidation of PECVD SiNx thin films," *Journal of Alloys and Compounds*, vol. 437, pp. 332-338, 2007.
[97] C. F. Lin, W. T. Tseng, and M. S. Feng, "Process optimization of plasma-enhanced chemical vapor deposited passivation thin films for improving nonvolatile memory IC performance," *Japanese Journal of Applied Physics Part 1-Regular Papers Short Notes & Review Papers*, vol. 37, pp. 6364-6368, Dec 1998.
[98] S. Mani and T. Saif, "Stress development in plasma-deposited silicon dioxide thin-films due to hydrogen evolution," *Thin Solid Films*, vol. 515, pp. 3120-3125, 2007.
[99] M. Schöning, "'"Playing around" with Field-Effect Sensors on the Basis of EIS Structures, LAPS and ISFETs," *Sensors*, vol. 5, pp. 126-138, 2005.
[100] B. Premanode and C. Toumazou, "A novel, low power biosensor for real time monitoring of creatinine and urea in peritoneal dialysis," *Sensors and Actuators B: Chemical*, vol. 120, pp. 732-735, 2007.
[101] K. Chang-Soo, S. Hwa-Il, L. Chae-Hyang, and S. Byung-Ki, "Miniaturized ISFET glucose sensor including a new structure actuation system," in *Solid State Sensors and Actuators, 1997. TRANSDUCERS '97 Chicago., 1997 International Conference on*, 1997, pp. 911-914 vol.2.
[102] P. Georgiou and C. Toumazou, "Chemical bionics - a novel design approach using Ion Sensitive Field Effect Transistors," in *Biomedical Circuits and Systems Conference, 2008. BioCAS 2008. IEEE*, 2008, pp. 229-232.
[103] D. Y. Chen, P. K. Chan, and M. S. Tse, "A CMOS ISFET interface circuit for water quality monitoring," in *Sensors, 2005 IEEE*, 2005, p. 4 pp.
[104] Y. H. Ghallab, W. Badawy, and K. V. I. S. Kaler, "A novel pH sensor using differential ISFET current mode read-out circuit," in *MEMS, NANO and Smart Systems, 2003. Proceedings. International Conference on*, 2003, pp. 255-258.
[105] S. Purushothaman, C. Toumazou, and C.-P. Ou, "Protons and single nucleotide polymorphism detection: A simple use for the Ion Sensitive Field Effect Transistor," *Sensors and Actuators B: Chemical*, vol. 114, pp. 964-968, 2006.

[106] D. M. Garner, B. Hua, P. Georgiou, T. G. Constandinou, S. Reed, L. M. Shepherd, *et al*., "A multichannel DNA SoC for rapid point-of-care gene detection," in *Solid-State Circuits Conference Digest of Technical Papers (ISSCC), 2010 IEEE International*, 2010, pp. 492-493.
[107] L. Bandiera, G. Cellere, S. Cagnin, A. De Toni, E. Zanoni, G. Lanfranchi, *et al*., "A fully electronic sensor for the measurement of cDNA hybridization kinetics," *Biosensors and Bioelectronics*, vol. 22, pp. 2108-2114, 2007.
[108] A. Poghossian, L. Berndsen, and M. J. Schöning, "Chemical sensor as physical sensor: ISFET-based flow-velocity, flow-direction and diffusion-coefficient sensor," *Sensors and Actuators B: Chemical*, vol. 95, pp. 384-390, 2003.
[109] A. Poghossian, L. Berndsen, H. Lueth, and M. J. Schoening, "Novel concept for flow-rate and flow-direction determination by means of pH-sensitive ISFETs," San Francisco, CA, USA, 2001, pp. 19-27.
[110] A. Poghossian and M. J. Schöning, "Detecting Both Physical and (Bio-)Chemical Parameters by Means of ISFET Devices," *Electroanalysis*, vol. 16, pp. 1863-1872, 2004.
[111] B.-K. Sohn and C.-S. Kim, "A new pH-ISFET based dissolved oxygen sensor by employing electrolysis of oxygen," *Sensors and Actuators B: Chemical*, vol. 34, pp. 435-440, 1996.
[112] C. V. Dodd and W. E. Deeds, "Analytical Solutions to Eddy-Current Probe-Coil Problems," *Journal of Applied Physics*, vol. 39, pp. 2829-2838, 1968.
[113] R. S. Sharpe, *Research techniques in nondestructive testing*, 1970.
[114] H. Tanaca and M. Hagi, "A Method of Measurement of Plasma Conductivity. I. -Theoretical Approach-," *Japanese Journal of Applied Physics*, vol. 3, p. 335.
[115] H. Tanaca and M. Hagi, "A Method of Measurement of Plasma Conductivity. II. -Example of Measurement-," *Japanese Journal of Applied Physics*, vol. 3, p. 338.
[116] J. H. Williamson, "A high resolution probe for measuring the electrical conductivity of a shock heated plasma," *British Journal of Applied Physics*, vol. 18, p. 317, 1967.
[117] P. Savic and G. T. Boult, "A frequency modulation circuit for the measurement of gas conductivity and boundary layer thickness in a shock tube," *Journal of Scientific Instruments*, vol. 39, p. 258, 1962.
[118] K. P. Dharmasena and H. N. G. Wadley, "Modeling multifrequency eddy current sensor interactions during vertical Bridgman growth of semiconductors," *Review of Scientific Instruments*, vol. 70, pp. 3125-3142, 1999.
[119] P. Wang, Z. Fu, and T. Ding, "A frameless eddy current sensor for cryogenic displacement measurement," *Sensors and Actuators A: Physical*, vol. 159, pp. 7-11, 2010.
[120] D. J. Sadler and C. H. Ahn, "On-chip eddy current sensor for proximity sensing and crack detection," *Sensors and Actuators A: Physical*, vol. 91, pp. 340-345, 2001.
[121] S. Reich, "Percolation and eddy currents in random close packed metal polymer composites," *Journal of Materials Science*, vol. 22, pp. 3391-3394, 1987.
[122] W. R. Myers, "An electrodeless method for the measurement of electrolytic conductivity and magnetic susceptibility," *Journal of Scientific Instruments*, vol. 35, p. 173, 1958.
[123] T. Ishida, K. Monden, and I. Nakada, "Electrodeless method for the measurement of ionic conductivity of RbAg[sub 4]I[sub 5]," *Review of Scientific Instruments*, vol. 57, pp. 3081-3084, 1986.
[124] I. A. Bakar and K. Shida, "New contactless eddy current sensor for the measurement of concentration of electrolyte solution," in *SICE '97. Proceedings of the 36th SICE Annual Conference. International Session Papers*, 1997, pp. 937-940.

[125] A. B. M. Ismail and K. Shida, "New Contactless Inductive Sensor for the Measurement of Concentration of an Electrolytic Solution," *Japanese Journal of Applied Physics,* vol. 36, p. 6558, 1997.
[126] A. B. M. Ismail and K. Shida, "Non-contact multi-sensing technique for the precise measurement of concentration of electrolytic solution," *Sensors and Actuators A: Physical,* vol. 69, pp. 152-155, 1998.
[127] A. B. M. Ismail, S. R. Khan, and K. Shida, "Use of multi-functional sensing for the measurement of electrolytic concentration in solution with higher accuracy," in *Industrial Electronics, 2001. Proceedings. ISIE 2001. IEEE International Symposium on*, 2001, pp. 2033-2037 vol.3.
[128] A. B. M. Ismail and K. Shida, "Estimation of electrolytic concentration in aqueous solution with higher accuracy using electromagnetic multi-functional sensing," *Sensors and Actuators A: Physical,* vol. 102, pp. 205-209, 2003.
[129] J. Heller and J. Feldkamp, "Auto-Tuned Induction Coil Conductivity Sensor for In-Vivo Human Tissue Measurements," *Measurement Science Review,* vol. 9, pp. 162-168, 2009.
[130] B. Ulker Karbeyaz and N. G. Gencer, "Electrical conductivity imaging via contactless measurements: an experimental study," *Medical Imaging, IEEE Transactions on,* vol. 22, pp. 627-635, 2003.
[131] G. Giovannetti, F. Frijia, L. Menichetti, V. Hartwig, V. Viti, and L. Landini, "An efficient method for electrical conductivity measurement in the RF range," *Concepts in Magnetic Resonance Part B: Magnetic Resonance Engineering*, vol. 37B, pp. 160-166, 2010.
[132] G. Laurent, L. M. Hagelsieb, D. Lederer, P. E. Lobert, A. Flandre, J. Remacle, *et al*., "DNA electrical detection based on inductor resonance frequency in standard CMOS technology," in *29th European Solid-State Circuits Conference*, Estoril, Portugal, 2003, pp. 337-340.
[133] N. Denef, L. Moreno-Hagelsieb, G. Laurent, R. Pampin, B. Foultier, J. Remacle, *et al*., "RF detection of DNA based on CMOS inductive and capacitive sensors," in *34th European Microwave Conference (EuMC)*, Amsterdam, NETHERLANDS, 2004, pp. 669-672.
[134] P. R. Nair and M. A. Alam, "Performance limits of nanobiosensors," *Applied Physics Letters,* vol. 88, p. 3, Jun 2006.
[135] R. P. Hertzberg and A. J. Pope, "High-throughput screening: new technology for the 21st century," *Current Opinion in Chemical Biology,* vol. 4, pp. 445-451, 2000.
[136] H.-L. Koh, W.-P. Yau, P.-S. Ong, and A. Hegde, "Current trends in modern pharmaceutical analysis for drug discovery," *Drug Discovery Today,* vol. 8, pp. 889-897, 2003.
[137] A. W. Newman and S. R. Byrn, "Solid-state analysis of the active pharmaceutical ingredient in drug products," *Drug Discovery Today,* vol. 8, pp. 898-905, 2003.
[138] R. F. Harrington, *Time-Harmonic Electromagnetic Fields*: Wiley-IEEE Press, 2001.
[139] A. B. Carlson, *Circuits*, 1st ed.: Brooks/Cole Thomson Learning, 2000.
[140] C. A. Brau, *Modern Problems in Classical Electrodynamics*: Oxford University Press, 2004.
[141] N. Ida, *Engineering Electromagnetics*, 2nd ed.: Springer, 2004.
[142] C. D. Nugent, *Personalised health management systems: the integration of innovative sensing, textile, information and communication technologies*: IOS Press, 2005.
[143] S. Grimnes and ò. G. Martinsen, *Bioimpedance and bioelectricity basics*: Academic, 2008.
[144] B. DiBartolo, *Classical Theory of Electromagnetism*: Prentice Hall, 1991.

[145] A. M. Niknejad and R. G. Meyer, "Analysis of eddy-current losses over conductive substrates with applications to monolithic inductors and transformers," *Microwave Theory and Techniques, IEEE Transactions on*, vol. 49, pp. 166-176, 2001.
[146] A. M. Niknejad and R. G. Meyer, *Design, simulation and applications of inductors and transformers for Si RF ICs*: Kluwer Academic Publishers, 2000.
[147] G.-A. Lee, D. Agahi, and F. De Flaviis, "On-chip spiral inductor in flip-chip technology," *International Journal of Microwave and Wireless Technologies*, vol. 1, pp. 431-440, 2009.
[148] R. Schmitt, *Electromagnetics explained: a handbook for wireless/RF, EMC, and high-speed electronics*: Newnes, 2002.
[149] W. R. P. I. S. Grant, *Electromagnetism*, 2nd ed.: Wiley, 2004.
[150] L. H. D. Jr, "Eddy current losses in transformer windings and circuit wiring," *Texas Instruments*.
[151] G. James, *Advanced modern engineering mathematics*: Pearsons Eductation Limited, 2004.
[152] J. Acero, R. Alonso, L. A. Barragan, and J. M. Burdio, "Modeling of Planar Spiral Inductors Between Two Multilayer Media for Induction Heating Applications," *Magnetics, IEEE Transactions on*, vol. 42, pp. 3719-3729, 2006.
[153] R. L. T. O. C. Zienkiewicz, *The Finite Element Method Set* vol. 1: BUTTERWORTH HEINEMANN, 2005.
[154] K. G. S. Alfred Schmidt, *Design of Adaptive Finite Element Software* vol. 42: Springer, 2005.
[155] S. J. Owen, S. A. Canann, and S. Saigal, "Pyramid elements for maintaining tetrahedra to hexahedra conformability," in *Proceedings of the 1997 Joint ASME/ASCE/SES Summer Meeting, June 29, 1997 - July 2, 1997*, Evanston, IL, USA, 1997, pp. 123-129.
[156] J. Barthel, H. Krienke, and W. Kunz, *Physical chemistry of electrolyte solutions: modern aspects*: Steinkopf, 1998.
[157] J. W. Cleary, R. E. Peale, D. J. Shelton, G. D. Boreman, C. W. Smith, M. Ishigami, *et al*., "IR permittivities for silicides and doped silicon," *J. Opt. Soc. Am. B*, vol. 27, pp. 730-734, 2010.
[158] G. G. Martin Dressel, *Electrodynamics of solids: optical properties of electrons in matter*: Cambridge University Press, 2002.
[159] T. Wessa, N. Barie, M. Rapp, and H. J. Ache, "Polyimide, a new shielding layer for sensor applications," *Sens. Actuators, B*, vol. B53, 1998.
[160] D. M. Pozar, *Microwave Engineering*: John Wiley & Sons, INC., 1998.
[161] R. L. Bunch, D. I. Sanderson, and S. Raman, "Quality factor and inductance in differential IC implementations," *Microwave Magazine, IEEE*, vol. 3, pp. 82-92, 2002.
[162] T. H. Lee, *Planar Microwave Engineering*: Cambridge University Press, 2004.
[163] C. E. Housecroft and E. C. Constable, *Chemistry: An Introduction to Organic, Inorganic, and Physical Chemistry*: Pearson Prentice Hall, 2006.
[164] A. C. Watson, D. Melendy, P. Francis, H. Kyuwoon, and A. Weisshaar, "A comprehensive compact-modeling methodology for spiral inductors in silicon-based RFICs," *Microwave Theory and Techniques, IEEE Transactions on*, vol. 52, pp. 849-857, 2004.
[165] A. Watson, P. Francis, H. Kyuwoon, and A. Weisshaar, "Wide-band distributed modeling of spiral inductors in RFICs," in *Microwave Symposium Digest, 2003 IEEE MTT-S International*, 2003, pp. 1011-1014 vol.2.

[166] G. Wei and Y. Zhiping, "Scalable compact circuit model and synthesis for RF CMOS spiral inductors," *Microwave Theory and Techniques, IEEE Transactions on*, vol. 54, pp. 1055-1064, 2006.
[167] S. Saremi-Yarahmadi, O. H. Murphy, and C. Toumazou, "RF inductive sensors for detection of change in the ionic strength and pH of liquid samples," in *Circuits and Systems (ISCAS), Proceedings of 2010 IEEE International Symposium on*, 2010, pp. 2279-2282.
[168] S. Saremi-Yarahmadi, K. Fobelets, and C. Toumazou, "Coupled RF inductive sensors for monitoring the conductivity of electrolyte solutions," in *Medical Information & Communication Technology (ISMICT), 2011 5th International Symposium on*, 2011, pp. 20-23.
[169] S. Saremi-Yarahmadi, K. Fobelets, and C. Toumazou, "Coupled inductive sensors for monitoring the pH of electrolyte solutions," in *Dielectric Liquids (ICDL), 2011 IEEE International Conference on*, 2011, pp. 1-4.
[170] P. K. Petrov, N. M. N. Alford, and S. Gevorgyan, "Techniques for microwave measurements of ferroelectric thin films and their associated error and limitations," *Measurement Science & Technology*, vol. 16, pp. 583-589, Feb 2005.
[171] M. Damnjanovic, L. Zivanov, G. Radosavljevic, A. Maric, and A. Menicanin, "Parameter extraction of ferrite transformers using S-parameters," in *Power Electronics and Motion Control Conference (EPE/PEMC), 2010 14th International*, 2010, pp. T8-31-T8-36.
[172] M. Q. Gordon, T. Yao, and S. P. Voinigescu, "65-GHz receiver in SiGe BiCMOS using monolithic inductors and transformers," in *Silicon Monolithic Integrated Circuits in RF Systems, 2006. Digest of Papers. 2006 Topical Meeting on*, 2006, p. 4 pp.
[173] C. Kyuchul and X. Ya-Hong, "High-performance on-chip transformers," *Electron Device Letters, IEEE*, vol. 26, pp. 557-559, 2005.
[174] R. F. Weiss, "Carbon dioxide in water and seawater: the solubility of a non-ideal gas," *Marine Chemistry*, vol. 2, pp. 203-215, 1974.
[175] Z. Moron, "Useful formulae enabling interpolation of experimental conductance data of electrolyte solutions, over a wide range of concentrations," *Electrochimica Acta*, vol. 38, pp. 799-805, 1993.
[176] A. Jeffrey, *Mathematics for Engineers and Scientists*, 5th ed.: Chapman & Hall, 1996.